Wireless Power and Data Transmission to High-performance Implantable Medical Devices

A Dissertation

Presented to

The Academic Faculty

By

Mehdi Kiani

In Partial Fulfillment

Of the Requirements for the Degree

Doctor of Philosophy in the

School of Electrical and Computer Engineering

Georgia Institute of Technology

May 2014

Wireless Power and Data Transmission to High-performance Implantable Medical Devices

Approved by:

Dr. Maysam Ghovanloo, Advisor
School of Electrical and Computer Engineering
Georgia Institute of Technology

Dr. Manos Tentzeris
School of Electrical and Computer Engineering
Georgia Institute of Technology

Dr. Farrokh Ayazi
School of Electrical and Computer Engineering
Georgia Institute of Technology

Dr. Joseph Manns
Department of Psychology
Emory University

Dr. Hua Wang
School of Electrical and Computer Engineering
Georgia Institute of Technology

Date Approved: December 13, 2013

To my family and friends

ACKNOWLEDGEMENTS

I would like to express my deepest gratitude to my advisor, Dr. Maysam Ghovanloo for his guidance and generous support. Indeed, it is my greatest honor and pleasure to work under his supervision for my Ph.D. research. His dedication to research, teaching, and students, has truly inspired and influenced me in many ways. If I ever become an educator one day, part of the reason will be because of him. I used to work with engineers, but now I enjoy working more with graduate students.

I would like to thank Dr. Hua Wang for taking time to serve as the chair of my Ph.D proposal examination. Dr. Wang has been really helpful and approachable during this stressful period. In addition, I am grateful to the rest of my committee members, Dr. Farrokh Ayazi, Dr. Joseph Manns, and Dr. Manos Tentzeris. They have been generous in sharing their expertise and suggestions, which helped to further improve my research.

It has been a very long journey. There are so many people to thank, but I would like to start by thanking all the people from my ex- and present colleagues from GT-Bionics lab for their contributions. My dissertation would never have completed without their support over the years. It was a great pleasure and a fun experience working with them. I have learned a lot from all of you.

I want to express my sincerest gratitude to my family for being so supportive of me over all these years. Although they have been far, they always supported me and encouraged me to finish my Ph.D. with high quality work. I would never complete my dissertation with your support. I love you all.

TABLE OF CONTENT

LIST OF TABLES

LIST OF FIGURES

SUMMARY

The objective of my research was to develop novel techniques for high-performance wireless power transmission and data interfacing to implantable medical devices (IMDs). Several system- and circuit-level techniques are proposed towards the development of a novel wireless data and power transmission link for a multi-channel inductively-powered wireless implantable neural-recording and stimulation system (WINeRS).

Such wireless data and power transmission techniques have promising prospects for use in IMDs such as biosensors and neural recording/stimulation devices, neural interfacing experiments in enriched environments, radio-frequency identification (RFID), smartcards, near-field communication (NFC), wireless sensors, and charging mobile devices and electric vehicles. In IMDs, due to battery size, weight, and lifetime limitations, power transmission across a pair of inductively-coupled coils is commonly utilized. The data link is also intended to handle wide bidirectional communication bandwidth with the IMD.

The expected long-term and uninterrupted operation in IMDs outlines the need for efficient design of the inductive link and power-management circuits in the power link. Low-power data transmission techniques in the presence of power interference become especially important for the inductively-powered IMDs where received power is limited. Moreover, neural interfacing in enriched environments for behavioral neuroscience studies on freely-behaving animal subjects outlines the need for automated instruments without the intervention from the human researcher. The proposed techniques in this work will address the abovementioned constraints.

My contributions in this research work are summarized as follows:

1. Development of an RFID-based closed-loop power transmission system
2. Development of a high-performance 3-coil link with optimal design procedure

3. Development of circuit-based theoretical foundation for magnetic-resonance-based power transmission using multiple coils
4. Proposing a figure-of-merit (FoM) for designing high-performance inductive links
5. Development of a low-power and adaptive power management and data transceiver (PMDT) chip to be used as a general-purpose power module for wireless electrophysiology experiments
6. Proposing Q-modulation technique for adaptive load matching and development of a Q-modulation power management (QMPM) chip
7. Development of a new modulation technique called pulse-delay modulation (PDM) for low-power and wideband near-field data communication
8. Development of a pulse-width-modulation impulse-radio ultra-wideband (PWM-IR-UWB) transceiver for low-power and wideband far-field data transmission

CHAPTER I

INTRODUCTION

Near-field power transmission is a viable technique to wirelessly power up devices, such as sensors and actuators, with a wide range of power requirements or recharge their batteries from a short range without any direct electrical contact between the energy source and the device. Moreover, it is possible to use the same short-range wireless link or a separate near-field/far-field link to establish wideband bidirectional data communication with those devices. Wireless implantable microelectronic devices (IMDs) are good examples of where power and data transmission links can be used effectively. IMDs have been significantly improved by going through many generations since the invention of the first implantable pacemaker in 1958 and their importance in several state-of-the-art medical treatments is on the rise [1]. IMDs have the potential to alleviate challenging types of disabilities such as blindness [2], [3], paralysis [4], and loss of limbs [5]. These devices need to transmit and receive information wirelessly across the skin barrier since breaching the skin with interconnect wires would be a source of morbidity for the patient and significantly increases the risk of infection.

In sensory prosthetic devices, which interface with the central nervous system (CNS) to restore a sensory function such as hearing or vision, the quality of perception enhances with the number of stimulating sites and electrodes and the rate of stimulation. These devices may stimulate the neural tissue by means of tens to thousands of stimulating channels and they generally require considerably high power and communication bandwidth [6].

Radio-frequency identification (RFID) takes advantage of inductive links to not only power up the ultralow-power RFID tags but also read the tags' stored information through back telemetry [7]. Because of the significant growth of handheld, wireless, and

mobile electronic devices and gadgets, such as smart phones, tablets, mobile laptops, etc. in recent years, efficient and safe wireless energy transfer to wirelessly charge such devices to cut the last cord has gained considerable attention [8], [9]. Fig. 1.1 shows the aforementioned applications for wireless power transmission. Using wireless power technology makes these devices/systems more convenient, environmentally sound, reliable, safer, and in some conditions even cheaper by removing wires, connectors, and power cords.

(a) (b) (c) (d)

Fig. 1.1. Different applications for wireless power transmission. (a) A visual prosthesis device, (b) RFID, (c) charging mobile devices, and (d) charging Electric vehicles.

Wireless power and data transmission can also be used in behavioral neuroscience research that applies the principles of neurobiology to the study of physiological, genetic, and developmental mechanisms of normal and abnormal behavior in humans and non-human animals [10]. Most typical experiments in behavioral neuroscience involve non-human animal models, which have implications for better understanding of the human nervous system and its pathology. Data from *in vivo* electrophysiology and behavioral neuroscience has helped in the treatment of disorders ranging from schizophrenia to epilepsy and depression. Most of these experiments involve multi-modal data acquisition during behavioral tasks from the monitoring of vital signs (body temperature, heart rate, blood pressure, ECG/EEG signals, etc.) to single and multi-unit neural activities, field potentials, concentration of certain chemicals in the blood stream, and tracking of the location, head orientation, and behavioral events from the animal subject. Furthermore, there are experiments that involve exposing the animal subjects to various stimuli in the form of electrical pulses, visual/auditory cues, mechanical/electrical stressors, or injection

of chemical agents. More recently, optical stimulus is added to the mix in the popular field of optogenetics [11]. Conducting this type of research on behaving animal subjects requires wireless instrumentation with sensing, stimulation, or actuation components attached to or implanted in the animal body.

There is a large body of research that signifies the effects and importance of the environmental enrichment (EE) in behavioral neuroscience [12]-[16]. It is found that EE has profound effects on brain neurochemistry and the resulting behavior, suggesting that EE has the potential to significantly modify these parameters in rats. It is also identified that the duration of the EE as one of the important variables in the EE [17]. A typical EE cage is shown in Fig. 1.2 that includes toys, rollers, and even multiple animals to resemble the cage to the natural habitat.

Fig. 1.2. An example of an enriched environment for *in vivo* animal experiments.

The majority of today's experiments require transferring animals from their home cage to the experimental space, one at a time, attachment and detachment of cables or in some cases wireless modules, close observation of the animal behavior by one or more researchers during the intervention and data collection, and returning the animal back to the home cage and eventually to the animal facility as shown in Fig. 1.3. This process

needs to be repeated for every single session that creates a stressful and impoverished environment for the animal subject and taking considerable amount of researchers' time.

Fig. 1.3. Georgia Institute of Technology animal facility with standard home cage.

Wireless power and data transfer technologies can be used to develop a system to fully-automate or semi-automate (depending on the experiment) intervention and physiologically relevant data collection on a continuous basis over an extended period of time to allow enriched environments equipped with the necessary instruments and tools for most popular type of species in behavioral neuroscience, i.e. the rodents.

Despite widespread use of deep brain stimulation (DBS), several aspects of the therapy remain controversial [18]. Moreover, multiple pilot studies have begun to examine the utility of the DBS for dystonia [19], epilepsy [20], and obsessive-compulsive disorder [21]. In dystonia, the beneficial effects of DBS can take weeks to months to manifest. Any intervention during this period in pre-clinical trials can compromise the results by deviating the experimental conditions from the clinical application.

One of the modalities employed to address DBS effects within the central nervous system (CNS) is neural recording during and after high frequency stimulation to address changes in neuronal activity [22]. However, today's experiments on rats and mice include only a few hours of DBS plus neural recording per day and cannot even go for a day. It is also very difficult to differentiate between the effects of intended and unintended

interventions when sessions are interrupted with cable entanglements or attachment/detachment of wireless devices. The wireless power and data transfer technologies will be able to keep an inductively powered DBS plus neural recording system up and running in mice and rats for 24/7/356, if needed.

Therefore, inductive links have the potential to power up wireless neural recording systems for freely behaving small animal subjects in enriched environments. Moreover, a key limitation of the current wireless neural recording systems that are developed for neuroscience applications is the need for the animal subject to carry a large payload of batteries for continuous recording over several hours or even days, which can affect the behavior of animals such as rats and mice [23], [24]. Therefore, users of such systems always have to make a compromise between the duration of the experiment and how much payload the animal can carry. We have used inductive power transfer technology in a system called EnerCage that allows neuroscientists to continuously run the neural interfacing experiments without replacing the batteries in arbitrary-shaped large experimental arenas. The EnerCage system, as shown in Fig. 1.4, is used to power up multi-channel neural wireless neural interfacing systems in an *in vivo* electrophysiology experiment [25], [26]. In EnerCage system, a power management and data transceiver (PMDT) is required to wirelessly provide a stable power and a robust communication link. The EnerCage system includes an array of coils for power transfer and either magnetic sensors or Microsoft Kinect for localization. The two key features of EnerCage are: 1) The wireless link power transfer efficiency should be increased all the way from the power amplifier to the load on the animal side in presence of distance variations between transmitter (Tx) and receiver (Rx) coils, load variations on the Rx side, and detuning of the Tx and Rx coils, and 2) Wideband and robust data communication between Tx and Rx should be established.

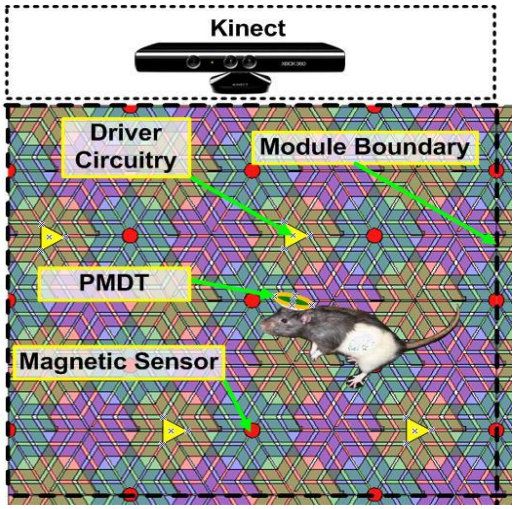

Fig. 1.4. The EnerCage system for wireless powering of neural interfacing devices/systems in freely behaving animal experiments [26].

1.1. Wireless Power Transmission

Three major techniques for wireless power transmission to IMDs have been applied so far: 1) Ultrasound power transmission, 2) High-frequency electromagnetic-wave transmission, and 3) Inductive-coupling power transmission.

1.1.1 Ultrasonic Power Transmission

Since the human body contains approximately 60% water, which attenuates the electromagnetic wave greatly [27], wireless power transmission by ultrasound has been considered [28]. However, ultrasound wireless power is only promising for the applications with low-power consumption because of their low efficiency (39% at 10 mm) [29]. The size of some ultrasonic systems is still too large to be implanted as shown in Figs. 1.5a and 1.5b. Although providing a two degrees-of-freedom device, which is shown in Figs. 1.5c and 1.5d, the power absorption of this energy converter is only 21.4 nW.

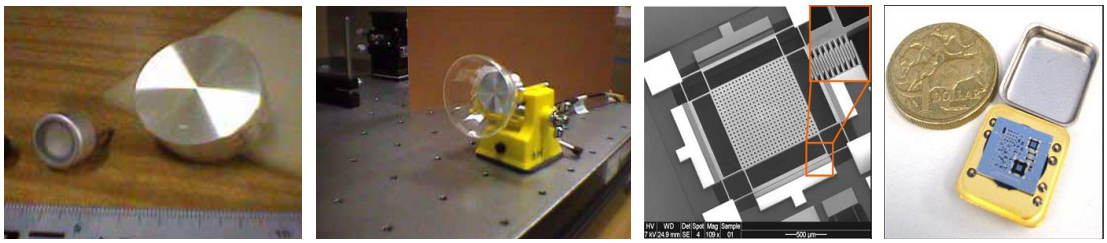

(a) (b) (c) (d)

Fig. 1.5. (a) The ultrasound air transducer (left: open-type, right: enclosed-type), (b) plastic horn for transmitter [28], (c) the ultrasonic converter, and (d) the packaged ultrasonic converter [29].

1.1.2. High-frequency Electromagnetic-wave Transmission

The techniques used for wireless power transmission by means of high-frequency electromagnetic waves are summarized in [30]. The high-frequency link can offer reliable communication, however, the received power by the high-frequency antenna is still small (in the order of microwatts) for most IMDs [31]. Furthermore, the significant electromagnetic-field absorption in the tissue increases the ohmic losses of the tissue and, therefore, increases the tissue temperature, which can cause safety issues.

1.1.3. Inductive Power Transmission

In inductive power transmission, which principle is based on the Faraday's law, a primary loop generates the varying magnetic field that results in an induced current in the secondary loop as shown in Fig. 1.6. In order to significantly increase the receiver voltage (V_3) at a certain frequency of interest, f_{res}, a capacitor, C_3, is added in parallel with L_3 to form an LC-tank circuit [32]. The resonance frequency of the L_3C_3-tank circuit should be tuned to match that of the external transmitter carrier frequency, f_0.

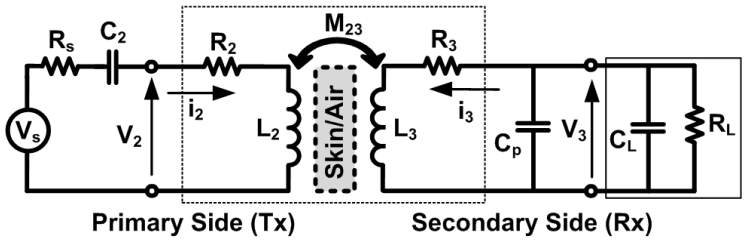

Fig. 1.6. An inductive link with resonance circuits to increase the secondary voltage, V_3.

The inductive-link power-transfer efficiency (PTE) depends on the coils' mutual inductance, M_{23}, and the quality factors, $Q_2 = \omega L_2/R_2$ and $Q_3 = \omega L_3/R_3$ [32]. It is well known that M_{23}, Q_2, and Q_3 are dependent on the coils' geometry, which in general can also include their relative distance, orientation, and number of turns. The coils could be either wire-wound or lithographically defined on a planar conductive surface, such as a printed-circuit board (PCB) or micromachined surface. Wire-wound coils are made of filament wires in the form of a single or multiple individually insulated strands twisted in a circular bundle. The latter type is also known as Litz wire, which helps reducing the resistive losses in the coil due to skin effects, especially at higher carrier frequencies [33]. Printed spiral coils (PSC), which are lithographically defined on a substrate, such as PCB, can be batch fabricated and offer more flexibility in optimizing their geometries and aspect ratios, deeming them attractive for IMD and RFID applications [34].

A key design requirement of power links for IMDs is to provide sufficient power delivered to the load (PDL) while maintaining high PTE. High PTE is required to reduce 1) heat dissipation within the coils, 2) exposure to electromagnetic field, which can cause additional heat dissipation in the power transmission medium, 3) size of the main energy source (e.g. battery), and 4) interference with nearby electronics to satisfy regulatory requirements [35]. At the same time, the link should provide sufficient PDL while considering practical limitations of the power amplifier (PA). Increasing the source voltage, V_s in Fig. 1.6, to increase the PDL can reduce the driver efficiency, require larger transistors in the PA, and make it more difficult to meet the safety requirements.

Several methods have been proposed for designing wireless power transmission links. In [36]-[38], geometries of the primary and secondary coils, L_2 and L_3 in Fig. 1.6, have been optimized to achieve the maximum voltage on the load, and consequently high PDL. PDL is a key design merit when the space is limited and coils need to be miniaturized, such as in the IMD applications. Similarly, design and geometrical

optimization of inductive links based on the PTE have been widely studied [32], [34], [39]-[42]. The approach proposed in [32] is somewhat different by first designing L_3 to maximize the PTE, and then optimizing L_2 to maximize the PDL. Apparently, the literature lacks a clear figure-of-merit (FoM) that incorporates both PTE and PDL, and guides designers to give proper weight to these important but contrasting parameters.

1.1.4. Coupled-mode Magnetic Resonance-based Power Transmission

The coupled-mode magnetic resonant-based power delivery, which has been recently proposed by physicists at MIT, is an alternative wireless power-transfer technique that typically uses four coils (driver, primary, secondary, and load coils) as shown in Fig. 1.7. The proposed method is based on the well-known principle of resonant coupling (the fact that two same-frequency resonant objects tend to couple) [43], [44].

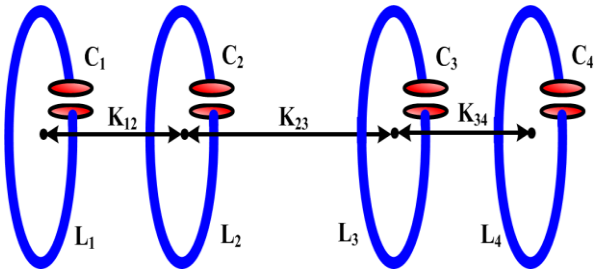

Fig. 1.7. A power link designed based on a coupled-mode magnetic resonance-based power transmission. L_1 is a coil of the driving circuit. L_2 and L_3 are the source and device coils, respectively. L_5 is a coil attached to the load [44].

This phenomenon, which has been explained by coupled-mode theory, can increase the PTE considerably at large coupling distances. The four-coil link has so far been studied from a circuit perspective for power transmission to multiple small receivers, transcutaneous powering, and recharging mobile devices [45]-[47]. However, an in-depth comparison between the coupled-mode and circuit-based theories, which would clarify the relationship between these two methods, is still lacking in the literature.

1.1.5. Closed-loop Wireless Power Transmission

The coupling coefficient, *k*, between transmitter (Tx) and receiver (Rx) coils, which was shown in Fig. 1.6, is the main factor in determining the PDL. Any changes in *k* can drastically change the received power. Misalignments and distance variations between the coils as a result of their relative movements are the main causes of variation in *k*. Load changes can also cause variation in the Rx coil voltage. Such variations are highly undesired in IMDs because too little power can cause malfunction and extra power can increase heat dissipation and damage the surrounding tissue.

One possible solution to stabilize the received power is to change the transmitted power in a closed loop in a way that the received power stays slightly above the minimum level that keeps the IMD operational. In such systems, the information about the received power is sent from the IMD to the outside of the body either through back telemetry based on load shift-keying (LSK) [48], [49] or actively along with data [50]-[52]. In [48], an analog-to-digital converter (ADC) digitizes the rectifier voltage to provide the power bits for digital communication. In [49]-[52], the rectifier voltage has been compared with a reference voltage, and a power bit is transmitted to the Rx. In the external unit, a detection circuit receives the data and a control unit provides the necessary voltage for the PA through a power-efficient DC-DC converter [48]. The Tx supply voltage is adjusted utilizing an *n*-bit digital-to-analog converter (DAC) followed by a Darlington-connected BJT pair in [49]. In [51], the IMD received power is regulated through a frequency control method in which the power carrier frequency is changed to detune the Rx coil and adjust the secondary voltage. It can be seen that these works have all developed an application-specific integrated-circuit (ASIC) through a long and costly process to close the power loop. Also the stability analysis of such a loop is only presented by [48] using a continuous-time model that does not consider the loop speed.

1.2. Wireless Data Transmission

Wideband data telemetry is one of the most important functions in a group of IMDs, known as neuroprostheses, which substitute sensory or motor modalities that are lost due to an injury or a disease. Well-known examples are the cochlear implants and visual prostheses, which need a large volume of data from external sensors to the IMD, or invasive brain-computer interfaces, which collect a massive amount of data from the central neural system and transfer the data to the outside of the body to control the patient's environment or prosthetic limbs after signal processing [2], [53]-[56].

In IMDs, high-bandwidth telemetry must be achieved at the lowest possible carrier frequencies because of the significant electromagnetic-field absorption in the tissue, which exponentially increases with the carrier frequency [57]. This requirement rules out the majority of commercially-available wideband wireless protocols, such as Bluetooth or WiFi, which operate at 2.4 GHz. There are also specific standards, such as Medical Implant Communication Service (MICS), operating in the 402-405 MHz band, which can only offer a limited bandwidth (300 kHz) [58]. Therefore, utilizing a pair of loosely-coupled coils is the most common method for establishing wideband data telemetry in IMDs. Achieving low-power consumption, small size, and wide bandwidth while maintaining robustness against external interference, distance variations, and coils misalignments, is among major challenges in establishing inductive telemetry links.

The majority of modulation techniques that have been used in inductive telemetry links are carrier based. Amplitude shift-keying (ASK), frequency shift-keying (FSK), binary/quadrature-phase shift-keying (BPSK/QPSK), and load shift-keying (LSK) are examples of such methods [59]-[65]. These carrier-based methods were attractive in the early IMDs because the same low-frequency carrier could be used for powering the IMD. In high-performance IMDs that require wider bandwidth, however, the power carrier has to be separated from the data carrier because the frequency of the power carrier cannot be

increased considering tissue loss at high frequencies. In addition, dependence of all these methods on carrier signals has resulted in high-power consumption on the Tx side.

The use of high-frequency data carriers for wideband communication in the IMDs requires complex and power-consuming frequency-stabilization RF circuits, which is not desired. Recently, we have devised and reported a new pulse-based data-transmission technique, called pulse-harmonic modulation (PHM), to further push the limits of power consumption and data rate (DR) in near-field telemetry links [66], [67]. There are also other pulse-based near-field data-transmission methods, developed for chip-to-chip communication and body area networks (BAN), in which inductive links with low quality factors are used to achieve wide bandwidth [68]-[70].

In 2002, the FCC issued a ruling deregulating the use of ultra-wideband (UWB) technique for low-power communications. A variation known as impulse-radio (IR) UWB, in which data is transmitted via sub-nanosecond pulses through wideband antennas, soon became quite popular for short-range ultra-low-power applications [71]-[73]. Low-power consumption in the IR-UWB transmitters is mainly because of being carrier-less, which leads to the elimination of continuously power-consuming high-frequency oscillators. These features make the IR-UWB an attractive choice for IMDs. However, the caveat is that the ordinary IR-UWB, which is intended for far-field interactions in the 3.1-10.6 GHz band, is highly absorbable in water and cannot penetrate or pass through tissue [74].

Although pulse-based methods offer high bandwidth, the strong power-carrier interference can dwarf the weak data-signal on the Rx side and make data recovery quite difficult if not impossible. Hence, the power-carrier interference needs to be filtered out and minimized, which will add to the power consumption and complexity of the Rx. This has motivated us to devise a new dual-band data and power transmission technique for near-field wideband applications, called Pulse-delay Modulation (PDM), which takes advantage of the undesired power-carrier interference on the wireless data link (as the

result of the proximity of power and data coils) to deliver the data. The proposed method saves the power and space needed for filtering out the power carrier interference, and also takes advantage of the low-power and low-complexity properties of the IR-UWB, particularly on the Tx side, to further reduce the IMD power consumption.

1.3. Multi-band Wireless Power and Data Transmission

The main advantage of using a single carrier for both power and data transmission is the relatively robust coupling between power coils, which can lead to more reliable data transfer. Another advantage is the saving in space by reusing the power coils for multiple purposes. However, achieving high PTE and high data-transmission bandwidth utilizing the same carrier would be challenging because of their conflicting requirements [57]. The primary issue is that modulating the power carrier in any form complicates the power Tx circuitry and reduces the PTE. Another important issue is the low frequency of the power carrier, which further limits the data transfer bandwidth to levels that are insufficient for most wireless applications.

This has motivated us to investigate the development of a multi-band wireless link with innovative system- and circuit-level techniques aimed at wideband, low-power, efficient, and robust wireless data and power transmission. Fig. 1.8 shows the proposed multi-band link that uses three carrier signals for power, downlink (forward data transmission), and uplink (back telemetry) with each carrier having its own pair of coils or antennas to decouple the data from the power link [57].

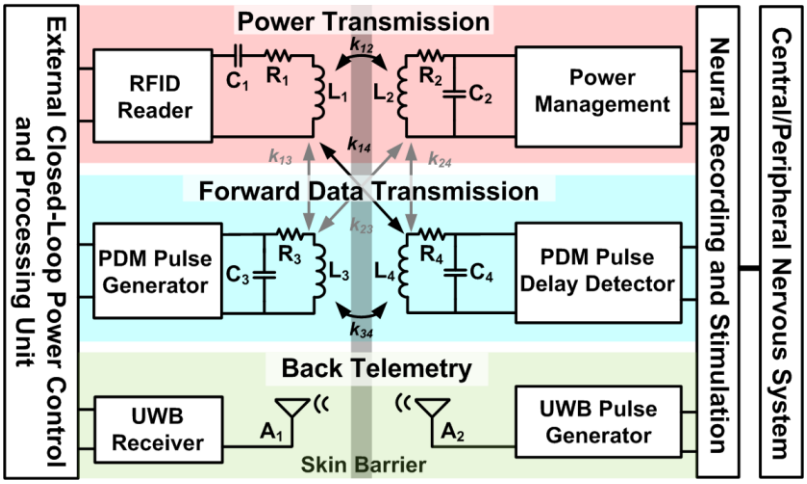

Fig. 1.8. Simplified block diagram of the wireless transmission of power and data across a multi-band inductive link. The wireless link consists of two inductive links, L_1-L_2 for power transmission and L_3-L_4 for forward data transmission using pulse delay-modulation (PDM), and a UWB link for back telemetry. The UWB link combined impulse radio (IR) and pulse width modulation (PWM) techniques to further reduce the power consumption at the transmitter. The power/data channel could be either skin in case of IMDs or air when the EnerCage system is used.

The structure of the dissertation is as follows: In Chapter II, an RFID-based closed-loop power transmission system is proposed with measurement and *in vivo* experimental results. Chapter III includes a high performance 3-coil inductive power transmission link by introducing the trade-offs in 4-coil links. A design procedure for multi-coil links is also presented. Chapter IV describes the circuit theory behind magnetic resonance-based power transmission systems. Two, three, and four coil links are analyzed based on coupled-mode and circuit theories and proved to be identical. Chapter V proposes a novel figure-of-merit (FoM) for high-performance inductive power transmission. This FoM could also help designers to choose the optimal link between 2-, 3-, and 4-coil links. Chapter VI shows the design and test results of the first implemented PMDT chip with novel feature of automatic resonance tuning of the Rx coil. Moreover, a Q-modulation technique is proposed for adaptive load resistance matching at Rx. Chapter VII presents the novel PDM and PWM-IR techniques for low-power, wideband, and robust data transmission. Chapter VIII describes the measurement and *in vivo* results of the second implemented PMDT chip on the EnerCage system. Finally, the contributions of this dissertation and suggested future works are summarized in Chapter IX.

CHAPTER II

RFID-BASED CLOSED-LOOP POWER TRANSMISSION

Passive radio-frequency identification (RFID) tags and certain implantable microelectronic devices (IMD), such as cochlear implants, do not include batteries due to cost, size, weight, safety, and lifetime limitations. Inductive power transmission provides these devices with the required power on a continuous basis [7], [75]. In these systems, wireless power transmission across a pair of loosely coupled coils is preceded by a power amplifier (PA) in the external unit, and followed by an efficient rectifier in the implanted unit to provide the IMD with an unregulated supply [76].

The coupling coefficient, *k*, between transmitter (Tx) and receiver (Rx) coils is the main factor in determining the amount of power that can be delivered to the IMD. Any changes in *k* can drastically change the received power. Misalignments and distance variations between the coils as a result of their relative movements are the main causes of variation in *k*. Changes in the received power can cause large voltage variations across the Rx coil. Load changes as a result of stimulation, for example, can also cause variation in the Rx coil voltage [32]. Such variations are highly undesired in IMDs because too little power can cause malfunction, and extra power can increase heat dissipation within the implant and damage the surrounding tissue. Therefore, stabilizing the IMD received power over a range of coupling and loading variations is imperative. One possible solution is to change the transmitted power in a closed loop in a way that the received power stays slightly above the minimum level that keeps the IMD operational [48]. Fig. 2.1 shows the simplified block diagram of such a closed loop power transmission system. A back telemetry circuit based on load shift keying (LSK) has been used to send information about the received power to the external transmitter. In the external unit, a detection circuit receives the back telemetry data, and a control unit provides the necessary voltage for a class-E PA through a DC-DC converter.

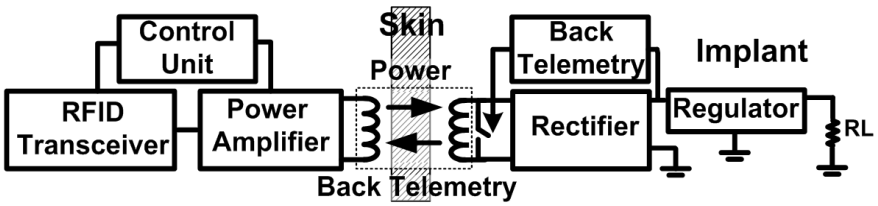

Fig. 2.2. Closed-loop inductive wireless power transmission across the skin.

Unlike previous works [48]-[52], instead of developing a custom application specific integrated circuit (ASIC) through a long and costly process, we are taking advantage of the built-in capabilities of a commercial off-the-shelf (COTS) RFID reader, TRF7960 (Ti, Dallas, TX), in the external unit to not only close the inductive power transmission loop through back telemetry, but also drive the transmitter coil. This is a novel application for COTS RFID readers to be part of a standalone closed-loop wireless power transmission system. Because before this work, RFID systems have often been operated open loop for one way data or power transmission. Since motion artifacts occur at low frequencies, the bandwidth offered by the COTS RFID back telemetry link (800 kb/s) is much higher than what is required for regulating the received power. Therefore, the excess bandwidth can be used for sending recorded biological information to the external unit.

Despite numerous publications on closed-loop power transmission systems, only [48] has presented a control model. However, even in this paper the authors have not considered the discrete time nature of the control loop. Hence, the sampling frequency has not been considered in the stability analysis. We have derived a discrete time model for the closed-loop system, which can more accurately predict the system behavior in response to perturbations.

2.1. System Architecture

Block diagram of the proposed RFID-based closed-loop power transmission system, which is composed of a power transmitter and a standalone transponder, is shown

in Fig. 2.2. In this system, power transfer takes place across the primary and secondary coils, L_1 and L_2, from the Tx to the IMD (Rx). The AC voltage across L_2 is rectified, digitized, and sent back to the Tx using LSK. An ultra-low power MSP430 microcontroller (Texas Instruments, Dallas, TX) with a 10-bit built-in ADC is used to digitize the rectifier voltage. Therefore, the Tx can adjust the transmitted power adaptively in order to maintain the rectifier voltage at a designated level with 10 bits of accuracy.

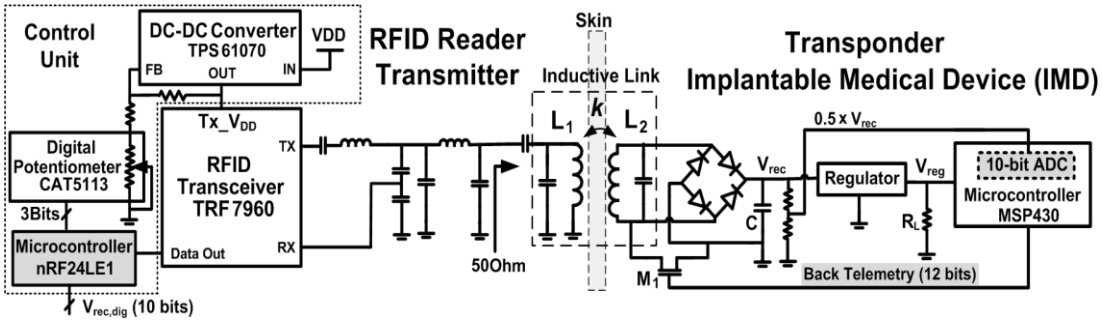

Fig. 2.2. Block diagram of the RFID-based closed loop power transmission system utilizing a 10-bit ADC on the transponder side (IMD) to report the actual rectifier voltage to the control mechanism on the external transmitter side.

2.1.1. Standalone IMD transponder

The IMD transponder consists of a rectifier, a 3.3 V regulator, LSK circuit, and an MSP430 microcontroller with a built-in 10-bit ADC. A wideband full-wave rectifier is used to convert the 13.56 MHz power carrier to a DC voltage, V_{rec}, which is attenuated ($0.5 \times V_{rec}$), sampled, and digitized with respect to a 3.3 V reference voltage at 500 Hz. The resulting 10 bits of information about the rectifier output voltage is combined with start bits, "01", and sent back to the Tx by closing M_1 switch (BSS138 MOSFET) at a rate of 250 kHz with short (375 ns) pulses to prevent unnecessary power dissipation. MSP430 microcontroller was operated by its 16 MHz internal clock, which resulted in a total power dissipation of 27 mW in the IMD transponder.

2.1.2. Power Transmitter

The transmitter should not only power up the transponder but also detect the back telemetry data, including the transponder power level information, in order to close the wireless power transmission loop. An RFID reader is a good candidate for this purpose because it can both drive a coil and recover LSK back telemetry data. Due to the short distance between Tx and Rx coils in IMD applications, the TRF7960 RFID reader chip from Texas Instruments was chosen, which is equipped with a built-in class-D PA that can provide up to 200 mW output power. The PA output power was adjusted by changing its supply voltage, Tx_V_{DD}, through an efficient DC-DC converter (TPS61070) with more than 90% power conversion efficiency.

The RFID reader detects the back telemetry data and delivers it to the control unit, which is composed of an nRF24LE1 microcontroller, a digital potentiometer, and the DC-DC converter, as shown in Fig. 2.2. Received raw data is oversampled by the microcontroller that operates with an accurate 16 MHz timebase from a crystal oscillator. The microcontroller always searches for the start bits, "01", and when they are detected, recovers the rest of the packet, which is the IMD rectifier voltage digitized in 10 bits and designated as $V_{rec,dig}$ in Fig. 2.2. In order to adjust V_{rec} = 3.8 V, which is 0.5 V above the desired regulator output, the decimal value of $V_{rec,dig}$ is compared with a threshold = 560 in the microcontroller. If the result is negative, the control unit increases the transmitted power and vice versa. The control unit also maintains the transmitted power when it receives 560, which implies that V_{rec} = 3.8 V. In the presence of any external disturbance, the control unit reduces or increases the transmitted power according to $V_{rec,dig}$ value until it receives 560. In steady state, the rectifier voltage has negligible ripple due to constant transmitted power, which is not the case when only one bit is sent to the Tx.

The DC-DC converter output voltage is proportional to its resistive feedback ratio. A counter inside the digital potentiometer, driven by a 500 Hz clock form the microcontroller, normally counts up and increases the resistive ratio of the feedback loop.

The 100 kΩ digital potentiometer can change the Tx_V_{DD} from 3.5 to 5 V in 100 steps. When microcontroller changes the direction of the potentiometer counter, the feedback resistive ratio of the DC-DC converter is decreased and consequently Tx_V_{DD} is reduced.

2.2. System Modeling

We have modeled the closed-loop power transfer system in Fig. 2.2 for stability analysis. Although all the voltages and currents in the system are continuous in time, the closed-loop system operates in discrete time because the digital potentiometer counter clock cycles determine the timing of every change in the system variables. In Fig. 2.3, the system has been simplified and divided into 4 key building blocks: 1) back telemetry circuit, 2) control unit, 3) RFID class-D PA and inductive link, and 4) resistive-capacitive (RC) load following the rectifier circuit. Reference voltage, V_{ref}, is the system's input and the rectifier voltage, V_{rec}, is its output. Back telemetry circuit has been modeled by an adder, which compares V_{ref} and V_{rec}. The control unit either increases or decreases the PA supply voltage according to the back telemetry data. Therefore, this unit is represented as an integrator, which gain, k_I, is determined by the number of digital potentiometer taps,

$$y[n] = y[n-1] + k_I\, x[n] \Rightarrow \frac{Y(z)}{X(z)} = \frac{k_I}{1 - z^{-1}}\,, \tag{2.1}$$

where *x[n]* is the input to the control unit (i.e. back telemetry data), and *y[n]* is the output of the control unit, which is the PA supply voltage.

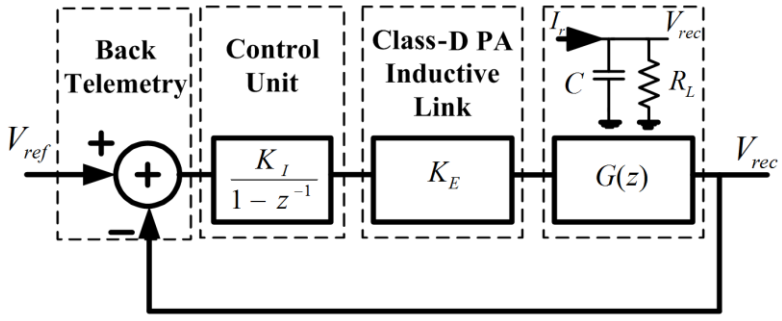

Fig. 2.3. Closed-loop power transfer discrete time model.

Because of the low back telemetry and power update frequencies and for simplicity, the class-D PA and inductive link are considered wideband and modeled only with a gain factor, K_E, which is the ratio of the average current delivered to the rectifier RC load (I_r) to the power amplifier supply voltage. The rectifier capacitive load current, $I_c[n]$, and resistive load current, $I_{RL}[n]$, are given by,

$$I_c[n] = \frac{q[n] - q[n-1]}{T} = \frac{C(V_{rec}[n] - V_{rec}[n-1])}{T}, \; I_{RL}[n] = \frac{V_{rec}[n]}{R_L}, \tag{2.2}$$

where T is the digital potentiometer counter clock period, $V_{rec}[n]$ is the rectifier voltage at time $t = nT$, and q is the total charge stored in the rectifier capacitor. $G(z)$, the impedance of the rectifier RC load can be found from,

$$G(z) = \frac{V_{rec}(z)}{I_r(z)} = \frac{R_L}{1 + \frac{R_L C}{T} - \frac{R_L C}{T} z^{-1}}. \tag{2.3}$$

Using (2.1), (2.2), and (2.3), the closed-loop system transfer function in the Z-domain can be written as,

$$\frac{V_{rec}(z)}{V_{ref}(z)} = \frac{k_E k_I R_L}{\frac{R_L C}{T} z^{-2} - \left(\frac{2R_L C}{T} + 1\right) z^{-1} + k_E k_I R_L + 1 + \frac{R_L C}{T}}, \tag{2.4}$$

which has two poles at

$$Z_{1,2} = \frac{\frac{2R_L C}{T} + 1 \pm \sqrt{1 - \frac{4{R_L}^2 C k_E k_I}{T}}}{2\left(k_E k_I R_L + \frac{R_L C}{T} + 1\right)}, \tag{2.5}$$

From basic control theory, a discrete-time system is stable if and only if every pole of its transfer function has a magnitude less than one, i.e. all poles must reside within the unit circle on the Z-plane. It can be shown that both poles in (2.5) are inside the unit circle, and the system is always stable. However, there are two different conditions for the system operation. If $4{R_L}^2 C k_E k_I / T \le 1$ then the poles are real and the system is over damped. Otherwise, the poles are complex and the system is under

damped. The magnitude of the poles in this case can be found from (2.6), which is obviously less than one.

$$\left|Z_{1,2}\right|^2 = \frac{\left(\frac{R_L C}{T}\right)^2 + \frac{R_L C}{T} + \frac{{R_L}^2 C k_E k_I}{T}}{\left(\frac{R_L C}{T}\right)^2 + \frac{2R_L C}{T} + \frac{2{R_L}^2 C k_E k_I}{T} + \left(k_E k_I R_L\right)^2 + 2k_E k_I R_L + 1}, \tag{2.6}$$

Using (2.5), it is possible to predict at what counter clock frequency, $1/T$, the system is over or under damped. In our design, the loop response is over-damped for $1/T$ < 1.2 kHz. The normalized step responses of the closed-loop system for two clock frequencies of 300 Hz and 3 kHz are shown in Fig. 2.4. Our measurements support the accuracy of this simplified model. However, it should be noted that increasing the potentiometer clock frequency, $1/T$, moves the poles closer to the unit circle, and results in poor stability of the system.

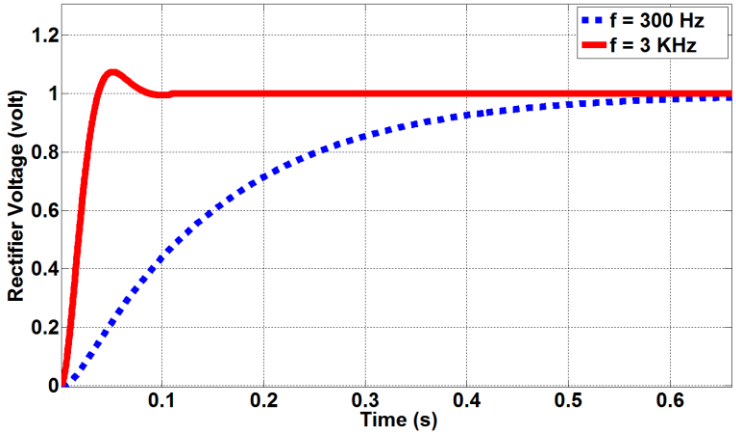

Fig. 2.4. Step response of the system for two counter clock frequencies.

2.3. Measurement Results

We used two methods to verify the functionality of the closed loop system. First, we looked at variations in k by changing the coupling distance, d, and coils' alignment. Fig. 2.5a shows V_{rec} and regulator voltage, V_{reg}, on the transponder and PA supply voltage and L_1 voltage on the transmitter side. When d = 2 cm, TX_V_{DD} is 5.5 V, V_{rec} = 3.6 V, and V_{reg} = 3.3 V. In about 200 ms after the beginning of the trace, d is suddenly

changed to 0.5 cm, while trying to maintain the coils alignment. As a result of this step increase in k, V_{rec} increases, while the closed-loop feedback starts reducing TX_V_{DD} to oppose this perturbation.

It takes ~0.4 s for V_{rec} to return back to 3.6 V, and TX_V_{DD} to settle in its new value, slightly more than 3 V. It can be seen that as a result of increased k, the transmitted power has been decreased, and the system behavior is over damped, as predicted by our model for $1/T$ = 300 Hz. ~1.1 s after the beginning of the trace, coils are returned back to their original position at d = 2 cm, resulting in TX_V_{DD} to return back to 5.5 V also. What is important is that during all these changes, the 1st trace from top in Fig. 2.5a, which shows the transponder regulator, V_{reg}, is maintained constant at 3.3 V.

Second, we observed the effects of changing the transponder loading, R_L, on the closed-loop system. This was done by connecting and disconnecting a 1.45 kΩ resistor across the regulator output. R_L changes the transponder power consumption from 11.2 mW to 18.7 mW. The transient response in Fig. 2.5b shows that the regulator and rectifier voltages decrease slightly by applying the load as the IMD power consumption suddenly increases. It can be seen that TX_V_{DD} increases to compensate for higher power demand on the transponder side. Conversely, after disconnecting the additional load, all voltages return back to their original values. A voltage limiting or detuning circuit is needed before the rectifier to avoid large voltages across L_2 when the coils move too close or when the IMD power consumption drops significantly, which results in a sudden increase in the loaded quality factor of L_2.

Power transfer efficiency (PTE) improvement is an added benefit of the closed-loop power transmission system. In an open loop system, the transmitter power is always constant while the received power can change as a result of variations in k and loading. To ensure functionality of the IMD in all conditions, the transmitter power should be high enough to energize the IMD in the worst case scenarios, such as the largest possible d, worst misalignments, or maximum loading. These result in poor efficiency when k is high

or loading is low. To make things worse, the extra power is dissipated as heat on both Tx and Rx sides, increasing the risk of tissue damage. In a closed-loop system, however, the transmitter power is increased only as much as needed based on *k* value and loading conditions.

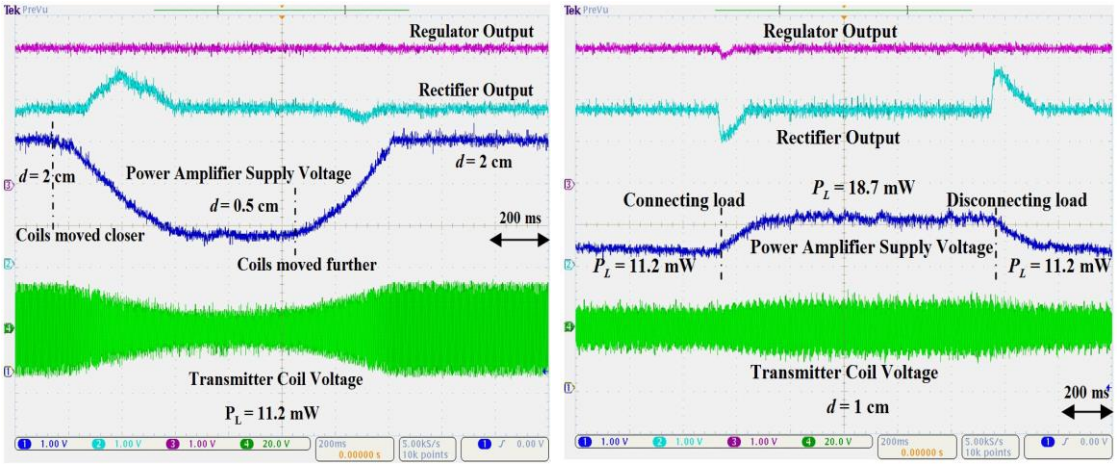

(a) (b)

Fig. 2.5. Closed-loop power transmission system measured waveforms: (a) Changing coils' relative distance from 2 to 0.5 cm, and coupling coefficient. (b) Changing the transponder loading from 11.2 to 18.7 mW.

Fig. 2.6a compares the measured and simulated overall power efficiency from battery in Tx unit to the transponder loading after the regulator ($\eta_{\text{DC-DC Converter}}\% \times \eta_{\text{PA}}\% \times \eta_{\text{inductive link}}\% \times \eta_{\text{rectifier}}\% \times \eta_{\text{regulator}}\%$) for the open-loop and closed-loop systems. As expected, closed-loop power control has increased η% significantly when the coils are close to each other. Load regulation capability of the system is demonstrated in Fig. 2.6b. The closed-loop system increases the transmitted power to keep the rectifier voltage constant for loads up to 8 mA which is the maximum power that Tx can provide in this system at d = 1 cm. In the open-loop system, V_{rec} decreases when the transponder load current increases because the transmitted power remains constant.

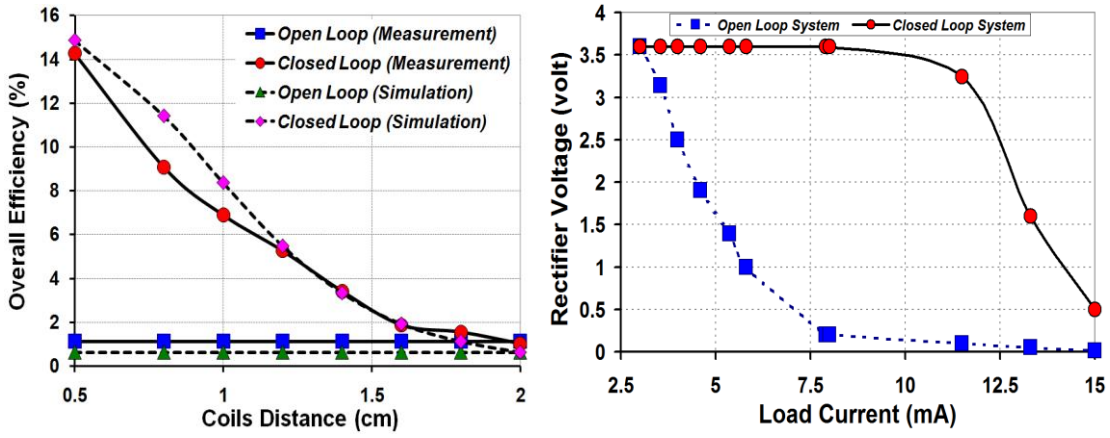

(a) (b)

Fig. 2.6. (a) Simulated and measured overall efficiencies vs. coils distance in open- and closed-loop conditions. (b) Open- and closed-loop load regulation.

2.4. Experimental *In Vivo* Results

Fig. 2.7 shows the RFID-based closed-loop power-transfer experimental setup. All experiments were conducted with prior approval from the Institutional Animal Care and Use Committee (IACUC) at Michigan State University. A 1 year old adult Sprague Dawley rat, weighing 400 g, was the animal model. A printed spiral coil (PSC) fabricated on FR4 printed circuit board and a wire-wound coil fabricated with Litz wire (AWG 30) were utilized as the Tx and Rx coils, respectively. Table I shows the optimal geometries of these coils for f_P = 13.56 MHz and other system specifications [34]. The Tx circuitry was placed in a PET box and mounted on the back of the rat using a special jacket. The Tx coil, L_1, was located at the bottom of the box, as shown in Fig. 2.7 right inset. The IMD transponder circuitry was mounted on top of the box and the Rx coil, L_2, was placed between the jacket and the box at ~7 mm separation from L_1 using plastic sheets. A 10 cm twisted pair of Litz wires connected the IMD transponder to L_2, as shown in Fig. 2.7 left inset.

A dual-axis thermal accelerometer (28017, Memsic, Rocklin, CA) was embedded in the box to measure vibrations with 1 mg resolution at 100 Hz. Acceleration in the X- and Y-axes indicate the misalignment and distance variations between L_1 and L_2,

respectively. The PA supply voltage (Tx_V_{DD}), received rectifier voltage ($V_{rec,dig}$), and accelerometer X- and Y-axis outputs were oversampled by a data acquisition module (USB-6259, National Instruments, Austin, TX) at 500 kHz. During the experiment, the operator tried to move the data acquisition module along with the animal. However, the tethering effect of interconnects possibly added to the motion artifacts between the two coils, which was not a major problem considering the purpose of this experiment.

Table 2.1: Optimal coil geometries and system specifications

Parameters	Designed Values
Tx printed spiral coil (L_1)	Outer/inner diameter = 2.7/1.1 cm Line width = 2 mm Number of turns = 4
Rx Litz wire-wound coil (L_2)	Dimension = 1.2 × 1 cm^2 Wire diameter = 0.25 mm Number of turns/strands = 6/44
Power transmission frequency	13.56 MHz
Back telemetry/Power update frequency	250/0.5 kHz
Weight of the Tx box/IMD transponder	26.1/0.8 g

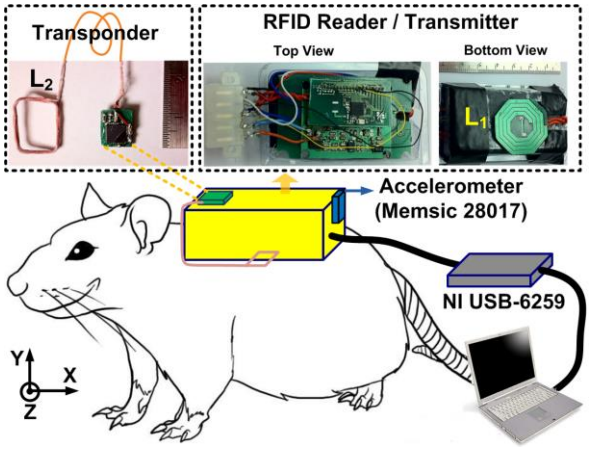

Fig. 2.7. RFID-based closed-loop power transfer *in vivo* experimental setup. L_2 was placed between a special jacket and the Tx box (not implanted).

An experiment was conducted to demonstrate the significance and functionality of the closed-loop power transmission system in comparison with the same system when it was open loop. Considering that open-loop systems need to operate based on the worst case conditions, in the first part of this test, we opened the power control loop in Fig. 2.2 by disconnecting Tx_V_{DD} from the DC-DC converter output and connecting it to a fixed

5 V, which was the maximum available supply level. Fig. 2.8 shows $V_{rec,dig}$ and the fixed Tx_V_{DD} vs. time. Here we are only showing a 60 s window of the recorded data, during which we observed the largest vibrations, resulting in up to ~1.8 V variations in $V_{rec,dig}$. It can be seen that $V_{rec,dig}$ is much higher than the desired 3.8 V because of maximizing Tx_V_{DD}, resulting in additional power dissipation in the IMD transponder.

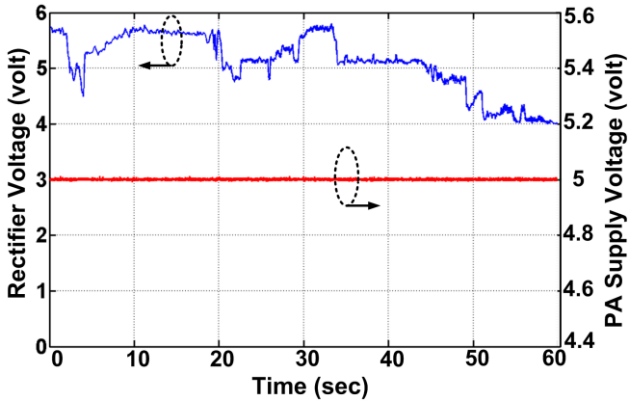

Fig. 2.8. Open-loop results for Tx power amplifier supply voltage (Tx_V_{DD}) and received rectifier voltage ($V_{rec,dig}$) in Fig. 2.2.

Figs. 2.9a and 2.9b show the acceleration in the X- and Y-axis, respectively. It can be seen that when acceleration along the X-axis is negative, the rectifier voltage has been reduced, while positive acceleration leads to increments in the rectifier voltage. This may be because of an initial misalignment between the coils, with the animal movements in positive direction helping to better align the coils while movements in the negative direction worsening the misalignment.

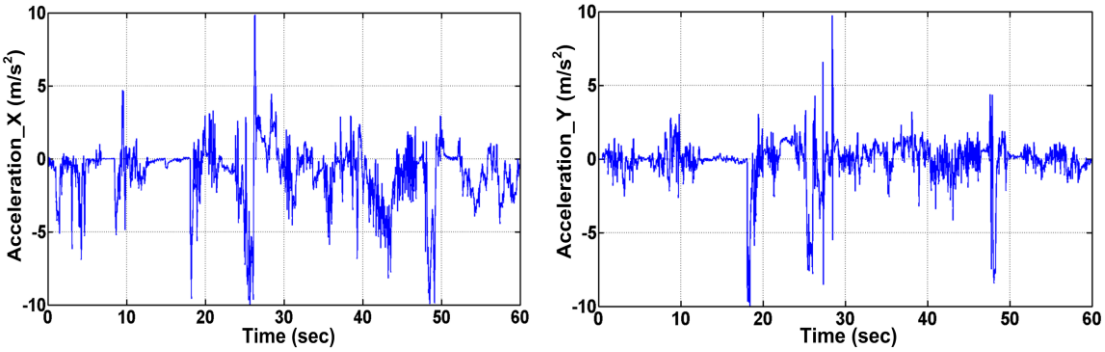

(a) (b)

Fig. 2.9. Open-loop inductive power transmission system measured waveforms: (a) Acceleration in X-axis. (b) Acceleration in Y-axis.

In the second part of the experiment, the closed-loop system was tested in similar conditions. Fig. 2.10 shows $V_{rec,dig}$ and Tx_V_{DD} vs. time. Comparing these waveforms with Fig. 2.8 shows that the closed-loop system has maintained the rectifier output voltage constant at the designated level (3.8 V) by changing Tx_V_{DD} within 4.2~4.6 V. Figs. 2.11a and 2.11b show the acceleration in the X- and Y-axis, respectively. It can be seen that the PA supply voltage increased when acceleration in the Y-axis was positive, which indicates that the coils' relative distance increased slightly during those times. Nonetheless, the coil vibrations were generally small in this experiment due to the mass of the Tx box and its contents. Our next step is to implant the Rx module inside the animal body and test the closed loop power transmission system in the most realistic condition.

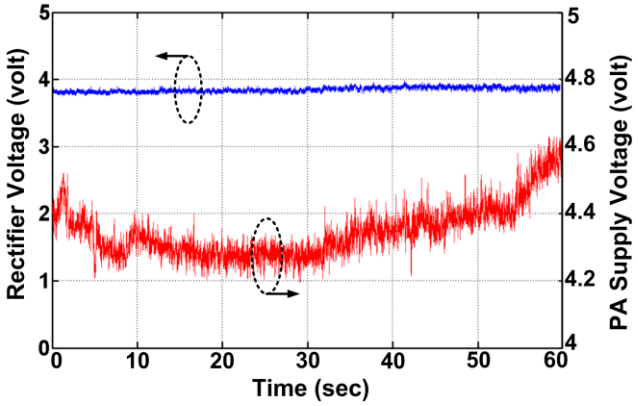

Fig. 2.10. Closed-loop results for Tx power amplifier supply voltage (Tx_V_{DD}) and received rectifier voltage ($V_{rec,dig}$) in Fig. 2.2.

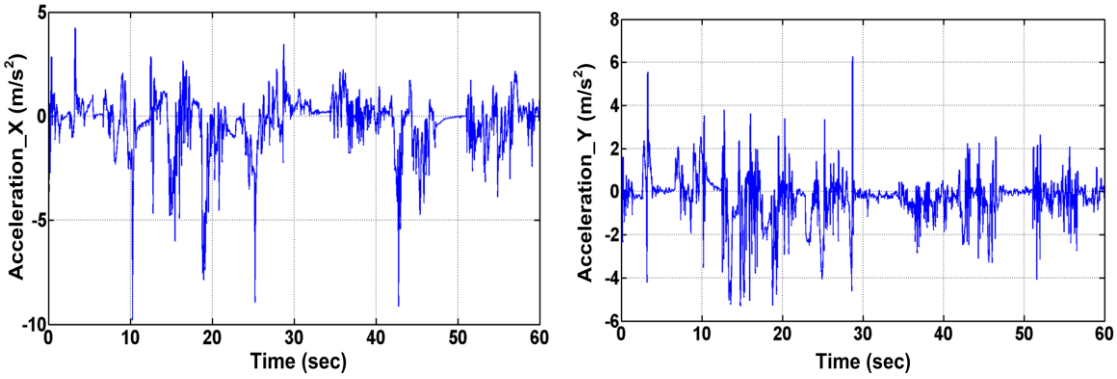

(a) (b)

Fig. 2.11. Closed-loop inductive power transmission system measured waveforms: (a) Acceleration in X-axis. (b) Acceleration in Y-axis.

CHAPTER III

DESIGN AND OPTIMIZATION OF MULTI-COIL INDUCTIVE POWER TRANSMISSION LINKS

Inductive power transmission can be used to either continuously power up a device or temporarily recharge its batteries without any direct electrical contact between the energy source and that device. A high efficiency power amplifier (PA), connected to the main energy source on the transmitter side (Tx), often drives the primary coil, which is mutually coupled to a secondary coil on the receiver side (Rx), which is connected to the load (R_L). The load can cover a wide range of applications from high performance and sophisticated implantable microelectronic devices (IMD) with relatively high power consumption (>100 mW), such as cochlear and retinal implants, to simple and low power radio frequency identification (RFID) tags that cannot use primary batteries due to their cost, size, or lifetime constraints [7], [77]-[80].

The mutual inductance between a pair of coupled coils, M, is proportional to d^{-3}, where d is the center-to-center spacing between the coils when they are in parallel planes and perfectly aligned [7]. A key requirement in all of the above applications is to deliver sufficient power to the load with high power transfer efficiency (PTE) when d is relatively large or the coils are misaligned, i.e. when M is very small (PTE is already large enough for small d). Large PTE is meant to reduce heat dissipation within the coils, tissue exposure to AC magnetic field, which can cause additional heat dissipation in IMDs, size of the main energy source, and interference with nearby electronics to satisfy regulatory requirements [35], [82], [83].

Design, theoretical analysis, and geometrical optimization of the conventional 2-coil inductive links have been covered extensively in the literature over the last three decades [32], [34], [41], [42], [84]-[91]. More recently, a 4-coil power transmission link was proposed in [92] to further increase the PTE, particularly at large d. In the 4-coil

arrangement, which schematic diagram is shown in Fig. 3.1a, a pair of coils is used on the Tx side, which are referred to as the driver, L_1, and primary, L_2, coils. A second pair of coils is used on the Rx side, which are referred to as the secondary, L_3, and load, L_4, coils. All of these coils are tuned at the same resonance frequency, f_0, using capacitors $C_1 \sim C_4$. The coils' parasitic resistances are also shown by $R_1 \sim R_4$. The 4-coil method has so far been adopted for transferring power to multiple small receivers, transcutaneous power transmission for d = 10~20 mm, and recharging mobile devices in [45]-[47], respectively. However, an in-depth comparative circuit analysis of this arrangement that can guide a design and optimization scheme for such applications is still lacking.

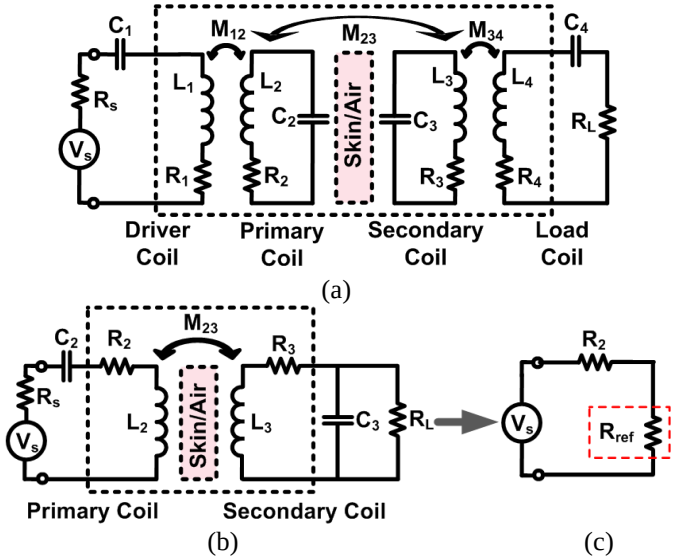

Fig. 3.1. Lumped circuit models of (a) 4-coil and (b) conventional 2-coil inductive links for wireless power transfer. (c) Equivalent circuit of the reflected load on to the primary loop at resonance (for the sake of simplicity, R_s, which is a property of the driving circuitry, has been merged with R_2).

We have analyzed the 4-coil inductive link utilizing the reflected load theory [7], which is more familiar to circuit designers than the coupled-mode theory used by the physicists in [44], and compared it with its conventional 2-coil counterpart. Our analysis shows that utilizing the 4-coil method increases the PTE at large d at the cost of a significant reduction in the power delivered to the load (PDL). Therefore, unless the application requires a small amount of power (10s of mW or less), a high driving voltage (V_s) will be required, which can reduce the driver efficiency and lead to safety issues in

medical applications. Instead, we have demonstrated that a 3-coil inductive power transfer link not only provides as high PTE as the 4-coil method but also offers a PDL that is significantly higher than both 2- and 4-coil links at large *d*.

3.1. Theory of Multiple Inductively-coupled Coils

Fig. 3.1b shows the simplified schematic diagram of a 2-coil inductive link. It is known that the highest PTE across this link can be achieved when both LC tanks are tuned at the same resonance frequency, $f_0 = 1/2\pi\sqrt{L_2C_2} = 1/2\pi\sqrt{L_3C_3}$ [32]. The effect of the Rx side on the Tx side can be modeled at resonance by calculating the reflected impedance,

$$R_{ref} = k_{23}^2 \omega_0 L_2 Q_{3L} = k_{23}^2 R_2 Q_2 Q_{3L}, \tag{3.1}$$

where $k_{23}=M_{23}/\sqrt{L_2L_3}$, $Q_2 = \omega_0 L_2/R_2$, and $Q_{3L} = Q_3Q_L/ (Q_3+Q_L)$, in which $Q_3 = \omega_0 L_3/R_3$ and $Q_L = R_L/\omega_0 L_3$ [7]. Q_L is often referred to as the load quality factor, and the value for M_{23} can be calculated from the Appendix. Hence, the primary loop can be simplified at resonance as the circuit shown in Fig. 3.1c. It should be noted that R_2 in Fig. 3.1c also includes R_s, the output impedance of the driver circuitry, V_s.

To derive an equation for the PTE at resonance, we should consider that the power provided by V_s divides between R_2 and R_{ref}, and the power delivered to R_{ref}, i.e. the power that is received by the secondary loop, divides between R_3 and R_L, which are the only power consuming components on the Rx side. This will lead to [32]

$$\eta_{2-coil} = \frac{k_{23}^2 Q_2 Q_{3L}}{1 + k_{23}^2 Q_2 Q_{3L}} \cdot \frac{Q_{3L}}{Q_L}. \tag{3.2}$$

Note that the first and second terms in (3.2) correspond to the power division between R_2 and R_{ref}, and R_3 and R_L, respectively.

The amount of power delivered to the load (PDL), on the other hand, can be calculated by multiplying the power provided by V_s, i.e. $V_s^2/2(R_2+R_{ref})$, by the PTE from (3.2)

$$P_{L,2-coil} = \frac{V_s^{\,2}}{2R_2}\frac{k_{23}^2 Q_2 Q_{3L}}{(1+k_{23}^2 Q_2 Q_{3L})^2}\cdot\frac{Q_{3L}}{Q_L}. \tag{3.3}$$

If the simple 2-coil inductive link in Fig. 3.1b is extended to an m-coil link, in which 1st and m^{th} coils are connected to the energy source and load, respectively, the reflected load from the $(j+1)^{th}$ coil to the j^{th} coil can be found from

$$R_{ref\ j,j+1} = k_{j,j+1}^2 \omega_0 L_j Q_{(j+1)L}, \quad j = 1, 2, \dots, m\text{-}1 \tag{3.4}$$

where $k_{j,j+1}$ is the coupling coefficient between the j^{th} and $(j+1)^{th}$ coils and all coils are tuned at the same resonance frequency, f_0. $Q_{(j+1)L}$ is the loaded quality factor of the $(j+1)^{th}$ coil which can be found from

$$Q_{jL} = \frac{\omega_0 L_j}{R_j + R_{ref\ j,j+1}} = \frac{Q_j}{1+k_{j,j+1}^2 Q_j Q_{(j+1)L}}, j = 1, 2, \dots, m\text{-}1 \tag{3.5}$$

where $Q_j = \omega_0 L_j/R_j$ and R_j are the unloaded quality factor and parasitic series resistance of the j^{th} coil, L_j, respectively. It should be noted that for the last coil, which is connected to the load in series, $Q_{mL} = \omega_0 L_m/(R_m+R_L)$ and for the first coil, which is connected to the source, R_1 also includes the source output impedance, R_s. Therefore, assuming that the coupling between non-neighboring coils is negligible, the PTE from the j^{th} coil to $(j+1)^{th}$ coil can be written as

$$\eta_{j,j+1} = \frac{R_{ref\ j,j+1}}{R_j + R_{ref\ j,j+1}} = \frac{k_{j,j+1}^2 Q_j Q_{(j+1)L}}{1+k_{j,j+1}^2 Q_j Q_{(j+1)L}}. \tag{3.6}$$

Using (3.4), (3.5), and (3.6), the overall PTE in such a multi-coil inductive link can be found from

$$\eta_{m-coil} = \prod_{j=1}^{m-1}\eta_{j,j+1}\cdot\frac{Q_{mL}}{Q_L}, \tag{3.7}$$

and the PDL from,

$$P_{L,m-coil} = \frac{V_s^2}{2R_1} \frac{1}{1+k_{12}^2 Q_1 Q_{2L}} \eta_{m-coil} . \quad (3.8)$$

For (3.7) and (3.8) to be valid, all coils should be tuned at the same resonance frequency to also achieve the highest PTE and PDL between each neighboring pair of coils [32], and maximize the PTE and PDL of the multi-coil link.

3.1.1. Optimal 2-coil Power Transfer Link

The PTE profile of the 2-coil inductive link according to (3.2) is a monotonically decreasing function of the coils' coupling distance, d_{23}. However, for a given set of Q_2, Q_3 and k_{23} values, there is an optimal load, $R_{L,PTE} = \omega_0 L_3 Q_{L,PTE}$, which can maximize the PTE at that particular d_{23}. $Q_{L,PTE}$ can be found by calculating the derivative of (3.2) vs. Q_L from

$$Q_{L,PTE} = \frac{Q_3}{(1+k_{23}^2 Q_2 Q_3)^{1/2}} . \quad (3.9)$$

The maximum PDL at a certain d_{23} can be achieved when the reflected impedance from (3.1) matches the primary coil impedance, i.e. $R_{ref} = R_2$. It should also be noted that in this condition, the PTE is always less than 50%, because half of the power is dissipated in R_2. Thus, the coupling coefficient which maximizes PDL for a certain R_L can be found from,

$$k_{23,PDL} = \frac{1}{(Q_2 Q_{3L})^{1/2}} . \quad (3.10)$$

Alternatively, by calculating the derivative of (3.3) vs. Q_L, one can find the optimal load, $R_{L,PDL} = \omega_0 L_3 Q_{L,PDL}$, which can maximize the PDL at a particular d_{23}, where

$$Q_{L,PDL} = \frac{Q_3}{1+k_{23}^2 Q_2 Q_3} . \quad (3.11)$$

It is important to note that according to (3.9) and (3.11), the maximum PTE and

PDL cannot be achieved simultaneously with the same R_L or d_{23}. In the 2-coil links, each of these conditions requires a specific set of k_{23}, Q_2, and Q_3, which may not be feasible within the designated constraints. On the other hand, a multi-coil solution provides the designer with more degrees of freedom to optimize the inductive link based on either one of the above requirements. This is the basic idea behind the 3- and 4-coil inductive links, despite their potential negative impact on the size-constrained applications.

3.1.2. Four-coil Power Transfer Inductive Link

The PTE in the 4-coil inductive link, shown in Fig. 3.1a, can be found by reflecting the resistive components to the left from the load coil back to the driver coil loop, one stage at a time using (3.4), and calculating the portion of the power that is delivered to the following stage, using (3.6), until it reaches R_L

$$\eta_{4-coil} = \frac{(k_{12}^2 Q_1 Q_2)(k_{23}^2 Q_2 Q_3)(k_{34}^2 Q_3 Q_{4L})}{[(1+k_{12}^2 Q_1 Q_2).(1+k_{34}^2 Q_3 Q_{4L})+k_{23}^2 Q_2 Q_3].[1+k_{23}^2 Q_2 Q_3+k_{34}^2 Q_3 Q_{4L}]} \cdot \frac{Q_{4L}}{Q_L}. \tag{3.12}$$

To simplify this equation, k_{13}, k_{14} and k_{24} have been neglected in comparison to coupling coefficients between neighboring coils, which are k_{12}, k_{23} and k_{34} [46]. Using the same method, the PDL in the 4-coil inductive link can be found from

$$P_{L,4-coil} = \frac{V_s^{\,2}}{2R_1} \frac{(k_{12}^2 Q_1 Q_2)(k_{23}^2 Q_2 Q_3)(k_{34}^2 Q_3 Q_{4L})}{[(1+k_{12}^2 Q_1 Q_2).(1+k_{34}^2 Q_3 Q_{4L})+k_{23}^2 Q_2 Q_3]^2} \cdot \frac{Q_{4L}}{Q_L} \tag{3.13}$$

The PTE between loosely coupled primary and secondary coils, L_2 and L_3, is the dominant factor in determining the overall PTE of the 4-coil link at a large coupling distance, d_{23}. When R_L reflects onto L_3 from L_4 according to (3.4), it reduces the quality factor of L_3 from $Q_3 = \omega_0 L_3/R_3$ to

$$Q_{3L} = \frac{Q_3}{1+k_{34}^2 Q_3 Q_{4L}}, \tag{3.14}$$

based on (3.5). In order to maximize the PTE between L_2 and L_3, Q_{3L} in (3.14) should satisfy (3.9). k_{34} in (3.14) is, therefore, a key parameter in 4-coil links which allows

designers to maximize the PTE for any arbitrary R_L. This flexibility is not available in a 2-coil link. Similarly, the total impedance in the secondary coil reflects onto the primary coil, based on (3.4), and reduces the primary coil's quality factor from $Q_2 = \omega_0 L_2/R_2$ to

$$Q_{2L} = \frac{Q_2}{1 + k_{23}^2 Q_2 Q_{3L}}. \tag{3.15}$$

From (3.15) and (3.6) it can be inferred that a strong coupling between the primary and secondary coils (i.e. a high k_{23}) reduces Q_{2L} and consequently η_{12}, which is the PTE between L_1 and L_2. It should also be noted that according to (3.15), Q_{2L} is roughly proportional to k_{23}^{-2}, where k_{23} is further proportional to d_{23}^{-3} [7]. Therefore, Q_{2L} is proportional to d_{23}^{6}, implying that η_{12} will significantly reduce at small d_{23} if k_{12} is not chosen large enough. This effect has been demonstrated in Fig. 3.2a, which shows the PTE of a 4-coil inductive link as a function of k_{12} and d_{23} for the coils used in our measurements and specified in Table 3.1. It can be seen that for small k_{12}, near the origin, the PTE has dropped at short coupling distances due to the small η_{12}. Therefore, small Q_1 and k_{12} will result in a significant drop in η_{12} at small coupling distances according to (3.6).

In order to avoid the above problem, k_{12} should be kept large, which according to (3.4) results in a large reflected load onto L_1. This can reduce the available power from the source, according to (3.8), unless V_s is increased. However, large V_s can cause safety issues in medical applications, and this is a major disadvantage of the 4-coil arrangement for inductive power transfer to IMDs, particularly when a high PDL is required.

Fig. 2b shows the PDL from (4.13) as a function of k_{12} and d_{23} for the coils in Table 3.1. It can be seen that increasing k_{12} results in reducing the PDL when V_s is kept constant. A comparison between Figs. 3.2a and 3.2b is instructive by observing that the high PTE and high PDL areas of these surfaces do not overlap, which means that in a 4-coil inductive link there is always a compromise between the highest PTE that can be achieved while delivering sufficient power to the load without surpassing safe V_s limits.

This can be seen in [47] where k_{12} has been purposely reduced to achieve a high PDL. The result of k_{12} reduction, however, is a drop in PTE from 70% to 10% in short coupling distances. Thus, considering the above issues power IMD applications is questionable.

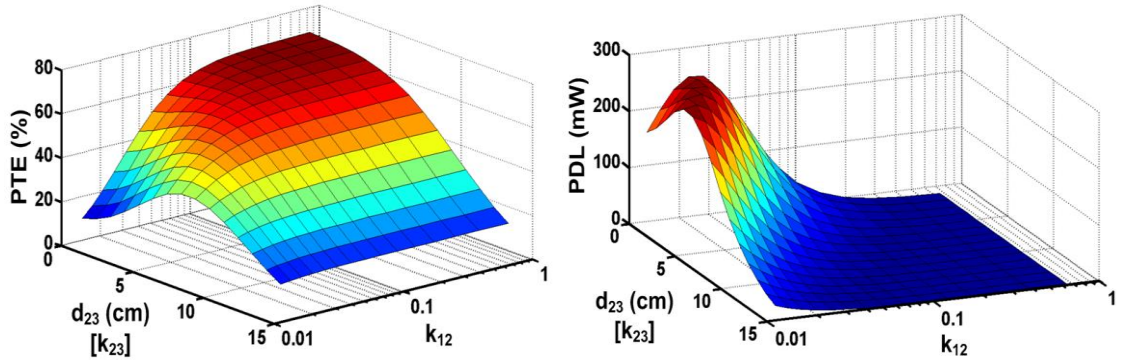

(a) (b)

Fig. 3.2. Simulated (a) power transfer efficiency (PTE) and (b) power delivered to the load (PDL) for a 4-coil inductive link as a function of k_{12} and d_{23} when k_{34} = 0.22 for the coils specified in Table 3.1. V_s = 1 V and R_L = 100 Ω.

The optimal PTE with respect to d_{23} in a 4-coil link can be found by differentiating (3.12) in terms of k_{23}, which gives

$$k_{23,PTE} = \left(\frac{\sqrt{1 + k_{12}^2 Q_1 Q_2}.(1 + k_{34}^2 Q_3 Q_{4L})}{Q_2 Q_3} \right)^{1/2}. \tag{3.16}$$

This equation helps designers to shift the peak of the PTE profile in Fig. 3.2a towards the nominal coupling distance for certain k_{12} and k_{34} values. Similarly, the optimal PDL, can be found by differentiating (3.13) in terms of k_{23}, which results in

$$k_{23,PDL} = \left(\frac{(1 + k_{12}^2 Q_1 Q_2).(1 + k_{34}^2 Q_3 Q_{4L})}{Q_2 Q_3} \right)^{1/2}. \tag{3.17}$$

3.1.3. Three-coil Power Transfer Inductive Link

The 3-coil inductive link circuit model, which comprises of the primary coil, L_2, on the Tx side and the secondary and load coils (L_3 and L_4) on the Rx side, has been shown in Fig. 3.3. The PTE of this link with no simplification can be found from

$$\eta_{3-coil} = \frac{(k_{23}^2 Q_2 Q_3)(k_{34}^2 Q_3 Q_{4L}) + k_{24}^2 Q_2 Q_{4L}}{\cos(\theta)\left(1 + k_{34}^2 Q_3 Q_{4L}\right)\sqrt{A^2 + B^2}} \cdot \frac{Q_{4L}}{Q_L} \tag{3.18}$$

where A, B, and θ are

$$A = 1 + k_{23}^2 Q_2 Q_3 + k_{34}^2 Q_3 Q_{4L} + k_{24}^2 Q_2 Q_{4L},$$
$$B = 2 Q_2 Q_3 Q_{4L} k_{23} k_{24} k_{34},$$
$$\theta = \tan^{-1}(B/A). \tag{3.19}$$

Also the PDL of the 3-coil inductive link can be found from

$$P_{L,3-coil} = \frac{V_s^2}{2R_2} \frac{(k_{23}^2 Q_2 Q_3)(k_{34}^2 Q_3 Q_{4L}) + k_{24}^2 Q_2 Q_{4L}}{A^2 + B^2} \cdot \frac{Q_{4L}}{Q_L}. \tag{3.20}$$

If we ignore k_{24} due to large separation between L_2 and L_4, then (3.18) is simplified to

$$\eta_{3-coil} = \frac{(k_{23}^2 Q_2 Q_3)(k_{34}^2 Q_3 Q_{4L})}{[(1 + k_{23}^2 Q_2 Q_3 + k_{34}^2 Q_3 Q_{4L})(1 + k_{34}^2 Q_3 Q_{4L})]} \cdot \frac{Q_{4L}}{Q_L} = \eta_{23}\eta_{34} \tag{3.21}$$

where

$$\eta_{23} = \frac{k_{23}^2 Q_2 Q_{3L}}{1 + k_{23}^2 Q_2 Q_{3L}} = \frac{k_{23}^2 Q_2 Q_3}{1 + k_{23}^2 Q_2 Q_3 + k_{34}^2 Q_3 Q_{4L}},$$

$$\eta_{34} = \frac{k_{34}^2 Q_3 Q_{4L}}{1 + k_{34}^2 Q_3 Q_{4L}} \cdot \frac{Q_{4L}}{Q_L}. \tag{3.22}$$

Similarly, (3.20) can be simplified to

$$P_{L,3-coil} = \frac{V_s^2}{2R_2} \frac{(k_{23}^2 Q_2 Q_3)(k_{34}^2 Q_3 Q_{4L})}{(1 + k_{23}^2 Q_2 Q_3 + k_{34}^2 Q_3 Q_{4L})^2} \cdot \frac{Q_{4L}}{Q_L}. \tag{3.23}$$

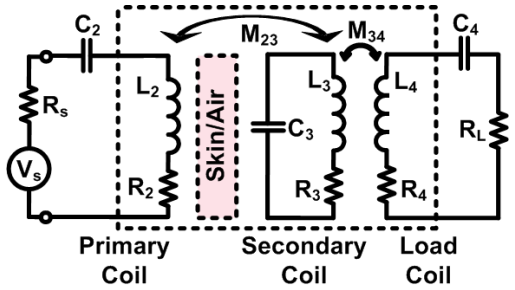

Fig. 3.3. Lumped circuit model of the 3-coil inductive link.

The problem with the optimal 2-coil power transfer link was that for a given set of Q_2, Q_3, and k_{23}, the optimal PTE could only be achieved for a certain load, $R_{L,PTE}$, which could be far from the nominal RL. In the 3-coil power transfer inductive link, however, L_3, L_4 and M_{34} in Fig. 3.3 can play the role of an impedance matching circuit (compare with Fig. 3.1b), which can convert any arbitrary R_L to $R_{L,PTE}$. This is equivalent to having a load quality factor of $Q_L = Q_{L,PTE}$ in the secondary loop of a 2-coil link, which was defined in (3.9).

This leverage in the design of the 3-coil links has been provided by $k_{34}^2 Q_3 Q_{4L}$ term in (3.21)-(3.23). Lowering $k_{34}^2 Q_3 Q_{4L}$ tends to increase η_{23} and at the same time reduces η_{34} in (3.22), both of which affect the overall PTE in (3.21). To better understand the PTE variations in a 3-coil inductive link, the effects of k_{34} and d_{23} on the PTE are shown in Fig. 3.4a for the coils specified in Table 3.1. The optimal value for $k_{34}^2 Q_3 Q_{4L}$ that maximizes the PTE for a certain d_{23} (or k_{23}) can be found by differentiating (3.21) with respect to k_{34},

$$k_{34,PTE} = \left(\frac{1 + k_{23}^2 Q_2 Q_3}{Q_3^2 Q_{4L}^2} \right)^{1/4} = \left(\frac{\left(1 + k_{23}^2 Q_2 Q_3\right)\left(1 + R_L / R_4\right)^2}{Q_3^2 Q_4^2} \right)^{1/4} . \tag{3.24}$$

For a certain R_L, if the choice of k_{34} in the design of a 3-coil link satisfies (3.24), then the reflected load onto the secondary loop will satisfy (3.9) and maximizes the PTE.

Fig. 3.4b shows the effects of k_{34} and d_{23} on the PDL of the 3-coil inductive link in Table 3.1, based on (3.23). It can be seen that there are optimal values for both k_{34} and k_{23}, which can maximize PDL, and in order to find them, (3.23) should be differentiated with respect to k_{34} and k_{23},

$$k_{23,PDL} = \left(\frac{1 + k_{34}^2 Q_3 Q_{4L}}{Q_2 Q_3} \right)^{1/2} , \tag{3.25}$$

$$k_{34,PDL} = \left(\frac{1 + k_{23}^2 Q_2 Q_3}{Q_3 Q_{4L}} \right)^{1/2} . \tag{3.26}$$

These values result in the reflected load on to the primary coil to be equal to R_2, in order to satisfy (3.11) for any arbitrary R_L.

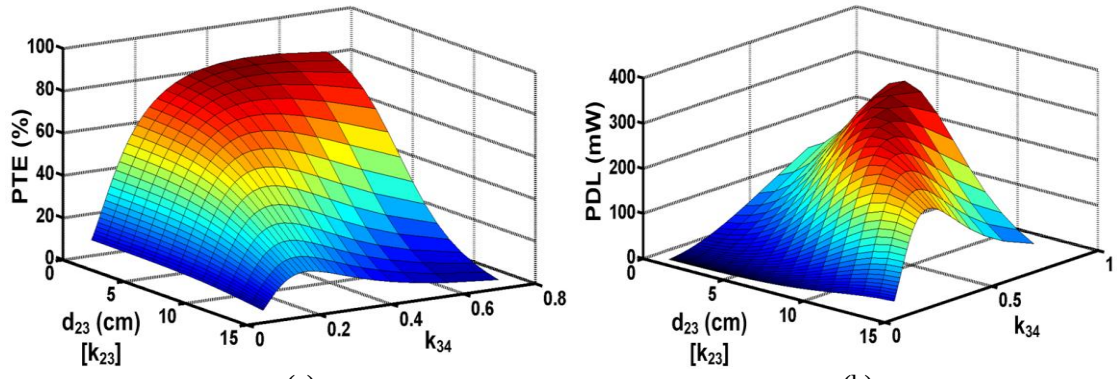

(a) (b)

Fig. 3.4. Simulated (a) PTE and (b) PDL for a 3-coil inductive link as a function of k_{34} and d_{23} for the coils in Table 3.1. V_s = 1 V and R_L = 100 Ω.

A comparison between Figs. 3.4 and 3.2 reveals a key advantage of the 3-coil links over their 4-coil counterparts, which suffer from poor PDL in areas of the curve that PTE is high. Comparing Figs. 3.4a and 3.4b, however, shows that by proper choice of k_{23} and k_{34}, which depend on the coil values and their geometries, designers can establish 3-coil inductive power transfer links that offer both high PTE as well as high PDL. Another advantage of the 3-coil links is that they are not affected by the inefficiency between the driver and primary coils ($\eta_{12} < 1$).

Fig. 3.5a compares the 2-coil and 3-coil links' optimal load quality factors, $Q_{L,PTE}$, vs. d_{23} to maximize the PTE for the coils in Table 3.1. Three important points to learn from these curves are: 1) The 2-coil link needs an exceedingly higher $Q_{L,PTE}$ as d_{23} increases, which may not be feasible, particularly small coils. On the other hand, the 3-coil link satisfies the PTE optimization requirement at various distances with much smaller $Q_{L,PTE}$, which is quite feasible by connecting R_L in series with L_4 as shown in Fig. 3.3. 2) The optimal $Q_{L,PTE}$ in the 3-coil link is adjustable with k_{34} based on (3.24), as shown in Fig. 3.5b, where the optimal PTE has been maintained for the 3-coil link in a wide range of R_L (10 Ω – 1 k Ω) at d_{23} = 5 cm. On the other hand, with a 2-coil link the

optimal PTE has been achieved in these conditions only for a specific $R_{L,PTE}$ = 200 Ω that satisfies (3.9). 3) At small d_{23}, the 2-coil link requires smaller $Q_{L,PTE}$, which is relatively easy to achieve. Therefore, for short distance inductive power transmission, which is the case in most transcutaneous IMD applications, a conventional 2-coil inductive link that is properly designed can be very close to the optimal choice [20], [21].

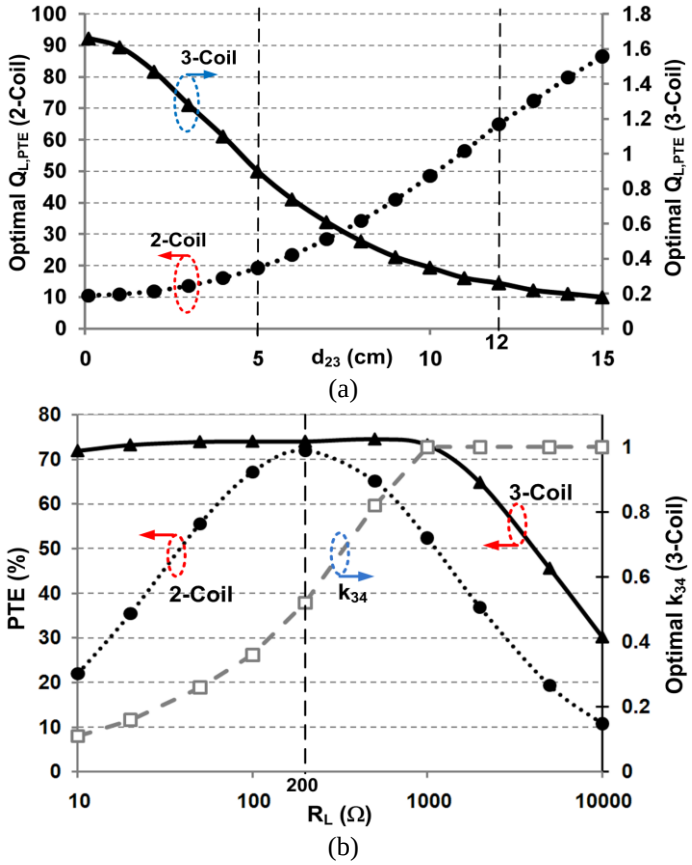

Fig. 3.5. (a) Optimal load quality factor, $Q_{L,PTE}$, needed to achieve the highest PTE vs. coils' spacing in 2- and 3-coil inductive links (k_{34} = 0.22, R_L = 100 Ω, and other parameters from Table 3.1). (b) k_{34} adjustments based on (3.24) to maintain the optimal PTE in a 3-coil link vs. R_L at d_{23} = 5 cm. The 2-coil link only reaches the optimal PTE for a specific R_L = 200 Ω that satisfies (3.9).

The additional degree of freedom provided by 3- and 4-coil inductive links via k_{34} allows designers to increase the loaded quality factor of L_3 (Q_{3L}). This leads to better immunity to misalignment but at the same time higher sensitivity to carrier frequency variations or detuning in multi-coil links. Note that misalignment only happens between L_2 and L_3, because L_1 and L_2 in 4-coil links and L_3 and L_4 in 3- and 4-coil links are often

housed together in the Tx and Rx sides, respectively. There is also little concern about detuning of L_4 and L_1 because these coils have very small loaded quality factors and therefore are much less sensitive to frequency shifts.

3.2. Optimal Design of Multi-coil Inductive Links

We extend the design and optimization procedure, which we introduced in [34] for maximizing the PTE in 2-coil wireless power transmission links to multiple coils. Either (3.18) or (3.21) can be used for the optimization of PTE in 3-coil links. However, the former can complicate the procedure, which may not be necessary if k_{24} is very small. As mentioned in [34], most of the design constraints are set by the inductive link application, and the rest of them by the coil fabrication process. For instance, in IMD applications the size of L_3 depends on the IMD location in the body. Because to maximize the PTE, the outer diameter of L_3, D_{o3}, should be increased to the largest size allowed by the application.

We choose an inductively powered wireless neural recording system for freely behaving small animal subjects as our design and optimization example [23], [24]. A key limitation of the current wireless neural recording systems that are developed for neuroscience applications is the need for the animal subject to carry a large payload of batteries for continuous recording over several hours or even days. This may not be a major issue for larger animal subjects such as non-human primates [35], [36]. However, such a payload can affect the behavior of smaller animals such as rats and mice, which are more common in behavioral neuroscience labs due to their lower cost [93], [94]. The goal here is to substitute the batteries by L_3 and L_4 in the animal headstage, and L_2 at the bottom of the cage. For such an application, we chose D_{o3}, d_{23}, and d_{34} equal to 4 cm, 12 cm, and 0.9 cm, respectively, as the starting point of this design example (see Table 3.1).

3.2.1. Design Procedure

It was shown that the optimal 3-coil link can be considered as the loosely coupled L_2-L_3 link when the arbitrary R_L is transformed to $R_{L,PTE}$, utilizing L_4 and k_{34} to satisfy (3.9). Therefore, the optimization procedure, shown in Fig. 3.6 flowchart, has two parts: First, η_{23} is maximized in (3.22) by maximizing $k_{23}^2 Q_2 Q_3$, which requires optimizing L_2 and L_3 geometries like what we did for a 2-coil inductive link in [34]. Second, the geometry of L_4 is optimized for k_{34} to satisfy (3.24), and consequently maximize η_{34} in (3.22) by maximizing $k_{34}^2 Q_3 Q_{4L}$.

One of the decisions that should be made early on is whether the coils are lithographically defined or wire-wound. Geometrical parameters of the printed spiral coils (PSC) that affect circuit parameters such as Q and k, and consequently the PTE, are the line width (w), line spacing (s), outer diameter (Do), and fill factor (φ: the ratio between the difference and the sum of a PSC's inner and outer diameters), which are described in [34]. In wire-wound coils (WWC) made of single filament solid wires, w is the wire diameter, the number of turns (n: integer) is used instead of φ, and s can be twice the thickness of the wire insulation. The relationship between circuit parameters and the coil geometries in this case can be found in the Appendix. In each step of this optimization scheme, the designer should derive k, Q, and other circuit parameters from the PSC and WWC geometries using the equations presented in [34] and the Appendix, respectively. Moreover, to consider the finite Q of the resonance capacitors and the resistance of their connections to the coils, an additional 0.1Ω was added to $R_{1\text{-}4}$ values.

In step-1, design constraints imposed by the application and coil fabrication technology are considered. The former defines the maximum values for D_{o3} and D_{o4}, while the latter indicates the minimum line width and line spacing (w_{min}, s_{min}) in the case of PSC, or the wire specifications in WWC. The nominal values for d_{12}, d_{23}, d_{34}, R_L and R_s are also required in this step, which are dependent on the application (d_{12} is needed

only for 4-coil links). For instance, d_{34} will depend on the implant thickness in IMD applications if L_3 and L_4 are going to be housed together. As mentioned earlier, R_s, which is a property of the driving circuitry, should be added to R_2 and R_1 in our procedure for the design of 3- and 4-coil links, respectively.

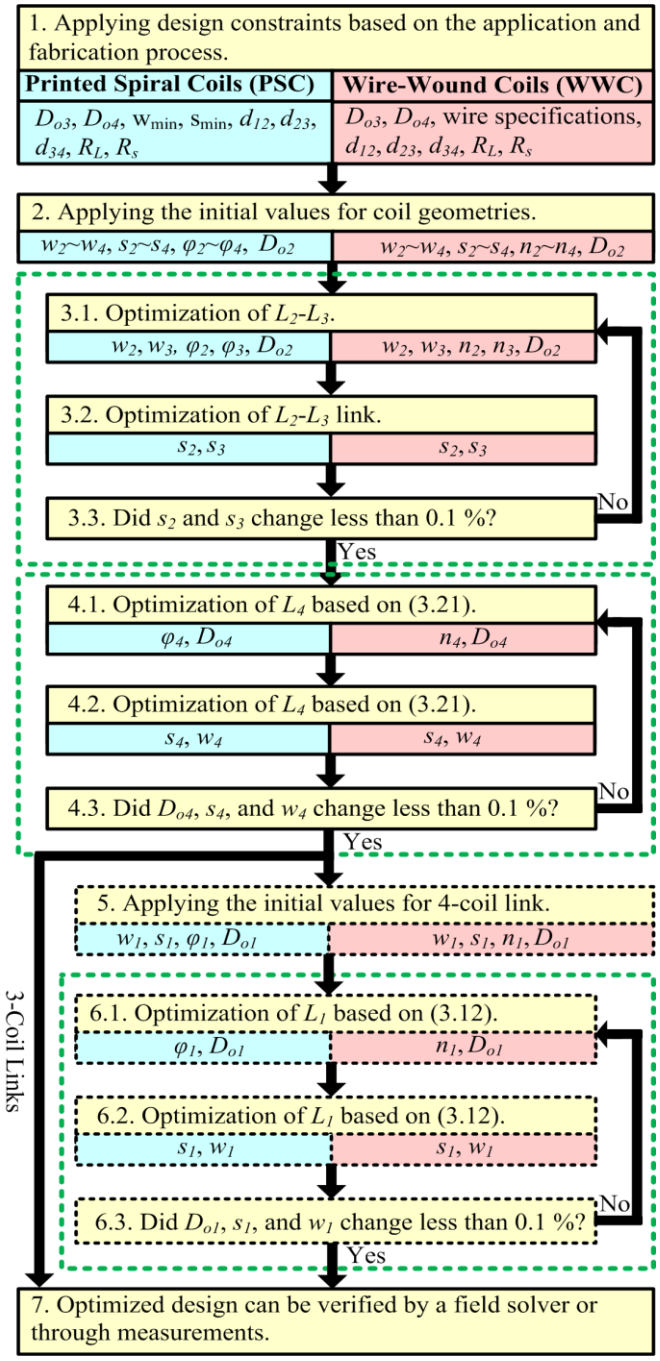

Fig. 3.6. Iterative multi-coil inductive link design optimization flowchart.

In step-2, the initial values for L_2~L_4 geometries are chosen, which are (w_2~w_4, s_2~s_4, φ_2~φ_4, D_{o2}) and (w_2~w_4, s_2~s_4, n_2~n_4, D_{o2}) for PSCs and WWCs, respectively. A more detailed discussion about how to choose these initial values can be found in [34].

L_2 and L_3 geometries are optimized in step-3 for $\eta_{23,max}$. In step-3.1, following the procedure in [34] provides the optimal values of (w_2, w_3, φ_2, φ_3, D_{o2}) for PSCs. Running the same iterative procedure while replacing (φ_2, φ_3) with (n_2, n_3) in the Appendix provides the optimal values of (w_2, w_3, n_2, n_3, D_{o2}) for WWCs. In step-3.2, values found in step-3.1 are used to sweep s_2 and s_3 in [34] or in the Appendix for PSCs or WWCs, respectively, such that the resulting k_{23}, Q_2, and Q_3 maximize $k_{23}^2 Q_2 Q_3$. The new s_2 and s_3 values are then fed back into step-3.1 to improve η_{23} further. Steps 3.1 and 3.2 are repeated iteratively until s_2 and s_3 values change less than 0.1% and satisfy the condition in step-3.3.

In step-4, the geometry of L_4 is optimized using L_2 and L_3 circuit parameters from step-3, such that the resulting k_{34}, R_4, and Q_4 satisfy (3.24). In step-4.1 for PSCs, φ_4 and D_{o4} are swept in [34] for the resulting k_{34} and Q_4 to maximize $\eta_{3\text{-}coil}$ in (3.21). Similarly for WWCs, n_4 and D_{o4} are swept for the resulting k_{34} and Q_4 from the Appendix to maximize $\eta_{3\text{-}coil}$. In step-4.2, the new φ_4 and D_{o4} values found in step-4.1 for PSCs are used to sweep s_4 and w_4 in [34] for the resulting k_{34} and Q_4 to further maximize $\eta_{3\text{-}coil}$ in (3.21). For WWCs, n_4 and D_{o4} values from step-4.1 are used to sweep s_4 and w_4 in the Appendix for the resulting k_{34} and Q_4 to further maximize $\eta_{3\text{-}coil}$. Steps 4.1 and 4.2 are repeated iteratively until s_4, w_4 and D_{o4} values change less than 0.1% and satisfy the condition in step-4.3. This step concludes the design of the 3-coil wireless power transmission link for maximum PTE, which can be further validated using field solvers, such as HFSS (Ansoft, Pittsburgh, PA).

The rest of steps in Fig. 3.6 are specific to 4-coil links to optimize the geometry of L_1 for the highest PTE based on (3.12). In step-5, the initial values for L_1 geometry, which are (w_1, s_1, φ_1, D_{o1}) and (w_1, s_1, n_1, D_{o1}) for the PSCs and WWCs, respectively, are

chosen. Step-6 is quite similar to step-4, which determined the optimal geometry of L_4. The iterative process in steps 6.1 and 6.2, and the condition in step-6.3 will ensure $\eta_{12,max}$ and consequently maximize $\eta_{4\text{-}coil}$ in (3.12), which can be validated by field solvers.

3.2.2. Design Example

Table 3.1 summarizes the results of optimization procedure for two sets of 2-, 3- and 4-coil inductive links that operate at f_0 = 13.56 MHz and deliver power to a load of R_L = 100 Ω as efficiently as possible from a nominal coupling distance of d_{23} = 12 cm. To discriminate between the losses that are specific to the inductive link and those that are related to the driver circuit, we considered a small R_s of only 0.1 Ω in our optimizations to account for the driver output resistance. Based on the requirements of our application, the coils on the Tx side were considered overlapping hexagonal shaped PSCs, fabricated on cost effective 1.5 mm thick FR4 printed circuit boards (PCB) with 1-oz copper weight (35.6 µm thick), and those on the Rx side were considered WWCs made of magnet wire (enameled copper).

In these designs, the PCB fabrication process requires w_{min} and s_{min} to be 150 µm. Also in the case of the 4-coil design, the overlapping L_1 and L_2 determine d_{12} by the PCB thickness. As mentioned earlier, to limit the size of the headstage, D_{o3} and d_{34} were also limited 4 cm and 0.9 cm, respectively. The first set of coils, designated by "optimal" in Table 3.1, are resulted from the iterative optimization process, as shown in Fig. 3.6, with no additional constraints. According to the equations, the optimized 3- and 4-coil inductive links can achieve PTE of 55% and 54%, respectively, compared to the 2-coil inductive link, which PTE is limited to 27.4% at d_{23} = 12 cm. Despite their similarity in PTE, a key difference between the 3- and 4-coil links is that the former has a PDL of 146 mW for V_s = 1 V, while the latter can only deliver 6.8 mW to the load because of the large reflected impedance, R_{ref}, onto the driver coil, L_1. The PDL of the 2-coil link in these conditions is 160 mW.

Table 3.1: Optimized geometries for design examples

Parameters		Symbols	2-Coil		3-Coil / 4-Coil	
			Meas	Optim	Meas	Optim
L_1	Inductance (μH)	L_1	-	-	- / 0.9	- / 0.18
	Outer diameter (cm)	D_{o1}	-	-	- / 16.8	- / 10.5
	Fill factor	Φ_1	-	-	- / 0.13	- / 0.14
	Num. of turns	n_1	-	-	- / 2	- / 1
	Line width (mm)	w_1	-	-	- / 8.66	- / 12
	Line spacing (mm)	s_1	-	-	- / 2.6	- / 35
	Quality factor	Q_1	-	-	- / 255	- / 131
L_2	Inductance (μH)	L_2	0.9	1.2	0.9	1.2
	Outer diameter (cm)	D_{o2}	16.8	27	16.8	27
	Fill factor	Φ_2	0.13	0.28	0.13	0.28
	Num. of turns	n_2	2	2	2	2
	Line width (mm)	w_2	8.66	12	8.66	12
	Line spacing (mm)	s_2	2.6	35	2.6	35
	Quality factor	Q_2	255	196	255	196
L_3	Inductance (μH)	L_3	0.12	0.058	0.4	0.47
	Coil diameter (cm)	D_{o3}	4			
	Wire diameter (mm)	w_3	0.64	5.68	0.64	2.2
	Num. of turns	n_3	1	1	2	3
	Line spacing (μm)	s_3	100	100	100	100
	Quality factor	Q_3	105.2	151.5	177	417
L_4	Inductance (μH)	L_4	-	-	0.4	0.22
	Coil diameter (cm)	D_{o4}	-	-	4	2.8
	Wire diameter (mm)	w_4	-	-	0.64	1
	Num. of turns	n_4	-	-	2	2
	Line spacing (μm)	s_4	-	-	100	100
	Quality factor	Q_4	-	-	177	142
L_1 - L_2 coupling distance (mm)		d_{12}	-		- / 1.5	
L_2 - L_3 coupling distance (mm)		d_{23}	120			
L_3 - L_4 coupling distance (mm)		d_{34}	-		9	
Power transfer efficiency (%)		η	15	27.4	37 / 35	55 / 54
Power delivered to load (mW)		PDL	170	160	260 / 4.4	146 / 6.8
Nominal load (Ω)		R_L	100			
Driver output resistance (Ω)		R_s	0.1			
Power carrier frequency (MHz)		f_0	13.56			

L_1 and L_2 are hexagonal overlapping PSCs, while L_3 and L_4 are WWCs.
Grayed cells indicate the design constraints.

In the second set of coils, designated by "measurement", the PSC diameter on the Tx side (D_{o1}, D_{o2}) was limited to 16.8 cm due to PCB fabrication constraints. The total weight of the Rx coils that are going to be mounted on the animal headstage was limited to $W_{3,4}$ = 1.6 g, which relate to the WWC geometries according the Appendix. Hence, WWC wire diameter on the Rx side (w_3, w_4) was limited to 0.64 mm (AWG-22) to observe the headstage weight limitation. This set of coils was fabricated and used in our measurements.

3.3. Simulation and Measurement Results

Two types of setups have been used in the past for PTE measurements. In the first method, shown in Fig. 3.7a, a network analyzer is directly connected to the primary and secondary coils to measure the S-parameters. Then the S-parameters are converted to Z-parameters [95] to obtain,

$$Q_2 = \frac{\mathrm{Im}(Z_{22})}{\mathrm{Re}(Z_{22})}, Q_3 = \frac{\mathrm{Im}(Z_{33})}{\mathrm{Re}(Z_{33})}, k_{23} = \sqrt{\frac{\mathrm{Im}(Z_{23}).\mathrm{Im}(Z_{32})}{\mathrm{Im}(Z_{22}).\mathrm{Im}(Z_{33})}}, \tag{3.27}$$

and find the PTE by substituting them in (3.2). This method is straightforward, but it does not involve any actual power transfer between the coils. It is bound to the assumptions and accuracy of the models within the theoretical PTE and PDL equations. It also becomes more complicated and less accurate in multi-coil links, which should be tuned at a certain resonance frequency in order to operate properly (see Fig. 3.1a).

In the second method, shown in Fig. 3.7b, a signal generator or PA drives the primary coil, tuned at f_0, and the transmitted power is calculated by directly measuring the current and voltage waveforms. The received power can also be found in the same way by probing the voltage across R_L. Even though this method is more realistic than the first one, it rapidly loses its accuracy at higher carrier frequencies, such as 13.56 MHz, due to the parasitic components introduced by measurement probes. Moreover, the oscilloscope ground connections can introduce additional complications due to ground loops and interference. Our experiments showed that using different values of R in Fig. 3.7b for sensing the inductive link input current could result in different values for the PTE and PDL.

We have devised a new method for PTE and PDL measurements, which seems to be more accurate particularly in multi-coil inductive links. In this method, resonance capacitors and R_L are connected to the primary and load coils, which are then considered a complete 2-port system along with the multi-coil inductive link, as shown in Fig. 3.7c. The network analyzer is then used to measure the S-parameters, and consequently the Z-

parameters are derived, as in the first method [95]. PTE and PDL are found from 2-port equations,

$$PTE = \frac{|Z_{42}|^2}{R_L |Z_{22}| \cos(\angle Z_{22})},\ PDL = \frac{|V_4|^2}{2R_L} = \frac{|V_2|^2}{2R_L |Z_{22}|^2} |Z_{42}|^2 \tag{3.28}$$

where $Z_{22} = V_2/I_2$ and $Z_{42} = V_4/I_2$ are derived when $I_4 = 0$. The $I_4 = 0$ requirement in calculating Z-parameters ensures that the network analyzer loading (often 50 Ω) on the inductive link does not affect the results. In this method, as the network analyzer sweeps a certain frequency range that includes f_0, actual power transfer does take place in the form of a small signal injected from Port-1 of the network analyzer to R_L. One can also measure the entire link power transfer efficiency all the way from the battery to the load by adding the equivalent of the source output resistance, R_s, in series with L_1 in the 4-coil link and L_2 in the 2- and 3-coil links.

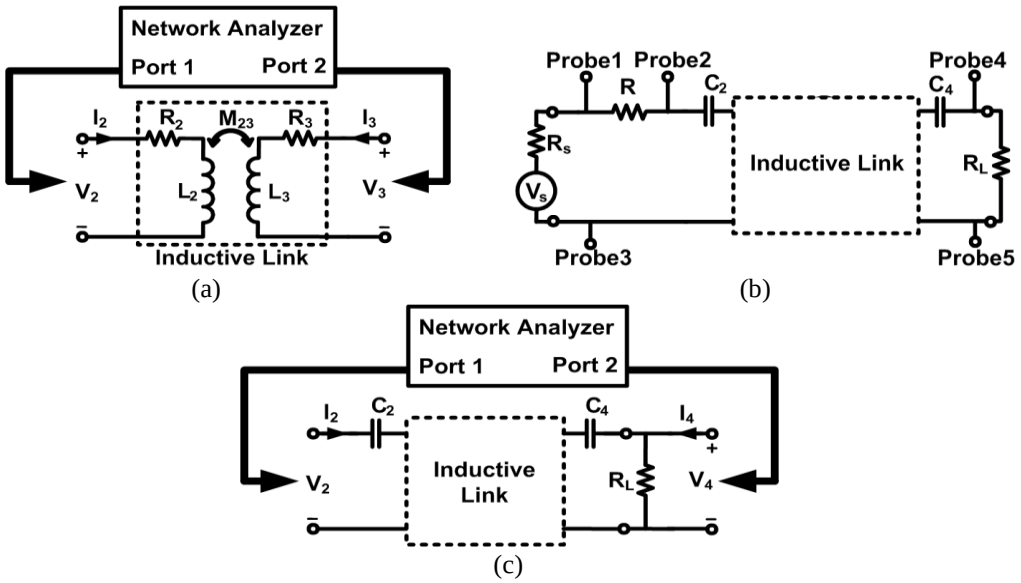

Fig. 3.7. PTE measurement setups for inductive links: (a) Conventional method using a network analyzer, (b) direct method using a signal source and current and voltage probe via oscilloscope, (c) the new method using network analyzer with all the coils tuned at the carrier frequency and R_L connected.

Figs. 3.8a and 3.9a show the experimental setup for measuring the PTE and PDL of the 3- and 4-coil inductive links, respectively. These coils were fabricated based on the values listed in the "Measurement" columns of Table 3.1, and held in parallel and

perfectly aligned using non-conducting Plexiglas sheets and plastic screws to prevent power loss due to eddy currents. Figs. 3.8b and 3.9b show 3-D models of the same coils constructed in the HFSS electromagnetic field simulator for 3- and 4-coil links, respectively. In the 4-coil setup, k_{12} was adjusted for a fixed d_{12} = 1.5 mm, by changing the amount of overlapping between similar L_1 and L_2 (see Fig. 3.9). L_3 and L_4 were also similar and provided k_{34} = 0.22 at d_{34} = 9 mm.

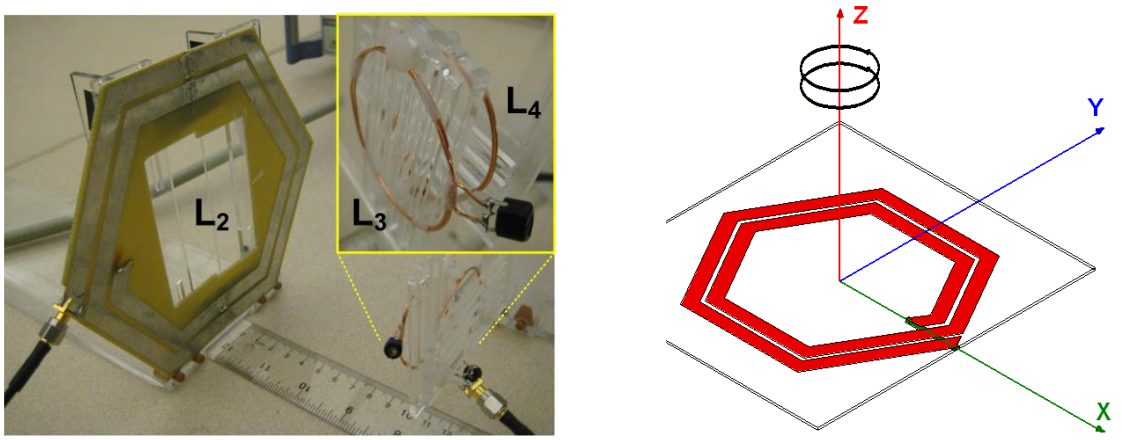

(a) (b)

Fig. 3.8. (a) Experimental setup for measuring the PTE and PDL in a 3-coil inductive link. (b) 3-coil inductive link model in the HFSS. Coil specifications are listed in Table 3.1.

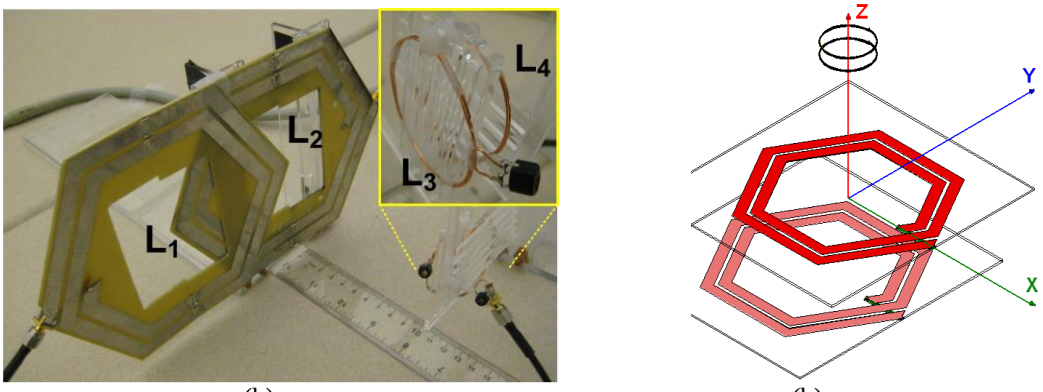

(b) (b)

Fig. 3.9. (a) Experimental setup for measuring the PTE and PDL in a 4-coil inductive link. (b) 4-coil inductive link model in the HFSS. Coil specifications are listed in Table 3.1.

Figs. 3.10a and 3.10b compare the measured, simulated (via HFSS), and calculated values of the PTE and PDL, respectively, vs. coupling distance, d_{23}, in 2-, 3- and 4-coil inductive links. The curves labeled as "Meas1" show the measurement results

according to the method proposed in Fig. 3.7c, using a ZVB4 network analyzer (R&S, Germany). It can be seen that these results are in very good agreement with HFSS simulation and calculation results, labeled "Sim" and "Calc", respectively.

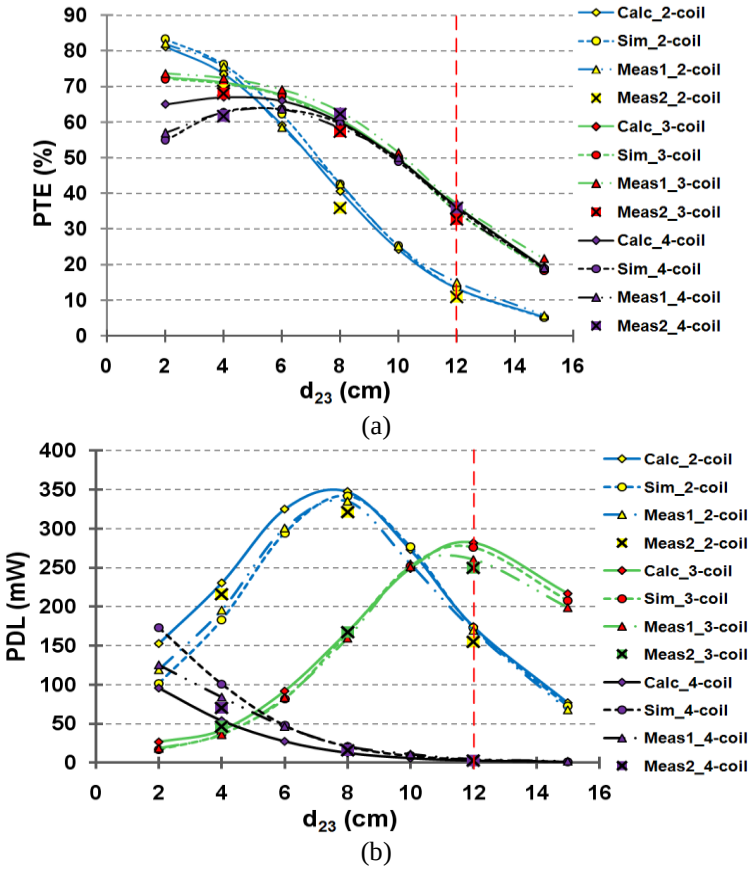

Fig. 3.10. Comparison between measured, simulated (HFSS), and calculated values of the (a) PTE and (b) PDL vs. d_{23} for 2-, 3-, and 4-coil inductive links specified in the "Measurement" columns of Table 3.1 (V_s = 1 V).

As an alternative, we also measured the PTE and PDL of the inductive links according to the method shown in Fig. 3.7b, using a class-D PA with known power efficiency (η_{PA} = 30%) and R = 15 Ω for 2- and 3-coil links, and R = 500 Ω for 4-coil link (due to low current levels) in three different distances of 4, 8, and 12 cm, which are labeled as "Meas2" in Fig 10. In this case the measurement results are probably less accurate because of the parasitic components added by the probes and the fact that the PA's power efficiency has some dependency on the reflected impedance onto the Tx side, which changes with d_{23}. Nonetheless they are close to the other values.

It can be seen in Fig. 3.10a that the 3- and 4-coil inductive link PTEs (37% and 35%, respectively) are significantly higher than the PTE of the 2-coil link (15%) at d_{23} = 12 cm. At the same coupling distance, however, the 3-coil inductive link has achieved a PDL of 260 mW from V_s = 1 V, which is 1.5 and 59 times higher than the PDL of 2- and 4-coil links, respectively, based on Fig. 3.10b. Despite its high PTE, the 4-coil link has only been able to deliver 4.4 mW to the load under these conditions, which may not be sufficient for most applications. It thus requires a much higher V_s (~7.7 times in this case) to become comparable to its 3-coil counterpart. It can also be seen from the 2-coil PTE profile in Fig. 3.10a that short and large distances have smaller PTE variation. However, there is a certain coupling distance in between where the PTE drops very rapidly. The second derivative of (3.2) can correlate $k_{23}=1/\sqrt{3Q_2Q_{3L}}$ to this distance. Q_2 and Q_{3L} should preferably be maximized to move this point to larger distances.

CHAPTER IV

THE CIRCUIT THEORY BEHIND COUPLED-MODE MAGNETIC RESONANCE-BASED WIRELESS POWER TRANSMISSION

Design and optimization of inductive power transmission links has been extensively studied in the literature over the last three decades [32], [34], [41], [42], [84]-[91]. The majority of these approaches model and analyze the inductive link from a circuit perspective, which differs, at least on the surface, from the coupled-mode theory (CMT) that was recently presented in a new form by physicists at MIT [43]. They utilized the CMT approach to propose multi-coil inductive links, which can increase the PTE considerably at large coupling distances [44], [92]. An in-depth comparison between the coupled-mode and circuit-based theories, which would clarify the relationship between these methods, often used by physicist and electrical engineers, is still lacking.

In this chapter, first the inductive link steady-state analysis using CMT is reviewed and then it is proved that both CMT and the more conventional circuit analysis i.e. reflected load theory (RLT) result in the same formulation for the inductive links' key performance measures, particularly the PTE. For the first time, the PTE equations are derived for multi-coil inductive links via CMT. The analysis shows that in the steady state mode, contrary to popular belief, both CMT and RLT are applicable to small and large coupling distances, d, as long as the coils interact in the near field regime. Because they are basically the same! Measurement results are also presented, which show the accuracy of both RLT and CMT models in estimating the PTE. On the other hand, the comparative transient analysis of a pair of capacitively loaded inductors reveals that CMT is accurate only if the mutual coupling, k, is small, e.g. due to large d, and coil quality factors, Q, are large, which limits the applicability of the CMT-based transient analysis to midrange coupling distances of large coils. It is also shown that utilizing CMT reduces the order of the differential equations by half compared to the circuit theory as it only

considers a first order equation for each resonant object. Hence, the CMT seems to be helpful in analyzing the transient behavior of complicated multi-coil inductive links despite being less accurate than its circuit based counterpart. For all other conditions, the RLT and similar circuit based methods will do just fine.

4.1. Coupled-mode Theory (CMT)

CMT is a framework to analyze energy exchange between two resonating objects [43]. Based on the CMT, the time-domain field amplitudes of two objects, $a_2(t)$ and $a_3(t)$, which are defined so that the energy contained in them are $|a_2(t)|^2$ and $|a_3(t)|^2$, respectively, at distance d_{23} can be found from [43],

$$\begin{aligned} \frac{da_2(t)}{dt} &= -(j\omega_2 + \Gamma_2)a_2(t) + jK_{23}a_3(t) + F_S(t) \\ \frac{da_3(t)}{dt} &= -(j\omega_3 + \Gamma_3 + \Gamma_L)a_3(t) + jK_{23}a_2(t) \end{aligned}, \qquad (4.1)$$

where ω_2 and ω_3 are the eigen frequencies, Γ_2 and Γ_3 are the resonance widths or rate of intrinsic decay due to the objects' absorption (ohmic) and radiative losses, Γ_L is the resonance width due to load resistance connected to the second object (proportional to $1/R_L$), $F_S(t)$ is the excitation applied to the first object, and K_{23} is the coupling rate between the two objects. The CMT method has been recently applied to a pair of capacitively-loaded conducting-wire loops, spaced by d_{23}, as shown in Fig. 4.1, forming a conventional inductive power transmission link, in which L_2 is the power Tx and L_3 is the power Rx inductors, both tuned at the same frequency, $\omega_2 = \omega_3 = \omega$.

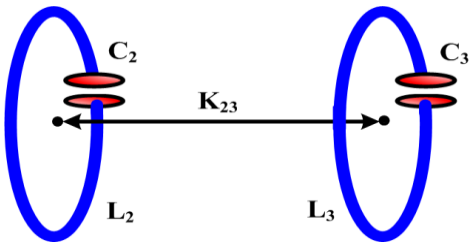

Fig. 4.1. A pair of capacitively loaded inductors used for efficiency calculation using the coupled-mode theory (CMT).

4.1.1. Steady-state Analysis via Coupled-mode Theory

In steady state analysis, which applies to the conventional inductive power transmission links, $F_S(t)$ in (4.1) is a sinusoidal signal described as $A_s e^{-j\omega t}$. In this condition, the alternating field amplitude in the primary inductor is constant, $a_2(t) = A_2 e^{-j\omega t}$, resulting in a constant field amplitude in the secondary inductor, $a_3(t) = A_3 e^{-j\omega t}$. It can be shown from (4.1) that $A_3/A_2 = jK_{23}/(\Gamma_3 + \Gamma_L)$ [43]. Therefore, the average power at different nodes of the power transmission system can be calculated. The power absorbed by L_2 and the power delivered to L_3 are $P_2 = 2\Gamma_2|A_2|^2$ and $P_3 = 2\Gamma_3|A_3|^2$, respectively. The power delivered to R_L is $P_L = 2\Gamma_L|A_3|^2$ and, therefore, based on the energy conservation theory, if we neglect the radiated power in the near field regime, the total power delivered to the system from source is $P_S = P_2 + P_3 + P_L$. Hence, the PTE of the 2-coil system can be found from

$$\eta_{23} = \frac{P_L}{P_S} = \frac{1}{1+\frac{\Gamma_3}{\Gamma_L}\left[1+\frac{1}{fom^2}\left(1+\frac{\Gamma_L}{\Gamma_3}\right)^2\right]}, \tag{4.2}$$

where $fom = K_{23}/\sqrt{\Gamma_2\Gamma_3}$ is the distance-dependent figure-of-merit for energy transmission systems [44]. To maximize the PTE based on (4.2), *fom* should be maximized and an optimal value should be chosen for Γ_L/Γ_3. Parameters that affect *fom* are obviously the coupling rate between the two objects, K_{23}, which should be increased and the resonance width of each object (intrinsic loss of each inductor), Γ, which should be decreased. These are quite similar to the coupling coefficient, k_{23}, and inverse of the quality factor, $1/Q$, used in conventional methods for optimizing inductive links [34]. The other key parameter, $\Gamma_{L,PTE}/\Gamma_3$, which shows the effect of R_L in optimizing the PTE, can be found by calculating the derivative of η_{23} in (4.2) with respect to Γ_L/Γ_3, resulting in [96],

$$\Gamma_{L,PTE} = \Gamma_3\left(1+K_{23}^2/\Gamma_2\Gamma_3\right)^{1/2}. \tag{4.3}$$

4.1.2. Transient Analysis via Coupled-mode Theory

The CMT can also be utilized in analyzing the transient behavior of the resonant-coupled inductors in Fig. 4.1 by setting $F_S(t) = 0$ in (4.1) and considering an initial energy stored in L_2. This analysis provides designers with better understanding of the dynamics of energy exchange in such inductively coupled systems. As the first step, we eliminate $a_3(t)$ in (4.1) to find an expression for the time varying field in the primary coil,

$$\frac{d^2a_2(t)}{dt^2} + (2j\omega + \Gamma_2 + \Gamma_3 + \Gamma_L)\frac{da_2(t)}{dt} + [K_{23}^2 + (j\omega + \Gamma_2)(j\omega + \Gamma_3 + \Gamma_L)]a_2(t) = 0 \qquad (4.4)$$

For the sake of simplicity, if similar to [97] we assume that the two inductors are identical, i.e. $\Gamma_2 = \Gamma_3 = \Gamma$, and $\Gamma_L = 0$ (no load condition, $R_L = \infty$), then $a_2(t)$ can be found from (4.4),

$$a_2(t) = e^{-j\omega t}[e^{-\Gamma t}(b_1 e^{jK_{23}t} + b_2 e^{-jK_{23}t})], \qquad (4.5)$$

where b_1 and b_2 are constants, which values depend on the initial conditions. Similarly, $a_3(t)$ can be calculated using (4.1) and (4.5) as,

$$a_3(t) = e^{-j\omega t}[e^{-\Gamma t}(d_1 e^{jK_{23}t} + d_2 e^{-jK_{23}t})] \qquad (4.6)$$

where d_1 and d_2 are also constants with values dependent on the initial conditions. The total energy in L_2 and L_3 can be found from $E_2(t) = |a_2(t)|^2$ and $E_3(t) = |a_3(t)|^2$, respectively. If one starts with 100% of the total energy normalized and initially stored in L_2, i.e. $|a_2(t=0)|^2 = 1$ and $|a_3(t=0)|^2 = 0$, the energy stored in each object over time can be found from

$$E_2(t) = e^{-2\Gamma t}\cos^2 K_{23}t, \quad E_3(t) = e^{-2\Gamma t}\sin^2 K_{23}t\ . \qquad (4.7)$$

It should be noted that E_2 and E_3 are not the instantaneous but the peak values (or envelopes) of the energy contents stored in L_2 and L_3, which are in resonance with C_2 and C_3, respectively, at the rate of 2ω.

4.2. Reflected-load Theory (RLT)

Fig. 4.2a shows a pair of inductively coupled coils, which will be referred to as the primary (L_2) and secondary (L_3). It can be shown that the highest PTE across such links can be achieved when both LC-tanks are tuned at the same resonance frequency, i.e. $\omega = 1/\sqrt{L_2C_2} = 1/\sqrt{L_3C_3}$.

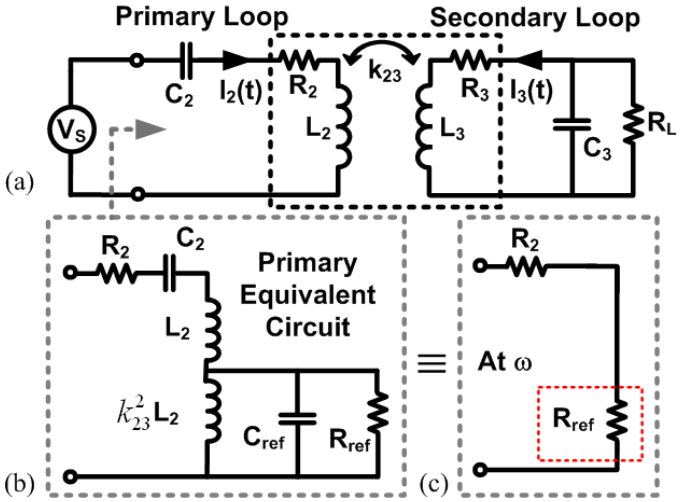

Fig. 4.2. (a) Simplified model of a 2-coil power transmission link with a resistive load. (b) Equivalent circuit seen across the driver. (c) Reflected load onto the primary loop at resonance frequency.

4.2.1. Steady-state Analysis via Reflected-load Theory

The inductive link PTE is mainly dependent on the mutual coupling between the coils, k_{23}, and their quality factors, $Q_2 = \omega L_2/R_2$ and $Q_3 = \omega L_3/R_3$ [34]. At resonance frequency, the secondary loop which is connected to R_L can be reflected onto the primary loop and represented by R_{ref} [7]. To find R_{ref}, the secondary loop is modeled with a parallel load as shown in Fig. 4.2a. R_3, the parasitic resistance of L_3, can be transformed to a parallel resistance equal to $R_{P3} = Q_3^2 R_3$ in parallel with R_L. Hence, if we define $R_P = R_{P3} \,||\, R_L$, then we can reflect the secondary impedance onto the primary side (Fig. 4.2b),

$$R_{ref} = k_{23}^2 (L_2/L_3) R_P = k_{23}^2 \omega L_2 Q_{3L}, \;\; C_{ref} = (L_3/L_2)(C_3/k_{23}^2) = 1/(\omega^2 L_2 k_{23}^2), \tag{4.8}$$

where $Q_{3L} = R_P/\omega L_3$ is the loaded quality factor of the secondary coil. At resonance, C_{ref} resonates out with $k_{23}^2 L_2$, leaving only the reflected resistance, R_{ref}, on the primary side, as

shown in Fig. 4.2c. In the simplified inductive link model of Fig. 4.2c, L_2 and C_2 also resonate out, and the input power provided by V_s simply divides between R_2 and R_{ref}. The power absorbed by R_2 is dissipated as heat in the primary coil and the power delivered to R_{ref}, i.e. the transferred power to the secondary loop, divides between R_3 and R_L, which are the only power consuming components on the secondary side. This will lead to

$$\eta_{23} = \frac{R_{ref}}{R_2 + R_{ref}} \frac{R_{P3}}{R_{P3} + R_L} = \frac{k_{23}^2 Q_2 Q_{3L}}{1 + k_{23}^2 Q_2 Q_{3L}} . \frac{Q_{3L}}{Q_L}, \tag{4.9}$$

where $Q_L = R_L/\omega L_3$ is often referred to as the load quality factor, and $Q_{3L} = Q_3 Q_L/(Q_3+Q_L)$ [32]. It can be seen from (4.9) that large k_{23}, Q_2, and Q_3 are needed to maximize the PTE. However, for a given set of Q_2, Q_3 and k_{23} values, there is an optimal load, $R_{L,PTE} = \omega L_3 Q_{L,PTE}$, which can maximize the PTE. $Q_{L,PTE}$ can be found by calculating the derivative of (4.9) with respect to Q_L from,

$$Q_{L,PTE} = \frac{Q_3}{(1 + k_{23}^2 Q_2 Q_3)^{1/2}} . \tag{4.10}$$

4.2.2. Transient Analysis via Circuit Theory

In this analysis, the primary and secondary loops are considered identical, i.e. $L_2 = L_3 = L$, $C_2 = C_3 = C$, $R_2 = R_3 = R$ and $R_L = \infty$, similar to the CMT criteria in [97]. We have also set $V_S = 0$ V (short circuit) to focus on the transient response while considering an initial condition (current) in L_2. Primary and secondary loop currents can be found from

$$\begin{aligned} \frac{1}{C}\int_0^t I_2(t)dt + RI_2(t) + L\frac{dI_2(t)}{dt} + M\frac{dI_3(t)}{dt} = 0 \\ \frac{1}{C}\int_0^t I_3(t)dt + RI_3(t) + L\frac{dI_3(t)}{dt} + M\frac{dI_2(t)}{dt} = 0 \end{aligned}, \tag{4.11}$$

where $M = k_{23} \times L$ is the mutual inductance between L_2 and L_3. Taking the derivative of (4.11) after substituting R/L and $1/LC$ with ω/Q and ω^2, respectively, result in

$$\begin{aligned} &\frac{d^2 I_2(t)}{dt^2} + \frac{\omega}{Q}\frac{dI_2(t)}{dt} + \omega^2 I_2(t) + k_{23}\frac{d^2 I_3(t)}{dt^2} = 0 \\ &k_{23}\frac{d^2 I_2(t)}{dt^2} + \frac{d^2 I_3(t)}{dt^2} + \frac{\omega}{Q}\frac{dI_3(t)}{dt} + \omega^2 I_3(t) = 0 \end{aligned}, \tag{4.12}$$

Utilizing Laplace transform, (4.12) can be written as

$$\begin{aligned} &(s^2 + \frac{\omega}{Q}s + \omega^2) I_2(s) + k_{23} s^2 I_3(s) = 0 \\ &k_{23} s^2 I_2(s) + (s^2 + \frac{\omega}{Q}s + \omega^2) I_3(s) = 0 \end{aligned}. \tag{4.13}$$

Characteristic equation in the S-domain can be found by setting the coefficient matrix determinant in (4.13) to zero,

$$(s^2 + \frac{\omega}{Q}s + \omega^2)^2 - k_{23}^2 s^4 = 0. \tag{4.14}$$

The roots of (4.14) are,

$$\begin{aligned} s_{1,2} &= \frac{-\omega'}{2Q'}(1 \pm \sqrt{1 - 4Q'^2}) = \frac{-\omega'}{2Q'} \pm j\omega'_d \\ s_{3,4} &= \frac{-\omega''}{2Q''}(1 \pm \sqrt{1 - 4Q''^2}) = \frac{-\omega''}{2Q''} \pm j\omega''_d \end{aligned}, \tag{4.15}$$

where

$$\begin{aligned} &\omega'_d = \frac{\omega'}{2Q'}\sqrt{4Q'^2 - 1}, \quad \omega''_d = \frac{\omega''}{2Q''}\sqrt{4Q''^2 - 1} \\ &Q' = Q\sqrt{1 - k_{23}}, \quad Q'' = Q\sqrt{1 + k_{23}} \\ &\omega' = \omega / \sqrt{1 - k_{23}}, \quad \omega'' = \omega / \sqrt{1 + k_{23}} \end{aligned}. \tag{4.16}$$

Therefore, $I_2(t)$ and $I_3(t)$ can be calculated from,

$$I_2(t) = e^{\frac{-\omega'}{2Q'}t}(a_{11}\cos\omega'_d t + b_{11}\sin\omega'_d t) + e^{\frac{-\omega''}{2Q''}}(a_{12}\cos\omega''_d t + b_{12}\sin\omega''_d t) \tag{4.17}$$

$$I_3(t) = e^{\frac{-\omega'}{2Q'}t}(a_{21}\cos\omega'_d t + b_{21}\sin\omega'_d t) + e^{\frac{-\omega''}{2Q''}}(a_{22}\cos\omega''_d t + b_{22}\sin\omega''_d t) \tag{4.18}$$

In order to find the unknown coefficients in (4.17) and (4.18), one should have at least four initial conditions. Two of them are $I_2(0) = I_0$, and $I_3(0) = 0$ A, which indicate that

100% of the total energy is initially stored in L_2. The other two initial conditions can be found from (4.11) when $t = 0$,

$$\frac{dI_2}{dt}(0) = \frac{-\omega}{Q}\frac{I_0}{1-k_{23}^2}, \qquad \frac{dI_3}{dt}(0) = \frac{-\omega}{Q}\frac{k_{23}I_0}{1-k_{23}^2}. \tag{4.19}$$

4.3. Coupled-mode vs. Reflected-load Theories

In this section, the formulation derived from CMT and RLT are compared for the 2-coil inductive link PTE as well as the transient response.

4.3.1. Two-coil Inductive Link Power Transfer Efficiency

Resonance widths, $\Gamma_{2,3}$, and coupling rate, K_{23}, in a pair of capacitively loaded inductors in Fig. 4.1 are equivalent in terms of circuit model parameters in Fig. 4.2 to $\omega/2Q_{2\text{-}3}$ and $\omega k_{23}/2$, respectively [44]. Similarly, the load resonance width, Γ_L, is equal to $\omega/2Q_L$. By substituting these in *fom* and Γ_L / Γ_3,

$$fom = \frac{K_{23}}{\sqrt{\Gamma_2\Gamma_3}} = \frac{\omega k_{23}}{2}\left(\frac{\omega}{2Q_2}\frac{\omega}{2Q_3}\right)^{-1/2} = k_{23}\sqrt{Q_2Q_3}, \qquad \frac{\Gamma_L}{\Gamma_3} = \frac{\omega}{2Q_L}/\frac{\omega}{2Q_3} = \frac{Q_3}{Q_L} \tag{4.20}$$

In the next step, we substitute the CMT parameters from (4.20) in (4.2) and recalculate the PTE,

$$\eta_{23} = \frac{1}{1+\frac{Q_L}{Q_3}\left[1+\frac{1}{k_{23}^2Q_2Q_3}(1+\frac{Q_3}{Q_L})^2\right]} = \frac{Q_3}{Q_3+Q_L+\frac{(Q_L+Q_3)^2}{k_{23}^2Q_2Q_3Q_L}} = \frac{k_{23}^2Q_2Q_3}{Q_L+Q_3+k_{23}^2Q_2Q_3Q_L}\cdot\frac{Q_LQ_3}{Q_L+Q_3} \tag{4.21}$$

After simplification and considering that $Q_{3L} = Q_LQ_3/(Q_L+Q_3)$, the PTE formula in (4.21) can be further simplified to,

$$\eta_{23} = \frac{k_{23}^2Q_2Q_3Q_L/(Q_L+Q_3)}{1+k_{23}^2Q_2Q_3Q_L/(Q_L+Q_3)}\cdot\frac{Q_{3L}}{Q_L} = \frac{k_{23}^2Q_2Q_{3L}}{1+k_{23}^2Q_2Q_{3L}}\cdot\frac{Q_{3L}}{Q_L}, \tag{4.22}$$

which is the same as (4.9) that was derived via RLT.

Similarly, it is straightforward to show that the optimum $\Gamma_{L,PTE}$ in (4.3) can be

linked to $Q_{L,PTE}$ in (4.10) by substituting the equivalent circuit parameters in (4.20), leading to

$$\frac{\Gamma_{L,PTE}}{\Gamma_3} = \frac{Q_3}{Q_{L,PTE}} = \left(1 + \frac{K_{23}^2}{\Gamma_2 \Gamma_3}\right)^{1/2} = (1 + k_{23}^2 Q_2 Q_3)^{1/2}. \tag{4.23}$$

Thus, we have shown mathematically that the CMT and RLT equations for the PTE and optimal loading of 2-coil power transmission links in steady state are basically the same.

4.3.2. Two-coil Inductive Link Transient Response

In order to arrive at the CMT transient response in (4.7), two assumptions were made. First, the coil quality factors were considered large (Q >>1), resulting in $\omega_d' \approx \omega'$ and $\omega_d'' \approx \omega''$ in (4.16). Second, the coupling distance, d_{23}, was considered large, resulting in small k_{23}, which simplifies the rest of (4.16) to

$$\omega'/Q' \approx \omega''/Q'' \approx \omega/Q, \quad \omega' \approx \omega(1 + k_{23}/2), \quad \omega'' \approx \omega(1 - k_{23}/2), \tag{4.24}$$

and (4.19) to

$$\frac{dI_2}{dt}(0) = \frac{-\omega}{Q} I_0, \qquad \frac{dI_3}{dt}(0) = 0. \tag{4.25}$$

Thus, $I_2(t)$ and $I_3(t)$ in (4.17) and (4.18) can be approximated as,

$$I_2(t) = e^{\frac{-\omega}{2Q}t}[a_{11}\cos\omega(1+k_{23}/2)t + b_{11}\sin\omega(1+k_{23}/2)t + a_{12}\cos\omega(1-k_{23}/2)t + b_{12}\sin\omega(1-k_{23}/2)t] \tag{4.26}$$

$$I_3(t) = e^{\frac{-\omega}{2Q}t}[a_{21}\cos\omega(1+k_{23}/2)t + b_{21}\sin\omega(1+k_{23}/2)t + a_{22}\cos\omega(1-k_{23}/2)t + b_{22}\sin\omega(1-k_{23}/2)t] \tag{4.27}$$

Unknown coefficients in (4.26) and (4.27) can be found by applying the initial conditions, which result in $a_{11} = a_{12} = I_0/2$, $b_{11} = b_{12} = -I_0/4Q$, $a_{21} = -a_{22} = -I_0/2$, and $b_{21} = b_{22} = 0$. When substituting these in (4.26) and (4.27),

$$I_2(t) = \frac{I_0}{2} e^{\frac{-\omega}{2Q}t}[\cos\omega(1+k_{23}/2)t + \cos\omega(1-k_{23}/2)t - \frac{1}{2Q}\sin\omega(1+k_{23}/2)t - \frac{1}{2Q}\sin\omega(1-k_{23}/2)t]$$

(4.28)

$$I_3(t) = \frac{I_0}{2} e^{\frac{-\omega}{2Q}t} [-\cos \omega(1+k_{23}/2)t + \cos \omega(1-k_{23}/2)t]. \quad (4.29)$$

The large Q assumption combined with the expansion of the sinusoidal functions in (4.28) and (4.29),

$$\cos(\alpha \pm \beta) = \cos\alpha\cos\beta \mp \sin\alpha\sin\beta, \quad \sin(\alpha \pm \beta) = \sin\alpha\cos\beta \pm \cos\alpha\sin\beta, \quad (4.30)$$

can further simplify the primary and secondary currents as

$$I_2(t) = I_0 e^{\frac{-\omega}{2Q}t} \cos\frac{\omega k_{23} t}{2} \cos\omega t, \quad I_3(t) = I_0 e^{\frac{-\omega}{2Q}t} \sin\frac{\omega k_{23} t}{2} \sin\omega t. \quad (4.31)$$

Considering that the energy stored in an inductor, L, that carries a current, I, is $0.5LI^2$, the normalized envelope of the energy inside L_2 and L_3 can be expressed as,

$$E_2(t) = e^{\frac{-\omega}{Q}t} \cos^2(\frac{\omega k_{23} t}{2}), \; E_3(t) = e^{\frac{-\omega}{Q}t} \sin^2(\frac{\omega k_{23} t}{2}). \quad (4.32)$$

By substituting $2\Gamma = \omega/Q$, and $K_{23} = \omega k_{23}/2$ in (4.32), we can arrive at (4.7), which was derived using CMT. Therefore, in calculating the transient response of the inductive links, CMT is only valid for midrange coupling distances (small k_{23}) between large coils (high-Q), as also indicated in [44].

In order to validate our theoretical calculations and demonstrate the level of accuracy (or lack thereof) in the transient CMT analysis for various coupling coefficients and Q factors, the 2-coil inductive link in Fig. 4.2 was simulated in the LT-SPICE circuit simulator (Linear Technology, Milpitas, CA), while setting V_S and initial L_2 current, $I_2(0)$, at 0 V and 1 A, respectively, for the two conditions summarized in Table 4.1. Fig. 4.3a shows the percentage of the energy stored in primary, L_2, and secondary, L_3, coils over time for a pair of large identical coils that are placed relatively far from each other (midrange, low k_{23}, high-Q). It can be seen that both CMT (4.7) and circuit-based (4.12) equations, solved in MATLAB (MathWorks, Natick, MA), match the LT-SPICE simulation results very well. In Fig. 4.3b, however, which represents a small pair of coils

that are very close to one another (short range, high k_{23}, low-Q) the CMT-based formulas have become quite inaccurate in predicting the energy exchange, while the circuit analysis still matches the LT-SPICE simulation output. In this condition, the inductor currents tend to have two harmonics, ω' and ω'' in (4.17) and (4.18), one of which has not been predicted by the CMT. Nonetheless, the simplicity of the CMT in analyzing the transient behavior of inductive links can be useful particularly in midrange high-Q conditions. This stems from the fact that CMT models each resonant object (e.g. RLC tank) with a first-order differential equation, while in the circuit analysis the order of the equations increases by each independent energy storage element regardless of being an inductor or a capacitor.

Table 4.1: Inductive link specifications for transient analysis

L_2 and L_3 Specifications*	**Symbol**	**Midrange High-Q**	**Short Range Moderate-Q**
Inductance (μH)	L	96.2	0.962
Series resistance (Ω)	R	0.76	1.08
Resonant capacitance (pF)	C	0.812	81.2
Quality factor	Q	1.4×10^{4}	100
Mutual coupling	k_{23}	0.153×10^{-3}	0.4
Resonance width (rad)	Γ	4039	5.65×10^{5}
Coupling rate (rad)	K_{23}	8652	22.6×10^{6}
Load resistance (Ω)	R_L	∞ (No load condition)	
Resonance frequency (MHz)	f	18	

*Primary and secondary coils are identical.

4.4. Multi-coil Inductive Power Transfer

CMT-based analysis took circuit designers by surprise when the group physicists at MIT demonstrated a method of achieving high PTE by utilizing multiple coils (3- and 4-coils) for wireless power transmission [96], [97]. Nonetheless, the closed-form CMT formulation presented in the literature was limited to 2-coils. In this section, the closed-form PTE equations are derived for multi-coil inductive links based on the CMT and

compared with parallel equations derived from RLT, particularly for 3- and 4-coil links. It is proved that both CMT and RLT result in the same set of equations.

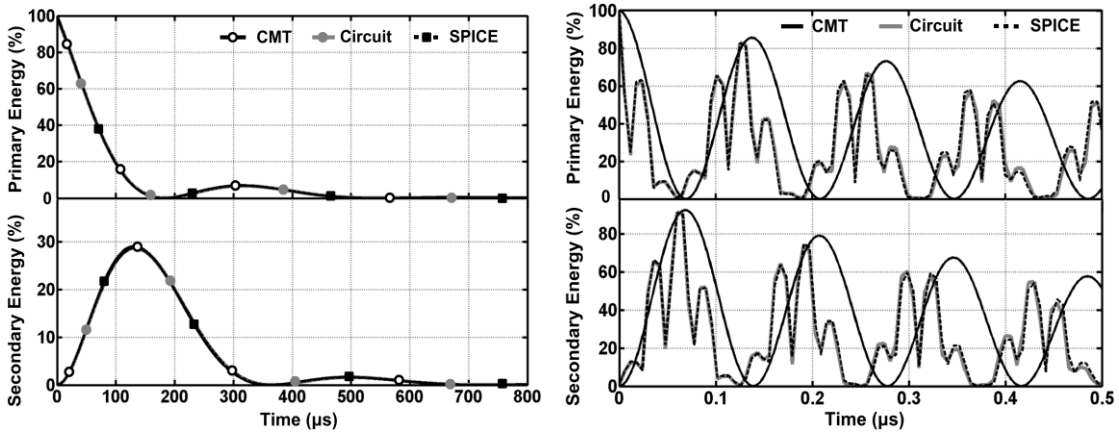

Fig. 4.3. The energy stored in the primary and secondary coils (E_2 and E_3) vs. time starting from an initial condition, $I_2(0)$ = 1 A, based on CMT (4.7), circuit theory (4.12), and SPICE simulations for 2-coil inductive links in: (a) midrange, high-Q, and (b) short range, low-Q conditions, as specified in Table 4.1.

Equations for a pair of capacitively loaded inductors in Fig. 4.1 can be extended to m inductors, in which the 1st and m^{th} inductors are connected to the energy source and load, respectively, while all inductors are tuned at the same resonance frequency, f. The time-domain field amplitudes of each inductor, $a_i(t)$, can be expressed as,

$$\frac{da_i(t)}{dt} = -(j\omega + \Gamma_i)a_i(t) + jK_{i-1,i}a_{i-1}(t) + jK_{i,i+1}a_{i+1}(t), \qquad i = 2, 3, \ldots, m\text{-}1 \tag{4.33}$$

where $K_{i,i+1}$ and Γ_i are the coupling rate between the i^{th} and $(i+1)^{th}$ inductor and resonance width of the i^{th} inductor, respectively. For the sake of simplicity, the coupling between non-neighboring inductors has been considered negligible. For the 1st and m^{th} inductors, the field amplitudes are,

$$\frac{da_1(t)}{dt} = -(j\omega + \Gamma_1)a_1(t) + jK_{12}a_2(t) + F_S(t)$$

$$\frac{da_m(t)}{dt} = -(j\omega + \Gamma_m + \Gamma_L)a_m(t) + jK_{m-1,m}a_{m-1}(t). \tag{4.34}$$

In the steady state mode, the field amplitudes in each inductor is considered constant, i.e. $a_i(t) = A_i e^{-j\omega t}$. Therefore, the differential equations in (4.33) and (4.34) result

in a set of m-1 equations,

$$\Gamma_i A_i - jK_{i-1,i}A_{i-1} - jK_{i,i+1}A_{i+1} = 0, \qquad i = 2, 3, \ldots, m\text{-}1$$

$$(\Gamma_m + \Gamma_L)A_m - jK_{m-1,m}A_{m-1} = 0. \tag{4.35}$$

One can solve (4.35) to find A_i constants based on the load field amplitude, A_m. From these values, the average power at different nodes of the inductive power transmission link can be calculated. The absorbed power by the i^{th} inductor and the delivered power to R_L can be expressed as $P_i = 2\Gamma_i|A_i|^2$ and $P_L = 2\Gamma_L|A_m|^2$, respectively, from which the total delivered power to the system from source can be found from $P_S = \sum_{i=1}^{m} P_i + P_L$, using the law of conservation of energy. Finally, the PTE of the m-coil system can be found from,

$$\eta_{m-coil} = \frac{P_L}{P_S} = \frac{\Gamma_L}{\Gamma_m + \Gamma_L + \sum_{i=1}^{m-1}\Gamma_i\left|\frac{A_i}{A_m}\right|^2}. \tag{4.36}$$

In an m-coil link, the reflected load from the $(i+1)^{th}$ coil onto the i^{th} coil can be found from,

$$R_{ref\,i,i+1} = k_{i,i+1}^2 \omega L_i Q_{(i+1)L}, \quad i = 1, 2, \ldots, m\text{-}1 \tag{4.37}$$

where $k_{i,i+1}$ is the coupling coefficient between the i^{th} and $(i+1)^{th}$ coils. $Q_{(i+1)L}$ is the loaded quality factor of the $(i+1)^{th}$ coil, which can be found from

$$Q_{iL} = \frac{\omega L_i}{R_i + R_{ref\,i,i+1}} = \frac{Q_i}{1 + k_{i,i+1}^2 Q_i Q_{(i+1)L}}, \qquad i = 1, 2, \ldots, m\text{-}1 \tag{4.38}$$

where $Q_i = \omega L_i/R_i$ and R_i are the unloaded quality factor and parasitic series resistance of the i^{th} coil (L_i), respectively. It should be noted that for the last coil, which is connected to the load in series, $Q_{mL} = \omega L_m/(R_m+R_L)$. Assuming that the coupling between non-neighboring coils is negligible, the partial PTE from the i^{th} coil to $(i+1)^{th}$ coil can be written as,

$$\eta_{i,i+1} = \frac{R_{ref\,i,i+1}}{R_i + R_{ref\,i,i+1}} = \frac{k_{i,i+1}^2 Q_i Q_{(i+1)L}}{1 + k_{i,i+1}^2 Q_i Q_{(i+1)L}}. \tag{4.39}$$

Using (4.37)-(4.39), the overall PTE in such a multi-coil inductive link can be found from,

$$\eta_{m-coil} = \prod_{i=1}^{m-1} \eta_{i,i+1} \cdot \frac{Q_{mL}}{Q_L} . \tag{4.40}$$

4.4.1. Three-coil Inductive Links

The 3-coil inductive power transfer link, shown in Fig. 4.4a, was initially proposed in [97] and analyzed based on the CMT. If K_{24} is ignored due to large separation between L_2 and L_4, the field amplitudes at each inductor can be calculated by solving a set of two equations in (4.35), which leads to

$$\frac{A_2}{A_4} = \frac{K_{34}^2 + \Gamma_3(\Gamma_4 + \Gamma_L)}{K_{23}K_{34}}, \qquad \frac{A_3}{A_4} = \frac{(\Gamma_4 + \Gamma_L)}{jK_{34}} . \tag{4.41}$$

PTE of the 3-coil link can then be found by substituting (4.41) in (4.36), which leads to (4.42) after some minor simplifications.

$$\eta_{3-coil} = \frac{K_{23}^2 K_{34}^2 \Gamma_L}{\Gamma_2[K_{34}^2 + \Gamma_3(\Gamma_4 + \Gamma_L)]^2 + K_{23}^2[\Gamma_3(\Gamma_4 + \Gamma_L)^2] + K_{23}^2 K_{34}^2(\Gamma_4 + \Gamma_L)} \tag{4.42}$$

The lumped circuit model for 3-coil inductive link has been shown in Fig. 4.4b. In this type of inductive links, k_{34} can be adjusted by changing the distance or geometry of L_4 to match the actual R_L with the optimal $R_{L,PTE}$ in (4.10) for the L_2-L_3 inductive link. It should be noted that R_2, which is the series resistance of L_2, can also include the source output resistance. The PTE of this circuit can be calculated by reflecting the resistive components of each loop from the load back towards the primary coil loop, one stage at a time, using (4.37) and calculating the percentage of the power that is delivered from one stage to the next, using (4.39), until it reaches R_L. According to (4.40), this procedure leads to,

$$\eta_{3-coil} = \frac{(k_{23}^2 Q_2 Q_3)(k_{34}^2 Q_3 Q_{4L})}{[(1 + k_{23}^2 Q_2 Q_3 + k_{34}^2 Q_3 Q_{4L})(1 + k_{34}^2 Q_3 Q_{4L})]} \cdot \frac{Q_{4L}}{Q_L} = \eta_{23}\eta_{34} \tag{4.43}$$

where k_{24} has been ignored due to large separation between L_2 and L_4, and

$$\eta_{23}=\frac{k_{23}^2Q_2Q_{3L}}{1+k_{23}^2Q_2Q_{3L}}=\frac{k_{23}^2Q_2Q_3}{1+k_{23}^2Q_2Q_3+k_{34}^2Q_3Q_{4L}},\ \eta_{34}=\frac{k_{34}^2Q_3Q_{4L}}{1+k_{34}^2Q_3Q_{4L}}.\frac{Q_{4L}}{Q_L}. \tag{4.44}$$

The resonance widths, $\Gamma_{2\text{-}4}$, and coupling rates, $K_{23,34}$, in CMT based on circuit parameters are defined as $\omega/2Q_{2\text{-}4}$ and $\omega k_{23,34}/2$, respectively. By substituting these parameters in (4.42) and multiplying both numerator and denominator with $Q_2Q_3^2Q_{4L}^2$, the 3-coil PTE can be found from

$$\eta_{3-coil}=\frac{k_{23}^2k_{34}^2Q_2Q_3^2Q_{4L}^2/Q_L}{[(k_{34}^2Q_3Q_{4L}+1)^2+k_{23}^2Q_2Q_3+k_{23}^2k_{34}^2Q_2Q_3^2Q_{4L}]}$$
$$=\frac{k_{23}^2k_{34}^2Q_2Q_3^2Q_{4L}}{[(1+k_{34}^2Q_3Q_{4L})^2+k_{23}^2Q_2Q_3(1+k_{34}^2Q_3Q_{4L})]}.\frac{Q_{4L}}{Q_L} \tag{4.45}$$

where $1/Q_{4L} = 1/Q_4 + 1/Q_L$. It can be seen that (4.45), which is derived from the CMT is the same as (4.43), which is based on the RLT. Therefore, these two formulations are no different in the steady state analysis.

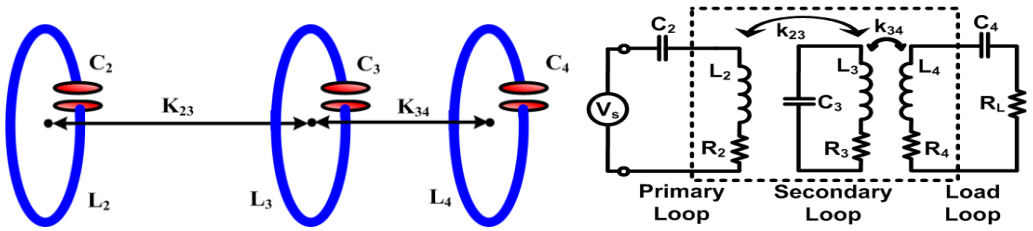

Fig. 4.4. (a) Three capacitively loaded, mutually coupled, inductors for wireless power transmission. (b) Lumped circuit model of the 3-coil inductive link.

4.4.2. Four-coil Inductive Links

Fig. 4.5a shows an inductive power transfer link consisting of four capacitively loaded inductors, in which L_2 and L_3 are the main coils responsible for power transmission, similar to the 2-coil link, while L_1 and L_4 are added for impedance matching. The field amplitudes at each inductor can be found by solving a set of three equations in (4.35). A_2 and A_3 can be found based on A_4 from (4.41) and A_1 can be found from,

$$A_1 / A_4 = -\frac{\Gamma_2\Gamma_3(\Gamma_4+\Gamma_L)+K_{34}^2\Gamma_2+K_{23}^2(\Gamma_4+\Gamma_L)}{jK_{12}K_{23}K_{34}}. \tag{4.46}$$

To simplify the analysis, K_{13}, K_{14} and K_{24} have been neglected in comparison to coupling rates between neighboring coils. One can find the 4-coil PTE utilizing CMT by substituting (4.41) and (4.46) in (4.36), which after simplification leads to

$$\eta_{4-coil} = \frac{K_{12}^2K_{23}^2K_{34}^2\Gamma_L}{D}, \tag{4.47}$$

where

$$\begin{aligned} D &= \Gamma_1[\Gamma_2\Gamma_3(\Gamma_4+\Gamma_L)+K_{34}^2\Gamma_2+K_{23}^2(\Gamma_4+\Gamma_L)]^2 \\ &+K_{12}^2\Gamma_2[K_{34}^2+\Gamma_3(\Gamma_4+\Gamma_L)]^2+K_{12}^2K_{23}^2\Gamma_3(\Gamma_4+\Gamma_L)^2+K_{12}^2K_{23}^2K_{34}^2(\Gamma_4+\Gamma_L) \end{aligned} \tag{4.48}$$

In the 4-coil lumped circuit schematic, shown in Fig. 4.5b, the PTE can be calculated from (4.40) if we ignore k_{13}, k_{14}, and k_{24} in comparison to k_{12}, k_{23} and k_{34},

$$\eta_{4-coil} = \frac{(k_{12}^2Q_1Q_2)(k_{23}^2Q_2Q_3)(k_{34}^2Q_3Q_{4L})}{[(1+k_{12}^2Q_1Q_2).(1+k_{34}^2Q_3Q_{4L})+k_{23}^2Q_2Q_3].[1+k_{23}^2Q_2Q_3+k_{34}^2Q_3Q_{4L}]}.\frac{Q_{4L}}{Q_L}. \tag{4.49}$$

It can be proved that CMT and RLT equations in (4.47) and (4.49) are basically the same by substituting the resonance widths, Γ_{1-4}, and coupling rates, K_{12}, K_{23}, and K_{34} in (4.47) and (4.48) with their equivalent circuit parameters, $\omega/2Q_{1-4}$, $\omega k_{12}/2$, $\omega k_{23}/2$, and $\omega k_{34}/2$, respectively. Once both numerator and denominator of (4.47) are multiplied by $Q_1Q_2^2Q_3^2Q_{4L}^2$, the CMT-based 4-coil PTE leads to,

$$\eta_{4-coil} = \frac{k_{12}^2k_{23}^2k_{34}^2Q_1Q_2^2Q_3^2Q_{4L}^2/Q_L}{A^2+k_{12}^2Q_1Q_2B^2+k_{12}^2Q_1Q_2k_{23}^2Q_2Q_3+k_{12}^2Q_1Q_2k_{23}^2Q_2Q_3k_{34}^2Q_3Q_{4L}} \tag{4.50}$$

where A and B are

$$A = B+k_{23}^2Q_2Q_3,\ B = 1+k_{34}^2Q_3Q_{4L}. \tag{4.51}$$

The third and fourth terms of the denominator in (4.50) can be written in terms of B as,

$$\eta_{4-coil} = \frac{k_{12}^2k_{23}^2k_{34}^2Q_1Q_2^2Q_3^2Q_{4L}^2/Q_L}{A^2+k_{12}^2Q_1Q_2B^2+k_{12}^2Q_1Q_2k_{23}^2Q_2Q_3B} = \frac{k_{12}^2k_{23}^2k_{34}^2Q_1Q_2^2Q_3^2Q_{4L}^2/Q_L}{A^2+k_{12}^2Q_1Q_2B(B+k_{23}^2Q_2Q_3)}. \tag{4.52}$$

By further manipulation of the numerator and denominator,

$$\eta_{4-coil} = \frac{k_{12}^2 k_{23}^2 k_{34}^2 Q_1 Q_2^2 Q_3^2 Q_{4L}^2 / Q_L}{A^2 + k_{12}^2 Q_1 Q_2 B(A)} = \frac{k_{12}^2 Q_1 Q_2 k_{23}^2 Q_2 Q_3 k_{34}^2 Q_3 Q_{4L}}{A(A + k_{12}^2 Q_1 Q_2 B)} \cdot \frac{Q_{4L}}{Q_L} =$$

$$= \frac{(k_{12}^2 Q_1 Q_2)(k_{23}^2 Q_2 Q_3)(k_{34}^2 Q_3 Q_{4L})}{A[B(1 + k_{12}^2 Q_1 Q_2) + k_{23}^2 Q_2 Q_3]} \cdot \frac{Q_{4L}}{Q_L}, \tag{4.53}$$

Once A and B are substituted from (4.51) in (4.53), it will be identical to (4.49), which was derived from the RLT.

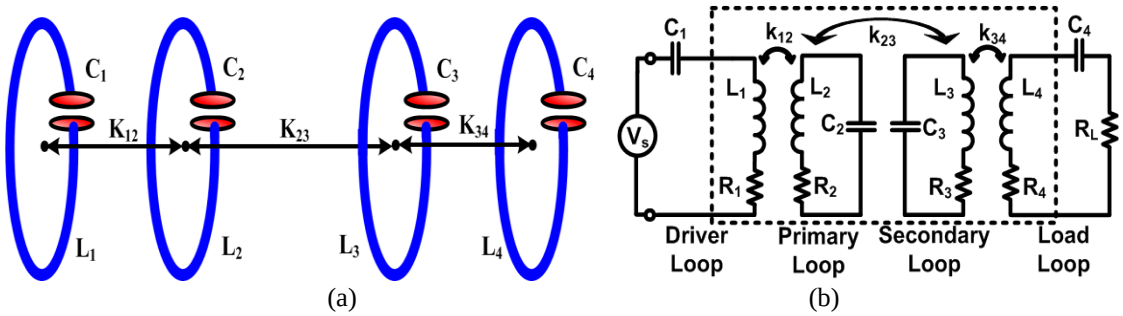

Fig. 4.5. (a) Four capacitively loaded, mutually coupled, inductors for wireless power transmission, in which L_1-K_{12} and L_4-K_{34} serve as impedance matching elements to improve the PTE. (b) Lumped circuit model of the 4-coil inductive link.

CHAPTER V

A FIGURE-OF-MERIT FOR DESIGNING HIGH-PERFORMANCE INDUCTIVE POWER-TRANSMISSION LINKS

A key design requirement in wireless power transfer is to provide sufficient power delivered to the load (PDL) while maintaining high power transfer efficiency (PTE). High PTE is required to reduce 1) heat dissipation within the coils, 2) exposure to electromagnetic field, which can cause additional heat dissipation in the power transmission medium, 3) size of the main energy source (e.g. battery), and 4) interference with nearby electronics that is necessary to satisfy regulatory requirements [35], [82], [83]. At the same time, the link should deliver sufficient power to the load while considering practical limitations of the energy source and the PA. When load (R_L) is constant, the PDL would be equivalent to the inductive link voltage gain all the way from the source to the load. Increasing the source voltage, V_s in Fig. 5.1a, to increase the PDL can reduce the driver efficiency, require larger transistors in the PA, and make it more difficult and costly to meet the safety requirements.

Several methods have been proposed for designing wireless power transmission links. In [36]-[38], geometries of the primary and secondary coils, L_2 and L_3 in Fig. 5.1a, have been optimized to achieve the maximum voltage on the load, and consequently a high PDL. PDL is a key design merit when the space is limited and coils need to be miniaturized, such as in the IMD applications. Similarly, design and geometrical optimization of the 2-coil inductive links based on the PTE have been widely studied [34], [39]-[42], [90]. The approach proposed in [32] is somewhat different by first designing L_3 to maximize the PTE for a given R_L, and then optimizing L_2 to achieve the desired voltage gain from source to the load, and consequently improve the PDL. However, the literature still lacks a clear figure-of-merit (FoM) that can incorporate both the PTE and the PDL, and guide designers to give proper weight to each of these

important but contrasting parameters. A well-defined FoM can provide designers with much needed insight on how to optimize their inductive power transmission links based on the application requirements.

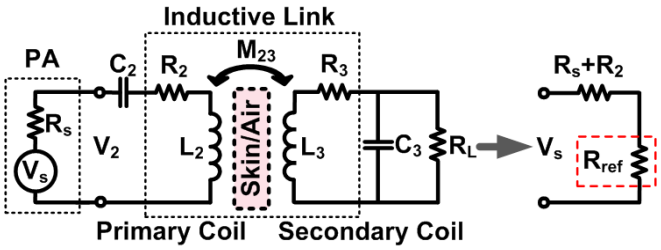

Fig. 5.1. (a) Lumped circuit model for a generic 2-coil inductive power transmission link with the power amplifier (PA) loss modeled as R_s. (b) Equivalent circuit at resonance showing the reflected load from the secondary loop onto the primary loop.

In this chapter, a new FoM, which serves two purposes, is proposed. First, it guides designers towards inductive power transmission links with the highest possible PTE and PDL. Second, it helps the designer to choose between the 2-, 3- and 4-coil link options for a given application.

5.1. A New FoM for Inductive Power Transmission

In Fig. 1a, key parameters that affect the design of this link from the energy source to the load, aside from the coils are: V_s, power required by the load (P_L), power amplifier (PA) supply voltage (V_{DD}), R_s (representing the PA loss), PA transistor breakdown voltage, and safety limits for the application [90]. In a class-E PA, zero-voltage-switching allows for high power efficiency with peak voltages across the primary coil and the PA transistor that are 1.07 and 3.56 times V_{DD}, respectively [98]. Therefore, when the application requires a large P_L, R_s should be reduced to make sufficient power available from the source, $P_{av} = V_s^2/8R_s$, at a reasonable V_s and V_{DD} [47], [90]. Unfortunately, to achieve a high PTE, the delivered power to L_2 would be much smaller than P_{av} because the impedance matching on the Tx side reduces the PA efficiency to 50%. Utilizing large transistors to reduce R_s results in increased dynamic switching losses

in the PA [32]. Therefore, the power transmission link should be designed in a way that it achieves high PTE and also provides sufficient PDL, while considering practical limitations of the PA circuit design.

It can be shown that the highest PTE and PDL for the inductive link, shown in Fig. 5.1a, can be achieved when both LC tanks are tuned at the same resonance frequency, $f_0 = 1/2\pi\sqrt{L_2C_2} = 1/2\pi\sqrt{L_3C_3}$. At resonance, the effect of the Rx on the Tx can be modeled by the reflected impedance,

$$R_{ref} = k_{23}^2 \omega_0 L_2 Q_{3L}, \tag{5.1}$$

where $k_{23}=M_{23}/\sqrt{L_2L_3}$, M_{23} is the mutual inductance between L_2 and L_3, and $Q_{3L} = Q_3Q_L / (Q_3+Q_L)$, $Q_3 = \omega_0 L_3/R_3$, and $Q_L = R_L/\omega_0 L_3$ for parallel load connection, which is often referred to as the load quality factor. At resonance, the primary loop can be simplified to the circuit shown in Fig. 5.1b.

To calculate the PTE at resonance, we should consider that the power provided by the PA (V_s) divides between $R_s + R_2$ and R_{ref}, and that portion of the power delivered to R_{ref}, i.e. the power that is received by the secondary loop, divides between R_3 and R_L, which are the only power consuming components. These assumptions lead to,

$$\eta_{2-coil} = \frac{R_{ref}}{R_s + R_2 + R_{ref}} \cdot \frac{Q_{3L}}{Q_L} = \frac{k_{23}^2 Q_2 Q_{3L}}{1 + k_{23}^2 Q_2 Q_{3L}} \cdot \frac{Q_{3L}}{Q_L}, \tag{5.2}$$

where $Q_2 = \omega_0 L_2 / (R_s + R_2)$ [32]. The first and second terms in (5.2) correspond to the power division between $R_s + R_2$ and R_{ref}, and R_3 and R_L, respectively. Therefore, according to (5.2), in order to achieve the highest PTE, R_{ref} should be maximized.

PDL can be calculated by multiplying the power provided by V_s, i.e. $V_s^2/2(R_s+R_2+R_{ref})$, with the PTE from (5.2),

$$P_{L,2-coil} = \frac{V_s^{\,2} R_{ref}}{2\left(R_s + R_2 + R_{ref}\right)^2} \cdot \frac{Q_{3L}}{Q_L} = \frac{V_s^{\,2}}{2(R_s + R_2)} \frac{k_{23}^2 Q_2 Q_{3L}}{(1 + k_{23}^2 Q_2 Q_{3L})^2} \cdot \frac{Q_{3L}}{Q_L}. \tag{5.3}$$

It can be seen in (5.3) that PDL does not necessarily increase by maximizing R_{ref}. Taking

the derivative of (5.3) with respect to R_{ref}, indicates that the maximum PDL at a certain coupling distance, d_{23}, is achieved when $R_{ref} = R_s + R_2$. Under this impedance-matched condition, PTE ≤ 50%, because at least half of the power is dissipated in $R_s + R_2$.

To better understand and manage the necessary compromise between the PTE and PDL when designing an inductive power transfer link, we propose a new FoM,

$$FoM = \frac{\eta^n \times P_L}{V_s^2} = \frac{\eta^{n+1}}{2(R_s + R_2 + R_{ref})} \tag{5.4}$$

where n depends on the importance of the PTE vs. PDL in a particular application. Interestingly, the FoM unit is in Siemens, which implies how conductive the wireless link is to electric power transfer. The FoM for a 2-coil link can be derived from other circuit parameters in Fig. 5.1 by substituting (5.2) and (5.3) in (5.4),

$$FoM_{2-coil} = \frac{(k_{23}^2 Q_2 Q_{3L})^{n+1}}{2(R_s + R_2)(1 + k_{23}^2 Q_2 Q_{3L})^{n+2}} \cdot \left(\frac{Q_{3L}}{Q_L}\right)^{n+1}. \tag{5.5}$$

According to (5.2), the PTE profile of a 2-coil link is a monotonically decreasing function of the coils' coupling distance, d_{23}. The PDL and FoM profiles, on the other hand, can be maximized at a particular d_{23} by calculating the derivatives of (5.3) and (5.5) with respect to k_{23}, respectively,

$$k_{23,PDL} = \frac{1}{(Q_2 Q_{3L})^{1/2}},\ k_{23,FoM} = \left(\frac{n+1}{Q_2 Q_{3L}}\right)^{1/2}. \tag{5.6}$$

By substituting $k_{23,FoM}$ in (5.2) and (5.3), one can find the PTE and PDL of the 2-coil link when the FoM is maximized at a particular d_{23},

$$\eta_{2-coil,FoM} = \frac{n+1}{n+2} \cdot \frac{Q_{3L}}{Q_L}, \quad P_{L,2-coil,FoM} = \frac{V_s^{\,2}}{2(R_s + R_2)} \cdot \frac{n+1}{(n+2)^2} \cdot \frac{Q_{3L}}{Q_L}. \tag{5.7}$$

These equations do not consider any additional constraints on the coils' geometries, which may result in further reductions in the PTE and/or PDL in order to meet those requirements. The proposed FoM in (5.4) reduces to the PTE or PDL if $n \to \infty$ or $n = 0$, respectively. Therefore, the maximum achievable PTE and PDL at a particular d_{23} can be

calculated from (5.7) by substituting n with ∞ and 0, respectively,

$$\eta_{2-coil,\max} = \frac{Q_{3L}}{Q_L},\ P_{L,2-coil,\max} = \frac{V_s^{\,2}}{8(R_s + R_2)}.\frac{Q_{3L}}{Q_L}. \tag{5.8}$$

Using (5.7) and (5.8), we can calculate the percentage of the PTE and PDL that the 2-coil link should forfeit when it is designed based on the optimal FoM,

$$\eta_{Loss,2-coil} = \frac{\eta_{2-coil,\max} - \eta_{2-coil,FoM}}{\eta_{2-coil,\max}} = \frac{1}{n+2},$$

$$P_{L,Loss,2-coil} = \frac{P_{L,2-coil,\max} - P_{L,2-coil,FoM}}{P_{L,2-coil,\max}} = \frac{n^2}{(n+2)^2}. \tag{5.9}$$

Fig. 2 shows the PTE and PDL losses vs. n, based on (5.9). The key points to be learned from these curves are: 1) If the 2-coil link is optimized for the PDL only, i.e. n = 0, it loses 50% of the PTE. 2) If the 2-coil link is optimized for the PTE only, i.e. $n \to \infty$, it loses 100% of the PDL. However in practice, the application and coil fabrication process constraints limit the PTE and allow a small amount of power to be delivered to the load (PDL > 0). 3) When n = 2, the PTE and PDL losses are balanced, equal to 25% each.

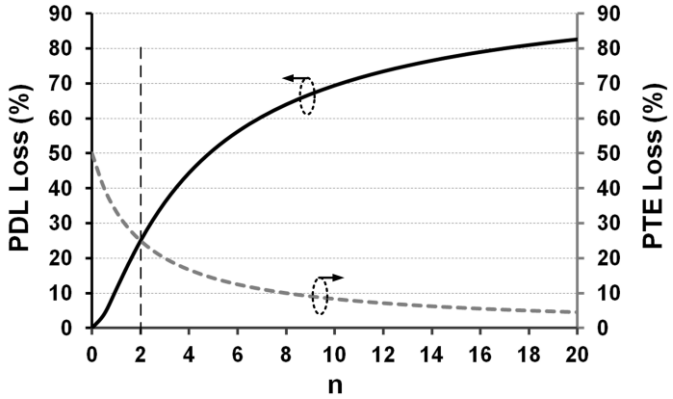

Fig. 5.2. PTE and PDL losses in percentage with respect to their maximum possible values vs. n when the 2-coil link is designed to maximize the proposed FoM in (5.4) as opposed to the PTE or PDL. It can be seen that n = 2 results in similar PTE and PDL losses, equal to 25%. Similar curves can be derived for the 3- and 4-coil links.

In a particular application, it is often possible to determine whether the PTE, PDL, or both are important. Based on this determination and Fig. 5.2, the designer can choose a suitable n for the proposed FoM in (5.4), and proceed with the design of the 2-coil link by

maximizing it. We believe that n = 2 can work well for the majority of applications, in which there is a need to achieve a large PDL with the highest possible PTE, while considering practical driver limitations. Even though in the rest of this paper we consider n = 2, our discussions are applicable to any desired n in the FoM, defined in (5.4).

It should also be noted that for a given set of Q_2, Q_3, and k_{23} values, there is an optimal load, $R_{L,FoM} = \omega_0 L_3 Q_{L,FoM}$, which maximizes the FoM of the 2-coil link at a particular d_{23}. Calculating the derivative of (5.5) with respect to Q_L leads to

$$Q_{L,FoM} = \frac{2(n+1)Q_3}{k_{23}^2 Q_2 Q_3 + \sqrt{(k_{23}^2 Q_2 Q_3)^2 + 4(n+1)^2(1+k_{23}^2 Q_2 Q_3)}}. \tag{5.10}$$

Similarly, the optimal load values for PTE and PDL can be calculated from (5.10) by substituting n with ∞ and 0, respectively [92].

$$Q_{L,PTE} = \frac{Q_3}{(1+k_{23}^2 Q_2 Q_3)^{1/2}}, \quad Q_{L,PDL} = \frac{Q_3}{1+k_{23}^2 Q_2 Q_3} \tag{5.11}$$

5.2. Comparison Between 2-coil Inductive Links Designed Based on FoM, PTE, and PDL

In this section, the performance of three different sets of 2-coil links, designed based on the PTE, PDL and the new FoM for IMD applications is compared. First, a design procedure is explained, based on which the optimal coil geometries are calculated. This design procedure will also be used for designing multi-coil links based on FoM. The effects of d_{23}, R_s and R_L, which are often imposed by the application, are studied on the 2-coil link design with respect to the FoM.

5.2.1. Two-coil Inductive Link Design Procedure

All design examples are based on wire-wound coils (WWC) made of single filament solid wires. The relationship between the inductive link parameters, such as k and Q, and the WWC geometries can be found in the Appendix. The 2-coil optimization flowchart in Fig. 5.3 is similar to the design procedure proposed in [34] with the

following differences: 1) WWC geometries are optimized here instead of printed spiral coils (PSCs). In the WWC models presented in the Appendix, the number of turns, n_i, in WWCs substitutes the fill factor, Φ, in PSCs while other geometrical parameters remain the same. 2) In Fig. 5.3, (5.2), (5.3), or (5.5) can be used to maximize the PTE, PDL, or FoM, respectively. The focus in this chapter will be on optimization based on the FoM, while [34] optimizes the PTE. 3) Another difference between Fig. 5.3 and [34] is that here a weight limit is added for the coils. This will lead to one more 3D surface for the weight of the WWC in each step.

Fig. 5.3 starts with the design constraints imposed by the application and coil fabrication technology. The former defines the maximum values for the outer diameter, D_{o3}, of the implantable coil, L_3, the maximum wire diameters for L_2 and L_3, $w_{2,max}$, $w_{3,max}$, and their weights, $W_{2,max}$, $W_{3,max}$, respectively. For instance, the size and weight of L_3 depend on the IMD location in the body. The weight of a circular-shaped WWC with n_i turns and a wire spacing of s between the surface of the conductors can be found from the Appendix. The minimum value for s is twice the thickness of the wire insulation. The nominal values for d_{23}, R_L and R_s are also required in step-1, all determined by the application or initial estimation. The nominal distance, d_{23}, is considered the average spacing between L_2 and L_3 during normal operation of the inductive link in every particular application.

In step-2, the initial values for L_2 and L_3 geometries, such as w_2, n_2, w_3, and n_3 are chosen. A more detailed discussion about how to choose these initial values can be found in [34]. In step-3.1, key geometrical parameters of L_2, i.e. D_{o2} and n_2 are swept, using (5.5) and the weight equation in the Appendix, leading to two 3D surfaces for the FoM and W_2. The FoM surface is similar to the PTE surface in [34] when D_{o2} and Φ_2 were swept. D_{o2} and n_2 values that result from the maximum FoM are first chosen. If such values lead to $W_2 > W_{2,max}$, i.e. the resulting optimal coil being too heavy, an imaginary horizontal plane should be drawn over the W_2 surface at $W_2 = W_{2,max}$ to find the best D_{o2}

and n_2 pair on the cross section that give the highest FoM.

Parameters associated with L_3 geometry, such as w_3 and n_3, are swept in step-3.2, using D_{o2} and n_2 values from step-3.1. They generate two 3D surfaces for FoM and W_3 using (5) and the weight equation in the Appendix. Similar to step-3.1, the FoM surface is similar to the PTE surface in [34] when w_3 and Φ_3 were swept. The w_3 and n_3 values that result in the highest FoM and $W_3 < W_{3,max}$ are then chosen. In step-3.3, w_2 and n_2 are swept to maximize the FoM in (5.5) and still satisfy the $W_2 < W_{2,max}$ condition.

Steps 3.1 - 3.3 are repeated iteratively until w_2 and n_2 values change < 0.1% from one iteration to the next, satisfying the condition in step-3.4. This step determines the optimal 2-coil link geometries that would achieve the maximum FoM. This can be further validated and fine-tuned using field solvers, such as HFSS (Ansoft, Pittsburgh, PA) or through measurements. It should be noted that in steps 3.2 and 3.3, w_2 and w_3 should be limited to $w_{2,max}$ and $w_{3,max}$, respectively.

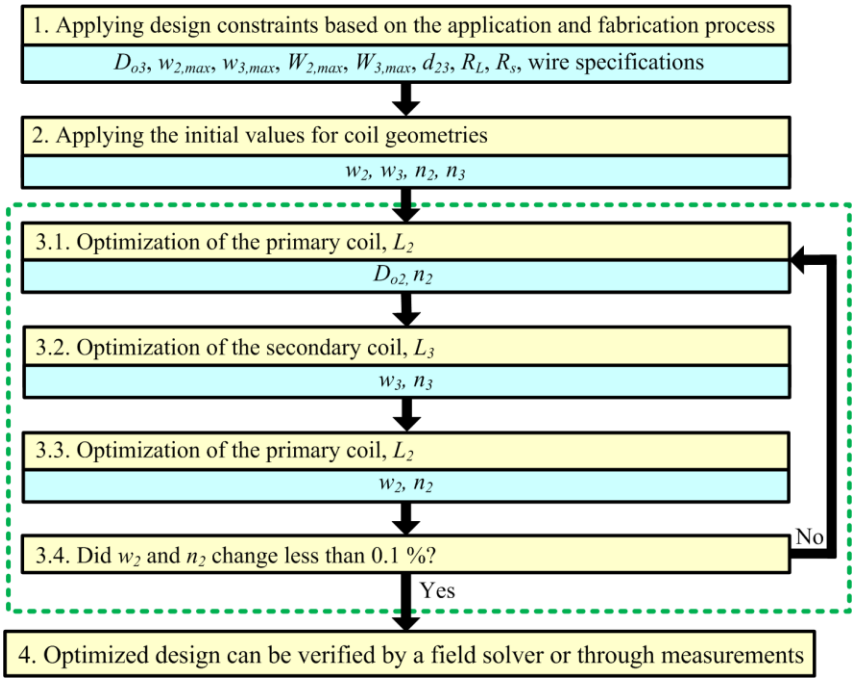

Fig. 5.3. Iterative 2-coil inductive link optimization flowchart.

For the IMD design example, a retinal implant is considered with the following assumptions: L_2 and L_3 were considered circular-shaped WWCs, operating at 13.56 MHz.

The link was designed to deliver 250 mW to an R_L = 100 Ω from a nominal coupling distance of d_{23} = 10 mm via a driver (PA) with output resistance of R_s = 0.5 Ω. Moreover, D_{o3} = 10 mm, $w_{3,max}$ = 0.51 mm (AWG24) to reduce the implant thickness, $W_{2,max}$ = 10 g, and $W_{3,max}$ = 0.5 g to limit the weights of L_2 and L_3 with respect to the electronics.

5.2.2. PTE vs. PDL Tradeoffs

Table 5.1 summarizes the results of the design procedure in Fig. 5.3 for three sets of 2-coil inductive links optimized based on the PTE, PDL, and FoM. It can be seen that the link optimized based on the FoM has not only achieved 1.47 times more PTE than the one optimized for PDL (71.3% vs. 48.5%) but also provided 16 times larger PDL compared to the one optimized for PTE (180.4 mW vs. 11.3 mW for V_s = 1 V). To deliver 250 mW to the load with a class-E PA, driving voltages of V_s = 1.18 V, 4.7 V, and 1.03 V are needed for FoM-, PTE-, and PDL-optimized links, creating peak voltages of 4.2 V, 16.7 V, and 3.7 V across the PA transistor, respectively [98].

These results clearly show the disadvantages of the links with low FoM. For instance, the PA for the PTE-optimized link cannot be implemented on-chip in most standard CMOS fabrication processes due to their lower transistor breakdown voltages. On the other hand, the PDL-optimized link, which relaxes the driver design, suffers from low PTE. It should be noted that the FoM-optimized link achieves its high ratings at the cost of only 24% drop in the PTE and PDL compared to the PTE- and PDL-optimized links. This was slightly less than the estimated 25% theoretical level in Fig. 5.2 due to WWC fabrication constrains. Hence, unless an application requires very small amount of power, an inductive link that is designed based on the proposed FoM would be preferable by simultaneously providing high PTE and high PDL.

Table 5.1. Two-coil inductive link specifications resulted from the PTE, PDL, and FoM-based optimizations.

Parameters		Symbols	Optimized Parameter		
			PTE	PDL	FoM
L_2	Inductance (μH)	L_2	2.37	0.095	0.135
	Outer diameter (mm)	D_{o2}	36	13	23.2
	Wire diameter (mm)	w_2	1.15	1.2	1.75
	Num. of turns	n_2	10	3	2
	Wire spacing (μm)	s_2	100		
	Quality factor*	Q_2	177.5	15.9	22.5
L_3	Inductance (μH)	L_3	0.024		
	Outer diameter (mm)	D_{o3}	10		
	Wire diameter (mm)	w_2	0.51		
	Num. of turns	n_3	1		
	Wire spacing (μm)	s_3	100		
	Quality factor	Q_3	1248		
L_2 - L_3 coupling distance (mm)		d_{23}	10		
Max. wire diam. of L_2 / L_3 (mm)		$w_{2/3,max}$	- / 0.51 (AWG24)		
Max weight of L_2 / L_3 (g)		$W_{2/3,max}$	10 / 0.5		
Nominal source resistance (Ω)		R_S	0.5		
Nominal load (Ω)		R_L	100		
Power carrier frequency (MHz)		f_0	13.56		
Power transfer efficiency (%)		η	93.4	48.5	71.3
Power delivered to load** (mW)		P_L	11.3	236.7	180.4
Figure-of-Merit ($m\Omega^{-1}$)		FoM	9.8	55.6	91.8

*Q_2 also includes R_s = 0.5 Ω.
**Delivered power when V_s = 1 V.
Grayed rows indicate the design constraints.

5.2.3. Coupling Distance Variations

In applications such as IMDs, d_{23} varies in a wide range and the inductive link should provide high PTE and PDL for the entire range. Severe misalignments also have a similar effect as increasing d_{23} by reducing k_{23}. Figs. 5.4a and 5.4b show the PTE, PDL and FoM of the links specified in Table 5.1 vs. d_{23}, respectively. Two important points to be made in these curves are: 1) The PTE and PDL of the PDL-optimized link are significantly reduced at large coupling distances, d_{23} > 13 mm, while the FoM-optimized link provides both large PTE and PDL, and consequently high FoM, over an extended range. 2) Within smaller coupling distances, d_{23} < 10 mm, the FoM-optimized link has achieved high PTE and PDL, while the PTE-optimized link suffers from very small PDL. Comparing the FoM of the three sets of links in Fig. 5.4b shows that the link that is

optimized based on the proposed FoM maintains the highest performance for a widest range of coupling variations.

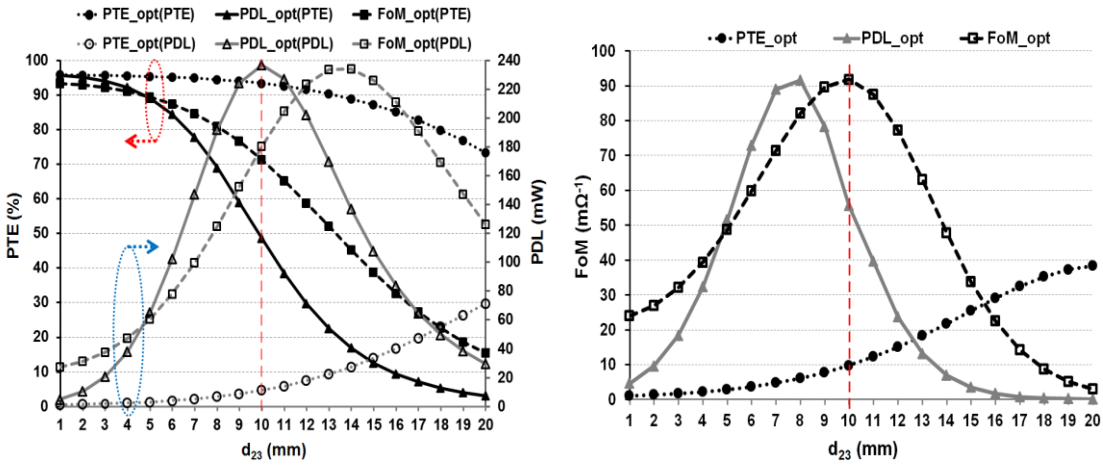

(a) (b)

Fig. 5.4. Comparison between three sets of 2-coil links optimized for the PTE, PDL, and FoM vs. coupling distance, d_{23}. R_s = 0.5 Ω and R_L = 100 Ω. a) The calculated values of the PTE and PDL for V_s = 1 V b) The FoM values defined in (5.4) with n = 2. The inductive links' specifications for the nominal distance of d_{23} = 10 mm are summarized in Table 5.1.

5.2.4. Source Resistance Effects

The driver output resistance, R_s, plays an important role in the optimization of the inductive link from the energy source to the load because R_s significantly affects the available power that the PA can deliver through the inductive link. To study the effects of R_s on the 2-coil inductive link design, we have optimized our IMD design example for R_s values from 0.1 Ω to 5 Ω. Fig. 5.5a shows that the FoM-optimized link has achieved high PTE and PDL especially when R_s is small (i.e. when large PDL is needed). For instance, at R_s = 0.1 Ω, the FoM-optimized link has achieved 53 times larger PDL than the PTE-optimized link and only 24.5% less PDL than the PDL-optimized link. On the other hand, the 71.6% PTE of the FoM-optimized link is almost half between the other two designs. As a result, the FoM-optimized link imposes ~7.3 times smaller voltage on the PA transistor compared to the PTE-optimized link for the same amount of PDL. Moreover, Fig. 5.5b shows how the FoM values are higher for the FoM-optimized link vs. R_s. For

large R_s, which translate to low PDL, the PTE is considered more important, and both PDL and FoM are small for all three links. Therefore, the link designed based on PTE is optimal.

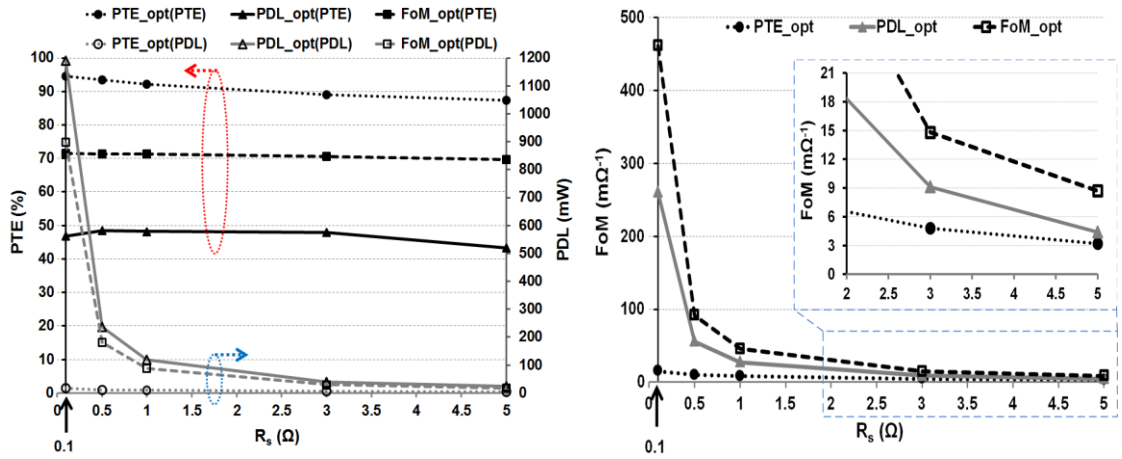

Fig. 5.5. Comparison between three sets of 2-coil links optimized for PTE, PDL, and FoM vs. the driver output resistance, R_s. R_L = 100 Ω. a) The calculated values of the PTE and PDL for V_s = 1 V b) The FoM values defined in (5.4) for n = 2. The inductive links' specifications for R_s = 0.5 Ω are summarized in Table 5.1.

5.2.5. Series vs. Parallel Connection of the Load Resistance

Inductive power transmission covers applications with a wide range of power requirements. A common question for designers is whether the secondary loop should be connected in parallel, similar to Fig. 5.1, or in series (as in Fig. 5.7). In [46], the loaded quality factor of the secondary loop, Q_{3L}, which only depends on the L_3 geometry and R_L, has been used to differentiate between parallel and series load connections. In [99], however, it is shown that the series or parallel load connection also depends on k_{23} and whether the link should be optimized for the PTE or PDL. Overall, the indication between whether the secondary loop should be connected in series or in parallel is not very clear.

The proposed FoM can clearly determine the superior secondary loop topology, while considering both PTE and PDL, which are already linked to k_{23} and coils geometries. The IMD design example has been optimized based on the FoM for different

R_L and R_s values for parallel and series secondary configurations, and depicted the results in Figs. 5.6a and 5.6b, respectively. All equations in this chapter are applicable for the series topology, except for Q_L, which should be defined as $\omega_0 L_3/R_L$. It can be seen that for $R_L < 10\ \Omega$ the series connection results in higher FoM, almost regardless of R_s, while for larger R_L the parallel connection is superior. Therefore, for the IMDs, in which R_L is often larger than 10 Ω, the parallel secondary configuration is preferred.

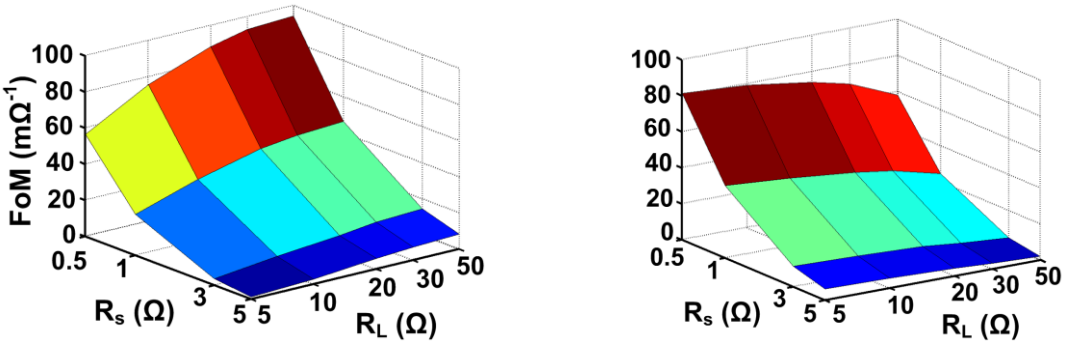

(a) (b)

Fig. 5.6. The FoM comparison for parallel and series load connection vs. R_L and R_s: a) Parallel load connection b) Series load connection. The inductive links specifications are summarized in Table 5.1.

5.3. Multi-coil Inductive Links

Multi-coil inductive power transmission in the form of 3- and 4-coil links has been proposed based on the coupled-mode theory to achieve high PTE especially at large distances. The comprehensive circuit-based analysis of multi-coil links was also presented in previous chapters. However, the optimal choice between the 2-, 3-, and 4-coil links for a particular application is yet another source of confusion for designers, which can be addressed by the proposed FoM.

In an m-coil link, the reflected load from the $(i+1)^{\text{th}}$ coil to the i^{th} coil can be found from,

$$R_{ref\,i,i+1} = k_{i,i+1}^2 \omega L_i Q_{(i+1)L}, \quad i = 1, 2, \ldots, m\text{-}1 \tag{5.12}$$

where $k_{i,i+1}$ is the coupling coefficient between the i^{th} and $(i+1)^{\text{th}}$ coils. $Q_{(i+1)L}$ is the loaded quality factor of the $(i+1)^{\text{th}}$ coil, which can be found from

$$Q_{iL} = \frac{\omega L_i}{R_i + R_{ref\,i,i+1}} = \frac{Q_i}{1 + k_{i,i+1}^2 Q_i Q_{(i+1)L}}, \qquad i = 1, 2, \ldots, m\text{-}1 \tag{5.13}$$

where $Q_i = \omega L_i/R_i$ and R_i are the unloaded quality factor and parasitic series resistance of the i^{th} coil (L_i), respectively. It should be noted that for the last coil, which is connected to the load in series, $Q_{mL} = \omega L_m/(R_m+R_L)$ and for the first coil, which is connected to the source in series, R_s should be added to R_1.

Assuming that the coupling between non-neighboring coils is negligible, the partial PTE from the i^{th} coil to $(i+1)^{th}$ coil can be written as,

$$\eta_{i,i+1} = \frac{R_{ref\,i,i+1}}{R_i + R_{ref\,i,i+1}} = \frac{k_{i,i+1}^2 Q_i Q_{(i+1)L}}{1 + k_{i,i+1}^2 Q_i Q_{(i+1)L}}. \tag{5.14}$$

Using (5.12)-(5.14), the overall PTE in such a multi-coil inductive link can be found from,

$$\eta_{m-coil} = \prod_{i=1}^{m-1} \eta_{i,i+1} \cdot \frac{Q_{mL}}{Q_L}. \tag{5.15}$$

PDL can be calculated by multiplying the power provided by the source, i.e. $V_s^2/2(R_s+R_1+R_{ref1,2})$, by the PTE from (5.15),

$$P_{L,m-coil} = \frac{V_s^{\,2}}{2(R_s + R_1 + R_{ref\,1,2})} \eta_{m-coil}. \tag{5.16}$$

5.3.1. Three-coil Inductive Links

The 3-coil inductive power transmission link, shown in Fig. 5.7, can be used to achieve high PTE and PDL by adjusting k_{34} to transform any arbitrary R_L into the optimal resistance required in the L_2-L_3 inductive link. The PTE of this circuit can be calculated by reflecting the resistive components of each loop from the load back towards the primary coil loop, one stage at a time, using (5.12), and calculating the percentage of the power that is delivered from one stage to the next, using (5.14), until it reaches R_L. According to (5.15), this leads to,

$$\eta_{3-coil} = \frac{(k_{23}^2 Q_2 Q_3)(k_{34}^2 Q_3 Q_{4L})}{[(1+k_{23}^2 Q_2 Q_3 + k_{34}^2 Q_3 Q_{4L})(1+k_{34}^2 Q_3 Q_{4L})]} \cdot \frac{Q_{4L}}{Q_L} \tag{5.17}$$

where k_{24} has been ignored due to the large separation between L_2 and L_4. One can also calculate the PDL of this circuit using (5.12)-(5.16),

$$P_{L,3-coil} = \frac{V_s^{\,2}}{2(R_2+R_s)} \cdot \frac{(k_{23}^2 Q_2 Q_3)(k_{34}^2 Q_3 Q_{4L})}{(1+k_{23}^2 Q_2 Q_3 + k_{34}^2 Q_3 Q_{4L})^2} \cdot \frac{Q_{4L}}{Q_L} \cdot \tag{5.18}$$

It should be noted that in (5.17) and (5.18), the driver output resistance should be considered in $Q_2 = \omega L_2 / (R_2+R_s)$.

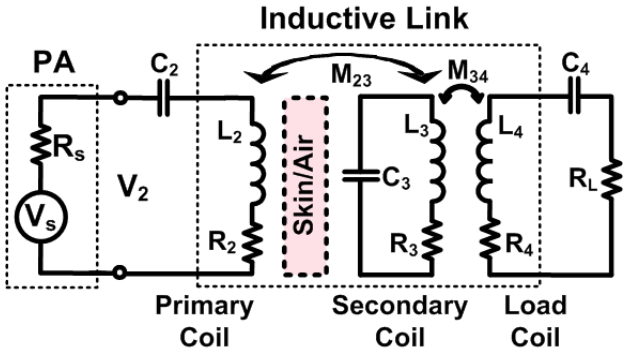

Fig. 5.7. Lumped circuit model of a 3-coil inductive power transmission link.

The FoM for a 3-coil inductive link can be found by substituting (5.17) and (5.18) in (5.4),

$$FoM_{3-coil} = \frac{1}{2(R_2+R_s)} \frac{(k_{23}^2 Q_2 Q_3)^{n+1}(k_{34}^2 Q_3 Q_{4L})^{n+1}}{(1+k_{23}^2 Q_2 Q_3 + k_{34}^2 Q_3 Q_{4L})^{n+2}(1+k_{34}^2 Q_3 Q_{4L})^n} \cdot \left(\frac{Q_{4L}}{Q_L}\right)^{n+1}. \tag{5.19}$$

It will be shown that, similar to 2-coil links, the PTE and PDL losses in 3-coil links follow Fig. 5.2 and (5.9), when optimized for the FoM in (5.4) and (5.19).

The PTE profile of the 3-coil link according to (5.17) is a monotonically decreasing function of the coils' coupling distance, d_{23}. However, the PDL and FoM profiles are maximized at a particular d_{23} that can be found by calculating the derivatives of (5.18) and (5.19) vs. k_{23}, respectively.

$$k_{23,PDL} = \left(\frac{1+k_{34}^2 Q_3 Q_{4L}}{Q_2 Q_3}\right)^{1/2}, \quad k_{23,FoM} = \left[\frac{(n+1)(1+k_{34}^2 Q_3 Q_{4L})}{Q_2 Q_3}\right]^{1/2} \tag{5.20}$$

By substituting $k_{23,FoM}$ in (5.17) and (5.18), one can find the PTE and PDL of the 3-coil link when it is designed to maximize the FoM at that particular d_{23},

$$\eta_{3-coil,FoM} = \frac{n+1}{n+2}\frac{k_{34}^2 Q_3 Q_{4L}}{1+k_{34}^2 Q_3 Q_{4L}}\cdot\frac{Q_{4L}}{Q_L},\ P_{L,3-coil,FoM} = \frac{V_s^{\ 2}}{2R_2}\frac{n+1}{(n+2)^2}\frac{k_{34}^2 Q_3 Q_{4L}}{1+k_{34}^2 Q_3 Q_{4L}}\cdot\frac{Q_{4L}}{Q_L} \quad (5.21)$$

Additional constraints on the coils' geometries in order to satisfy the application or fabrication requirements may result in further reductions in the PTE and/or PDL. The maximum achievable PTE and PDL at a particular d_{23} can be calculated from (5.21) by substituting n with ∞ and 0, respectively,

$$\eta_{3-coil,\max} = \frac{k_{34}^2 Q_3 Q_{4L}}{1+k_{34}^2 Q_3 Q_{4L}}\cdot\frac{Q_{4L}}{Q_L},\ P_{L,3-coil,\max} = \frac{V_s^{\ 2}}{8(R_s+R_2)}\cdot\frac{k_{34}^2 Q_3 Q_{4L}}{1+k_{34}^2 Q_3 Q_{4L}}\cdot\frac{Q_{4L}}{Q_L} \quad (5.22)$$

Using (5.21) and (5.22), we can calculate the losses in PTE and PDL when the link is designed based on the optimal FoM,

$$\eta_{Loss,3-coil} = \frac{\eta_{3-coil,\max} - \eta_{3-coil,FoM}}{\eta_{3-coil,\max}} = \frac{1}{n+2},$$

$$P_{L,Loss,3-coil} = \frac{P_{L,3-coil,\max} - P_{L,3-coil,FoM}}{P_{L,3-coil,\max}} = \frac{n^2}{(n+2)^2}. \quad (5.23)$$

The results are exactly the same as those found in (5.9) for the 2-coil links. It should be noted that in comparison to 2-coil links, the 3-coil inductive links have an additional degree of freedom owing to k_{34}, which allows them to transform any arbitrary R_L to the optimal values for FoM, PTE, and PDL in (5.10) and (5.11). 2-coil links fail to achieve the optimal Q_Ls in (5.10) and (5.11), which become quite large when k_{23} drops as a result of large d_{23} or severe misalignments.

5.3.2. Four-coil Inductive Links

Fig. 5.8 shows a 4-coil inductive power transmission link, which is capable of achieving a high PTE by adjusting k_{12} when there is a large R_s, imposed by a weak driver. In 4-coil inductive links there is a tradeoff between the highest PTE that can be achieved

at short distances while maintaining sufficient PDL at large distances. The PTE of the 4-coil link can be calculated using (5.12)-(5.15),

$$\eta_{4-coil} = \frac{(k_{12}^2 Q_1 Q_2)(k_{23}^2 Q_2 Q_3)(k_{34}^2 Q_3 Q_{4L})}{(B + k_{23}^2 Q_2 Q_3)(A + k_{23}^2 Q_2 Q_3)} \cdot \frac{Q_{4L}}{Q_L}, \tag{5.24}$$

$$A = 1 + k_{34}^2 Q_3 Q_{4L},\ B = (1 + k_{12}^2 Q_1 Q_2).(1 + k_{34}^2 Q_3 Q_{4L}), \tag{5.25}$$

where k_{13}, k_{14}, and k_{24} are ignored in comparison to k_{12}, k_{23} and k_{34}. Using (5.14)-(5.16), PDL of the 4-coil inductive links can be found from,

$$P_{L,4-coil} = \frac{V_s^{\,2}}{2(R_1 + R_s)} \frac{(k_{12}^2 Q_1 Q_2)(k_{23}^2 Q_2 Q_3)(k_{34}^2 Q_3 Q_{4L})}{(B + k_{23}^2 Q_2 Q_3)^2} \cdot \frac{Q_{4L}}{Q_L}. \tag{5.26}$$

It should be noted that in (5.24)-(5.26), the driver output resistance should be considered in $Q_1 = \omega L_1 / (R_1 + R_s)$.

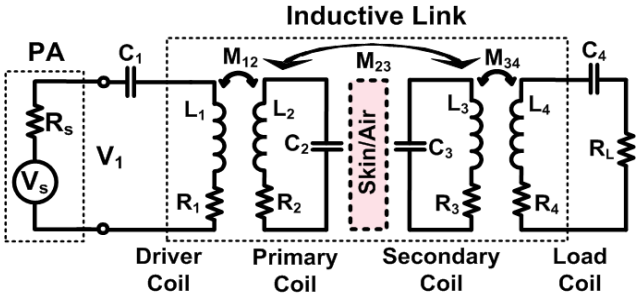

Fig. 5.8. Lumped circuit model of a 4-coil inductive power transmission link.

The 4-coil FoM can be calculated by substituting (5.24) and (5.26) in (5.4),

$$FoM_{4-coil} = \frac{1}{2(R_1 + R_s)} \frac{\left[(k_{12}^2 Q_1 Q_2)(k_{23}^2 Q_2 Q_3)(k_{34}^2 Q_3 Q_{4L})\right]^{n+2}}{(B + k_{23}^2 Q_2 Q_3)^{n+2}(A + k_{23}^2 Q_2 Q_3)^n} \cdot \left(\frac{Q_{4L}}{Q_L}\right)^{n+2}. \tag{5.27}$$

The 4-coil PTE, PDL and FoM profiles are maximized at a particular d_{23} that can be found by calculating the derivatives of (5.24), (5.25), and (5.27) with respect to k_{23}, respectively,

$$k_{23,PTE} = \left(\frac{\sqrt{AB}}{Q_2 Q_3}\right)^{1/2},\ k_{23,PDL} = \left(\frac{B}{Q_2 Q_3}\right)^{1/2}$$

$$k_{23,FoM}=\left[\frac{1}{2Q_2Q_3(n+1)}\left(B-A+\sqrt{A^2+B^2+4AB(n^2+2n+1/2)}\right)\right]^{1/2}. \quad (5.28)$$

The optimal $k_{23,FoM}$ in (5.28) is too complicated to be used for calculating the PTE and PDL losses as a result of FoM-based optimization. Therefore, we apply some approximation. In 4-coil links, we know that k_{12} should be large in order to achieve a high PTE between L_1 and L_2 ($\eta_{12} \approx 1$), especially at short coupling distances where L_2 is strongly loaded by L_3 [92]. Assuming $k_{12}^2 Q_1 Q_2 >> 1$, we can conclude that in (5.25), B >> A. Therefore, $k_{23,FoM}$ in (5.28) can be further simplified to,

$$k_{23,FoM}=\left(\frac{B}{Q_2Q_3(n+1)}\right)^{1/2}. \quad (5.29)$$

By substituting $k_{23,FoM}$ in (5.24) and (5.26), and assuming B >> A, one can find the PTE and PDL of the 4-coil link when the FoM is maximized at a particular d_{23},

$$\eta_{4-coil,FoM} \approx \frac{(k_{12}^2Q_1Q_2)(k_{34}^2Q_3Q_{4L})}{\left[B+B/(n+1)\right]}\cdot\frac{Q_{4L}}{Q_L},$$

$$P_{L,4-coil,FoM} \approx \frac{V_s^{\,2}}{2(R_1+R_s)}\frac{(k_{12}^2Q_1Q_2)[B/(n+1)](k_{34}^2Q_3Q_{4L})}{\left[B+B/(n+1)\right]^2}\cdot\frac{Q_{4L}}{Q_L} \quad (5.30)$$

The maximum achievable PTE and PDL at a particular d_{23} are calculated by substituting n with ∞ and 0, respectively,

$$\eta_{4-coil,\max} \approx \frac{(k_{12}^2Q_1Q_2)(k_{34}^2Q_3Q_{4L})}{B}\cdot\frac{Q_{4L}}{Q_L},$$

$$P_{L,4-coil,\max} \approx \frac{V_s^{\,2}}{8(R_s+R_1)}\cdot\frac{(k_{12}^2Q_1Q_2)(k_{34}^2Q_3Q_{4L})}{B}\cdot\frac{Q_{4L}}{Q_L} \quad (5.31)$$

Using (5.30) and (5.31), similar to the 2- and 3-coil links, we can calculate the losses in PTE and PDL when the 4-coil link is designed based on the optimal FoM,

$$\eta_{Loss,4-coil}=\frac{\eta_{4-coil,\max}-\eta_{4-coil,FoM}}{\eta_{4-coil,\max}} \approx \frac{1}{n+2},$$

$$P_{L,Loss,4-coil} = \frac{P_{L,4-coil,\max} - P_{L,4-coil,FoM}}{P_{L,4-coil,\max}} \approx \frac{n^2}{(n+2)^2}. \quad (5.32)$$

Interestingly, the results are consistent with those found in (5.9) and (5.23). Therefore, designers can use the PTE and PDL loss curves in Fig. 5.2 to find the best n for a given application.

5.3.3. Design Procedure for Multi-coil Links Based on the FoM

Earlier in this chapter, an iterative optimization procedure for 2-coil inductive links based on the new FoM was presented, which has been extended for multi-coil links. In step-1 of Fig. 5.9 flowchart, the design constraints imposed by the application and coil fabrication technology are applied. Using the weight equations in the Appendix, the weight of the coils on the Tx side, W_t, is defined as the weight of L_2 or the sum of the weights of L_1 and L_2 for 3- and 4-coil links, respectively. The weight of the Rx coils, W_r, also equals the sum of the weights of L_3 and L_4 for both 3- and 4-coil links. The nominal values for D_{o3}, d_{12}, d_{23}, d_{34}, R_L and R_s are also required in this step, which are defined by the application (d_{12} is needed only for the 4-coil link). D_{o3} is often chosen to be the maximum allowed by the application, particularly in IMDs. The designer should also limit the coils' wire diameters, $w_{1,max} \sim w_{4,max}$, to account for the overall thickness of the inductors in the given application. The minimum wire spacing between the surface of the conductors, $s_1 \sim s_4$, are considered twice the thickness of the wire insulation in WWCs.

In step-2, the initial values for L_1~L_4 geometries namely w_1~w_4, n_1~n_4, D_{o1}, D_{o2}, and D_{o4} are chosen. In step-3, L_2-L_3 link is optimized using the design procedure shown in Fig. 5.3, with (5.19) and (5.27) used instead of (5.5) for 3- and 4-coil links, respectively. This step provides the interim optimal values for w_2, w_3, n_2, n_3, and D_{o2} based on the initial values for L_1 and L_4 geometries.

L_4 geometry is optimized in step-4 by sweeping n_4 and D_{o4}, followed by sweeping n_4 and w_4 using (5.19) and (5.27) for 3- and 4-coil links, respectively. In each step, two 3-

D surfaces for FoM and W_r are obtained while n_4 and D_{o4} or n_4 and w_4 values that result in the maximum FoM and $W_r < W_{r,max}$ are chosen. Steps 4.1 and 4.2 are repeated iteratively until D_{o4} and w_4 change less than 0.1% and satisfy the condition in step-4.3.

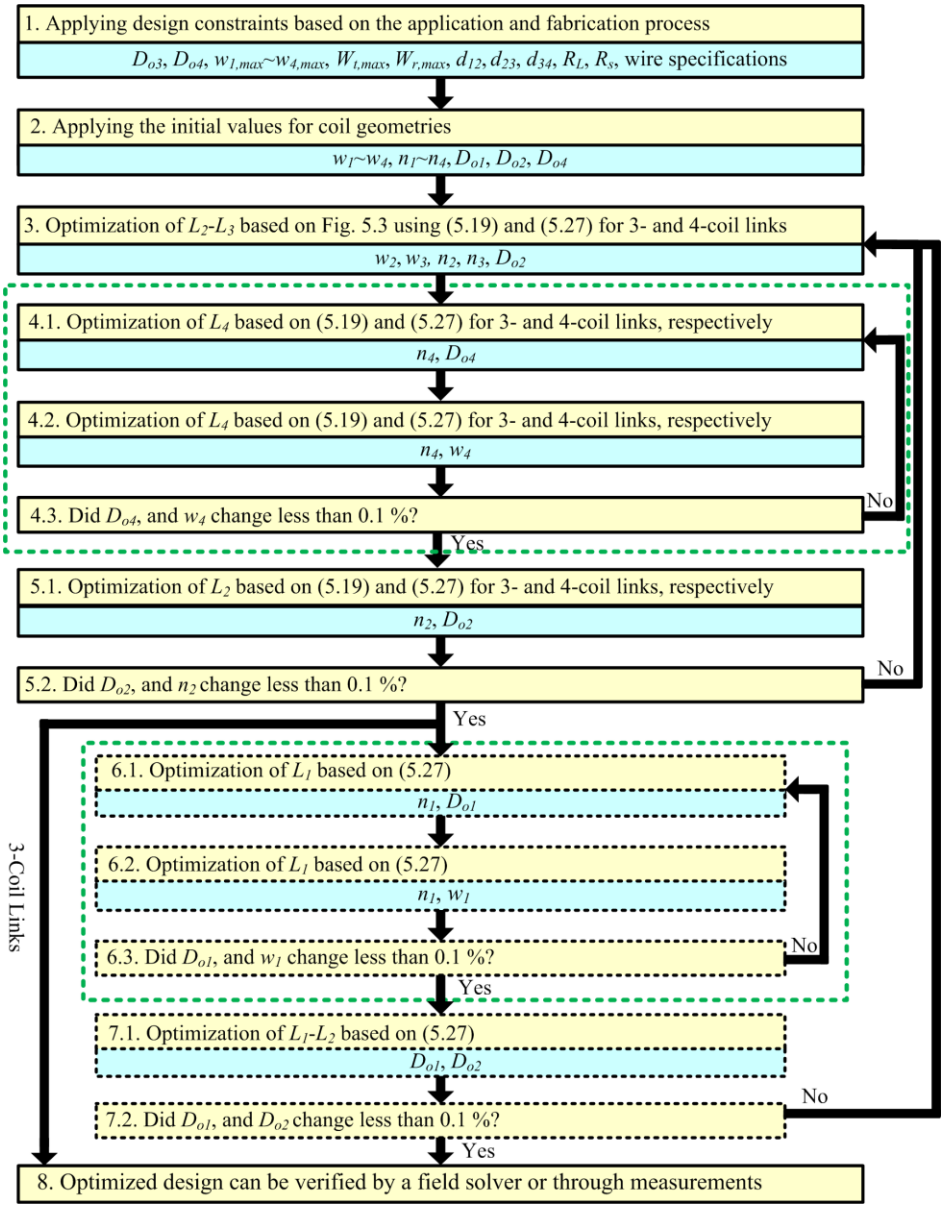

Fig. 5.9. Iterative multi-coil links optimization flowchart based on the proposed FoM.

In step-5, key parameters in the geometry of L_2, i.e. n_2 and D_{o2}, are swept to maximize the FoM in (5.19) and (5.27) for 3- and 4-coil links, respectively, while maintaining $W_t < W_{t,max}$. Step-5 also verifies whether the L_4 geometry resulted from step-4 is optimal. This is because L_4 was optimized in step-4 with respect to L_3 to achieve the

desired k_{34} while L_2-L_3 link had been optimized in step-3 with non-optimized L_1 and L_4 geometries. Steps-3 and 4 are repeated iteratively until n_2 and D_{o2} change less than 0.1%, and satisfy the condition in step-4.3. This step concludes the 3-coil link design for maximum FoM, which can be further validated using field solvers, such as HFSS (Ansoft, Pittsburgh, PA).

The rest of steps in Fig. 5.9 are specific to 4-coil links to optimize the geometry of L_1 for the highest FoM based on (5.27). Step-6 is similar to step-4, which determines the optimal geometry of L_1. However, step-7 verifies if the L_2 geometry is still optimal for the new L_1 geometry from step-6. Therefore, D_{o1} and D_{o2} are swept in step-7.1 to maximize FoM in (5.27) while keeping $W_t < W_{t,max}$. The new D_{o1} along with n_1 and w_1 from step-6.2 are used to start a new iterative optimization loop from step-3, as long as D_{o1} and D_{o2} change more than 0.1% in step-7.2. The 4-coil link is designed for maximum FoM if the condition in step-7.2 is satisfied.

5.4. Discussion

There are a number of parameters that can guide designers towards the optimal inductive power transmission link for their specific application. The amount of power delivered to the load (P_L), driver output resistance (R_s), source voltage (V_s), nominal coupling distance (d_{23}), and the range of coupling distance variations or coil misalignments are among important parameters in addition to the application-based limitations on the coils geometries. The optimization procedure can be made much simpler if it can be shaped around a single measure that would best fit the application. Power transfer efficiency (PTE), which has been dominantly used in the past, is a good measure when P_L is small or R_s is large. However, delivering sufficient PDL becomes challenging when there are stringent limitations on the PA driver. Hence, for the majority of applications, in which achieving high PTE and PDL are both important, the proposed FoM would be a better choice.

Another challenge for designers is how to choose between different topologies, i.e. 2-, 3-, and 4-coil links, for their given application. As demonstrated three examples across a wide range of power levels, most often the proposed FoM can clearly show the topology that fits the best. If two different topologies achieve similar or close FoMs, one can change the parameter n in (5.4) to give a heavier weight to PTE (higher) or PDL (lower). The recommendation is going for a higher PTE because the necessary PDL can be achieved by increasing V_s, as long as the PA transistors can handle the higher voltage levels. According to FoM, the 2-, 3-, and 4-coil links are suitable for these conditions: 1) 2-coil links are chosen when the coils are strongly coupled and a large PDL is needed i.e. R_s is small. This is because the optimal Q_Ls for FoM, PTE, and PDL in (5.10) and (5.11) are easier to achieve with a large k_{23}. Another justification for using a 2-coil link is extreme size constraints. 2) 3-coil links are chosen when the coils are loosely coupled, the coupling distance varies in a wide range, and a large PDL is needed. 3) Finally, 4-coil links are optimal when the PTE is paramount, the load power consumption is very small, the coils are loosely coupled, and their relative distance and alignment are stable.

CHAPTER VI

HIGH-EFFICIENCY AND ADAPTIVE POWER MANAGEMENT

Inductive power transmission across the skin is currently the only viable solution for providing sufficient power to IMDs such as retinal and cochlear implants without the size and power constraints imposed by batteries. The use of inductive power transmission is expected to see an explosive growth over the next decade, as engineers try to cut the power cord from mobile electronics, small home appliances, and even the electric vehicles. Power transfer efficiency (PTE) of the inductive link is highly dependent on how accurately the transmitter (Tx) and receiver (Rx) high-Q coils are tuned to the carrier frequency, f_c. In the above applications, the environment around the Rx LC-tank is quite variable, and there is a need for the Rx to automatically tune itself to f_c to maintain high PTE. Moreover, the load resistance in all abovementioned applications would change significantly especially during wireless charging. As shown in multi-coil links, a load matching is needed at Rx to maximize PTE for the nominal load. In this chapter, two ideas are presented for automatic tuning of the Rx coil and automatic impedance matching of the load resistance.

6.1. Adaptive Power Management and Data Transceiver (PMDT)

A complete adaptive power-management and low-power data-transceiver (PMDT) application-specific integrated circuit (ASIC) has been developed for robust wireless power transmission through inductive links. Fig. 6.1 shows the block diagram of PMDT, which includes an active rectifier, a battery charger, an adaptive super-cap charger (ASCC), a 3.3-V regulator (LDO), an automatic-resonance tuning (ART), and a low-power back telemetry (BT) and ASK demodulator as the data transceiver. A power amplifier (PA) drives the Tx coil, L_1, at the designated carrier frequency (f_c=13.56MHz). The AC signal across the Rx L_2C_2-tank, which is tuned at f_c, is rectified by the rectifier.

The rectifier output, V_{REC}, is then applied to the battery charger and the ASCC. A decision circuit connects either V_{REC} or battery voltage (V_{BAT}) to the LDO input if V_{REC} > 3.6 or < 3.6, respectively. The ASCC charges the super-cap from V_{REC} with the maximum current provided from the inductive link when V_{REC} = 3.8V, which leads to fast start-up and charging compared to conventional constant current/voltage charging mechanisms [100]. The ART ensures that L_2C_2-tank is always tuned at f_c by sweeping two 5-bit binary-weighted on-chip (1pF, 2pF, 4pF, 8pF, 16pF) and off-chip (30pF, 60pF, 120pF, 240pF, 480pF) capacitor banks resulting in 0-480pF capacitance change across L_2C_2-tank with 0.5pF resolution. A hysteresis comparator also detunes L_2C_2-tank by a C_{ovp}=100nF when V_{REC} > 4.8V to protect PMDT when coupling distance, d_{12}, is small or R_L is large. The BT and ASK demodulator can be used to send the Rx power information to the Tx to close the power control loop and configure registers in the Rx, respectively.

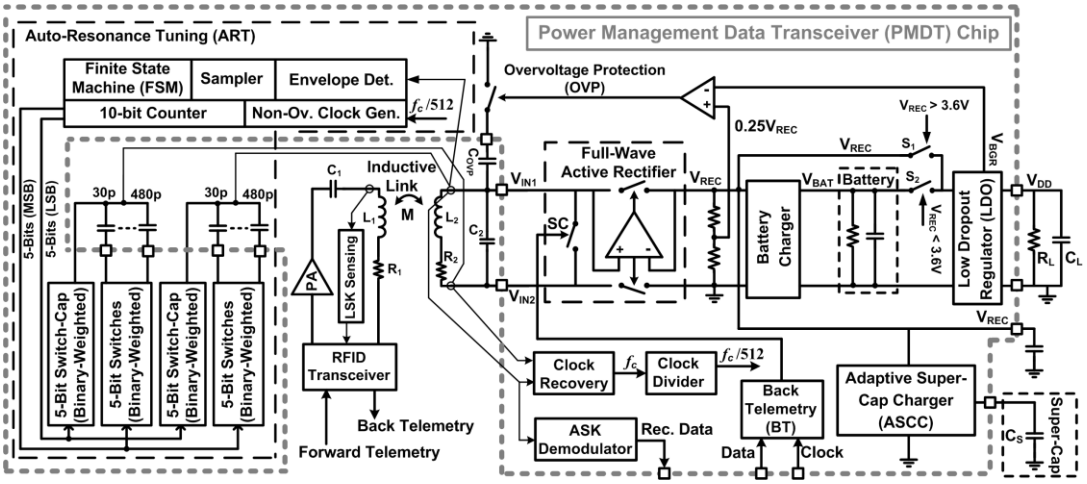

Fig. 6.1. Block diagram of the highly efficient and adaptive PMDT ASIC with the unique feature of automatic-resonance tuning (ART) of the Rx coil.

6.1.1. Circuit Implementation

Fig. 6.2a shows a simplified schematic diagram of the active rectifier, consisting of PMOS and NMOS pass transistors, which are driven by two high-speed offset-controlled comparators [101]. The start-up circuit monitors V_{REC} and sets CTL = 0 when V_{REC} is low. Hence, $P_{1,2}$ are diode-connected and form a passive rectifier, which charges

V_{REC} regardless of the comparators' status up to the point that V_{REC} reaches a stable minimum level (1.6 V). Then CTL toggles to enable the rectifier to operate normally.

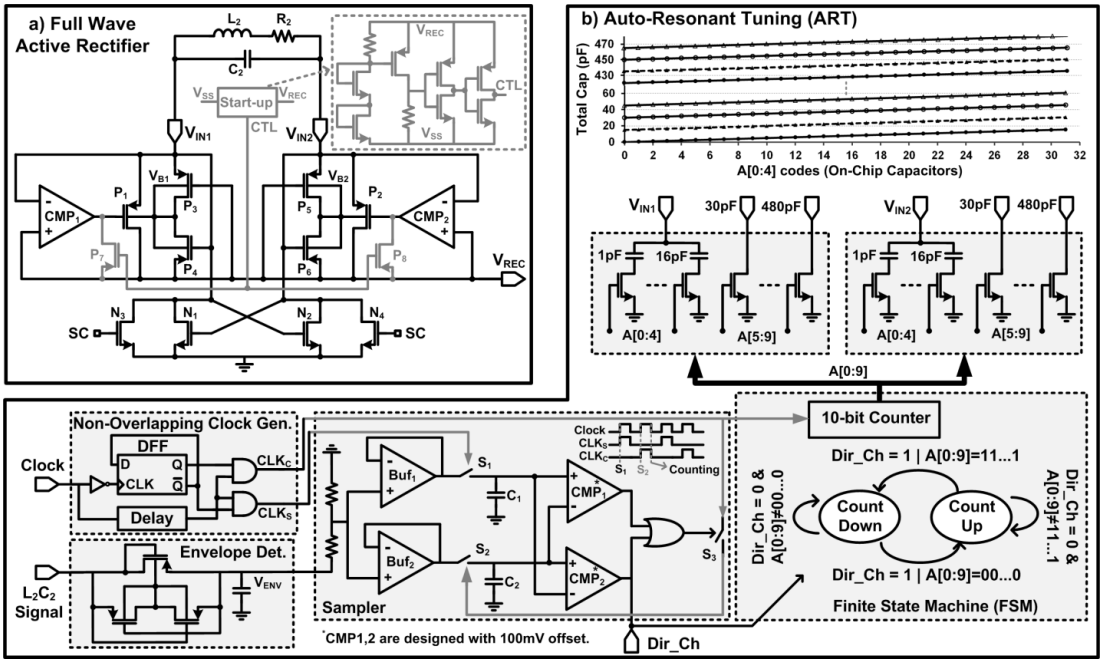

Fig. 6.2. (a) Schematic diagram of the full-wave active rectifier, and (b) detailed schematic diagram of the automatic-resonance tuning (ART).

Fig. 6.2b shows the detailed schematic diagram of the ART block. The ART sweeps two identical 10-bit capacitor banks, which are connected to a 10-bit counter, in a certain direction (up or down) until the voltage envelope across L_2C_2-tank (V_{ENV}) reduces by 100 mV. Then the sweeping direction changes until V_{ENV} again reduces by 100 mV. This up and down cycle ensures that L_2C_2-tank is always tuned at f_c with a small offset. In the ART, V_{ENV} is first detected by a passive rectifier, divided by 1.4, and then buffered before being sampled. Two non-overlapping clocks, CLK_C and CLK_S, are generated from the 26.4 kHz (f_c/512) signal from the clock recovery block (Fig. 6.1). The first sampler, S_1, always samples V_{ENV} at the rising edge of CLK_S while S_2 only samples V_{ENV} at the rising edge of CLK_C when V_{ENV} increases or reduces by 100 mV. Because $CMP_{1,2}$, which are 100-mV offset comparators, output high and close S_3 when the difference between C_1 and C_2 voltages is ±100 mV. Therefore, CMP_2 output (Dir_Ch) changes the counting

direction of the counter according to a finite state machine (FSM) because V_{ENV} has reduced by 100 mV. The FSM starts the counter from the middle (240 pF across L_2C_2-tank) when PMDT is powered and avoids any overflows. The counter operates at the falling edge of CLK_C to be time-separated from V_{ENV} samplings, which occur at the rising edges.

In order to avoid Rx power discontinuities in the presence of small R_L, large d_{12}, or coils' misalignment and rotation, secondary energy sources such as rechargeable batteries and super-caps can be used. For applications such as optogenetics, in which instantaneous power levels in the order of watts should be delivered to LEDs, a super-cap is preferred because of its higher power density [100]. The ASCC provides the maximum charging current available from the inductive link in different conditions to achieve V_{REC} > 3.8 V (Fig. 6.3a). In ASCC, $0.31V_{REC}$ is compared with V_{BGR} = 1.18 V to control the two identical current sources, which act as a charge pump. The voltage across C_1 adjusts the N_1 current, which is mirrored onto P_2, which in turn charges the super-cap. When V_{REC} > 3.8 V, which implies that the received power is high, the UP signal becomes high, C_1 is charged, and super-cap charging current (I_C) increases slowly. The increase in I_C will eventually lead to V_{REC} < 3.8 V and, therefore, the DN signal becomes high, C_1 is discharged, and I_C reduces to reach V_{REC} > 3.8 V. In this condition, ASCC again increases I_C. This up and down cycling continues until the super-cap is fully charged. The battery charger provides a Li-Ion battery with a constant charging current of 12 mA as long as V_{BAT} < 4.2 V, and connects the battery to a 4.2-V LDO when V_{BAT} = 4.2 V as shown in Fig. 6.3b.

The low-power data transceiver includes a back telemetry (BT) circuitry based on load-shift-keying modulation and an amplitude-shift-keying demodulation circuitry. The BT creates narrow pulses (~250 ns) when data is "1" to short L_2C_2-tank by closing the short-coil (SC) switches in the rectifier as shown in Fig. 6.4a. The schematic diagram of the ASK demodulator is shown in Fig. 6.4b. The ASK demodulator detects L_2C_2-tank

amplitude variations using two paths with different time constants, $R_1C_1 < R_2C_2$, which are connected to a comparator.

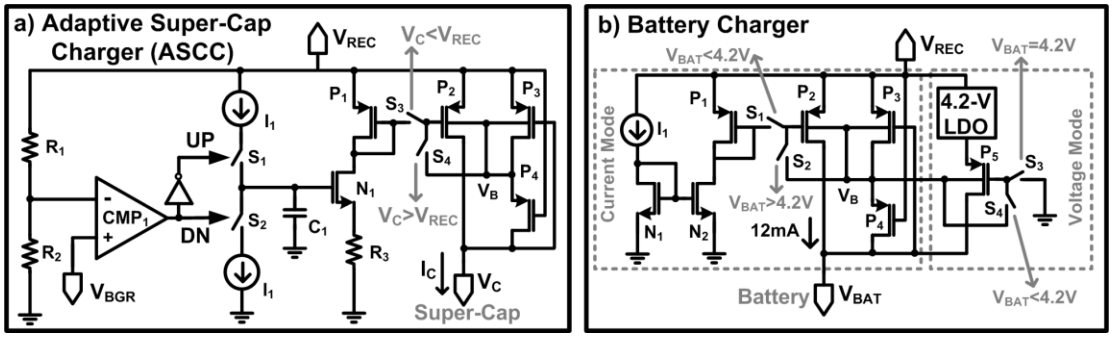

Fig. 6.3. Schematic diagrams of the (a) adaptive super-cap charger (ASCC), and (b) battery charger.

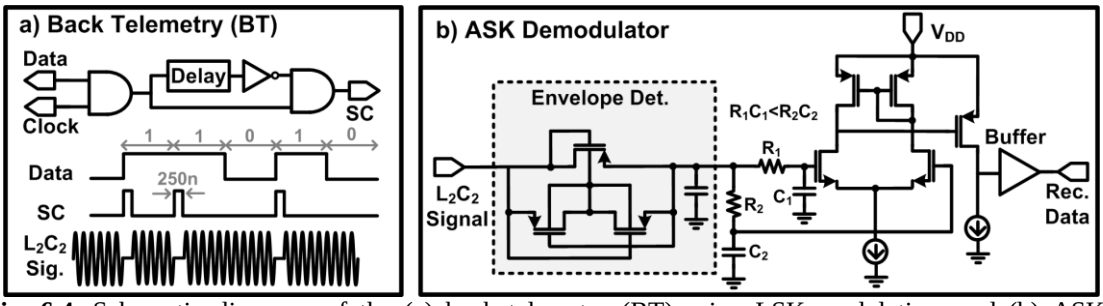

Fig. 6.4. Schematic diagrams of the (a) back telemetry (BT) using LSK modulation, and (b) ASK demodulator for forward telemetry.

6.1.2. Measurement Results

The PMDT chip was fabricated in the TSMC 0.35-μm 4M2P standard CMOS process, occupying 2.54 mm^2. Fig. 6.5 shows the PMDT chip micrograph with floor planning of each block. Fig. 6.6 shows measured input/output waveforms in the rectifier, the LDO output (V_{DD}), and the measured rectifier power conversion efficiency (PCE) vs. V_{REC} with R_L = 0.5 kΩ and 1 kΩ at f_c = 13.56 MHz. It can be seen that the active rectifier has achieve a high PCE of 76.2% at V_{REC} = 4 V and R_L = 0.5 kΩ.

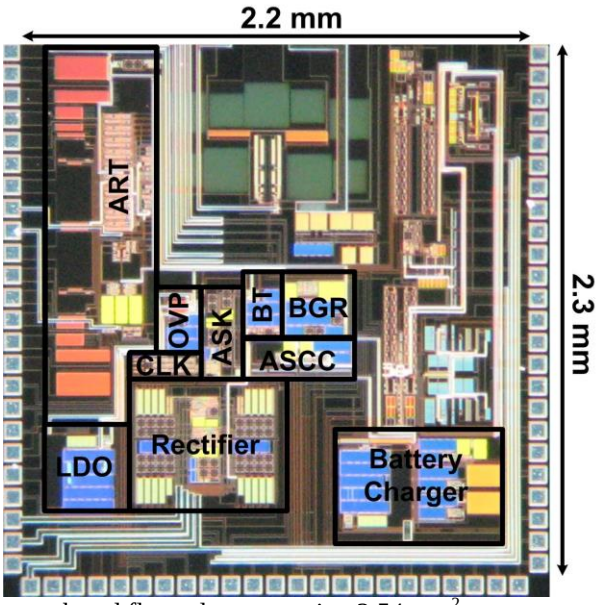

Fig. 6.5. PMDT die micrograph and floor plan occupying 2.54 mm^2

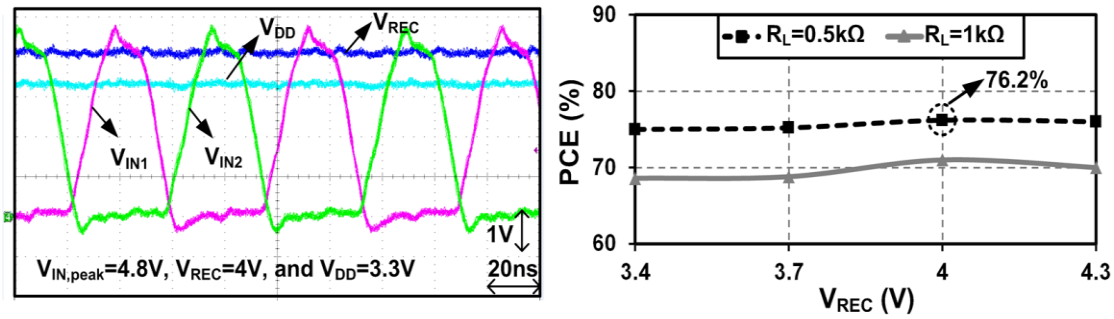

Fig. 6.6. Measured input/output voltage waveforms in the rectifier for R_L = 0.5 kΩ and PCE vs. V_{REC} for R_L = 0.5 kΩ and 1 kΩ at f_c=13.56 MHz.

Fig. 6.7 shows the functionality of ASCC and over voltage protection (OVP) blocks. Thanks to adaptive charging mechanism, PMDT started-up ~10 ms after the Tx turned on when charging a 0.11 F capacitor at d_{12} = 7 cm with 1 W Tx output power. The start-up time would increase to 70 s if super-cap was directly connected to V_{REC}. The measured I_C variation was between 0 and 17 mA to maintain V_{REC} around 3.8 V. When the super-cap was charged to V_C = 3 V, close to V_{REC} = 3.8 V, I_C slowly reduced and the OVP block turned on to keep V_{REC} < 4.8 V as shown in Fig. 6.7.

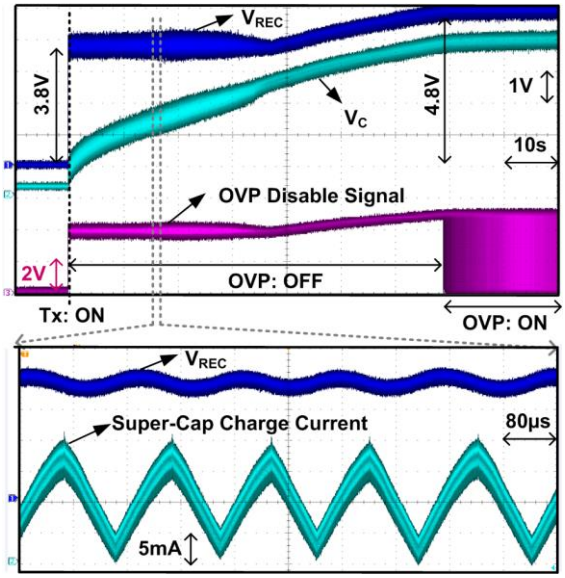

Fig. 6.7. The rectifier, super-cap and OVP disable signals with fast start-up when charging a 0.11 F capacitor at d_{12} = 7 cm with 1 W Tx output power. The charging current adaptively changed between 0 and 17 mA to maintain V_{REC} around 3.8 V.

Fig. 6.8 shows the V_{REC} waveform when ART is enabled. The Dir_Ch signal periodically became high when V_{REC} reduced by 0.3 V, to reverse the counting direction. Hence, V_{REC} has increased after each Dir_Ch high signal. V_{REC} peaks between two consecutive Dir_Ch high signals show that ART has reached to the optimal resonance capacitance, around which ~16 pF was swept. Fig. 6.8 also shows that PMDT would fail with > 20 pF detuning of L_2C_2-tank if ART was disabled, while ART can maintain V_{REC} constant at 4V for > 100 pF detuning. In this measurement, the resonance capacitance of L_2 was intentionally changed up to 100 pF.

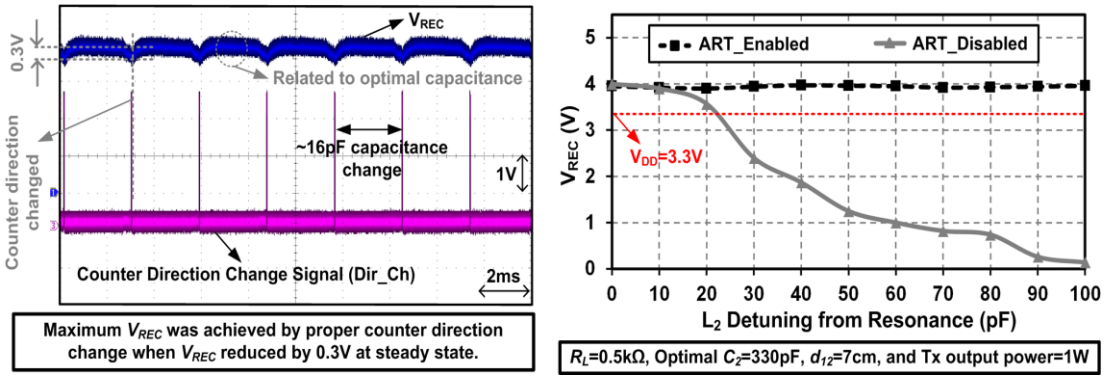

Fig. 6.8. Measured waveforms for the auto-resonance tuning (ART) block. It can be seen that the ART block can result in high efficiency over a wide span of L_2 detuning.

Fig. 6.9a shows the current/voltage profile of the battery charger. A 4.2V 12mAh Li-Ion battery was used in this measurement. The 100-kbps OOK-modulated random data on the power carrier using an RFID reader (TRF7960) was successfully detected by the ASK demodulator as shown in Fig. 6.9b. Table 6.1 summarizes the specifications of the PMDT ASIC.

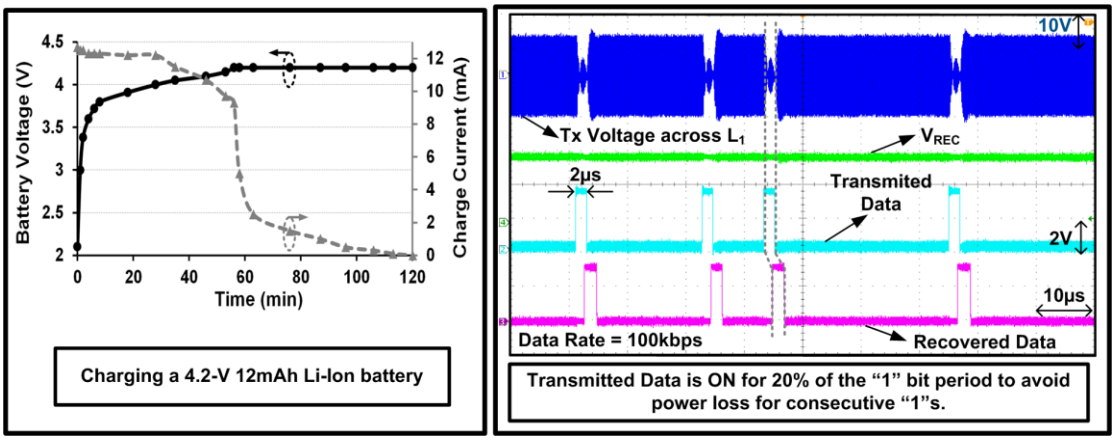

(a) (b)

Fig. 6.9. (a) Measured current/voltage profile of the battery charger block, and (b) Measured waveforms of the ASK demodulator with a random data bit stream applied to an RFID reader, TRF7960 for R_L = 0.5 kΩ, d_{12} = 7 cm, and Tx output power = 1 W.

Table 6.1. Specifications of the PMDT ASIC

Power Management and Data Transceiver (PMDT)	
Fabrication technology	TSMC 0.35µm 4M2P Std. CMOS
Die size (mm^2)	2.54
Supply voltage (V)	3.3
Total current consumption (µA)	68
Rectifier Specifications	
Rectifier efficiency (%)	76.2
Nominal V_{REC} (V)	4
Nominal R_L (kΩ)	0.5
Operation frequency (MHz)	13.56
Automatic-resonance Tuning (ART) Specifications	
Operation frequency (kHz)	26.4
Tuning capacitance range (pF)	On-chip : 0-16 (5-bits) Off-chip : 15-480 (5-bits)
Data Transceiver Specifications	
Back telemetry data rate (kbps)	250
Forward telemetry data rate (kbps)	100
ASK demodulator sensitivity (mV)	150
Current consumption (µA)	10

*when super-cap and battery chargers are off.

6.2. Q-modulated Inductive Link

Three-coil links were proposed in Chapter III to increase power transfer efficiency (PTE) by transforming the load resistance (R_L) to the optimal load required by the inductive link by adding an additional resonator in the receiver (Rx) side. Implementing matching circuits in the Rx with discrete off-the-shelf inductors and capacitors have also been proposed to increase PTE [102], [103]. In such systems, a matching network transforms R_L to the optimal load required by the link. To cover a wide range of R_L variations, however, this method needs bulky switched networks of capacitor and inductors to adaptively adopt the matching circuit to the new R_L during operation, which occupies a large volume and also adds power dissipations.

We propose a method that provides flexibility in the Rx side of the conventional inductive links in adjusting to changes in R_L during operation, without significant loss of PTE. It provides a switching mechanism, by which the Rx subsystem controls the quality factor (Q) of the Rx LC-tank, and hence limits the system losses when R_L changes occur. The theory and circuit implementation of this method, which is termed Q-modulated inductive link, will be presented in this Chapter.

The proposed Q-modulated inductive link consists of one coil at the Tx side as shown in Fig. 6.10. An additional Tx coil (L_1) can be added to the link similar to the conventional 4-coil links to decouple the high-Q coil, L_2, from the power amplifier (PA) source resistance (R_s) and enhance the overall PTE. However, the Rx only consists of one high-Q coil (L_3) but with a unique switching mechanism, an automatic resonance tuning (ART) block, and an adaptive duty cycle control (ADCC). The rectifier, regulator, and DC load resistance ($R_{L,DC}$) can all be modeled with an *AC* resistance (R_L). The proposed link in Fig. 6.10 is similar to conventional 3-coil links.

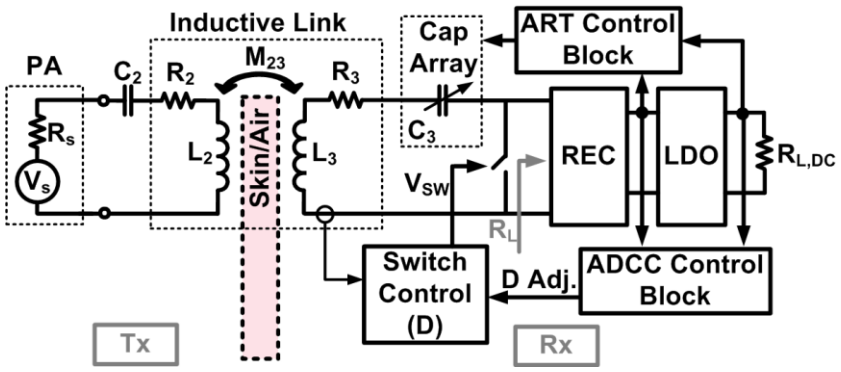

Fig. 6.10. Proposed Q-modulated inductive link to enhance PTE.

In the proposed link, a switch control block monitors the Rx coil (L_3) current and controls a switch in parallel with the L_3C_3-tank via V_{SW} signal. The onset and duty cycle of V_{SW} are determined based on R_L. The ADCC block monitors the rectifier output and changes the switching duty cycle (D) such that the rectifier voltage maintains at its maximum (highest PTE) at each R_L.

In the proposed technique, during half period of the power carrier cycle ($T_p/2$), the Rx LC-tank is shorted or opened, which depends whether series or parallel Rx resonance is used, for a certain time (T_{ON}) to establish a high-Q link by disconnecting R_L from the Rx coil. For the rest of the time in each $T_p/2$, i.e. $T_p/2$-T_{ON}, the coil is connected to R_L to deliver the stored energy inside the LC-tank to R_L. By connecting R_L to the Rx LC-tank, Q_3 is reduced and, therefore, the Rx LC-tank experiences an average Q_3, which can be controlled by the switching duty cycle, $D = 2T_{ON}/T_p$. This degree of freedom (D) in modulating Q_3 or R_L, which could be controlled electronically, is not present in multi-coil links, in which the physical distance or relative geometries of the two Rx coils determine the transformed R_L.

While this technique can improve the PTE of loosely-coupled inductive links, the resonance frequency of the Rx coil changes when the Q-modulation is applied. Therefore, an automatic resonance tuning (ART) method, which introduced earlier in this Chapter, is needed to achieve the highest possible PTE using the proposed technique.

6.2.1 Effect of Q-modulation on an RLC Network

To simplify the analysis, the inductive link in Fig. 6.10 is simplified to a series RLC-network as shown in Fig. 6.11. If L_3C_3-tank is tuned at ω_p, the current in L_3 can be found from,

$$\frac{d^2I(t)}{dt^2}+\frac{\omega_p}{Q}\frac{dI(t)}{dt}+\omega_p^2 I(t)=V_s(t)=A\sin(\omega_p t) \tag{6.1}$$

where Q is the quality factor of L_3C_3-tank that would be different when the switch mode changes. The general solution for (6.1) when the switch with internal resistance of R_{sw} turns on at $t = 0$ (phase-I in Fig. 6.12) can be written as,

$$I(t)=\exp(\frac{-\omega_p}{2Q_3}t)(a_1\cos(\omega_{d1}t)+b_1\sin(\omega_{d1}t)+A\sin(\omega_p t)/R_3 \tag{6.2}$$

where $Q_3 = \omega_p L_3 / R_3$, $R_{sw} = 0$ for simplicity, and the damping frequency

$$\omega_{d1}=\omega_p\sqrt{1-\frac{1}{4Q_3^{\,2}}} \quad . \tag{6.3}$$

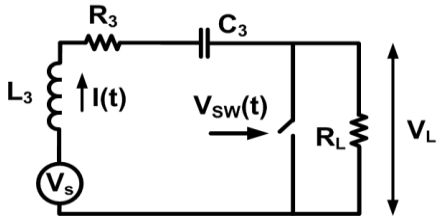

Fig. 6.11. Schematic diagram of a series RLC tank, in which R_L is switched or Q is modulated.

The inductor current when the switch turns off at $t = T_{ON}$ (phase-II in Fig. 6.12) can be found in a similar way as,

$$I(t)=\exp(\frac{-\omega_p}{2Q_{3L}}(t-T_{ON}))(a_2\cos(\omega_{d2}(t-T_{ON}))+b_2\sin(\omega_{d2}(t-T_{ON}))+A\sin(\omega_p t)/(R_3+R_L) \tag{6.4}$$

where $Q_{3L} = \omega_p L_3 / (R_3 + R_L)$, $R_{sw} = 0$ for simplicity, and the damping frequency

$$\omega_{d2} = \omega_p \sqrt{1 - \frac{1}{4Q_{3L}^{\ 2}}} \quad . \tag{6.5}$$

Using the current in L_3 and the voltage across C_3 at the end of each phase, the two unknown parameters i.e. a_1 and b_1 in phase-I and a_2 and b_2 in phase-II could be found. It can be seen from (6.2) and (6.4) that $I(t)$ is still a sinusoidal signal in each phase.

Fig. 6.12 shows the proposed switching diagram that switch is turned on at the zero crossing of $I(t)$ in the phase-I and turned off after a certain time, T_{ON}, in phase-II. The same pattern is periodically repeated every $T_p/2$, where $T_p = 1/f_p$ is one cycle of the excitation signal. Therefore, the duty cycle of the switching is $D = 2T_{ON}/T_p$. Fig. 6.13 shows the Spice simulation results for the RLC-network shown in Fig. 6.11 for D = 50%. There are three important points to learn from Fig. 6.13: 1) Although L_3C_3-tank is tuned to the excitation frequency (f_p = 1MHz), there is a 30.6 degrees phase shift between the $V_s(t)$ and $I(t)$ that implies that the resonance frequency of the switched L_3C_3-tank has shifted to 1.05 MHz. Therefore, the L_3C_3-tank needs to be re-tuned. 2) The equivalent Q of the switched L_3C_3-tank is 6.3 according to the amplitude and phase of $I(t)$, which is different from Q_3 = 157 and Q_{3L} = 3. Therefore, we have been able to change the Q or equivalent R_L of the RLC network by switching the load. 3) The current in the inductor can safely be approximated with a sinusoid.

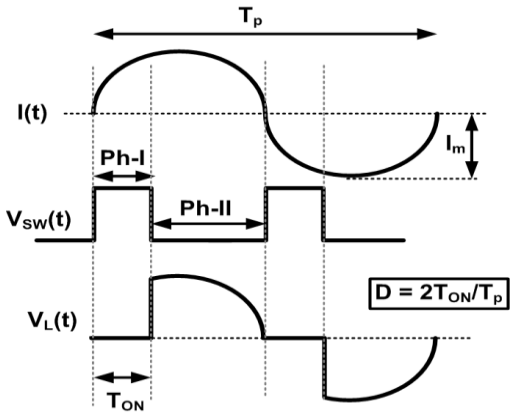

Fig. 6.12. The switching diagram that the switch turns on at the zero crossing of the current in the inductor, $I(t)$, for a certain time of T_{ON} in each $T_p/2$. This results in switching duty cycle of $D = 2T_{ON}/T_p$.

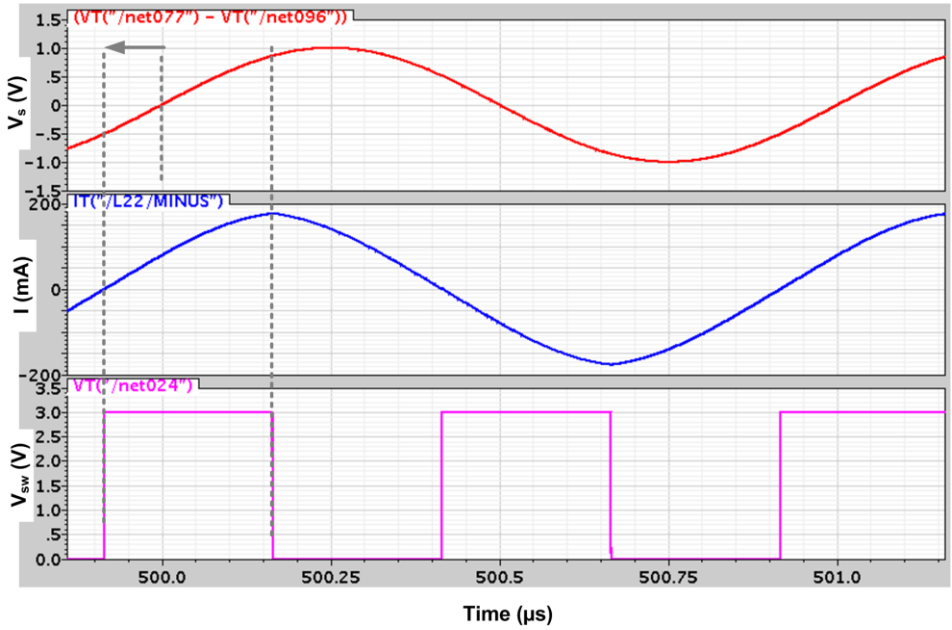

Fig. 6.13. Spice simulation results for the switched RLC-network in Fig. 6.11. It can be seen that there is a phase difference between $I(t)$ and $V_s(t)$ that implies that the switched L_3C_3-tank has been detuned from f_p = 1 MHz to 1.05 MHz. L_3 = 5 µH, C_3 = 5 nF, R_3 = 0.2 Ω, R_L = 10 Ω, f_p = 1 MHz, R_{sw} = 0, and D = 50%.

Although the onset of switching is the zero crossing of $I(t)$ in the following analysis, a similar theory could be developed for any switching onset relative to $I(t)$. The equivalent Q of the switched-RLC network in Fig. 6.11 can be found by calculating the ratio of the energy inside the LC-tank to the average power dissipation in steady state,

$$Q_{3L,eq} = \omega_p \frac{0.5L_3 |I_m|^2}{P_{Rsw} + P_{R3} + P_{RL}} \tag{6.6}$$

where I_m is the peak current in the inductor (L_3), and P_{Rsw}, P_{R3}, and P_{RL} are the average power dissipations in the switch (R_{sw}), R_3, and R_L, respectively. Because, the current in R_3 was approximated to be a sinusoid, P_{R3} can be written as,

$$P_{R3} = 0.5R_3 |I_m|^2. \tag{6.7}$$

However, current flows in R_{sw} and R_L only for $2T_{ON}$ and $2\times(T_p\text{-}T_{ON})$ portion of time in each T_p cycle (see Fig. 6.12). Therefore, the power dissipation in R_{sw} and R_L could be calculated as,

$$P_{Rsw} = R_{sw} \mid I_m \mid^2 \frac{\omega_p}{2\pi}(T_{ON} - \frac{1}{2\omega_p}\sin(2\omega_p T_{ON})) = 0.5R_{sw} \mid I_m \mid^2 (D - \frac{1}{2\pi}\sin(2\pi D))$$
$$P_{RL} = R_L \mid I_m \mid^2 \frac{\omega_p}{2\pi}(\frac{\pi}{\omega_p} - T_{ON} + \frac{1}{2\omega_p}\sin(2\omega_p T_{ON})) = 0.5R_L \mid I_m \mid^2 (1 - D + \frac{1}{2\pi}\sin(2\pi D)) \quad (6.8)$$

Using the power dissipations in (6.7) and (6.8), one calculate $Q_{3L,eq}$ as,

$$Q_{3L,eq} = \frac{\omega_p L_3}{R_3 + R_{sw}(D - \frac{1}{2\pi}\sin(2\pi D)) + R_L(1 - D + \frac{1}{2\pi}\sin(2\pi D))} \quad (6.9)$$

It can be seen from (6.9) that for D = 0, in which switch is always off and L_3C_3-tank is loaded by R_L, $Q_{3L,eq} = \omega_p \times L_3 / (R_3 + R_L)$. On the other hand for D = 1 or 100%, in which switch is always on and R_L is short circuit, $Q_{3L,eq} = \omega_p \times L_3 / R_3 = Q_3$.

To verify the accuracy of (6.9), the calculated and Spice simulated $Q_{3L,eq}$ values of a switched RLC-network are compared in Fig. 6.14. It can be seen that there is a fairly good match between calculated and simulated $Q_{3L,eq}$ values. The small discrepancies are because we assumed that *I(t)* is a perfect sinusoid while it is not 100% accurate according to (6.2), (6.4), and Fig. 6.13.

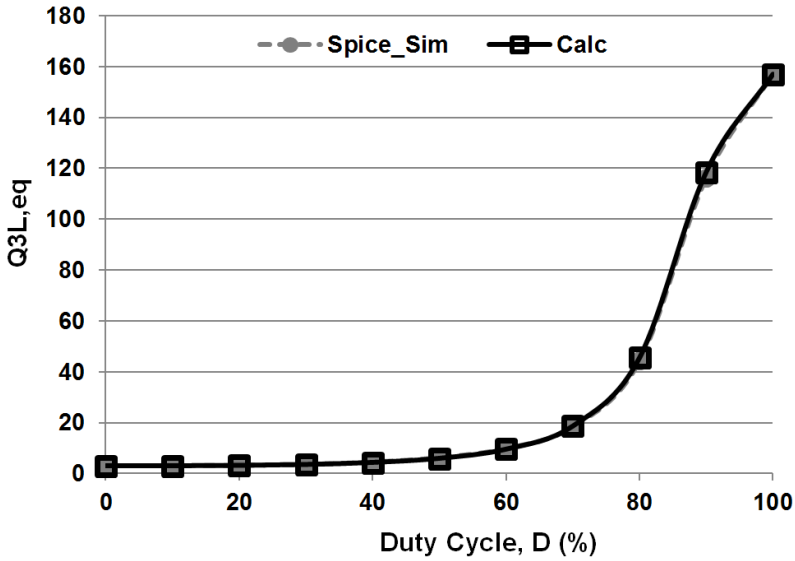

Fig. 6.14. Calculated vs. Spice simulated $Q_{3L,eq}$ in (6.9) for the switched RLC-network in Fig. 6.11. It can be seen that there is a good match between the calculation and simulation results, which validate the accuracy of (6.9). L_3 = 5 µH, C_3 = 5 nF, R_3 = 0.2 Ω, R_L = 10 Ω, R_{sw} = 0, and f_p = 1 MHz.

6.2.2 Q-modulation Effect on the Power Transfer Efficiency (PTE)

The PTE of the Q-modulated inductive link in Fig. 6.10 can be written as,

$$\eta_{Q-2coil} = \frac{k_{23}^2 Q_2 Q_{3L,eq}}{1+k_{23}^2 Q_2 Q_{3L,eq}} \cdot \frac{Q_{3L,eq}}{Q_{L,eq}} \tag{6.10}$$

where k_{23} is the coupling between coils, $Q_2 = \omega_p \times L_2 / R_2$, and $Q_{3L,eq}$ was defined in (6.9). $Q_{L,eq}$ in (6.10) is defined as,

$$Q_{L,eq} = \frac{\omega_p L_3}{R_L(1-D+\frac{1}{2\pi}\sin(2\pi D))} = \frac{\omega_p L_3}{R_{L,eq}}. \tag{6.11}$$

Therefore, similar to conventional 2-coil links, to maximize the PTE, $Q_{L,eq}$ need to match an optimal $Q_{L,PTE}$, which can be found from

$$Q_{L,eq} = \frac{\omega_p L_3}{R_{L,eq}} = Q_{L,PTE} = \frac{Q_3}{(1+k_{23}^2 Q_2 Q_3)^{1/2}}. \tag{6.12}$$

Therefore, the optimal duty cycle, D, for switching can be found by solving,

$$\frac{1}{2\pi}\sin(2\pi D) - D = \frac{R_3(1+k_{23}^2 Q_2 Q_3)^{1/2}}{R_L} - 1. \tag{6.13}$$

As seen from (6.13), the Q-modulated inductive link can achieve high PTE for a wide range of R_L by choosing the proper D.

Fig. 6.15 compares the calculated and Spice-simulated PTE of the proposed Q-modulated inductive link with a conventional 3-coil link, in which two coils are used in the Rx for impedance matching. There are four important points to learn from Fig. 6.15: 1) The Q-modulated link archives the highest PTE at D = 80%. This implies that the optimal $Q_{L,PTE}$ condition in (6.12) is satisfied at D = 80%. 2) At D = 0, in which switch is always off, the Q-modulated link is basically a 2-coil link without impedance matching and, therefore, PTE is low. 3) The Q-modulated link needs a retuning at each D to

achieve the highest PTE. This is the reason that an automatic resonance tuning (ART) is required. 4) For a constant R_L, the conventional 3-coil link and proposed Q-modulated inductive link achieved the same PTE at D = 80%. This further validates the theory that the proposed switching mechanism changes the Q of the Rx coil, which is proportional to R_L.

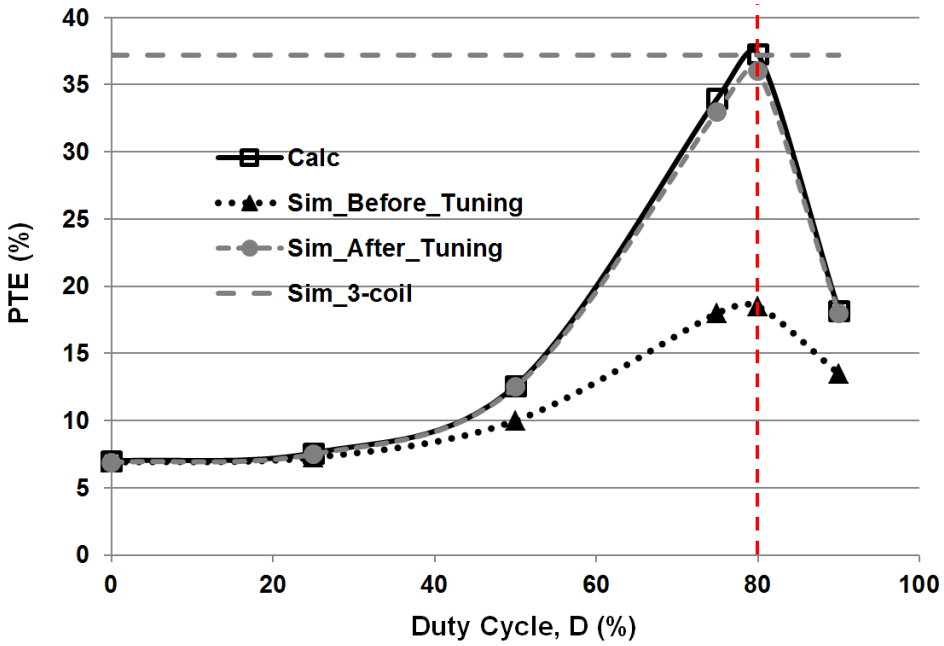

Fig. 6.15. PTE comparison between the conventional 3-coil link and proposed Q-modulated inductive link. At D = 80% maximum PTE is achieved because optimal $Q_{L,PTE}$ is achieved. Retuning the Rx coil in the Q-modulated link has significantly increased the PTE. L_2 = 12 µH, C_2 = 2.1 nF, R_2 = 0.3 Ω, L_3 = 5 µH, C_3 = 5 nF, R_3 = 0.2 Ω, k_{23} = 0.01, R_L = 10 Ω, R_{sw} = 0; and f_p = 1 MHz. In the 3-coil link, L_4 = 5 µH, C_4 = 5 nF, R_4 = 0.2 Ω, and k_{34} = 0.08.

In order to show the advantage of the proposed Q-modulated inductive link over conventional 3-coil links, R_L has been swept from 1 Ω to 100 Ω in Fig. 6.16. It can be seen that the 3-coil link achieves highest PTE at R_L = 10 Ω because k_{34} is optimal at this condition. However, the Q-modulated link achieves high PTE in a wide range of R_L by adjusting D. This degree of freedom is not provided by the traditional 3-coil link, in which k_{34} depends on the relative distance and geometries of the L_3 and L_4 coils.

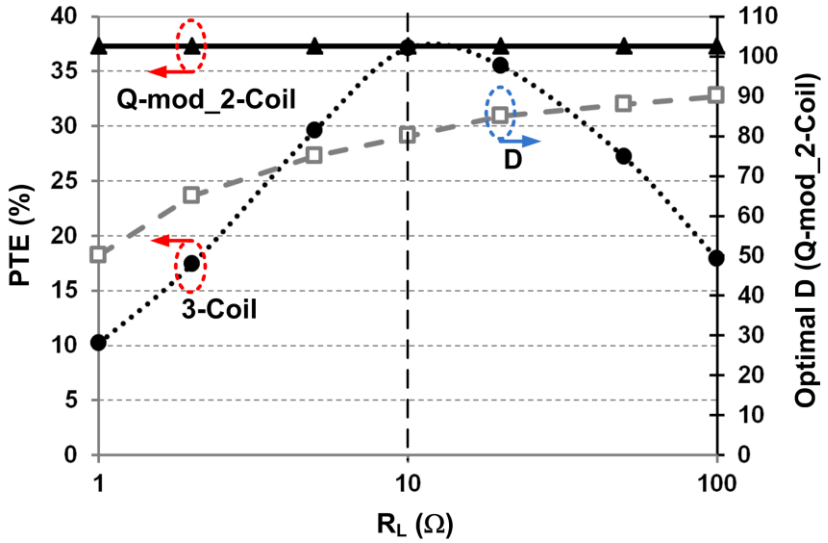

Fig. 6.16. PTE comparison between the conventional 3-coil link and proposed Q-modulated inductive link vs. R_L. It can be seen that the proposed Q-modulated link achieves high PTE for a wide range of R_L by adjusting D, however, the 3-coil link only achieves highest PTE at R_L = 10 Ω , in which k_{34} is optimal. Inductive link specifications are the same as those of Fig. 6.14.

6.2.3. Q-modulation Power Management (QMPM)

A power-management ASIC based on the proposed Q-modulation technique (QMPM) has been developed for efficient recharging of mobile electronics consuming power as large as 5 kW. Fig. 6.17 shows the block diagram of QMPM, which includes a full-wave passive rectifier, a 3-V regulator (LDO), an automatic duty-cycle control (ADCC) to adaptively perform the load transformation, and over-voltage protection (OVP) circuitry. A power amplifier (PA) drives the Tx coil, L_2, at the designated carrier frequency (f_c = 2 MHz). The AC signal across the Rx L_3C_3-tank, which is tuned at f_c, is rectified by the rectifier. The rectifier output, V_{REC}, is then applied to the LDO input to create a constant 3-V output for the rest of the system. The ADCC ensures that the inductive link experience the optimal load resistance in the presence of load variation by adjusting the duty cycle of shorting the switch in parallel with the series L_3C_3-tank. A hysteresis comparator also detunes L_3C_3-tank by a C_{ovp} = 100 nF when V_{REC} > 4.8V to protect QMPM when coupling distance, d_{23}, is small or R_L is large. A clock recovery detects the carrier frequency i.e. f_c = 2 MHz and divides it by 64 for the ADCC operation.

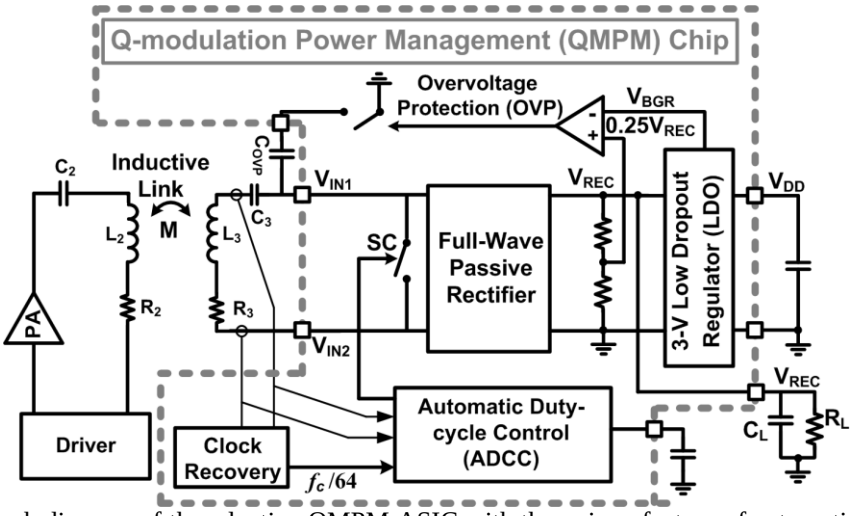

Fig. 6.17. Block diagram of the adaptive QMPM ASIC with the unique feature of automatic impedance matching of R_L.

Fig. 6.18 shows the schematic diagram of the full-wave passive rectifier, consisting of NMOS transistors ($N_{1\text{-}4}$) for AC voltage rectification and PMOS pass transistors with threshold-voltage cancellation technique to reduce the drop voltage of the main pass transistors i.e. P_1 and P_4 [104]. Diode-connected P_2 and P_5 transistors are used for start-up. The width of transistors are chosen large enough (38.4 mm for NMOS and 54.1 mm for PMOS) to reduce the voltage drop when a large current pass through the rectifier. In post-layout simulations, for a 14 W output power, the rectifier shows 0.8 V drop with the power conversion efficiency of 78 %.

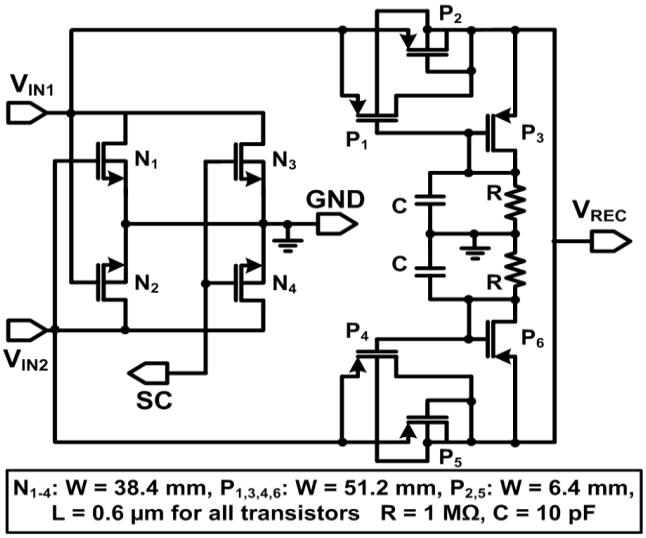

Fig. 6.18. Schematic diagram of the full-wave passive rectifier with threshold-voltage cancelation.

Fig. 6.19 shows the detailed schematic diagram of the ADCC block. The ADCC control charge/discharge of a charge pump in a certain direction (up or down) until the voltage envelope across L_3C_3-tank (V_{ENV}) reduces by 100 mV. Then the charge/discharge direction changes until V_{ENV} again reduces by 100 mV. This up and down cycle ensures that R_L is transformed to an optimal resistance needed by the inductive link with a small offset. In the ADCC, V_{ENV} is first detected by a passive rectifier, divided by 1.4, and then buffered before being sampled. Two non-overlapping clocks, CLK_C and CLK_S, are generated from the 30 kHz (f_c/64) signal from the clock recovery block. The first sampler, S_1, always samples V_{ENV} at the rising edge of CLK_S while S_2 only samples V_{ENV} at the rising edge of CLK_C when V_{ENV} increases or reduces by 100 mV. Because $CMP_{1,2}$, which are 100-mV offset comparators, output high and close S_3 when the difference between C_1 and C_2 voltages is ±100 mV. Therefore, CMP_2 output (Dir) changes the charging or discharging direction of a charge pump according to a finite state machine (FSM) because V_{ENV} has reduced by 100mV. The charge pump output, V_{CP}, adjusts the reference voltage (V_{REF}) of two comparators inside mono-stable circuits. By adjusting V_{CP}, the duty cycle of short coil signal, SC, can be adjusted. Two inverters connected to the L_3C_3-tank terminals detect the zero crossings of the tank voltage, which are the same as those of the current waveform. The SC signal includes two pulses with variable width at the zero crossing of the voltage across L_3C_3-tank. The pulse width, which is proportional to the duty cycle of the signal, is determined by the comparators in the mono-stable circuits. Therefore, charge pump output goes high and low to find the optimal duty cycle, in which the arbitrary R_L is transformed to the desired load. The QMPM chip was fabricated in the TSMC 0.35-μm 4M2P standard CMOS process, occupying 4.8 mm^2. Fig. 6.20 shows the QMPM chip micrograph with floor planning of each block. Full characterization of the QMPM chip is our future plan.

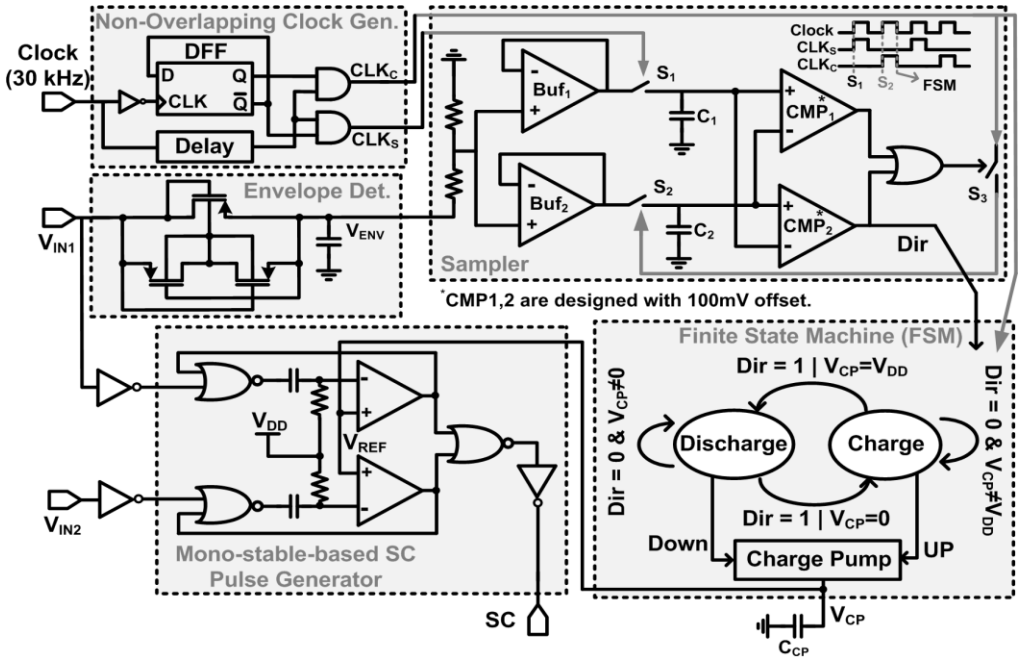

Fig. 6.19. Schematic diagrams of the ADCC block.

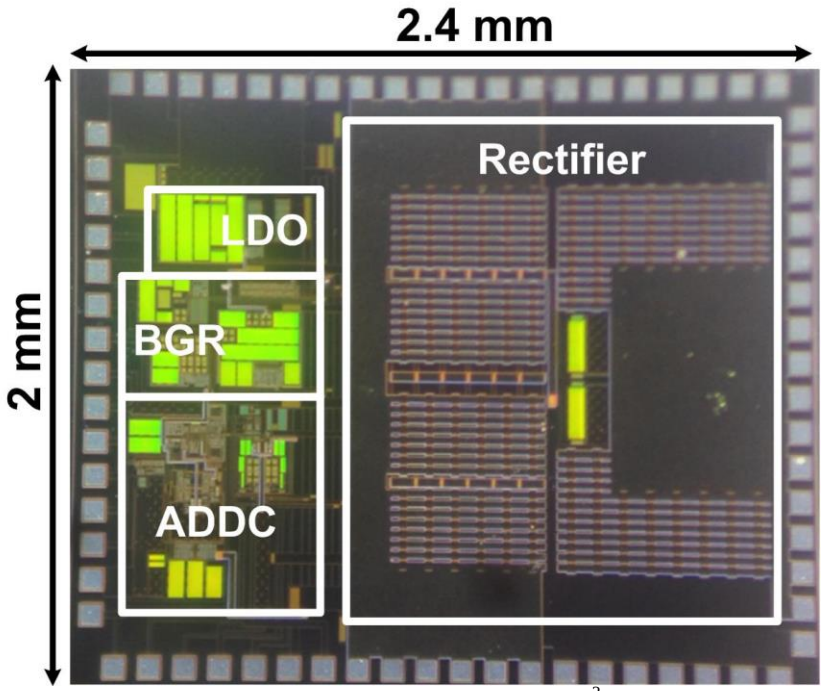

Fig. 6.20. QMPM die micrograph and floor plan occupying 2×2.4 mm^2.

CHAPTER VII

LOW-POWER WIDEBAND DATA COMMUNICATION

In this chapter two novel modulation techniques are presented for low-power, wideband data communication in near-field and far-field regions. The pulse delay modulation (PDM) technique that takes advantage of impulse-radio ultra wideband (IR-UWB) in near-field domain offers a robust dual-band power and data transmission link. The novelty is to use the power carrier interference in such dual-band link to transmit data. A pulse-width modulation (PWM) IR-UWB technique is also presented to further reduce the power consumption of the far-field UWB transmitters.

7.1. Pulse-delay Modulation (PDM)

The majority of modulation techniques that have been devised for near-field data transmission modify the amplitude, frequency, or phase of a sinusoidal carrier signal based on the data to be transferred across the inductive link. Amplitude shift keying (ASK), frequency shift keying (FSK), load shift keying (LSK), and binary/quadrature phase shift keying (BPSK/QPSK) are examples of such methods [56], [59], [62]-[65], [105]. The use of power carrier signal along with these methods was attractive in the early IMDs because the same inductive link could be used for both power and data transmission.

In high-performance IMDs that require wider bandwidth, however, a separate power carrier from the data carrier is preferred because increasing the frequency of the high amplitude power carrier can lead to unsafe temperature elevation due to excessive power loss in the tissue. To achieve high power transfer efficiency (PTE) and high data rate, a high frequency carrier (> 50 MHz) is required for the data link while the power carrier frequency should be kept below 20 MHz [57]. This has led to the use of dual-carrier power/data links with each carrier linking a separate pair of coils [62]-[64], [105].

A major challenge in dual-carrier designs is the cross-coupling between the two pairs of coils, which need to be miniaturized and co-located inside the IMD. In particular, the strong power carrier interference can dwarf the weak data signal on the receiver (Rx) side and make data recovery quite difficult, if not impossible. In other words, to achieve a low bit-error-rate (BER), a large signal-to-interference ratio (SIR) is needed. While innovative coil designs can help with reducing the coils' cross-coupling [106]-[108], it is still necessary to filter out the power carrier interference at the Rx input electronically at the cost of adding to the power consumption and complexity of the IMD [109]. Moreover, achieving high data rates via traditional modulation schemes requires power consuming frequency-stabilization RF circuits, such as phase-locked loops (PLL), which are not desired on the IMD side.

The data carrier was recently substituted with a series of narrow pulses in near-field, similar to far-field IR-UWB, to further reduce the transmitter (Tx) power consumption and increase the data rate [66]-[70]. Unfortunately, none of these methods are robust against strong power carrier interference, i.e. they operate only when the SIR at Rx input is high. Hence, there is a need for low-power, wideband, and low BER data transmission links that can withstand simultaneous power transmission within the small space available inside the IMD.

This was the motivation behind a new carrier-less data transmission scheme, called Pulse Delay Modulation (PDM), for near-field simultaneous data and power transmission. PDM saves the power and space needed for filtering out the power carrier interference on the Rx side, and at the same time enjoys power saving properties of the near-field IR-UWB, particularly on the Tx side, by eliminating the data carrier. The key improvements of PDM compared to the state-of-the-art in simultaneous wireless data and power transmission across an inductive link include: 1) increasing data rate, 2) reducing both Tx and Rx power consumption and die area, and 3) improving robustness against power carrier interference by reducing the required SIR to achieve the same BER.

7.1.1. PDM Theory and Operation

Inside the PDM Tx, shown in the left dashed box in Fig. 7.1, a clock generator block creates two non-overlapping clocks from an external master clock signal, Tx-Clk, at the desired carrier frequency, f_p, for a class-D power amplifier (PA), which generates the power carrier signal at a desired output power level that can be adjusted by its supply voltage, PA_V_{DD}. The power carrier is delivered to L_1 after passing through a 50 Ω matching circuit to induce current in L_2. Using the same Tx-Clk, a pulse pattern generator (PPG) generates two narrow pulses, which are in sync with the power carrier and spaced by half a power carrier cycle, $T_p/2$, for each Tx-Data bit "1". No pulses are generated for Tx-Data bit "0". The LC driver circuit transmits each pulse across L_3-L_4 data link. Each data pulse generates a decaying ringing response at a carrier harmonic frequency that the L_4C_4-tank is tuned at. Within every data bit "1" period, ringing from these two pulses alter the timing of the power carrier interference zero-crossings across L_4C_4-tank, which is induced through k_{14} and k_{24} cross couplings.

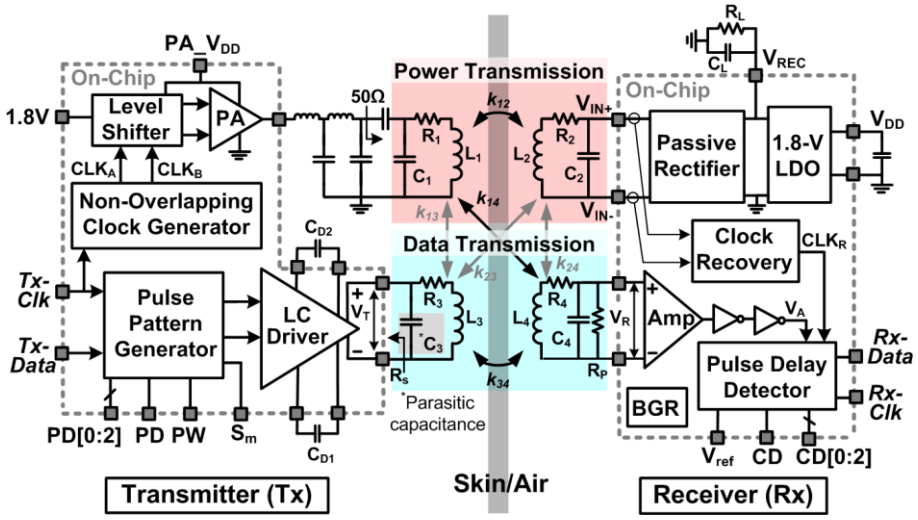

Fig. 7.1. Block diagram of the wireless power and data transmission circuit across a dual-band inductive link using the Pulse Delay Modulation (PDM) scheme. The first prototype PDM transceiver ASIC includes all the blocks inside the Tx and Rx dashed boxes. Direct (k_{12} and k_{34}) and cross (k_{13}, k_{14}, k_{23}, and k_{24}) couplings across two pairs of coils are also presented.

Inside the Rx block, which is the right dashed box in Fig. 7.1, a passive full-wave rectifier is followed by a 1.8 V low drop-out (LDO) regulator to provide the IMD power

supply, V_{DD}. A clock recovery circuit extracts the internal IMD clock, CLK_R, from the received power carrier across L_2C_2-tank. V_R is the Rx input signal across L_4C_4-tank and the superposition of the power carrier interference through k_{14} and k_{24} and PDM pulses through k_{34}. V_R is amplified to create a square waveform, V_A, and then a pulse delay detector integrates the time shifts between V_A and CLK_R to recover the received data bit stream.

In the PDM data link in Fig. 7.1, since k_{34} is relatively small, we can neglect the effect of the L_4C_4-tank on the L_3C_3-tank to simplify the inductive link equations. The pulse generator in Fig. 7.1 can be modeled by a voltage source in series with output resistance, R_s, driving L_3C_3-tank. L_4C_4-tank is tuned at f_d, while the L_3C_3-tank can be either tuned at f_d or left at its self-resonance frequency (SRF), in which case C_3 in Fig. 7.1 represents the parasitic capacitance of L_3. The inductive data link transfer function in the S-domain i.e. the ratio of the voltage across the L_4C_4-tank, V_R, to the LC driver output, V_T, can be described as,

$$H_{34}(s) = \frac{M_{34}s}{(R_sL_3C_3s^2 + (R_sR_3C_3 + L_3)s + R_s + R_3)(L_4C_4s^2 + R_4C_4s + 1)} \tag{7.1}$$

where all circuit parameters are the lumped elements in Fig. 7.1 and $M_{34} = k_{34} \times (L_3L_4)^{0.5}$ is the mutual inductance between L_3 and L_4. $H_{34}(s)$ is composed of two 2nd-order terms, one originating from the data Tx and the other from the data Rx tanks, each of which can be expressed as,

$$\frac{1}{s^2 + 2\zeta\omega_n s + \omega_n^2} = \frac{1}{(s + s_1)(s + s_1^*)},\ s_1 = \zeta\omega_n + j\omega_d,\ 0 \le \zeta < 1 \tag{7.2}$$

where ζ is the damping ratio, ω_n is the natural frequency, and $\omega_d = \omega_n \times (1\text{-}\zeta^2)^{1/2}$ is the natural damping frequency of the system. From (7.1) and (7.2), these 2nd-order system parameters can be expressed in terms of the lumped circuit elements in Fig. 7.1,

$$\zeta_1\omega_{n_1} = \frac{(R_sR_3C_3 + L_3)}{2R_sL_3C_3} \cong \frac{1}{2R_sC_3},\quad \omega_{n_1}^2 = \frac{R_s + R_3}{R_sL_3C_3} \cong \frac{1}{L_3C_3}\ , \tag{7.3}$$

$$\zeta_2\omega_{n_2} = \frac{R_4}{2L_4},\ \ \omega_{n_2}^2 = \frac{1}{L_4C_4}. \tag{7.4}$$

Assuming both 2nd-order systems are under damped, $\zeta_1 < 1$ and $\zeta_2 < 1$, which is often the case for LC-tanks used in data telemetry links, (7.1) can be rearranged as,

$$H_{34}(s) = \frac{M_{34}s}{R_sL_3C_3(s+s_1)(s+s_1^*)\times L_4C_4(s+s_2)(s+s_2^*)}, \tag{7.5}$$
$$s_j = \zeta_j\omega_{n_j} + j\omega_{d_j},\ j = 1,2$$

Now we can break $H_{34}(s)$ up into the sum of its first order components,

$$H_{34}(s) = \left[\frac{A_1}{(s+s_1)} + \frac{A_1^*}{(s+s_1^*)} + \frac{A_2}{(s+s_2)} + \frac{A_2^*}{(s+s_2^*)}\right], \tag{7.6}$$

where,

$$A_1 = \frac{-M_{34}s_1}{R_sL_3C_3(s_1^*-s_1)\times L_4C_4(s_2-s_1)(s_2^*-s_1)} = a_1 + jb_1, \tag{7.7}$$

$$A_2 = \frac{-M_{34}s_2}{R_sL_3C_3(s_1-s_2)(s_1^*-s_2)\times L_4C_4(s_2^*-s_2)} = a_2 + jb_2, \tag{7.8}$$

and apply the inverse Laplace transform to find the impulse response for the inductive link,

$$h_{34}(t) = 2e^{-\zeta_1\omega_{n_1}t}(a_1\cos(\omega_{d_1}t) + b_1\sin(\omega_{d_1}t)) + 2e^{-\zeta_2\omega_{n_2}t}(a_2\cos(\omega_{d_2}t) + b_2\sin(\omega_{d_2}t)). \tag{7.9}$$

This response is a ringing, which envelope builds up rapidly with $1/\zeta_1\omega_{n1}$ but decays slowly with $1/\zeta_2\omega_{n2}$ [66].

The impulse response of the power interference link due to k_{14}, i.e. $H_{14}(s)$, can be found from (7.5) by substituting L_3C_3-tank circuits parameters and M_{34} with L_1C_1-tank parameters and M_{14}, respectively. Because the voltage across L_1 is much larger than that of L_2, we can safely neglect the effect of L_2C_2-tank on the L_4C_4-tank through k_{24}. Therefore, the amplitude and phase of the power carrier interference across the L_4C_4-tank, i.e. the power carrier component of V_R, can be calculated using $|H_{14}(j\omega_p)|$ and $\angle H_{14}(j\omega_p)$, respectively, where $\omega_p = 2\pi f_p$.

Considering that L_1C_1 and L_2C_2 are both high-Q and tuned at f_p, the induced power carrier on the L_2C_2-tank is much stronger than that of the low-Q L_4C_4-tank. Therefore, the transmitted data pulses do not have any noticeable effects on the power transmission link. Since no pulses are transmitted for a bit "0", any delay between signals across L_4C_4- and L_2C_2-tanks represent a bit "1", which can be easily detected using a simple phase detector circuit after sharpening the received waveforms.

Using the inductive link impulse responses, one can calculate V_R in Fig. 7.1. Instead of a data carrier for each data bit "1", two narrow pulses, equal but opposite in amplitudes with $t_{pw} \leq \sqrt{2}/\pi f_d$ and spaced by $T_p/2 = 1/2f_p$, are transmitted across L_3C_3-tank. These pulses initiate ringing patterns across L_4C_4-tank based on (7.9), as shown in Fig. 7.2. To minimize inter-symbol-interference (ISI) within consecutive "1"s, it is important for these ringing to dampen quickly. It can be seen from (7.9) and (7.4) that increasing $\zeta_2\omega_{n2}$, which is proportional to R_4, helps damping the ringing faster. Therefore, Q_4 of the L_4C_4-tank in Fig. 7.1 is intentionally reduced by increasing R_4.

When present, the abovementioned data pulse ringings change the shape of the received power carrier interference across L_4C_4-tank. To facilitate the detection of these changes, our solution is to select the timing of the data pulses at V_T in a way that they alter the zero-crossing times of the interfering sinusoidal power carrier, which are the most sensitive points of the signal to an external disturbance. Hence, the Tx pulses for every bit "1" are applied at the beginning and in the middle of every bit period in sync with the power carrier, and after a specific delay, t_d, which is selected such that the voltage peaks of the data ringing at V_R coincide with the original zero-crossing times of the power carrier interference at V_R. The result is a shift in the V_R zero-crossings in a certain direction for bit "1", as shown Fig. 7.2. The PPG block in Fig. 7.1 sets t_d at,

$$t_d = nT_p + \frac{\angle H_{14}(j\omega_p)}{\omega_p} - \frac{\angle H_{34}(j\omega_d)}{\omega_d} - \frac{3}{4f_d} + t_{PA} \ , \tag{7.10}$$

where n is an integer number, $\angle H_{14}(j\omega_p)/\omega_p$ and $\angle H_{34}(j\omega_d)/\omega_d$ are the delays for power

carrier interference and data pulses from L_1 to L_4 and L_3 to L_4, respectively, and t_{PA} is the total delay from the Tx-Clk to the power carrier across L_1C_1-tank in Fig. 7.1.

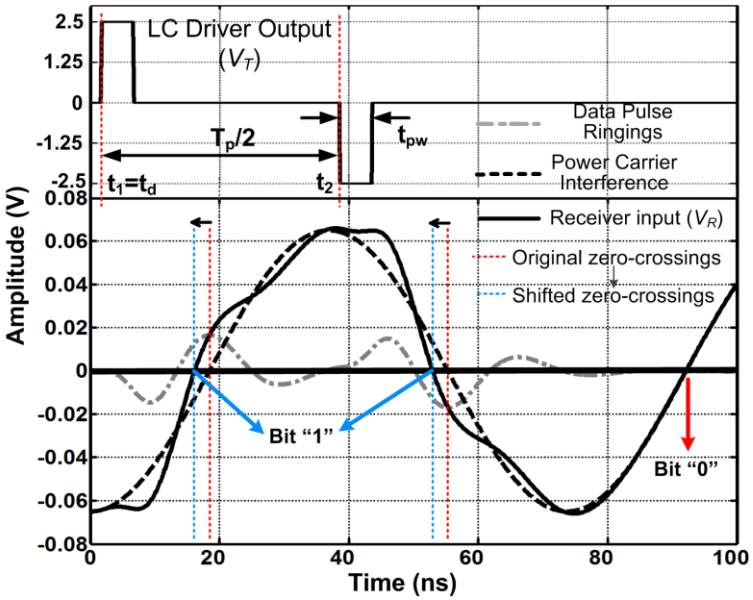

Fig. 7.2. PDM key waveforms simulated in MATLAB. The inductive link specifications can be found from Table 7.1.

Fig. 7.2 shows the transient simulation results of the simplified PDM model in Fig. 7.1, based on (7.9) and the dual-carrier inductive link specifications in Table7.1. The power carrier across L_1C_1-tank in this simulation was a 50 $V_{P\text{-}P}$ sinusoid with 90° phase shift at f_p = 13.56 MHz. V_T in Fig. 7.1 is shown on the top trace in Fig. 7.2 with two t_{pw} = 5 ns pulses with equal but opposite 2.5 V amplitudes at $t_1 = t_d$ = 1.6 ns and $t_2 = t_d + T_p/2$ = 38.4 ns delay times with respect to the negative peak of the power carrier interference. The resulting signal across L_4C_4- tank, shown in dashed gray, demonstrate how these f_d = 50 MHz ringings dampen rapidly by t = ~35 ns and t = ~70 ns before the beginning of the next pulse due to the lowered Q_4 = 5.

Without data pulse ringing, the induced power carrier interference across L_4C_4-tank is a clean sinusoid, which is the dashed black waveform labeled as Power Carrier Interference in Fig. 7.2. The actual received signal, V_R, however, which is shown in solid black, results from the superposition of the data and power components. It can be seen

that PDM has shifted the zero-crossings of the superimposed waveform, V_R, for a bit "1" by 2.5 ns to the left from $t_{zc1(0)}$ = 18.4 ns and $t_{zc2(0)}$ = 55.3 ns in the dashed waveform to $t_{zc1(1)}$ = 15.9 ns and $t_{zc2(1)}$ = 52.8 ns in the solid waveform, respectively.

Considering that L_1C_1 and L_2C_2 tanks are both high-Q and tuned at f_p for efficient power transmission, the induced power carrier on L_2C_2-tank is much stronger than that from L_3C_3 and L_4C_4 tanks. Therefore, the transmitted data pulses do not have any noticeable effects on the power link and the recovered clock signal, CLK_R. Since no pulses are transmitted for data bit "0", the delay between zero-crossings of signals across L_4C_4 and L_2C_2 tanks would be a clear representation of data bit "1", which can be detected by the pulse delay detector circuit in Fig. 1 to recover the serial data bit stream, Rx-Data.

7.1.2. PDM Transceiver Architecture

The PDM transceiver prototype was designed to operate at 13.56 MHz within the industrial-scientific-medical (ISM) band. In the PDM power Tx, a class-D power amplifier (PA), which schematic diagram is shown in Fig. 7.3, drives L_1 through a 50 Ω matching circuit. The PA is driven by a pair of non-overlapping clocks to avoid instantaneous large currents in the output stage transistors, N_1 and P_1, which operate as switches with 4 Ω on resistance. The PA supply, PA_V_{DD}, is adjustable from 1.8 V to 5 V to control the PA output power up to 340 mW. A pair of level shifters at the PA input converts the non-overlapping clocks from 1.8 V to the PA_V_{DD} level.

The PDM data transmitter, which schematic is shown in Fig. 7.4, includes a pulse pattern generator (PPG) and an LC driver. During each T_p period, the PPG block in Fig. 7.4a generates two pulses (S_1 and S_2) with adjustable width and delay for data bit "1", which are spaced at T_p/2, and none for bit "0". Therefore, the data rate (*DR*) in this PDM implementation is always the same as f_p. The width of data pulses, t_{pw}, is continuously adjustable from 3-8 ns via the PW input node. The data pulse delay, t_d, is accurately

adjustable from 5-71 ns to compensate for process variations by a combination of a coarse delay, controlled by three binary-weighted bits ($PD_{0\text{-}2}$) from 0-56 ns with 8 ns steps, and a fine delay, controlled by an analog input (PD), from 5-15 ns. The coarse delay is generated by accumulating propagation delays of a series of capacitively- loaded inverters. The parasitic capacitances of two PMOS transistors, M_P, which vary with their gate voltage, PD, generate the fine delay. S_1 and S_2 are combined in an OR gate to generate S_m in Fig. 7.4a, which is used for monitoring.

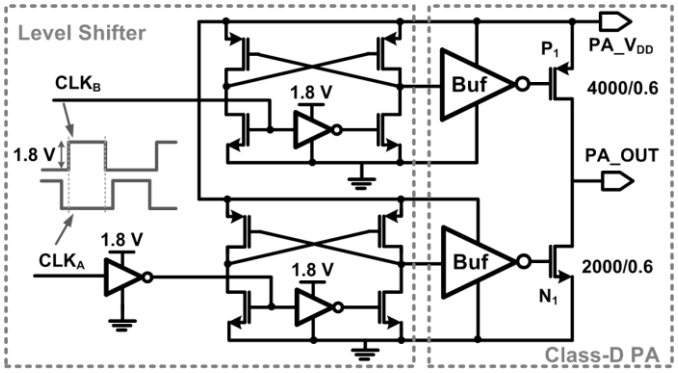

Fig. 7.3. Schematic diagram of the class-D PA followed by the level shifter. The maximum PA output power is 340 mW when PA_V_{DD} = 5 V.

Fig. 7.4b shows the schematic diagram of the novel LC driver, which is capable of quadrupling the supply voltage, V_{DD}, across the Tx data coil, L_3, which is twice the conventional H-bridge drivers. For each data bit "0", $S_1 = S_2 = 0$, $T_{1,2}$ and $P_{1,2}$ turn on, and $N_{1,2}$ turn off. Therefore, both L_3 nodes are connected to V_{DD} and off-chip C_{D1} and C_{D2} capacitors are charged to V_{DD} via $P_{1,2}$, as shown on the top of Fig. 7.4c. In this condition, no current passes through L_3 and no voltage change is induced across the L_4C_4-tank. For each data bit "1", after a delay of t_d, S_1 toggles to "1" for t_{pw}, during which P_2 and T_1 turn off, N_1 turns on, and C_{D2} is in series with L_3 while the left node of L_3 is connected to ground via N_1. Therefore, as shown in the middle of Fig. 7.4c, the voltage across L_3 increases to $2\times V_{DD}$ and its current, i_3, starts ramping up (from right to left) at a rate of $di_3/dt = 2\times V_{DD}/L_3$, if we ignore the voltage drops across N_1 and T_2 in this simplified analysis. The di_3/dt is responsible for inducing a voltage across L_4C_4-tank, which is the

data part of $V_R = M_{34}di_3/dt \propto 2\times V_{DD}$. To end the first pulse, S_1 is toggled back to "0", at which time T_1 shorts the left node of L_3 to V_{DD} and provides a path for i_3 to return back to zero without causing undesired ringing. After a delay of $T_p/2$, S_2 toggles to "1", resulting in a current pulse in L_3, similar to that of S_1 but in the opposite direction (left to right), as shown in the bottom of Fig. 7.4c. In the driver circuit, $P_{3\text{-}6}$ dynamically bias the bulks of $P_{1,2}$ to the highest voltage to avoid current flow in the bulk.

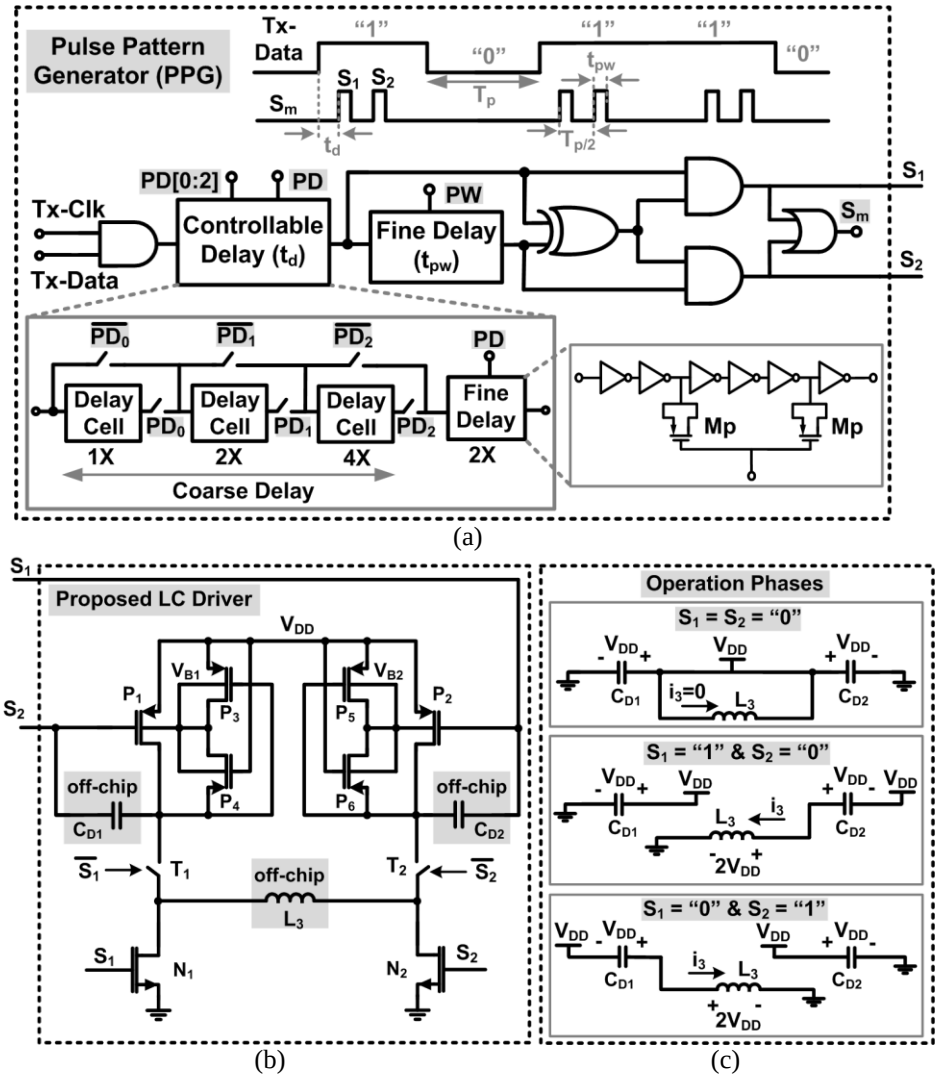

Fig. 7.4. Schematic diagram of the data Tx block in the PDM transceiver. (a) The pattern pulse generator (PPG) block generates two pulses with $T_p/2$ spacing, which width (t_{pw}) and delay (t_d) are adjustable. (b) The LC driver applies narrow pulses across L_3, which amplitudes are twice the conventional H-bridge drivers. (c) Three operating phases of the proposed LC driver. C_{D1} and C_{D2} are 100 pF off-chip capacitors.

By doubling the voltage across L_3 in each direction, the proposed LC driver can

improve the communication range and robustness of inductively powered telemetry links, especially those designed in low-voltage technology nodes. It should be noted that in this design, since S_2 is already out-of-phase with respect to S_1, resulting in i_3 flowing in opposite directions, the induced data pulse ringings across L_4C_4-tank also have opposite polarity, and change the zero-crossing times of power carrier interference in the same direction, as shown in Fig. 7.2.

Fig. 7.5 shows the schematic diagram of the full-wave passive rectifier in the PDM power receiver with self-threshold-cancellation scheme [102]. In this scheme, initially V_{REC} reaches V_{INR} - $V_{Th(P2)}$ through P_2, leading to $V_C = V_{REC}$ - $V_{Th(P3)} = V_{INR}$ - $2V_{Th(P2,3)}$. Since $V_{SG(P1)} = V_{INR}$ - $V_C = 2V_{Th(P2,3)} > V_{Th(P1)}$, P_1 is pushed into triode, and V_{REC} is charged up until V_C becomes V_{INR} - $V_{Th(P1)}$. Therefore, V_{REC} finally reaches V_{INR} - $V_{Th(P1)}$ + $V_{Th(P3)}$, which means that P_{1-3} play the role of a diode with effective voltage drop of $V_{Th(P1)}$ - $V_{Th(P3)}$. This significant reduction in the threshold voltage improves the power conversion efficiency (PCE). N_1, N_2, P_4, and P_5 are used for full-wave rectification.

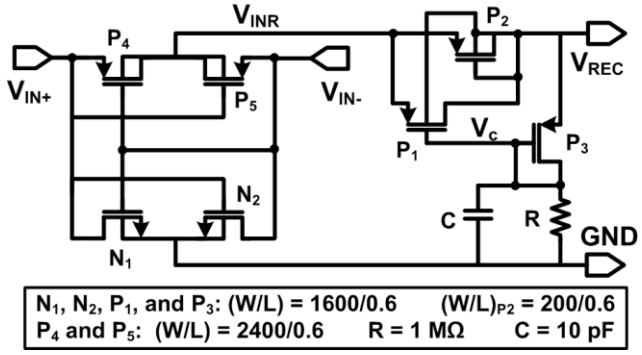

Fig. 7.5. Schematic diagram of the full-wave passive rectifier with self- threshold-cancellation scheme. In this circuit, P_{1-3} play the role of a diode with effective voltage drop of $V_{Th(P1)}$ - $V_{Th(P3)}$, which improves the PCE.

In the data Rx block in Fig. 7.1, V_R is amplified by a high gain amplifier followed by two inverters to create a square waveform, V_A. A pulse delay detector is then used to detect the phase shift (delay) between V_A and the recovered clock from the L_2C_2-tank (CLK_R) to detect "1"s and "0"s in the data bit stream. Fig. 7.6 shows the schematic diagram of the pulse delay detector with its key internal node waveforms. First, the delay

between V_A and CLK_R is detected by an XOR gate, which is represented by V_{PD}. During one T_p, an integrator accumulates the energy inside V_{PD} pulses by charging a capacitor, C = 1.1 pF, with I = 100 µA. The integrator output, V_{INT}, is then compared with an externally-adjustable reference voltage, V_{ref}, to detect data bit "1". V_{ref} is adjusted such that the integrator output is greater than V_{ref} for "1"s and smaller than V_{ref} for "0"s. V_A and CLK_R are also combined in a NOR gate to generate the reset signal, V_{RST}, to discharge C and prepare the integrator for the next data bit. To recover short pulses at the comparator output, a D-type flip flop is clocked at the rising edge of V_{RST}. Therefore, Rx-Data is ready to be sampled at the rising edge of the Rx-Clk.

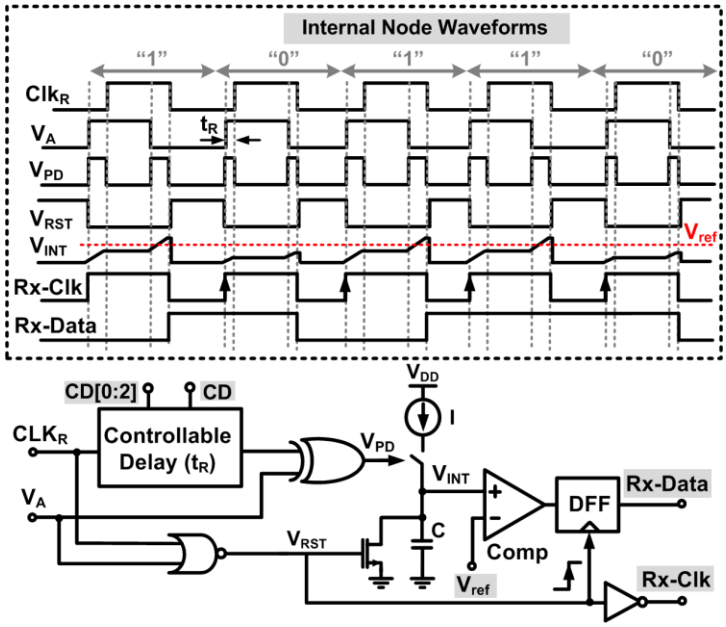

Fig. 7.6. Schematic diagram of the pulse delay detector with its operating waveforms to recover the data bit stream and clock. Rx-Data is ready to be sampled at the rising edge of the Rx-Clk as shown in the waveforms. A small delay (t_R) between CLK_R and V_A is required to set the integrator output, V_{INT}, within the input common mode range of the comparator. t_R is continuously adjustable from 5-71 ns to compensate for process variations by a combination of fine and coarse delays, controlled by CD and CD[0:2], respectively.

Figs. 7.7a and 7.7b show the schematic diagrams of the PDM Rx amplifier in Fig. 7.1 and the high speed comparator in Fig. 7.6, respectively. Because nMOS differential pair is used in the comparator, a small delay between CLK_R and V_A, t_R in Fig. 7.6 inset, is required for the data bit "0" to set V_{INT} within the input common mode range (ICMR) of the comparator. A controllable delay with a circuit diagram identical to the one in Fig. 7.4

generates t_R. The amplifier gain is 22.5 dB at f_d = 50 MHz and the static power consumptions of the amplifier and comparator are 156 µA and 127 µA, respectively.

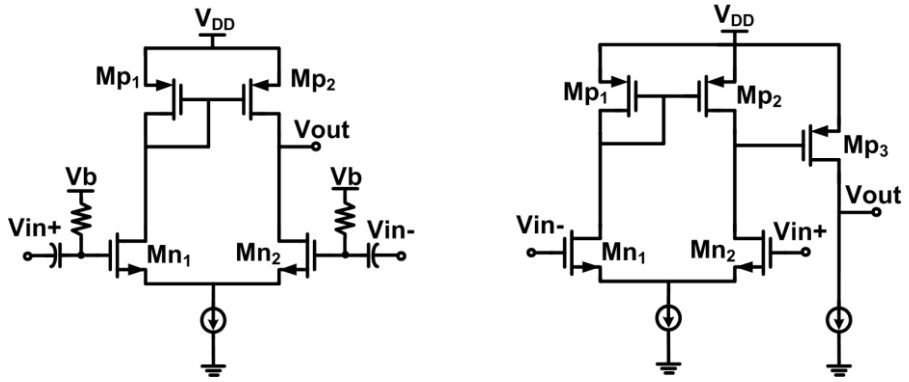

Fig. 7.7. Schematic diagrams of (a) Rx amplifier in Fig. 1 with 22.5 dB gain at f_d = 50 MHz. (b) Rx comparator in Fig. 7.6. The static power consumptions of the amplifier and comparator are 156 µA and 127 µA, respectively.

7.1.3. Measurement Results

The PDM transceiver prototype, shown in Fig. 7.8, was fabricated in a 0.35-µm 2P4M standard CMOS process, occupying 1.6 mm^2 of chip area. Two PDM chips were used in our experimental setup, shown in Fig. 7.9. They were wirebonded to QFN packages mounted on 2-layer FR4 printed circuit boards (PCBs). Each PCB included a planar figure-8 coil for data transmission as shown in Fig. 7.9 inset [105]. The geometries of a printed spiral coil in the Tx and a wire-wound coil in the Rx were optimized at 13.56 MHz for power transmission [34]. L_1 and L_2 were glued onto L_3 and L_4, respectively, following careful alignment to minimize undesired cross couplings between power and data coils, k_{13} and k_{24}. The specifications of power and data coils are summarized in Table 7.1.

At PA_V_{DD} = 5 V, which is the maximum voltage in this process, the class-D PA delivered 340 mW to a 50 Ω load with measured 61.8% power efficiency at f_p = 13.56 MHz. Fig. 7.10a shows the passive rectifier measured input and output voltage waveforms when loaded by C_L = 10 µF and R_L = 0.4 kΩ. In this condition, for V_{REC} = 2.5

V, the peak of the 13.56 MHz carrier was 3.6 V. Fig. 7.10a also shows the regulator output, V_{DD} = 1.8 V, across a 10 µF capacitor. The maximum ripple on V_{DD} was 50 mV, which was acceptable in our digital-based Rx. Fig. 7.10b shows the rectifier measured PCE vs. R_L at 13.56 MHz for different V_{REC} values. As R_L increases, the voltage drop across rectifier pass transistor i.e. P_1 in Fig. 7.5 reduces, which decreases the rectifier power loss and, therefore, increases the PCE. At high V_{REC} values, PCE is slightly increased because the rectifier voltage drop is relatively smaller. For a wide range of R_L, the rectifier PCE is > 50%.

Table 7.1. Measured power and data coils specifications

Link	Coil	Size (mm)	#Turns	Line Width (mm)	L (nH)	$^{**}R$ (Ω)	f (MHz)	Q	SRF (MHz)	Mutual Coupling (k) ×10^{-3}			
										L_1	L_2	L_3	L_4
Power	L_1	32 × 32	5	2	500	0.5	13.56	85.2	116	-	37	9	6.4
	$^{*}L_2$	10 × 10	3	0.255	195	0.34	13.56	48.8	237	37	-	4.2	8.5
Data	L_3	30 × 30	1	1	165	0.48	50	108	255	9	4.2	-	19
	L_4	10 × 10	1	0.4	56.8	0.44	50	$^{+}$40.5	550	6.4	8.5	19	-

* L_2 was an AWG30 wire-wound coil. ** From measurements at the operating frequency, f.
$^{+}$ Q_4 was reduced to 5 by adding R_P = 100 Ω.

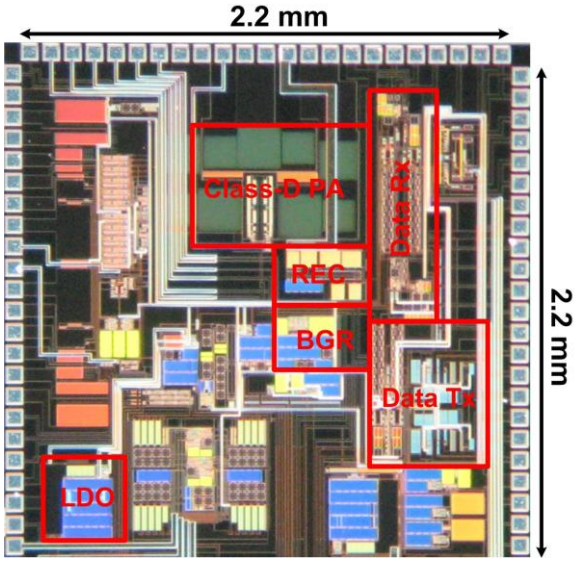

Fig. 7.8. PDM transceiver chip microphotograph occupying 1.6 mm^2.

To measure the wireless link BER, the coils were held in parallel and perfectly aligned using Plexiglas sheets, as shown in Fig. 7.9. The surface-to-surface distance, d, between the two PCBs, each of which had 1.5 mm thickness, was 10 mm. Thus, the

coupling distances for the data and power links were 10 mm and 13 mm, respectively. A pair of Tektronix GB1400 (GigaBERT) were used to generate the random serial data bit stream and synchronized clock, Tx-Data and Tx-Clk in Fig. 7.1, and measure the wireless link BER of the recovered data, Rx-Data, in real time.

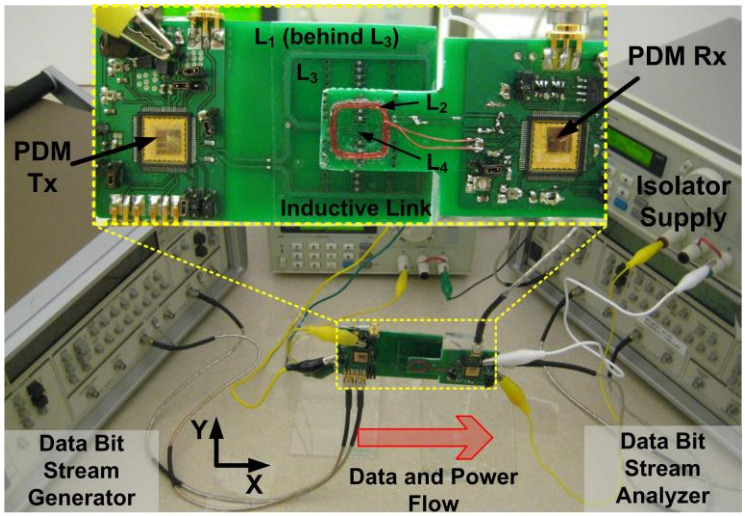

Fig. 7.9. PDM transceiver measurement setup. Inset: inductive links made of printed-spiral and wire-wound coils for power transmission (L_1 and L_2 in Fig. 7.1) and a pair of planar figure-8 coils on FR4 PCB for data transmission (L_3 and L_4 in Fig. 7.1). L_1 was carefully aligned and glued behind L_3 to minimize k_{13}. L_2 was also glued over L_4 with careful alignment to minimize k_{24}.

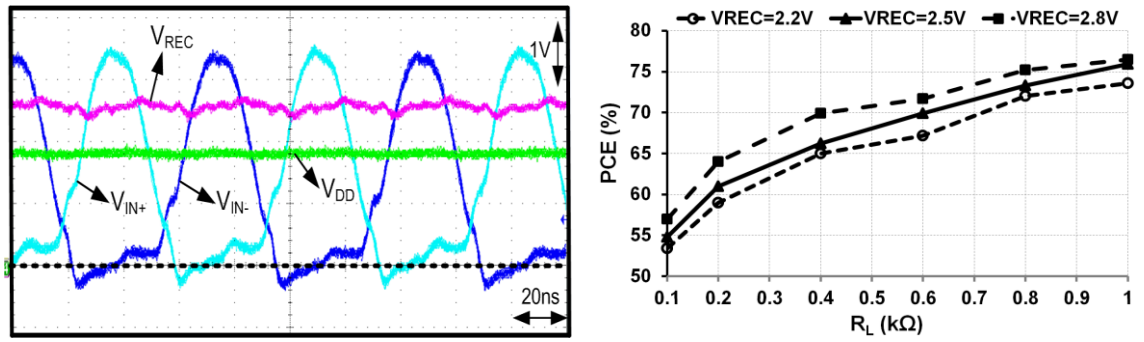

(a) (b)

Fig. 7.10. (a) Passive rectifier measured input and output waveforms at 13.56 MHz when loaded by C_L = 10 µF and R_L = 0.4 kΩ. The regulator output at V_{DD} = 1.8 V has also been shown. (b) Rectifier PCE vs. R_L for different V_{REC} values.

In order to test the link in a truly wireless setup and avoid any ground loops, we used a dual channel voltage isolator (Si8620, Silicon Labs, TX), which was supplied at 2.5 V on the Rx side, to deliver Rx-Data and Rx-Clk to the GigaBERT for BER measurements. The PDM Rx was inductively powered through the on-chip power

management block, which generated the regulated V_{DD} for the rest of the chip. Hence, the Rx PDM chip was completely isolated from the Tx chip. To avoid probing the inductive link directly in observing the effects of PDM on the Rx signal, we used the discrete custom RF amplifier in [66] in addition to the PDM receiver in Fig. 7.9.

In order to achieve the high data rate (*DR*) of 13.56 Mbps, the data ringing across L_4C_4-tank initiated by each Tx pulse had to be suppressed within $T_p/2$ = 36.8 ns. With a large Q_4, the data ringing will have a slow decaying pattern and multiple cycles should be dedicated during $T_p/2$ by tuning L_4C_4-tank at $f_d >> 2f_p$. However, this method makes PDM more sensitive to variations in t_d as will be discussed later.

Q_4 was reduced to 5 by adding R_P = 100 Ω in parallel with L_4C_4-tank (tuned at f_d = 50 MHz), as shown in Fig. 7.1, to limit the number of data ringing and avoid ISI. Fig. 7.11 from the top shows the transmitted data bits "1" and "0" at 13.56 Mbps, the PPG output (S_m in Fig. 7.4), and different waveforms across the L_4C_4-tank after 20 dB amplifications: data ringing when power carrier was not present, power carrier interference when data ringings were not present, and the superposition of data and power components in the received signal when both power carrier and data pulses are present. The data ringings have shifted the zero-crossings of the power carrier to the left by 2.3 ns. In this measurement, d = 10 mm, t_d = 28 ns, and PA_V_{DD} = 4 V, power link was able to deliver 42 mW of regulated power to the Rx and measured SIR was -18.5 dB. It should be noted that SIR is defined as the ratio of the energy inside data pulse ringings for the data bit "1" to that inside the power carrier interference during one data bit period (T_p).

Fig. 7.12 shows a snapshot of the key measured waveforms in the PDM transceiver setup of Fig. 7.9. From top, the transmitted serial data bit stream at *DR* = 13.56 Mbps, PPG output (S_m in Fig. 7.4), recovered serial data bit stream, and recovered clock are shown at d = 10 mm and SIR = -18.5 dB, when 42 mW of regulated power was delivered to a resistive load.

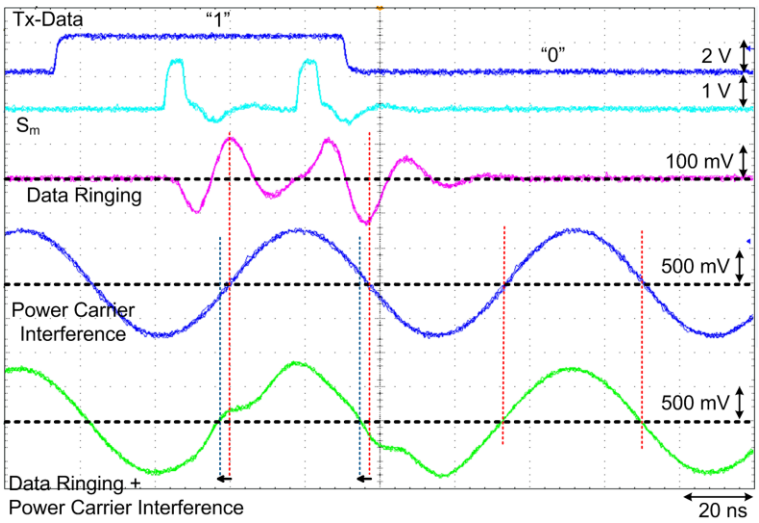

Fig. 7.11. Transmitter waveforms for data bits "1" and "0" at 13.56 Mbps and PPG output (S_m in Fig. 7.4), and L_4C_4-tank waveforms after a 20 dB amplification by a discrete RF amplifier.

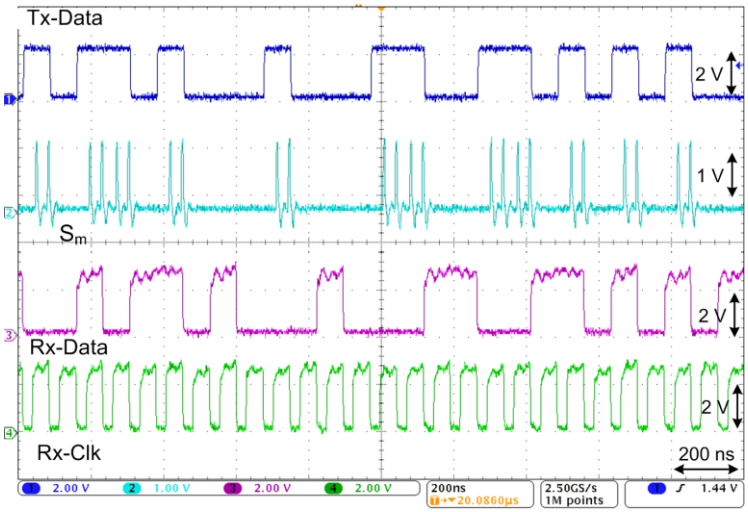

Fig. 7.12. PDM transceiver waveforms from the top: Transmitted serial data bit stream at 13.56 Mbps, the PPG output signal (S_m in Fig. 7.4), recovered data bit stream, and recovered clock. Rx-Data and Rx-Clk were measured through an isolator that was supplied at 2.5 V. d = 10 mm, t_d = 28 ns, t_{pw} = 5 ns, PA_V_{DD} = 4 V, V_{REC} = 2.5 V, V_{dd} = 1.8 V, V_{ref} = 0.9 V, t_R = 4 ns, and SIR = -18.5 dB.

Fig. 7.13a shows the measured BER at 13.56 Mbps for various amounts of power delivered to the load (PDL), while changing d from 4 to 10 mm. These results indicate that if the acceptable BER limit is considered 10^{-6}, this PDM transceiver achieves DR = 13.56 Mbps while delivering 42 mW at d = 10 mm. Fig. 7.13b shows the measured BER values vs. PDL for different d. At d = 10 mm, for PDL > 42 mW, the SIR decreases and leads to higher BER. In these measurements, the data Tx and Rx supply voltages were

constant at 1.8 V while the PA_V_{DD} was swept between 3.3 V and 5 V to achieve different PDL values. The PDM data Tx and Rx power consumptions were 960 pJ/bit and 162 pJ/bit, respectively. Key specifications of the prototype PDM transceiver ASIC are summarized Table 7.2.

Table 7.2. PDM-based transceiver specifications

Technology (TSMC)		0.35-µm 2P4M CMOS
Data transceiver supply voltage, V_{dd}		1.8 V
Class-D PA supply voltage, PA_V_{DD}		1.8-5 V
Power carrier frequency, f_p		13.56 MHz
Data rate, *DR*		13.56 Mbps
Pulse specs: t_d / t_{pw}		28 ns / 5 ns
Bit-error-rate (BER)		4.3×10^{-7}
Nominal coils distance, *d*		10 mm
Nominal delivered power to the load		42 mW
Power consumption (Data)	Tx	960 pJ/bit
	Rx	162 pJ/bit
Area on chip (Power and Data)	Tx	0.88 mm^2
	Rx	0.72 mm^2

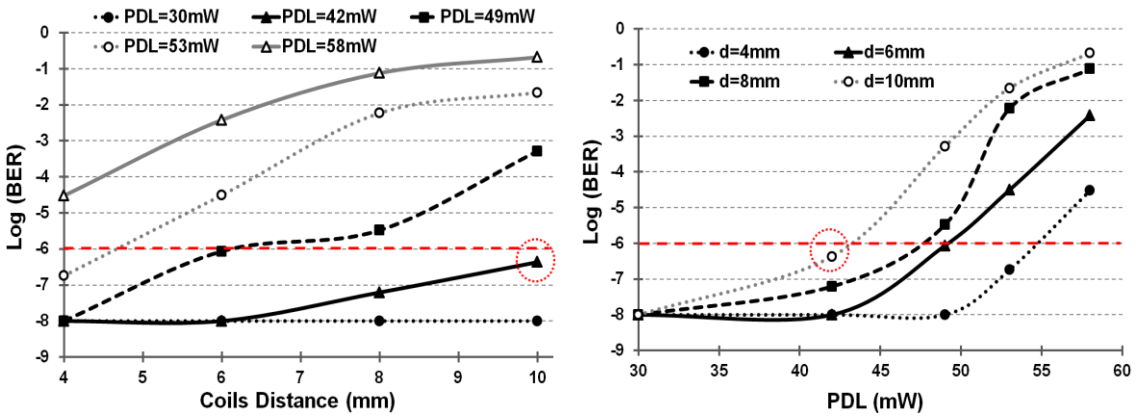

(a) (b)

Fig. 7.13. Measured BER at 13.56 Mbps vs. (a) coupling distance, *d*, for different amounts of power delivered to the load (PDL); (b) PDL for different values of *d*. PA_VDD was swept between 3.3 V and 5 V to adjust PDL, while data Tx supply was constant at 1.8 V and *DR* = 13.56 Mbps.

Fig. 7.14a shows the changes in the BER due to coil misalignments along the X and Y axes at *d* = 10 mm and PDL = 42 mW. These curves show that figure-8 coils are more robust against misalignments along the X-axis (lower BER at the same misalignment) compared to the Y-axis, which is in agreement with our earlier observations in [106], based on variations in the coils' coupling. Fig. 7.14b shows the measured BER vs. SIR across L_4C_4-tank, indicating that for an acceptable BER of 10^{-6},

minimum required SIR for this PDM receiver is about -18.5 dB. At lower SIR, data ringings across L_4C_4-tank have less effect on shifting the zero-crossings of the power carrier interference, leading to smaller variations on the integrator output in Fig. 7.6 for the data bit "1" and higher BER.

Table 7.3 benchmarks PDM against recent methods for simultaneous power and data transmission. To the best of our knowledge, PDM is the first pulse-based technique for simultaneous power and data transmission at high data rates. Our current PDM transceiver can achieve a data rate of 13.56 Mbps with a BER of 4.3×10^{-7} across a 10 mm inductive link. Data Tx and Rx power consumptions under these conditions are only 960 and 162 pJ/bit, respectively, while a separate power link delivers 42 mW of regulated power to the load. Compared to the state-of-the-art [109], we have not only increased the data rate by a factor of 6.7 but also reduced the data Rx power consumption 19 folds. It should be noted that in [63], a first order off- chip low-pass filter (LPF) has been used to improve the SIR to -6 dB while the required SIR for the PDM receiver is -18.5 dB. A 2^{nd}-order LPF has also been used in [109] to further suppress the power carrier interference. The LSK data link in [65] achieved 2.8 Mbps with smaller Tx power consumption. However, LSK can only be used for the uplink while PDM can be used for both up and downlink. Moreover, LSK consumes low power for data transfer at the cost of reducing the PDL by up to 50% at high data rates.

Table 7.3. Benchmarking of recent inductively-powered data telemetry links

Reference	Mod.	*d* (mm)	Data Carrier (MHz)	Power Carrier (MHz)	Data Rate (Mbps)	Tx/Rx Power (pJ/bit)	CMOS Tech. (µm)	SIR (dB)	Die Area (mm^2) (Data Tx/Rx)	V_{DD} (V)	BER
2004, [59]	pcFSK	5	5/10	5/10	2.5	-/152	1.5	-	-/0.29	5	10^{-5}
2005, [62]	BPSK	15	10	10	1.12	-/625	0.18	-	-/0.2	1.8	10^{-5}
2008, [65]	LSK[++]	20	25	25	2.8	35.7/1250	0.5	-	2.2/2.2[**]	2.8	10^{-6}
2012, [105]	FSK	20	-/5	5	1.25	-	0.8	-	-	2.7	-
2012, [105]	BPSK	20	48	5	3	1962/-	0.8	-	2.3[**]	2.7	2×10^{-4}
2010, [64]	QPSK	5	13.56	1	4.16	-	-	-	-	-	2×10^{-6}
2008, [63]	BPSK	15	20	2	2	-/3100	0.35	-12[*]	-/4.4	4.5	10^{-7}
2013, [109][+]	DPSK	-	20	2	2	-	0.18	-	-	1.8	10^{-7}
This Work	**PDM**	**10**	**50**	**13.56**	**13.56**	**960/162**	**0.35**	**-18.5**	**0.34/0.37**	**1.8**	**4.3×10^{-7}**

[*] A 1^{st}-order off-chip filter was used to improve SIR to -6 dB. [**] Including pads.
[+] Second-order filter was used to improve SIR. [++] LSK is only used for uplink.

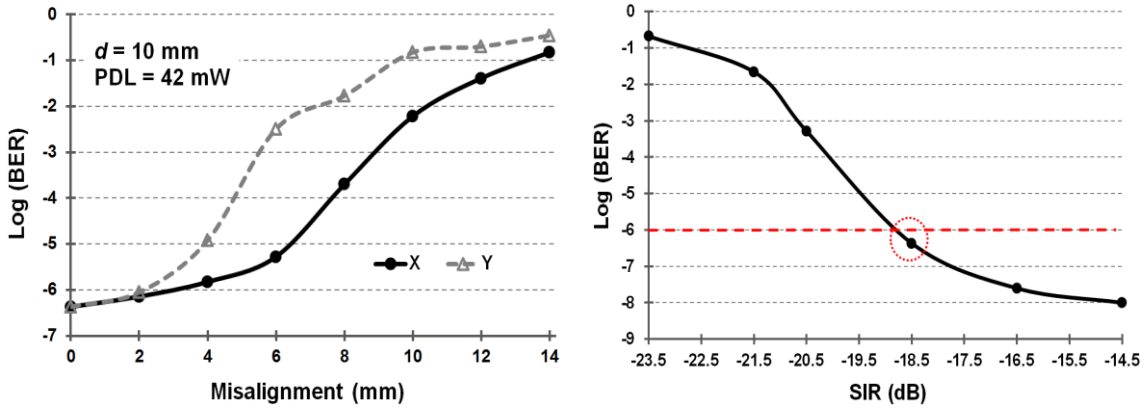

(a) (b)

Fig. 7.14. Measured BER vs. (a) misalignment along X and Y axes (see Fig. 7.9) at d = 10 mm and DR = 13.56 Mbps while 42 mW was delivered to the Rx via L_1-L_2 link, and (b) SIR across L_4C_4-tank. For an acceptable BER of 10^{-6}, minimum required SIR for this PDM receiver is about -18.5 dB.

7.2. PWM-IR-UWB Communication

To address the limitation of high power consumption in wideband neural interfacing, IR-UWB transmission has become more popular recently [110]-[112]. This scheme enables short-range telemetry at high data rates using simple Tx architectures with low-power consumption and small die area. The IR-UWB transmission has been combined with well know modulation techniques such as on-off keying (OOK), pulse-position multiplexing (PPM), and binary-phase shift keying (BPSK), in which a short pulse represents data bit "1" and either nothing in OOK or another short pulse in PPM and BPSK represents data bit "0". Among these modulations, PPM and BPSK are more popular because they maintain synchronization between Tx and Rx especially when many consecutive "0"s need to be transmitted.

In order to further reduce the Tx power consumption, a PWM-IR-UWB is proposed, in which digital data bits are converted to time (digital-time conversion) to create a PWM signal and one pulse per edge is transmitted similar to our WINeR system in [23]. This leads to n times smaller power consumption compared to PPM and BPSK if the PWM signal has n bits of accuracy. We have designed and fabricated a low-power wideband PWM-IR-UWB transceiver in UMC 0.13-µm CMOS process. The IR-UWB

transceiver includes a low-power all-digital Tx and a wideband Rx based on a non-coherent energy-detection (ncED) scheme, which the block diagram is shown in Fig. 7.15. The floor-plan of the chip occupying 1.5 mm^2 is also shown in Fig. 7.16. This chapter focuses on the characterization of the PWM-IR-UWB Tx and the Rx characterization is our future work.

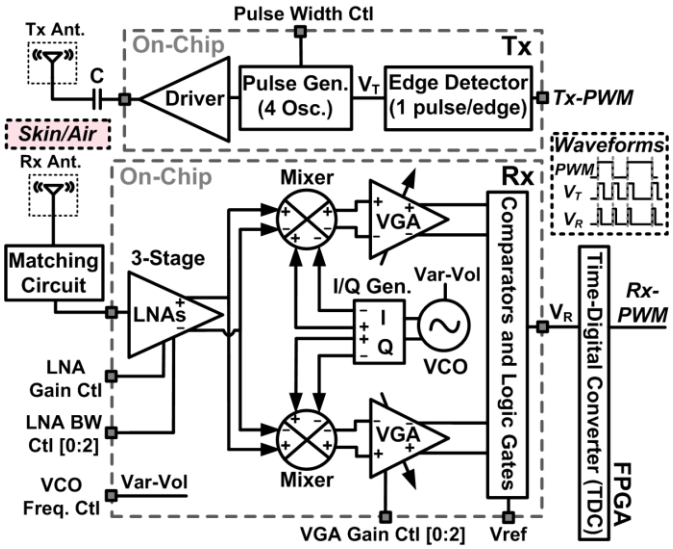

Fig. 7.15. PWM-IR-UWB transceiver block diagram including a low-power Tx and a wideband Rx based on a non-coherent energy detection (ncED) scheme with PWM input.

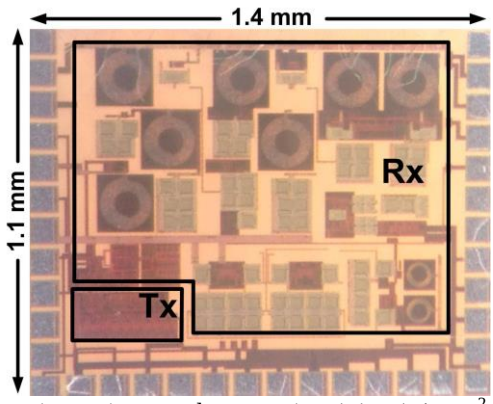

Fig. 7.16. PWM-IR-UWB transceiver micrograph occupying 1.1 × 1.4 mm^2.

In Tx, a digital circuit detects the edges of the PWM signal and a pattern of oscillations is created using a pulse generator. Fig. 7.17 shows the pulse generator schematic diagram including a string of delay-controlled current-starved inverters. In the pulse generator, the input square-wave signal is delayed in 9 steps and the edge of the

signal after each delay step is combined to create a sharp pulse. The current resulted from 8 sharp pulses are then summed in a resistor to create 4 oscillations and amplified by two stages of properly-sized inverter to drive 50-Ω antenna. By adjusting the "Pulse Width Ctl" signal, which controls the current in current-starved inverters, the oscillation frequency could be adjusted.

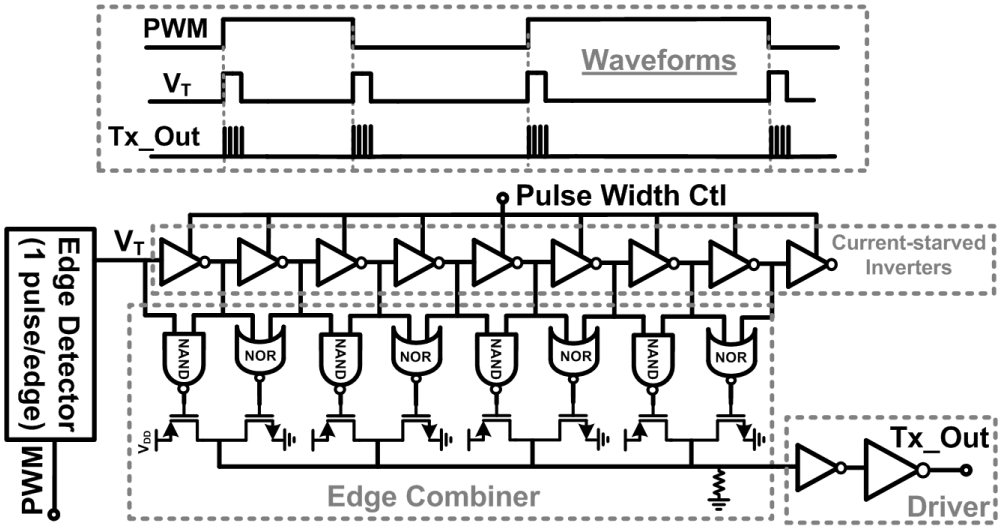

Fig. 7.17. The pulse generator schematic diagram that generates 4 oscillations for the input signal.

Figs. 7.18a and 7.18b show the measured transient and spectrum of the Tx output loaded by a 50 Ω, respectively. The Tx circuit generated 4 oscillations per edge of the PWM input signal with the frequency of 10-MHz (period: 100 ns). The 4 oscillations per one edge are also shown in Fig. 7.18a. The center frequency of the oscillations could be adjusted between 700-MHz to 4.2 GHz. In these measurements, the center frequency was adjusted to 4.2 GHz. The amplitude of the oscillations is ~ 200 mV in average. The power consumption of the Tx circuit for a 10-MHz PWM signal was 0.96 mW from a 1.2-V power supply when the oscillations were tuned to 4.2 GHz. This results in 48 pJ/bit of energy consumption for a digital transmission. Combining the proposed UWB Tx with the PWM-based WINeR system in [23], which has 8 effective number of bits, leads to the energy consumption of 12 pJ/bit, which is two times and four times smaller than that of digital transmission using OOK, and PPM/BPSK, respectively.

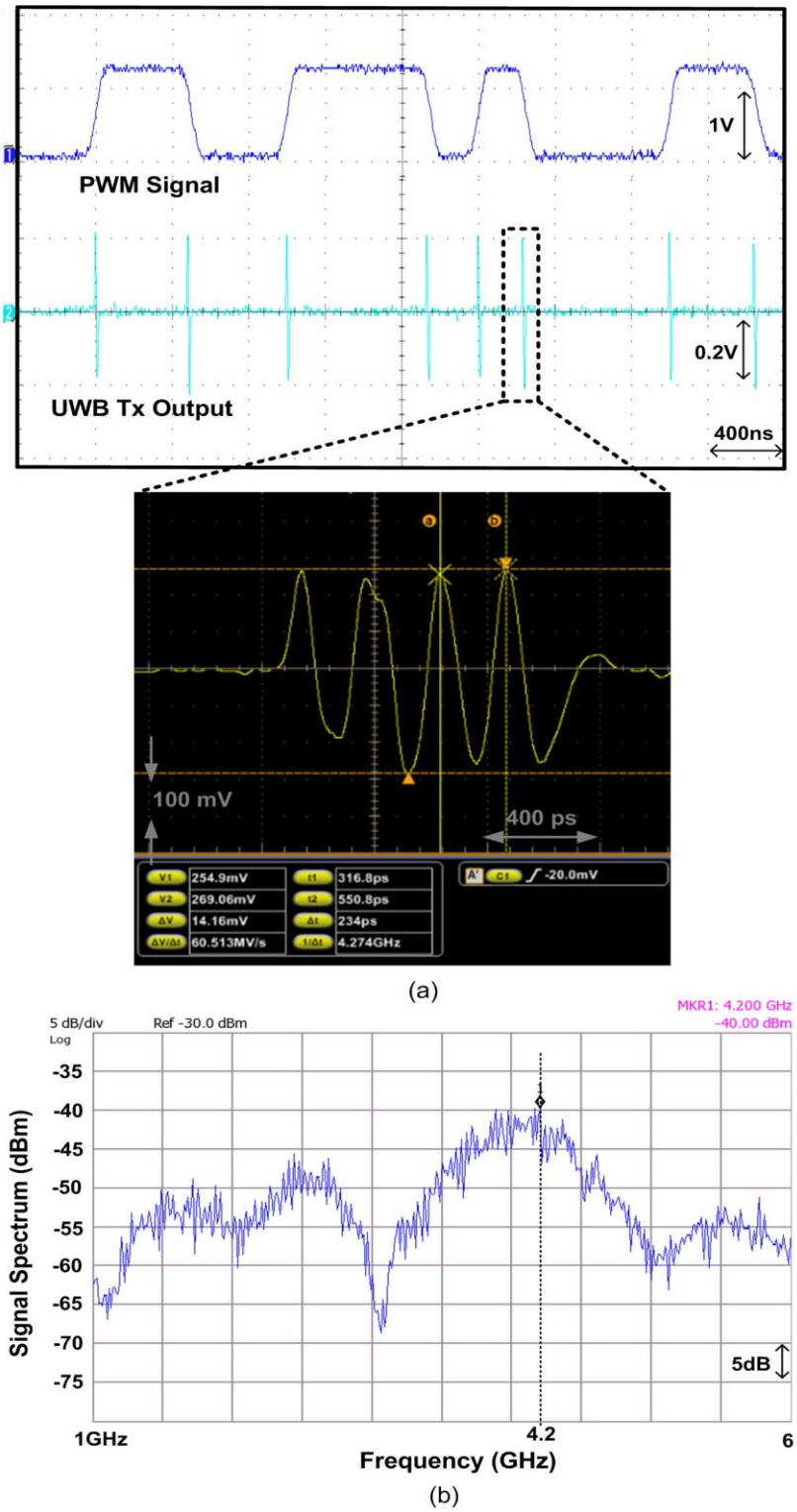

Fig. 7.18. Measurement results of the PWM-IR-UWB Tx (a) The transient waveform of the 10-MHz PWM signal and the Tx output with the 4 oscillations per edge, and (b) The frequency spectrum of the UWB output with 10-MHz PWM signal as the input.

CHAPTER VIII

GENERAL-PURPOSE POWER SUPPLY FOR WIRELESS ELECTROPHYSIOLOGY EXPERIMENTS

The proposed techniques in previous chapters could lead to the design and development of a general-purpose power supply for any wireless electrophysiology experiment on small freely-behaving animal subjects to eliminate batteries for continuous operation. The wireless power supply can be used in the EnerCage system [25], [26] that include an array of coils and power drivers for power transmission and either magnetic sensors or Microsoft Kinect for subject localization as shown in Fig. 8.1.

The proposed general-purpose power supply in the EnerCage system can be used in many experiments that require collecting real-time biological information, such as neural signals, body temperature, blood pressure, physical activities, blood chemical concentrations, and neurotransmitters as well as experiments that require applying uninterrupted electrical, chemical, or mechanical stimulation.

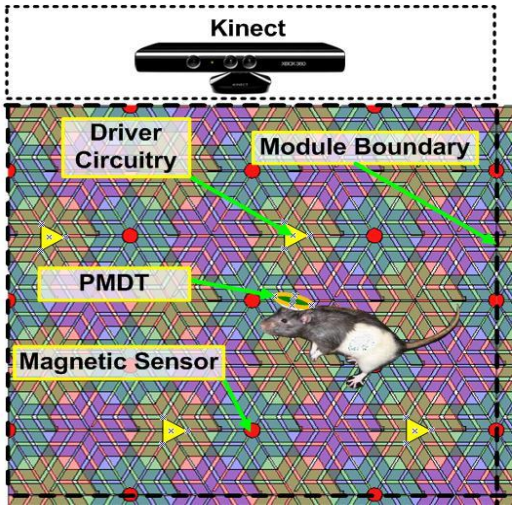

Fig. 8.1. The EnerCage system for wireless powering of neural interfacing devices/systems and any electrophysiology bio-instrument in freely behaving animal experiments [26].

8.1. General-purpose Wireless Power Supply

Although the proposed power supply can be used for any electrophysiology experiment, in this dissertation we have specifically designed and developed the power supply for a multi-channel wireless implantable neural recording and stimulation system called WINeRS-7, which the block diagram is shown in Fig. 8.2. The WINeRS-7 system includes three main blocks: 1) A high-efficiency power management and data transceiver (PMDT) block, 2) 8-channel neural recording analog front-end, and 3) 4-channel switched-capacitor-based stimulation (SCS) with stimulus artifact rejection. As shown in Fig. 8.2, the 25-mm^2 WINeRS-7 system-on-chip (SoC) has been designed by combining three chips. The focus of this dissertation is on the PMDT block.

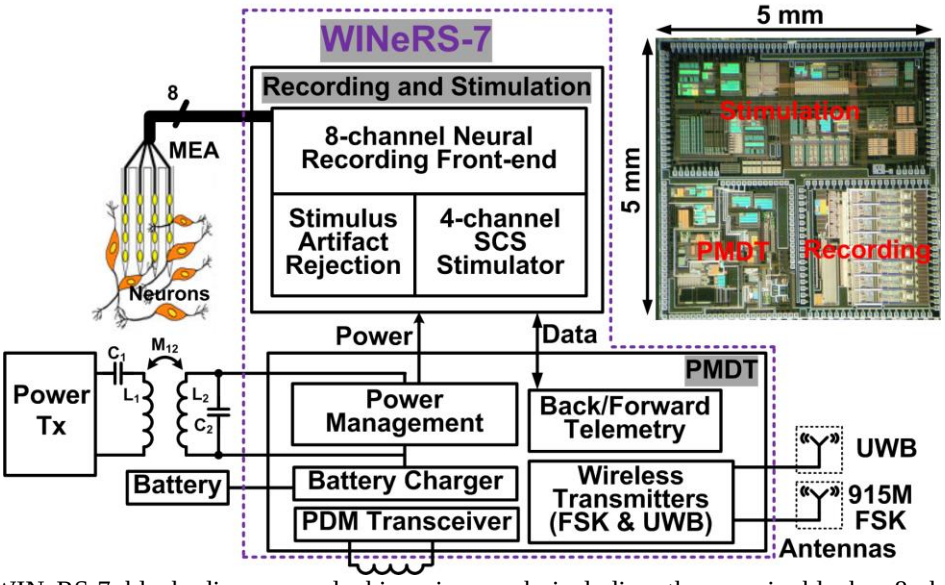

Fig. 8.2. WINeRS-7 block diagram and chip micrograph including three main blocks: 8-channel recording front-end, 4-channel switched-capacitor-based stimulation (SCS), and power-management and data transceiver (PMDT).

Fig. 8.3 shows the block diagram of PMDT, which includes an active positive/negative rectifier, a battery charger, three regulators (LDOs) at 2.1 V, -0.3 V, and -2.1 V, an automatic-resonance tuning (ART), a low-power PWM-IR-UWB transmitter (Tx), a 915-MHz FSK Tx, PWM-ASK demodulator and PDM transceiver. A power amplifier (PA) drives the Tx coil, L_2, at the designated carrier frequency, which

can be either f_c=13.56MHz or 2 MHz in this design by controlling the rectifier. The AC signal across the Rx L_3C_3-tank, which is tuned at f_c, is rectified by the positive/negative rectifier. The rectifier outputs, V_{RECP} = 2.3 V and V_{RECN} = -2.3 V, are then applied to the battery charger. A decision circuit connects the battery output (V_{BAT}) to the LDO input if V_{RECP} < 2.1 V. Three LDOs create constant V_{DD} = 2.1 V, V_{DDA} = -0.3 V and V_{SS} = -2.1 V, which V_{DD} and V_{SS} are used for stimulation and FSK Tx while V_{DDA} and V_{SS} provide a 1.8 V supply for the recording blocks, UWB Tx, and PDM transceiver. The ART ensures that L_3C_3-tank is always tuned at f_c by sweeping a 5-bit binary-weighted on-chip (3 pF, 6 pF, 12 pF, 24 pF, 48 pF) and a 3-bit binary-weighted off-chip (100 pF, 200 pF, 400 pF) capacitor banks resulting in 0-800 pF capacitance change across L_3C_3-tank with 3 pF resolution. A hysteresis comparator detunes L_3C_3-tank by a C_{ovp} = 1 nF when V_{RECP} > 2.4 V to protect PMDT from large input voltages.

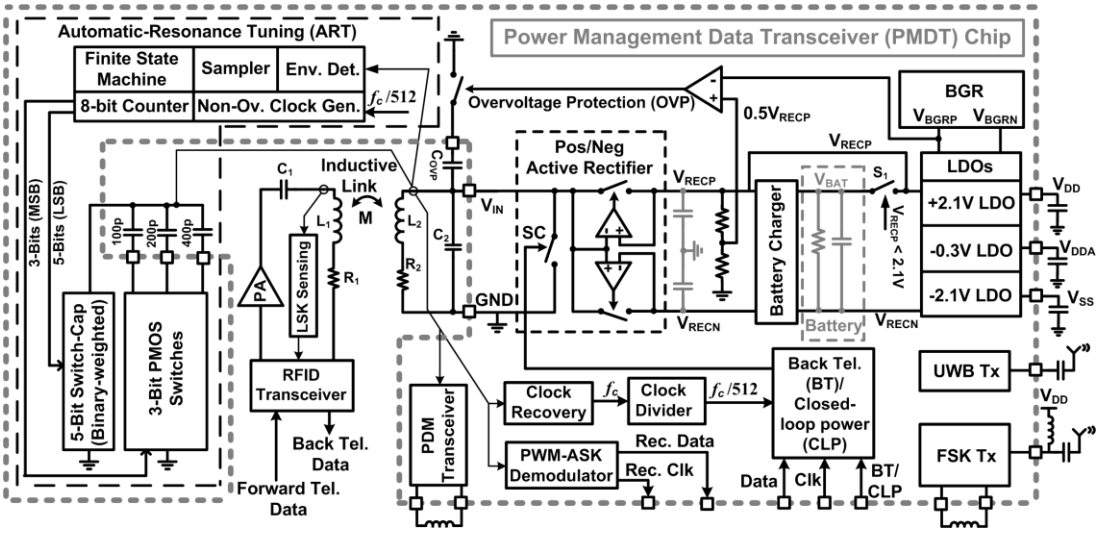

Fig. 8.3. Block diagram of the highly efficient and adaptive PMDT block of the WINeRS-7 system.

Fig. 8.4 shows a simplified schematic diagram of the active positive/negative rectifier, consisting of PMOS and NMOS pass transistors, which are driven by two high-speed offset-controlled comparators, for positive and negative outputs, respectively. The start-up circuit monitors V_{RECP}/V_{RECN} and sets CTL = 0 when V_{RECP}/V_{RECN} are low. Hence, P_1 and N_1 are diode-connected and form a passive rectifier, which charges V_{RECP}/V_{RECN}

regardless of the comparators' status up to the point that V_{RECP}/V_{RECN} reaches a stable minimum level. Then CTL toggles to enable the rectifier to operate normally. Fig. 8.5 shows the simplified schematic diagram of the V_{RECP} comparator i.e. CMP1 in Fig. 8.4 with the focus on dual frequency operation. For 13.56 MHz operation, S_2 is closed to minimize the comparator delay, however, S_1 is closed for 2 MHz operation to increase the comparator delay and reduce its speed. CMP2 in Fig. 8.4 is the dual of the CMP1 by swapping the PMOS and NMOS transistors.

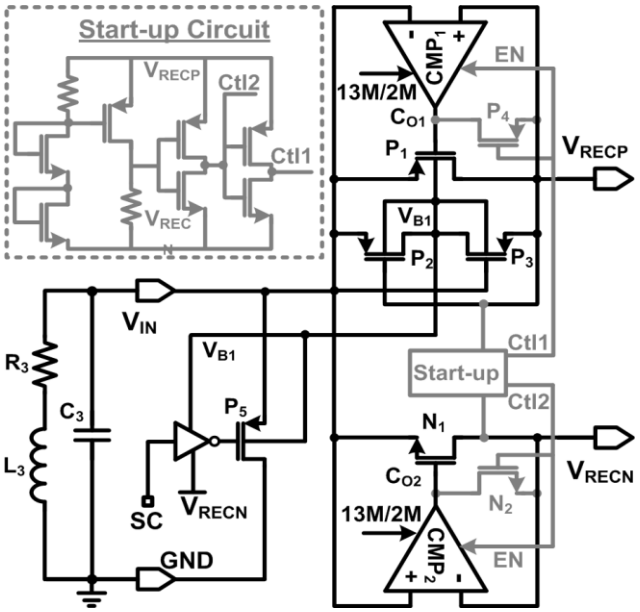

Fig. 8.4. Schematic diagram of the active positive/negative rectifier operating at 13.56 MHz/ 2 MHz.

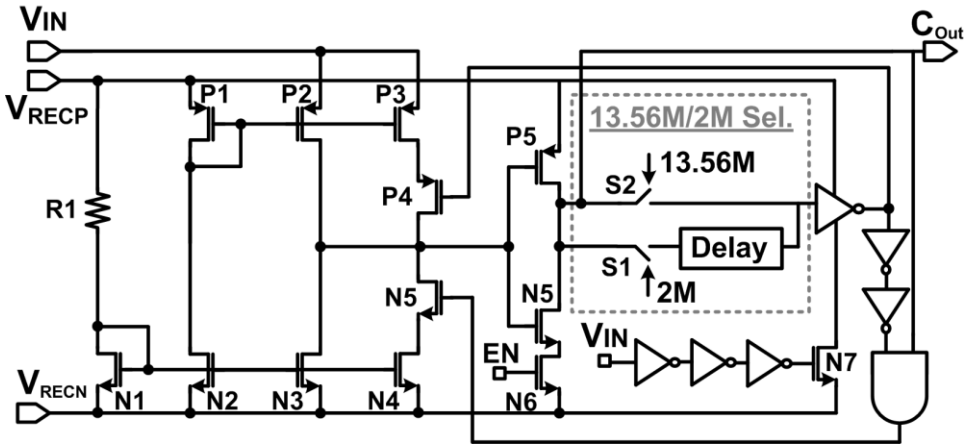

Fig. 8.5. Schematic diagram of the comparator for positive rectifier switch i.e. CMP1 in Fig. 8.4. The delay of the comparator can be increased for 2 MHz operation by closing S_1 and opening S_2. CMP2 in Fig. 8.4 is the dual of CMP1.

Fig. 8.6 shows measured input/output waveforms in the positive/negative rectifier for both 13.56 MHz and 2 MHz operations. The measured rectifier power conversion efficiency (PCE) for R_L = 250 Ω was 74.3% and 81% for 13.56 MHz and 2 MHz operations, respectively. It can be seen that the active rectifier has achieve a higher PCE at 2 MHz because the dynamic power dissipation is less and the requirements for comparator switching are more relaxed at lower frequencies.

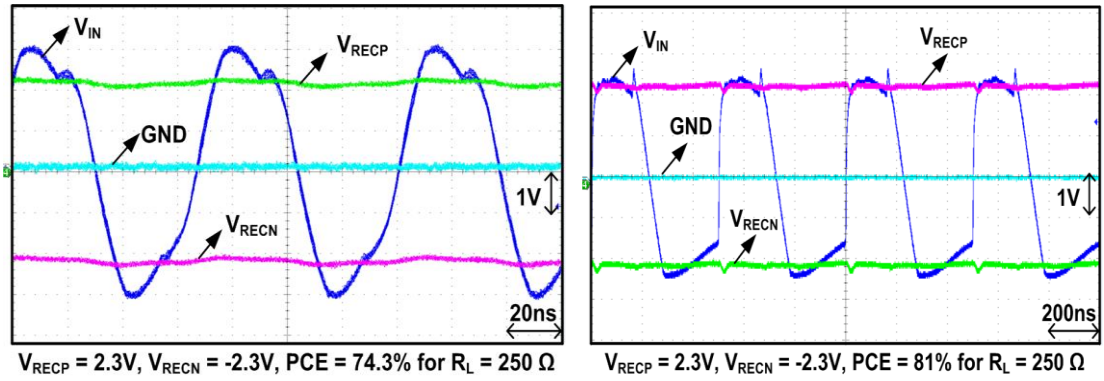

Fig. 8.6. Measured input/output voltage waveforms in the rectifier for (a) 13.56 MHz operation and (b) 2 MHz operation. R_L = 250 Ω.

Fig. 8.7 shows the detailed schematic diagram of the ART block, which is very similar to the one discussed in Chapter VI. The ART sweeps an 8-bit capacitor bank, which is connected to an 8-bit counter, in a certain direction (up or down) until the voltage envelope across L_3C_3-tank (V_{ENV}) reduces by 100 mV. Then the sweeping direction changes until V_{ENV} again reduces by 100 mV. These up and down cycles ensure that L_3C_3-tank is always tuned at f_c with a small offset. In the ART, V_{ENV} is first detected by a passive rectifier, divided by 1.4, and then buffered before being sampled. The first sampler, S_1, always samples V_{ENV} at the rising edge of CLK_S while S_2 only samples V_{ENV} at the rising edge of CLK_C when V_{ENV} increases or reduces by 100 mV. Because $CMP_{1,2}$, which are 100-mV offset comparators, output high and close S_3 when the difference between C_1 and C_2 voltages is ±100 mV. Therefore, CMP_2 output (Dir_Ch) changes the counting direction of the counter according to a finite state machine (FSM) because V_{ENV}

has reduced by 100 mV. One difference between this system and the one presented in Chapter VI is that the total amount of tuning capacitance can be selected in this design by two bits. This design offers four conditions: 1) Only on-chip capacitors are used, 2) On-chip and 100 pF off-chip capacitors are used, 3) On-chip, 100 pF, and 200 pF off-chip capacitors are used, and 4) All capacitors are used. These four conditions help to make the system more stable when the detuning is negligible by using less capacitance.

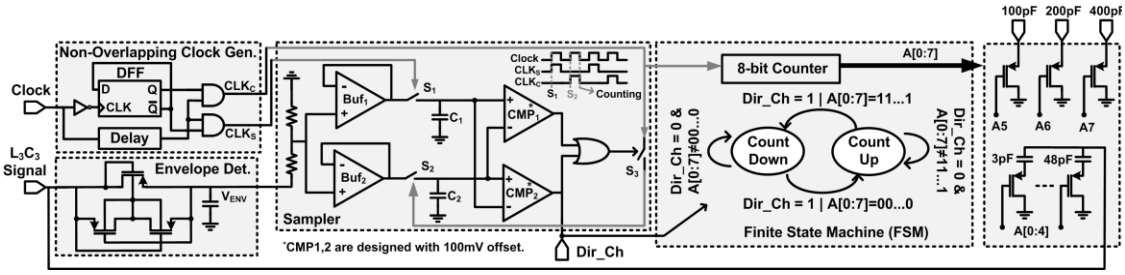

Fig. 8.7. Schematic diagram of the automatic-resonance tuning (ART) block.

The FSK transmitter consists of a voltage-controlled oscillator (VCO) with an off-chip inductor followed by a power amplifier (PA), as shown in Fig. 8.8. A nonlinear class-AB PA is used to help with the transmitter output matching with miniature 50 Ω antennas, and extend the transmission range. Complementary negative-G_m structure is used for the VCO core due to its low power and superior phase noise performance [113]. Coarse and fine VCO tunings are done with the choice of off-chip inductor and a 2-bit on-chip capacitor bank (V_C0:1), respectively. The VCO varactors are PMOS transistors, in which the gates are connected to the VCO outputs, bulks are tied to V_{DD}, and sources and drains are tied together and connected to the PWM signal from the recording block to generate the FSK signal. The FSK index can also be adjusted using 2-bit varactor bank, which the control signal can be connected to the PWM signal through a switch. The PA can be configured in single and differential mode operations. In differential mode operation, two antennas with 180 degrees orientation could be used to increase the coverage. In single mode, gate of M_7 is connected to V_{SS} to turn off the left branch of PA. The maximum single-tone output power of the PA in single mode 0.4 dBm (3.4 dBm in

differential mode) when the FSK Tx consumes 12 mA current. Fig. 8.8 also shows the FSK spectrum at two frequencies i.e. f_1 = 903 MHz and f_2 = 916 MHz with the output power of -17 dBm.

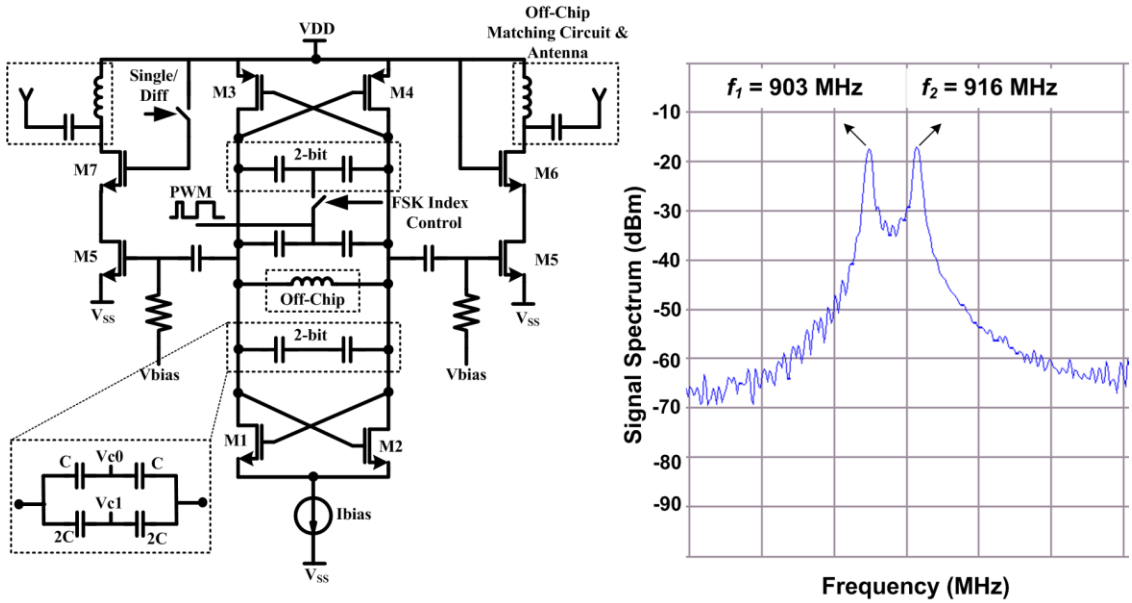

Fig. 8.8. Schematic diagram of the 915-MHz FSK transmitter with the measured FSK spectrum.

Fig. 8.9 shows the schematic diagram of the sub-GHz-range PWM-IR-UWB. Since 0.35-µm process is not suitable to design a 3-5 GHz range UWB Tx, therefore, we have reduced the frequency to < 1 GHz. In this Tx, the PWM rising and falling edges are first detected and three pulses per edge with ns delay are created shown as S_1 in Fig. 8.9 inset. A simple all-digital pulse generator creates three sharp pulses. The reason that three pulses are used is to increase the transmitted power for each edge to make it easier for the receiver to detect such small pulses over long communication distances. Fig. 8.10 shows the measurement results of the UWB Tx when the output was connected to the oscilloscope terminated by 50 Ω. The input is the PWM signal directly fed by the recording chip on the same die. It can be seen that a pulse is generated per each edge of the PWM signal. Considering that the WINeRS-7 effective number of bits is ~8, the proposed PWM-IR-UWB reduces the power consumption by 4 times compared to UWB digital communication using pulse-position modulation (PPM).

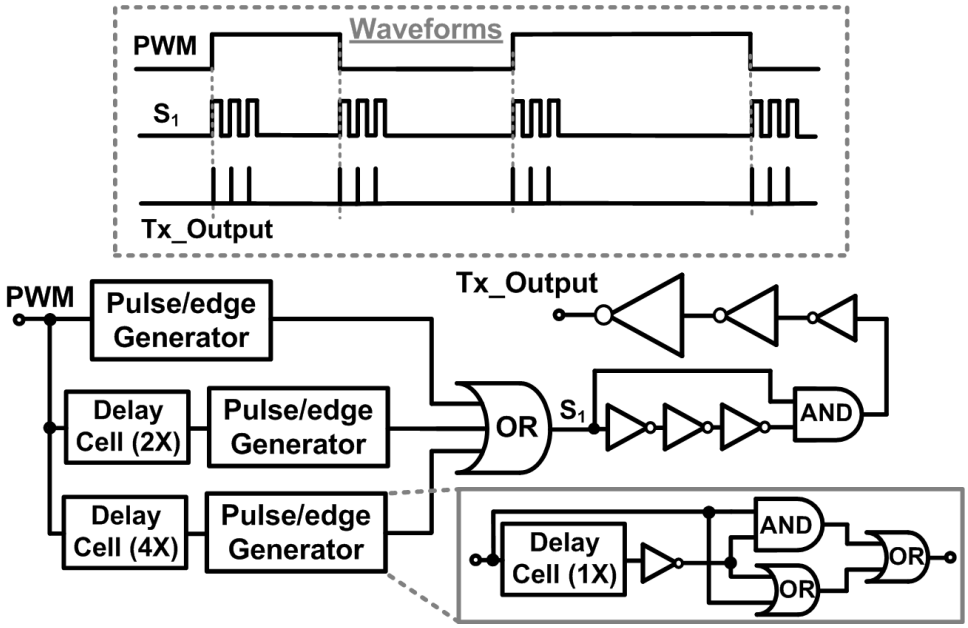

Fig. 8.9. Schematic diagram of sub-GHz-range PWM-IR-UWB.

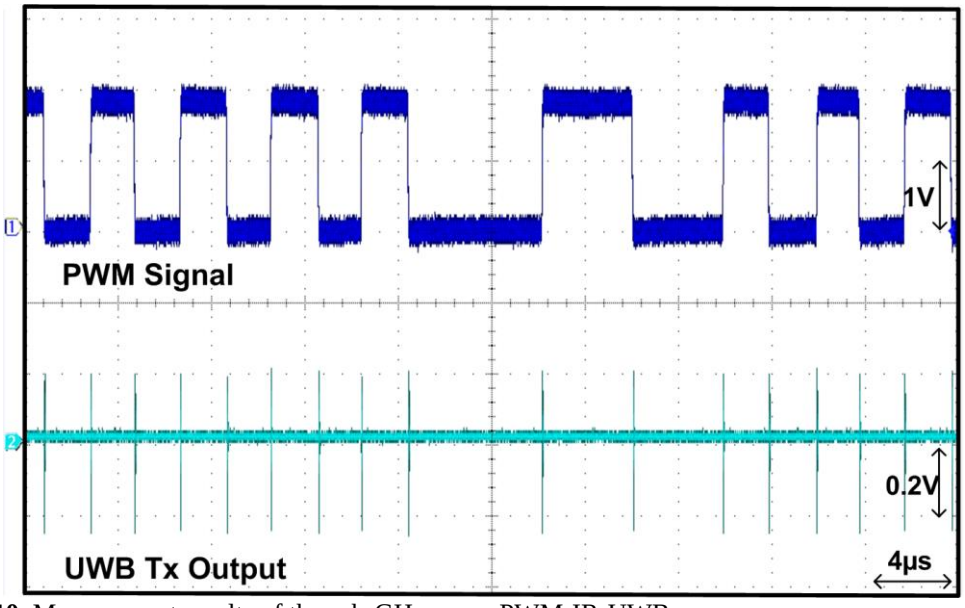

Fig. 8.10. Measurement results of the sub-GHz-range PWM-IR-UWB.

The WINeRS-7 chip was fabricated in the TSMC 0.35-µm 4M2P standard CMOS process, occupying 25 mm^2 while the PMDT occupies only 2.54 mm^2. Fig. 6.5 shows the PMDT chip micrograph with floor planning of each block.

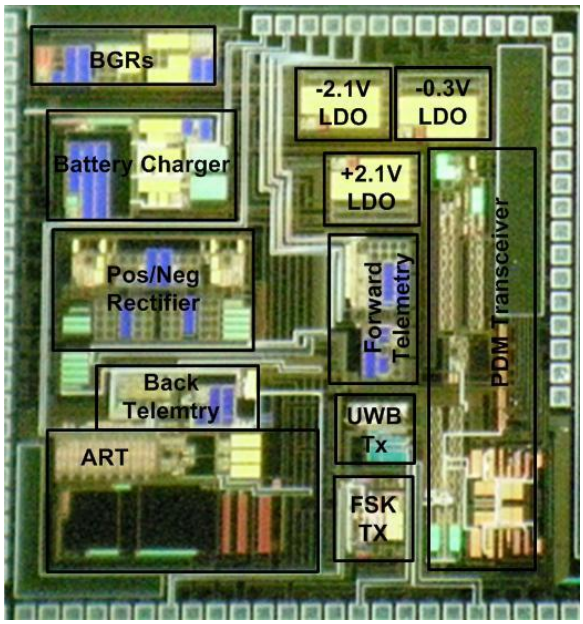

Fig. 8.11. PMDT die micrograph and floor plan in the WINeRS-7 system occupying 2.54 mm^2.

8.2. Animal Experiment Results

Today's technologies [100], [114]-[117] cannot create an automated enriched environment for long-term experiments on small animal subjects because of either imposing severe limitation on the size of the cage or being too bulky to fit inside standard animal facility racks. Such systems need to be detached from the animal before returning the animal back to the animal facility, which creates a stressful and impoverished environment for the animal subject, limits the experiment duration to couple of hours, and takes considerable amount of researchers' time.

The EnerCage system, however, could eliminate most of abovementioned issues for long term electrophysiology experiment [26]. The key components in the EnerCage system are: 1) A geometrically optimized array stationary overlapping coils unit that are designed based on the 3- and 4-coil coupling. Unlike today's technologies, the EnerCage system concentrates the magnetic field at the position of the animal without wasting power anywhere else in the cage. 2) RFID-based driver unit with closed-loop power control. 3) Either magnetic or optical-based tracking unit: capable of accurately tracking

the position of the animal subject in < 1 cm resolution, using either multiple axial magnetic sensors distributed under the coils or a Microsoft Kinect installed above the experimental arena. 4) A coin-sized general-purpose highly integrated closed-loop inductive data and power management unit, which was presented earlier in this chapter. The detailed design and characterization of the EnerCage system is out of the scope of this dissertation and have completely been discussed in detail in [25], [26].

In order to demonstrate the functionality of the system in a real-world experiment, the PMDT ASIC was tested *in vivo* in a 30 × 28 × 18 cm^3 standard home cage. Fig. 18.12 shows the simplified block diagram of the system used in the animal experiment. A Microsoft Kinect was installed above the cage to localize the animal position to turn on/off the Tx coils. The images taken by Kinect every 33 ms were processed and the position of the animal was found by subtracting the images taken from the cage with the animal from the one before the animal was placed in the cage. An IGLOO FPGA received the localization data via a WLAN link and controlled the switches in series with the coils based on the position of the animal. On the mobile unit, an nRF24LE1 microcontroller, which equips a 2.4 GHz wireless transceiver and a 10-bit analog-to-digital converter (ADC) was used for two main tasks: 1) The positive rectifier voltage (V_{RECP}) was digitized by the ADC to be used as a measure of how well the system is operating and also for closing the power loop. It should be noted that the goal of the experiment was to show that a constant 20-mW power can be delivered to the mobile unit in presence of normal behavior of the animal subject. 2) The wireless transmitter (Tx) tuned at 2.4 GHz was used to send the V_{RECP} digitized data to the PC every 100 ms to close the power loop. At the Tx side, the V_{RECP} digitized data is received by an nRF-based wireless receiver and delivered to PC through USB port. In a custom-designed LabVIEW program, V_{RECP} was compared with 2.35 V, which was the nominal value in the design of PMDT, and a single bit that shows whether $V_{RECP} > 2.35$ V or $V_{RECP} < 2.35$ V was sent to the closed-loop power control unit (CLPC) through XPORT communication. In the

CLPC unit, the data is received by an MSP430 microcontroller and a digital potentiometer in the resistive feedback of a DC-DC converter controls the supply voltage of a class-C PA from 5 V to 20 V similar to the closed-loop system described in Chapter II. Two C_s = 220 mF super capacitor were connected to the positive and negative rectifier outputs (V_{RECP}, V_{RECN}) to supply the mobile unit when the inductive coupling is weak due to large distance or rotation of the coil in the mobile unit.

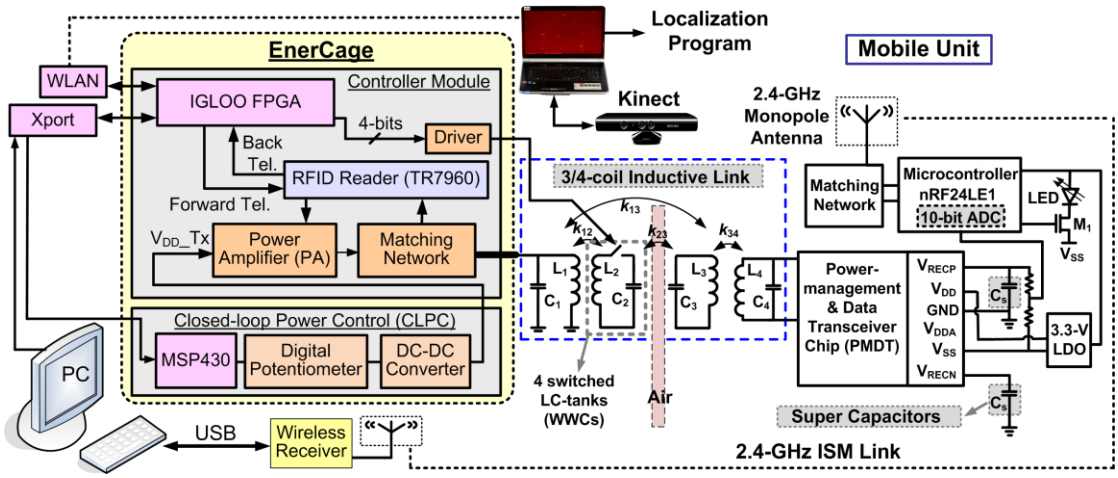

Fig. 8.12. Simplified block diagram of the EnerCage system and proposed general-purpose power supply used in the animal experiment in a standard home cage. A Microsoft Kinect was used during the experiment to localize the animal position. A wireless microcontroller was used to digitize the V_{RECP} and send the information back to the PC to close the power loop.

The *in vivo* experimental setup including the fabricated mobile unit and coils is shown in Fig. 8.13. All experiments were conducted with prior approval from the Institutional Animal Care and Use Committee (IACUC) at the Georgia Institute of Technology. The animal subject was a one-year-old Long-Evans Rat weighing 300 g. Table 8.1 shows the optimal geometries for the inductive link and system specifications. The geometry of the coils in the mobile unit i.e. L_3 and L_4 were optimized based on the design procedure in Chapter III to maximize the PTE at 7 cm coupling distance with AC load resistance of 300 Ω, which related to 20 mW output power. The maximum diameter of L_3 was limited to 2.5 cm to reduce the weight and size of the mobile unit. The maximum supply voltage for the PAs, V_{DD}_Tx, was 20 V to provide a maximum of 10 W while the minimum

VDD_Tx was 5 V to provide 0.7 W. The PA efficiency was 46% to 49% in the whole VDD_Tx range.

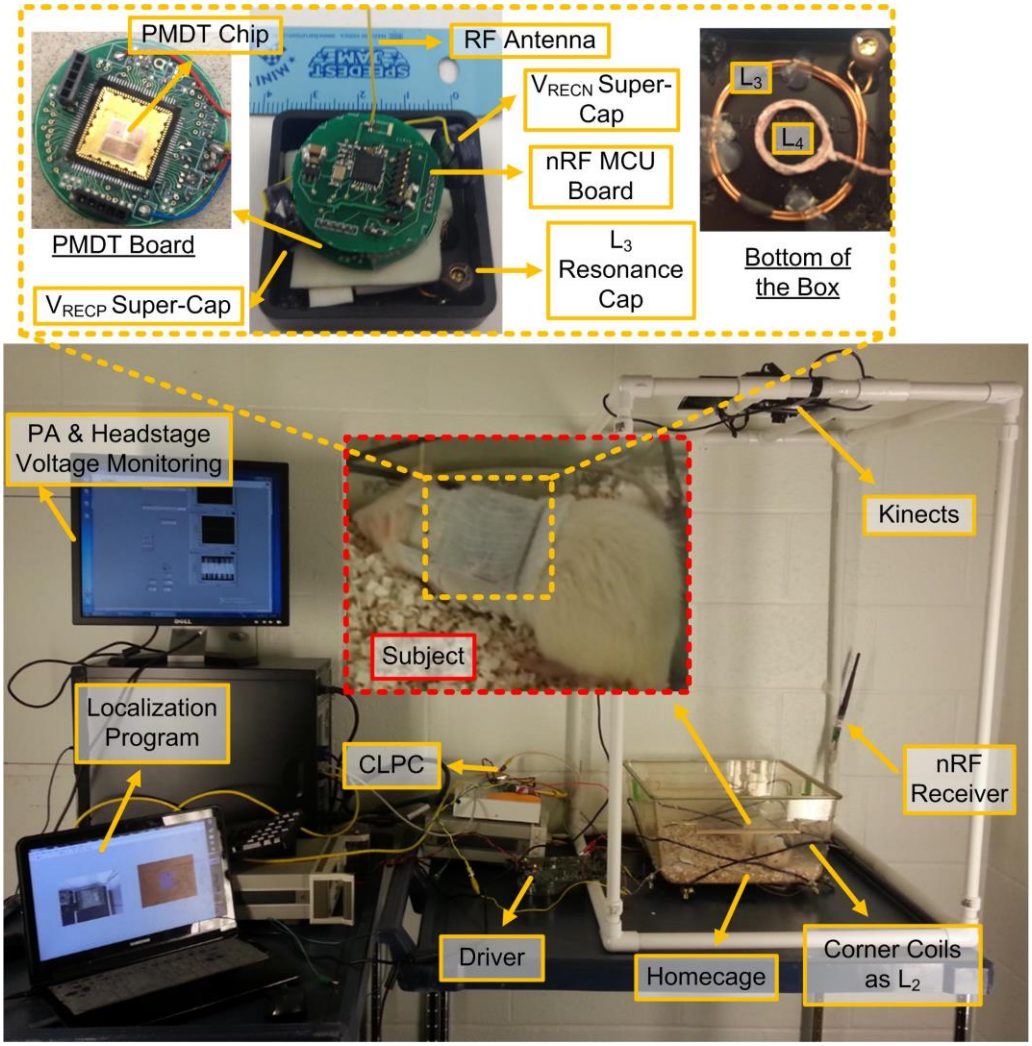

Fig. 8.13. The experimental setup to test the general-purpose wireless supply in the EnerCage system on a freely-behaving animal subject. A Kinect installed above the cage was used to localize the animal position.

The animal experiment was conducted for 30 minutes without interruption, and the results are shown in Figs. 8.14 and 8.15. During the experiment, the PA voltage (V_{DD}_Tx) ranged from 5-20 volts and the positive rectifier voltage (V_{RECP}) at the mobile unit designated at 2.35 V were monitored. It can be seen in Fig. 8.14 that during 30 minutes, V_{RECP} was maintained around 2.35 V with small changes due to the animal

movement. It should be noted that because V_{DD} = 2.1 V, the goal was to keep V_{RECP} > 2.1 during the experiment. This was achieved except in a small portion of the time, in which V_{RECP} reduced to 2.1 V but closed-loop system increased V_{DD}_Tx to compensate for this reduction. Overall, an average V_{DD}_Tx = 9 V was enough to power up the mobile unit in this experiment.

Table 8.1: Optimal coil geometries and system specifications

Parameters	Designed Values
Tx wire-wound coil (L_1)	Diameter = 23 cm Wire width = 2.59 mm (AWG10) Number of turns = 1 Inductance = 0.7 µH Quality factor = 193
Tx wire-wound coil (L_2)	Diameter = 30 cm Wire width = 2.59 mm (AWG10) Number of turns = 1 Inductance = 0.89 µH Quality factor = 204
Rx wire-wound coil (L_3)	Diameter = 2.5 cm Wire width = 0.64 mm (AWG 22) Number of turns = 2 Inductance = 0.48 µH Quality factor = 136
Rx Litz wire-wound coil (L_4)	Diameter = 1 cm Wire diameter = 0.25 mm Number of turns/strands = 6/44 Inductance = 5.8 µH Quality factor = 12
Power transmission frequency	13.56 MHz
Power update frequency	10 Hz
Weight of the mobile unit box/electronics	7/6 g

Fig. 8.14 shows two time periods of the results, in which notable variations were observed on both V_{RECP} and V_{DD}_Tx. The voltage variations during "A" period are shown in Fig. 8.15a. At t = 6.5 min when the first drop in V_{RECP} occurs, the PA voltage starts increasing to increase V_{RECP} to reach 2.35 volts. At t = 8.5 min, V_{RECP} has increased > 2.35 V that has caused V_{DD}_Tx to reduce to decrease the V_{RECP}. These waveforms show the true operation of the system. The voltage variation for "B" period has shown in Fig. 8.15b. At t = 21 to 22 min, V_{DD}_Tx has increased to keep V_{RECP} constant at 2.35 V. The

sudden voltage drop in V_{RECP} due to the low coupling has been compensated by sudden increase in PA voltage at t = 22.3 min. However, the rat quickly moved to a high PTE region and V_{RECP} was significantly increased because V_{DD}_Tx voltage was high. To compensate for this, the PA voltage has reduced again to make V_{RECP} around 2.3 V. Overall, the experimental results showed that the PMDT chip accompanied with receiver coils and nRF wireless transmitter operated well to receive 20 mW inside EnerCage system in a real-world experimental setup.

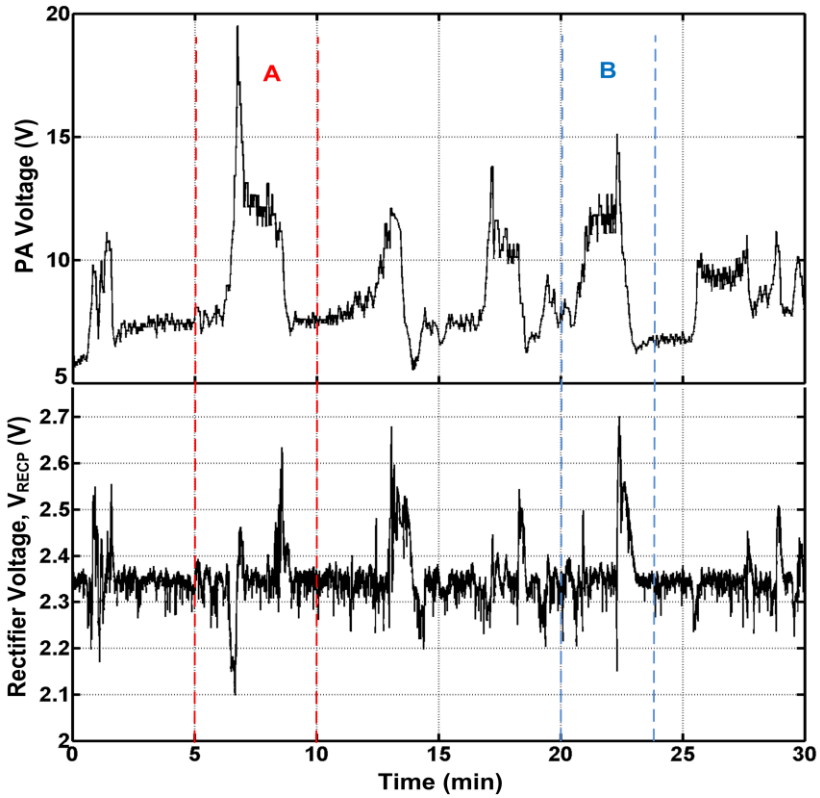

Fig. 8.14. The *in vivo* results for the PA supply voltage (V_{DD}_Tx) and rectifier positive voltage (V_{RECP}) during 30 min. The closed-loop system has maintained V_{RECP} around designated 2.35 V by changing V_{DD}_Tx adaptively with animal movements.

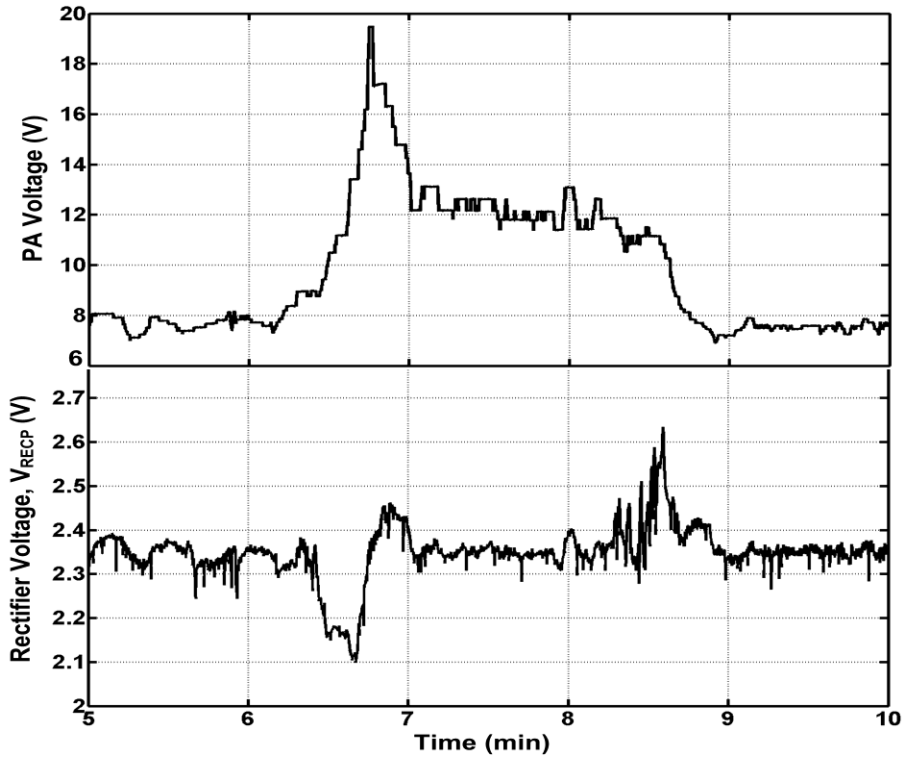

(a)

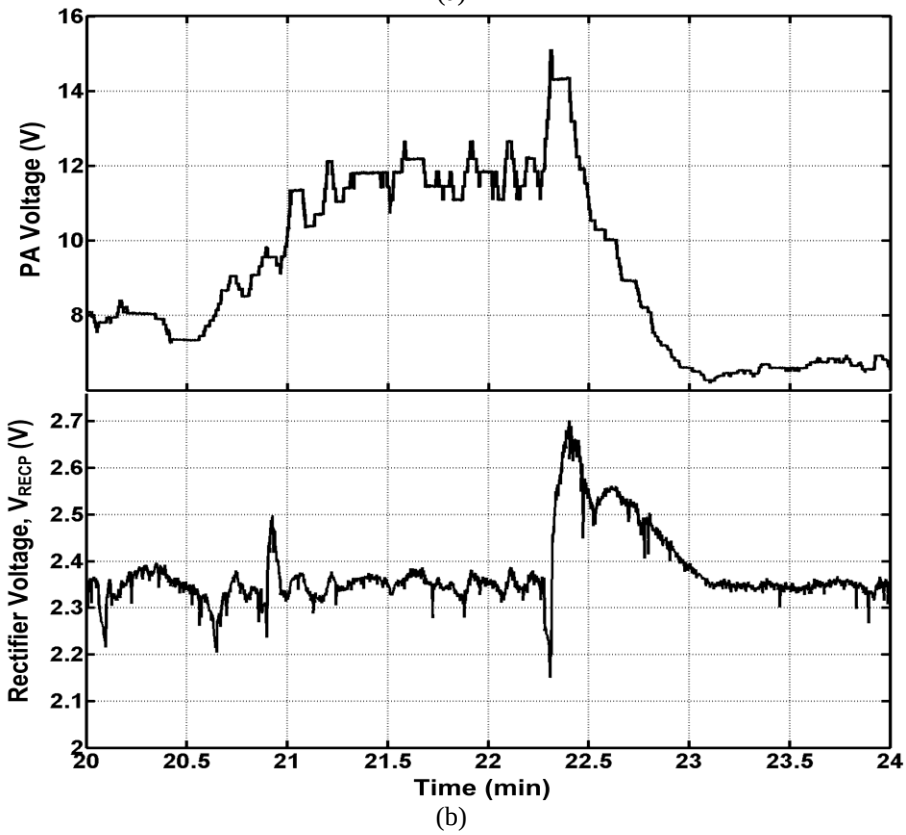

(b)

Fig. 8.15. (a) Time period "A" in Fig. 8.14: Sudden movement by the rat to a non-efficient area resulted in V_{DD}_Tx to reach its maximum. (b) Time period "B" in Fig. 8.14: A high-efficiency area, in which V_{RECP} > 2.6 V and closed-loop compensated for it by decreasing the V_{DD}_Tx.

CHAPTER IX

CONCLUSIONS AND FUTURE WORKS

This dissertation focuses on developing the system- and circuit-level techniques for high-performance wireless power and data transmission to biomedical Microsystems, which has resulted in several conference and journal publications [23], [25], [26], [67], [118]-[136]. Several techniques such as multi-coil power transfer, closed-loop power transmission, high-efficiency adaptive power management, and Q-modulation power management could significantly increase the PTE of power transfer link. The pulse-delay-modulation (PDM) and PWM-IR-UWB techniques also offers wideband and low-power data communication in presence of strong power-carrier interference. To further validate the feasibility of the power and data transfer techniques, such methods have been combined in an ASIC and tested on a freely behaving animal subject inside the EnerCage system as the power transmitter. This Chapter summarizes the results and scientific contributions of this dissertation and the future works.

9.1. Conclusions

9.1.1. High-efficiency Adaptive Inductive Power Transmission

A standalone closed-loop wireless power transmission system was proposed to maintain the delivered power to a transponder, representing an IMD, constant over loading or coupling variations. Instead of designing a custom ASIC, we have taken advantage of a single-chip 13.56 MHz commercial RFID reader to send power and detect back telemetry data.

We have presented detailed formulation for calculating the PTE based on circuit and physics (coupled-mode) theories for a conventional 2-coil inductive power transmission link, and extended the solutions in the steady state to 3-, 4-, and *m*-coil systems. We proved that both physics and circuit theories lead to the exact same set of

equations, and therefore, both are applicable to short- and mid-range coil arrangements. Moreover, we have derived equations describing the transient behavior of the 2-coil inductive power transmission links. Theoretical analysis and simulation results show that in this case, coupled-mode theory only accurate when coils have small coupling and large quality factors. However, it simplifies the analysis by reducing the order of the differential equations by half, compared to the circuit-based approach.

A design procedure was also presented to maximize the PTE in 2-, 3-, and 4-coil inductive links. We have shown that the 3-coil inductive links can significantly improve the PTE and delivered power to the load (PDL), particularly at large coupling distances by transforming any arbitrary load impedance to the optimal impedance needed at the input of the inductive link. We showed that the recently proposed 4-coil inductive links transform the load impedance to a very high reflected resistance across the driver coil, which limit the available power from source and drastically reduce PDL, particularly at large coupling distances.

A new figure-of-merit (FoM) was also proposed to design high-performance inductive power transmission links. We have demonstrated the tradeoffs between maximizing the PTE and PDL, simultaneously, to help designers choose the best measure for a particular application. We have proposed a design procedure based on the new FoM for 2-coil links and extended it to multi-coil arrangements for designing state-of-the-art inductive power transmission links. The FoM guides designers to choose 2-coil links for strongly-coupled coils used in applications that need large PDL, 3-coil links for loosely-coupled coils where the coupling distance varies considerably, and 4-coil links when small PDL is required at high PTE and the coils are loosely-coupled but have a stable coupling distance and alignment.

9.1.2. Adaptive and High-efficiency Power Management

A complete adaptive power-management and low-power data-transceiver (PMDT) ASIC with automatic receiver (Rx) coil resonance frequency tuning capability was presented. PMDT also includes an adaptive super-cap charger, which reduces the start-up and charging time, a battery charger and an active rectifier with measured power conversion efficiency (PCE) of 76.2 %. In an exemplary setup, PMDT successfully compensated for > 100 pF detuning in Rx coil and adaptively charged a 0.11 F super-cap with 0-17mA current allowing for ~10 ms start-up time.

A new method for enhancing wireless power transmission through an inductive link was presented called Q-modulated inductive link, which uses only one coil at the receiver (Rx) side. The Rx has been equipped with a switch that would control the quality factor (Q) of the Rx coil. This technique offers two main advantages compared to multi-coil coupling: 1) The physical size of the Rx is reduced by using only one coil, and more importantly, 2) The PTE can be maintained at the highest possible level for a wide range of load values by adjusting the switching duty cycle of the Rx coil. A Q-modulation power management (QMPM) ASIC was also developed that includes a high-efficiency passive rectifier operating at 2 MHz with > 5 W output power. A novel automatic duty-cycle control (ADCC) was also developed to adaptively adjust the quality factor of the Rx coil during the operation in presence of load variations.

The PMDT chip was also modified to inductively provide a constant power for a wireless implantable neural recording and stimulation system (WINeRS-7). An active positive/negative rectifier provides 2.3 V and -2.3 V for three low-dropout regulators (LDO) to create constant 2.1 V and -2.1 V for stimulation and -0.3 V for recording blocks. The WINeRS-7 chip also includes 915-MHz frequency-shift keying (FSK), sub-GHz ultra-wideband (UWB) transmitters, and a pulse-delay modulation (PDM) transceiver for data communication. The WINeRS-7 was tested in the EnerCage system

on a freely behaving animal subject. The *in vivo* results showed that PMDT received a closed-loop constant 20-mW power during half an hour of experiment.

9.1.3. Wideband and Low-power Data Communication

A new modulation technique, called pulse delay modulation (PDM), has been proposed to solve two key issues in near-field wireless data and power transmission links. First, it significantly increases the bandwidth while simplifying the Tx and Rx circuitry and, consequently, their power consumptions. Second, it addresses the problem of power carrier interference with received data in multi-coil transcutaneous inductive links without affecting the power transfer efficiency. We have also presented the first ASIC implementation of a low-power PDM-based transceiver. The PDM transceiver achieved a data rate of 13.56 Mbps with a BER of 4.3×10^{-7} across a 10 mm dual-band inductive link, while delivering 42 mW of regulated power to the load. To the best of our knowledge, this is the best overall performance for near-field simultaneous data and power telemetry.

I have also developed a 3-5 GHz range UWB transceiver in UMC 0.13-µm process for low-power far-field data communication. The novelty in this system is to combine pulse-width modulation (PWM) and impulse-radio (IR) techniques to further reduce the power consumption in conventional IR-UWB transmitters. In the proposed PWM-IR-UWB Tx only two pulses are transmitted for 8-10 digital bits that results in 4-5 times power reduction.

9.2. Future Works

Several research groups have considered using meta-materials to further increase the PTE by focusing the Tx magnetic field on the Rx and, therefore, increasing the mutual coupling. However, these efforts are still at early stages and their possible applications in IMDs have not been explored. Moreover, designing efficient coils, inductive links, and antennas inside and around the body, while considering the complex implant and body environment, still needs additional work.

The Q-modulation power management (QMPM) and automatic-resonance tuning can be utilized as a new generation of power management with on-chip load modulation and resonance tuning. The QMPM chip will be tested and the effect of load switching on the PTE of the link as well as the link resonance frequency could further be studied in a realistic measurement setup.

The neural signal acquisition scheme in brain machine interface (BMI) can be categorized into three levels: 1) Electroencephalogram (EEG), which is taken from sensors which are on top of head. Although this is simple method, the spatial resolution is poor, because one EEG recording represents the summation of electrical activity of a large number of neurons, and brain and bone act as a low-pass filter resulting in the degradation of information. 2) Electrocorticogram (ECoG) is obtained by implanting the electrodes under the skull. This allows higher spatial resolution due to the reduced filtering effect of tissue and bone. However, the resolution obtained from ECoG is still very limited. 3) The highest spatial resolution can be obtained by recording single unit activity (SUA), where the electrode is directly attached to a single brain cell. Another problem of aforementioned signal acquisition schemes is that only limited brain area could be covered because traditional methods have relied on a single centralized implant. Therefore, there is a need for development of a wireless system for acquisition and transmission of multichannel SUA signal all over the brain area using mm-sized implants. There are two main challenges in so-called distributed implants. First, the optimal frequency for powering mm-sized implants is different from large implants powered in near-field domain. For small implants, sub-GHz frequencies have been shown to be optimal and, therefore, a lot of work should be done for optimization of these links form the power Tx to the load. Second, communication with such small implants in the presence of power interference and small power budget is another challenge.

In PDM, the future goal is to add mechanisms to adaptively adjust delays to increase the PDM robustness against the coils' distance variation and misalignments.

Automatic gain control (AGC) is needed in most wireless transceivers intended for communications under conditions of fading and distance variation, such as in IMDs to avoid voltage saturation at small distance or weak signals at large distance. Although the PDM transceiver does not require AGC, because received signal is amplified to create a square waveform, a similar mechanism can adaptively adjust delay in the Rx. In this condition, delay values that are too small or too large will result in recovered data to be continuously “0” or “1”, respectively. What is needed in this case is a local feedback mechanism that monitors a certain parameter in the recovered data, e.g. cyclic redundancy checking (CRC), and compensates for delay variations.

There are multiple tests that should be conducted for the PWM-IR-UWB to measure its robustness against power interference and the animal tissue. The UWB antennas have been optimized for air, however, at high frequencies, electromagnetic power absorption in the tissue can increase the antenna losses and the design optimization should be reconsidered in saline and other tissue simulants. Furthermore, in order to miniaturize the size of the implantable devices, the micromachining (MEMS) technology with smaller feature size could be used to further shrink the volume of the implantable coils and antennas. The MEMS technology could also offer a flexible substrate to conform the IMD to the body curvatures.

The animal body could affect the Tx coil resonance frequency and, therefore, another tuning loop at the Tx could be used. Combining this loop with closed-loop power and automatic resonance tuning, and even automatic duty-cycle control in QMPM is another challenge. Finally, there are many experiments that require collecting real-time biological information, such as neural signals, body temperature, blood pressure, physical activities, blood chemical concentrations, and neurotransmitters. Even more challenging is experiments that require applying uninterrupted electrical, chemical, or mechanical stimulation, which are more power consuming, over long periods of time.

APPENDIX

WIRE-WOUND COILS (WWCS) MODELING

Wire-wound coils (WWCs) are often modeled as distributed RLC networks with a self-inductance in series with a resistance, both of which are in parallel with the coil parasitic capacitance [91]. An analytical expression for the self-inductance of a one turn circular conductive loop can be found from [137],

$$L_i = 0.5\mu_0\mu_r D_o \ln\left(\frac{D_o}{w}\right), \tag{A.1}$$

where μ_0 and μ_r are the permeability of space and of the conductor, respectively. D_o is the diameter of the loop and w is the diameter of the wire. For mutual inductance, M, a WWC can be considered a set of concentric single-turn loops with various diameters, all connected in series. Using Maxwell equations, M_{ij} between a pair of parallel single-turn circular loops at radii $r_i = D_i/2$ and $r_j = D_j/2$ can be found from [34],

$$M_{ij} = \frac{2\mu}{\alpha}\sqrt{r_i \cdot r_j}\left[\left(1-\frac{\alpha^2}{2}\right)K(\alpha)-E(\alpha)\right], \tag{A.2}$$

where,

$$\alpha = 2\sqrt{\frac{r_i.r_j}{\left(r_i+r_j\right)^2+d_{ij}^2}}\,. \tag{A.3}$$

In this equation, d_{ij} is the coupling distance between the two coils and $i \neq j$. $K(\alpha)$ and $E(\alpha)$ are the complete elliptic integrals of the first and second kind, respectively [34]. Therefore, the mutual inductance between two coils with n_i and n_j number of turns can be found from,

$$M = \sum_{k=1}^{n_i}\sum_{l=1}^{n_j} M_{k,l}\,. \tag{A.4}$$

Hence, the self-inductance of a WWC can be found from

$$L_{Self} = \sum_{i=1}^{n_i} L_i + \sum_{k=1}^{n_i} \sum_{j=1}^{n_i} M_{k,j} \qquad \text{for} \qquad k \neq j. \tag{A.5}$$

To model the series parasitic resistance of the WWC, its DC resistance should be calculated from

$$R_{DC} = \frac{\rho_c}{\pi (w/2)^2} \cdot \pi \left[n_i D_o - (n_i - 1)(w + s) \right], \tag{A.6}$$

where ρ_c is the resistivity of the conductive material, s is the wire spacing between the surface of the conductors, and n_i is i^{th} coil total number of turns. As the operating frequency increases, the skin effect increases the series resistance, which can be modeled as [138]

$$R_S \cong R_{DC} \cdot \frac{w^2}{4\delta \cdot (w - \delta)}, \tag{A.7}$$

where,

$$\delta = \sqrt{\frac{\rho_c}{\pi \cdot \mu \cdot f}}\ . \tag{A.8}$$

When the wire spacing, s, is smaller than the wire diameter, w, the AC resistance of the coil in (A.7) increases due to the proximity effect at higher frequencies [139].

The parasitic capacitance between two turns of a WWC can be found from [91]

$$C_{turn} = \varepsilon_0 \varepsilon_r \int_0^{\theta_e/2} \frac{\pi \cdot D_o \cdot w/2}{\varsigma + (w/2)\varepsilon_r (1 - \cos\theta) + 0.5\varepsilon_r \cdot s'} d\theta \tag{A.9}$$

where ε_r is the relative permittivity of the insulation material, ς is the thickness of the insulation layer, θ_e is the effective angle between turn i and turn j, i.e. 90°, and s' is the wire spacing between the surface of the insulation layers. Hence, the sum of the turn-to-turn parasitic capacitance from (A.9) leads to the total parasitic capacitance, C_P.

Finally, considering R_S in series with L_{self} and C_P in parallel with both, the quality factor of a WWC at operating frequency, ω_0, can be found from [34]

$$Q = \frac{\omega_0 L_{self} - \omega_0 ({R_S}^2 + \omega_0^2 L_{self}^2) C_P}{R_S} \approx \frac{\omega_0 L_{self}}{R_S}, \tag{A.10}$$

which is valid for low frequency and small C_P.

The weight of a circular-shaped WWC with n_i turns, wire spacing of s between the surface of the conductors, and wire diameter of w can be written as

$$W = \frac{\rho \pi^2 w^2}{4} \left[n_i D_o - (n_i - 1)(w + s) \right], \tag{A.11}$$

where ρ is the density of the conducting material, which is 8.96 g/cm^3 for copper. In (A.11) we have ignored the weight of the insulating material.

REFERENCES

[1] D. Zhou and E. Greenbaum, *Implantable neural prostheses 1*. Springer, New York, NY, 2009

[2] K. Chen, Z. Yang, L. Hoang, J. Weiland, M. Humayun, and W. Liu, "An integrated 256-channel epiretinal prosthesis," *J. Solid State Cir.*, vol. 45, pp. 1946-1956, Sept. 2010.

[3] D. Shire, S. Kelly, C. Jinghua, P. Doyle, M. Gingerich, S. Cogan, W. Drohan, O. Mendoza, L. Theogarajan, J. Wyatt, and J. Rizzo, "Development and implantation of a minimally invasive wireless subretinal neurostimulator,", *IEEE Trans. Biomed. Eng.*, vol. 56, pp. 2502-2511, Oct. 2009.

[4] A. Schwartz, T. Cui, D. Weber, and D. Moran, "Brain-controlled interfaces: movement restoration with neural prosthetics," *Neuron*, vol. 52, pp. 205-220, Oct. 2006.

[5] T. Kuiken, L Miller, R. Lipschutz, B. Lock, K. Stubblefield, P. Marasco, P. Zhou, and G. Dumanian, "Targeted reinnervation for enhanced prosthetic arm function in a woman with a proximal amputation: a case study," *Lancet*, vol. 369, pp. 371-380, Feb. 2007.

[6] K. Mathieson, J. Loudin, G. Goetz, P. Huie, L. Wang, T. Kamins, L. Galambos, R. Smith, J. Harris, A. Sher, and D. Palanker, "Photovoltaic retinal prosthesis with high pixel density," *Nature Photonics*, vol. 6, pp. 391-397, May 2012.

[7] K. Finkenzeller. *RFID-Handbook*. 2nd Ed., Wiley, Hoboken, NJ, 2003.

[8] A. Karalis, J. Joannopoulos, and M. Soljacic, "Efficient wireless non-radiative mid-range energy transfer," *Annals of Physics*, vol. 323, pp. 34-48, Apr. 2007.

[9] J. Fernandez, and J. Borras, "Contactless battery charger with wireless control link," *US patent* 6,184,651, 2001.

[10] M. Rosenzweig, S. Breedlove, and N. Watson, *Biological Psychology: An Introduction to Behavioral and Cognitive Neuroscience*, 4th ed., Sinauer Associates Inc., 2004.

[11] E. Boyden, "A history of optogenetics: the development of tools for controlling brain circuits with light," Biology Report, May 2011.

[12] H. Van Praag, G. Kempermann, and F. Gage, "Running increases cell proliferation and neurogenesis in the adult mouse dentate gyrus," *Nature Neuroscience*, vol. 2, pp. 266–270, 1999.

[13] H. Van Praag, G. Kempermann, and F. Gage, "Neural consequences of environmental enrichment," *Nat Rev Neuroscience*, vol. 1, pp. 191-198, Dec. 2000.

[14] G. Kempermann, H. kuhn, and F. Gage, "More hippocampal neurons in adult mice living in an enriched environment," *Nature*, vol. 386, pp. 493-495, Apr. 1997.

[15] A. Belayev, I. Saul, Y. Liu, W. Zhao, M. Ginsberg, M. Valdes, R. Busto, L. Belayev, "Enriched environments delays the onset of hippocampal damage after global cerebral ischemia in rats," *Brain Research*, vol. 964, pp. 121-127, 2003.

[16] A. Brauner, D. Kurjiaka, A. Ibragimov, and A. Baldwin, "Imapct of cage size and enrichment (tube and shelf) on heart rate variability in rats," *Science*, vol. 37, 2010.

[17] J. Simpson, and J. Kelly, "The impact of environmental enrichment in laboratory rats-behavioural and neurochemical aspects," Behavioural Brain Research, vol. 222, pp. 246-264, 2011.
[18] A. Benabid, "Deep brain stimulation for Parkinson's disease," *Current Opinion in Neurobiology*, vol. 13, pp. 696-706, 2003.
[19] J. Yianni, P. Bain, N. Giladi, M. Auca, R. Gregory, C. Joint, D. Nandi, J. Stein, R. Scott, and T. Aziz, "Globus pallidus internus deep brain stimulation for dystonic conditions: a prospective audit," *Mov. Disord*, vol. 18, pp. 436-442, 2003.
[20] M. Hodaie, R. Wennberg, J. Dostrovsky, and A. Lozano, "Chronic anterior thalamus stimulation for intractable epilepsy," *Epilepsia*, vol. 43, pp. 603-608, 2002.
[21] L. Gabriels, P. Cosyns, B. Meyerson , S. Andreewitch, S. Sunaert, A. Maes, P. Dupont, J. Gybels, F. Gielen, and H. Demeulemeester, "Long-term electrical capsular stimulation in patients with obsessive-compulsive disorder," Neurosurgery, vol. 52, pp. 1263-1274, 2003.
[22] C. Cameron, et al., "Uncovering the mechanism(s) of action of deep brain stimulation: activation, inhibition, or both," *Clinical Neurophysiology*, vol. 115, pp. 1239-1248, 2004.
[23] S. Lee, H. Lee, M. Kiani, U. Jow, and M. Ghovanloo, "An inductively-powered scalable 32-channel wireless neural recording system-on-a-chip for neuroscience applications," *IEEE Trans. Biomed. Cir. Syst.*, vol. 4, pp. 360-371, Dec. 2010.
[24] M. Chae, Z. Yang, M. Yuce, L. Hoang, and W. Liu, "A 128-channel 6 mW wireless neural recording IC with spike feature extraction and UWB transmitter," IEEE Trans. Neural Syst. Rehab. Eng., vol. 17, pp. 312-321, Aug. 2009.
[25] U. Jow, M. Kiani, X. Huo, and M. Ghovanloo, "Towards a smart experimental arena for long-term electrophysiology experiments," *IEEE Transaction on Biomedical Circuits and Systems*, vol. 6, pp. 414-423, Oct. 2012.
[26] U. Jow, P. McMenamin, M. Kiani, and M. Ghovanloo, "EnerCage: A Smart Experimental Arena with Scalable Architecture for Behavioral Experiments," *IEEE Transaction on Biomedical Engineering*, 2013.
[27] S. Gabriel, R. Lau, and C. Gabriel, "The dielectric properties of biological tissues: II. Measurements in the frequency range 10 Hz to 20 GHz," *Phys. Med. Biol.*, vol. 41, pp. 2251-2269, Nov. 1996.
[28] S. Ozeria, D. Shmilovitza, S. Singera, and C. Wang, "Ultrasonic transcutaneous energy transfer using a continuous wave 650 kHz Gaussian shaded transmitter," *Ultrasonics*, vol. 50, pp. 666-674, Jun. 2010.
[29] Y. Zhu, S. Moheimani, and M. Yuce, "Ultrasonic energy transmission and conversion using a 2-D MEMS resonator," *IEEE Electron Device Letters*, vol. 31, pp. 374-376, Apr. 2010.
[30] W. Brown, "The history of power transmission by radio waves," *IEEE Trans. Microwave Theory Tech.*, vol. 32, pp. 1230–1242, Sept. 1984.
[31] A. Poon, S. O'Driscoll, and T. Meng, "Optimal frequency for wireless power transmission into dispersive tissue," *IEEE Trans. on Antennas and Propagation*, vol. 58, pp. 1739-1750, May 2010.
[32] M. Baker and R. Sarpeshkar, "Feedback analysis and design of RF power links for low-power bionic systems," *IEEE Trans. Biomed. Cir. Syst.*, vol. 1, pp. 28-38, Mar. 2007.
[33] G. Kendir, W. Liu, G. Wang, M. Sivaprakasam, R. Bashirullah, M. Humayun, and J. Weiland, "An optimal design methodology for inductive power link with class-E amplifier," *IEEE Trans. Cir. Syst. I*, vol. 52, pp. 857-866, May 2005.
[34] U. Jow and M. Ghovanloo, "Design and optimization of printed spiral coils for efficient transcutaneous inductive power transmission," *IEEE Trans. Biomed. Cir. Syst.*, vol. 1, pp. 193-202, Sep. 2007.
[35] IEEE Standard for Safety Levels With Respect to Human Exposure to Radio Frequency Electromagnetic Fields, 3 kHz to 300 GHz, IEEE Standard C95.1, 1999.
[36] W. J. Heetderks, "RF powering of millimeter and submillimeter-sized neural prosthetic implants," *IEEE Trans. Biomed. Eng.*, vol. 35, pp. 323-327, May 1988.
[37] C. Neagu, H. Jansen, A. Smith, J. Gardeniers, and M. Elwanspoek, "Characterization of a planar microcoil for implantable microsystems," *Sens. Actuat. A*, vol. 62, pp. 599-611, Jul. 1997.
[38] S. Chen and V. Thomas, "Optimization of inductive RFID technology," *in Proc. IEEE Int. Symp. Electron. Environ.*, pp. 82-87, May 2001.
[39] C. Zierhofer and E. Hochmair, "High-efficiency coupling-in sensitive transcutaneous power and data transmission via an inductive link," *IEEE Trans. Biomed. Eng.*, vol. 37, pp. 716-722, Jul. 1990.

[40] C. Zierhofer and E. Hochmair, “Geometric approach for coupling enhancement of magnetically coupled coils,” *IEEE Trans. Biomed. Eng.*, vol. 43, pp. 708-714, Jul. 1996.
[41] R. Harriso n, “Designing efficient inductive power links for implantable devices,” *IEEE Int. Symp. Cir. Syst.*, pp. 2080-2083, May 2007.
[42] U. Jow and M. Ghovanloo, “Modeling and optimization of printed spiral coils in air, saline, and muscle tissue environments,” *IEEE Trans. Biomed. Cir. Syst.*, vol. 3, pp. 339-347, Oct. 2009.
[43] H. Haus and W. Huang, “Coupled-mode theory,” *Proc. of the IEEE*, vol. 79, pp. 1505-1518, Oct. 1991.
[44] A. Karalis, J. Joannopoulos, and M. Soljacic, “Efficient wireless non-radiative mid-range energy transfer,” *Annals of Physics*, vol. 323, pp. 34-48, Apr. 2007.
[45] L. Cannon, J. Hoburg, D. Stancil, and S. Goldstein, “Magnetic resonant coupling as a potential means for wireless power transfer to multiple small receivers,” *IEEE Trans. Power Electronics*, vol. 24, pp.1819-1825, Jul. 2009.
[46] A. RamRakhyani, S. Mirabbasi, and M. Chiao, “Design and optimization of resonance-based efficient wireless power delivery systems for biomedical implants,” *IEEE Trans. Biomed. Cir. Syst.*, vol. 5, pp. 48-63, Feb. 2011.
[47] A. Sample, D. Meyer, and J. Smith, “Analysis, experimental results, and range adaptation of magnetically coupled resonators for wireless power transfer,” *IEEE Trans. Indus. Elect.*, vol. 58, Feb. 2011.
[48] G. Wang, W. Liu, M. Sivaprakasam, and G. Kendir, “Design and analysis of an adaptive transcutaneous power telemetry for biomedical implants,” *IEEE Trans. Cir. Syst. I*, vol. 52, pp. 2109-2117, Oct. 2005.
[49] R. Bashirullah, W. Liu, Y. Ji, A. Kendir, M. Sivaprakasam, G. Wang, and B. Pundi, “A smart bi-directional telemetry unit for retinal prosthetic device,” *IEEE Intl. Symp. Cir. Syst.*, vol. 5, pp. V5-V8, May 2003.
[50] N. Chaimanonart, M. Zimmerman, and D. Young, “Adaptive RF power control for wireless implantable bio-sensing network to monitor untethered laboratory animal real-time biological signals,” *IEEE Sensors Conf.*, pp. 1241-1244, Oct. 2008.
[51] P. Si, A. Hu, S. Malpas, and D. Budgett, “A Frequency control method for regulating wireless power to implantable devices,” *IEEE Trans. Biomed. Cir. Syst.*, vol. 2, pp.22-29, March 2008.
[52] T. Dissanayake, A. Hu, S. Malpas, L. Bennet, A. Taberner, L. Booth, and D. Budgett, “Experimental study of a TET system for implantable biomedical devices,” *IEEE Trans. Biomed. Cir. Syst.*, vol. 3, pp. 370-378, Dec. 2009.
[53] R. Normann, “Technology insight: future neuroprosthetic therapies for disorders of the nervous system,” *Nature Clinical Practice*, vol. 3, pp. 444-452, Aug. 2007.
[54] N. Lovell, J. Morely, S. Chen, L. Hallum, and G. Suaning, “Biological-machine systems integration: engineering the neural interface,” *Proc. of the IEEE*, vol. 98, pp. 418-431, Mar. 2010.
[55] A. Sodagar, G. Perlin, Y. Yao, K. Najafi, and K. Wise, "An implantable 64-channel wireless microsystem for single-unit neural recording," *IEEE J. Solid-State Cir.*, vol. 44, pp. 2591-2604, Sept. 2009.
[56] R. Harrison, R. Kier, C. Chestek, V. Gilja, P. Nuyujukian, S. Ryu, B. Greger, F. Solzbacher, and K. Shenoy, "Wireless neural recording with single low-power integrated circuit," *IEEE Trans. Neural Syst. Rehab. Eng.*, vol. 17, pp. 322-329, Aug. 2009.
[57] M. Ghovanloo and S. Atluri, “A wideband power-efficient inductive wireless link for implantable microelectronic devices using multiple carriers,” *IEEE Trans. Cir. Syst. I*, vol. 54, pp. 2211-2221, Oct. 2007.
[58] FCC Rules and Regulations, MICS Band Plan, Part 95, 2003.
[59] M. Ghovanloo and K. Najafi, "A wideband frequency-shift keying wireless link for inductively powered biomedical implants," *IEEE Trans. Cir. Sys. I*, vol. 51, pp. 2374-2383, Dec. 2004.
[60] A. Shameli, A. Safarian, A. Rofougaran, M. Rofougaran, J. Castaneda, and F. Flaviis, "A UHF near-field RFID system with fully integrated transponder," *IEEE Trans. Microwave Theory Tech.*, vol. 56, pp. 1267-1277, May 2008.
[61] G. Suaning and N. Lovell, “CMOS neuro-stimulation ASIC with 100 channels, scalable output, and bidirectional radio-freq. telemetry,” *IEEE Trans. Biomed. Eng*., vol. 48, pp. 248-260, Feb. 2001.
[62] Y. Hu and M. Sawan, “A fully integrated low-power BPSK demodulator for implantable medical devices,” *IEEE Trans. Cir. Sys. I*, vol. 52, pp. 2552-2562, Dec. 2005.

[63] M. Zhou, M. Yuce, and W. Liu, "A non-coherent DPSK data receiver with interference cancellation for dual-band transcutaneous telemetries," *IEEE J. Solid-State Cir.*, vol. 43, pp. 2003-2012, Sep. 2008.
[64] G. Simard, M. Sawan, and D. Massiocotte, "High-speed OQPSK and efficient power transfer through inductive link for biomedical implants," *IEEE Trans. Biomed. Cir. Syst.*, vol. 4, pp. 192-200, Jun. 2010.
[65] S. Mandal and R. Sarpeshkar, "Power-efficient impedance-modulation wireless data links for biomedical implants," *IEEE Trans. Biomed. Cir. Syst.*, vol. 2, pp. 301-315, Dec. 2008.
[66] F. Inanlou and M. Ghovanloo, "Wideband near-field data transmission using pulse harmonic modulation," *IEEE Trans. Cir. Syst. I*, vol. 58, pp. 186–195, Jan. 2011.
[67] F. Inanlou, M. Kiani, and M. Ghovanloo, "A 10.2 Mbps pulse harmonic modulation based transceiver for implantable medical devices," *IEEE J. Solid-State Cir.*, vol. 46, pp.1296-1306, Jun. 2011.
[68] N. Miura, et al., "A 195-Gb/s 1.2-W inductive inter-chip wireless superconnect with transmitter power control scheme for 3-D-stacked system in a package," *IEEE J. Solid-State Cir.*, vol. 41, pp. 23-33, Jan. 2006.
[69] J. Yoo, S. Lee, and H. Yoo, "A 1.12 pJ/b inductive transceiver with a fault tolerant network switch for multi-layer wearable body area network applications," *IEEE J. Solid-State Cir.*, vol. 44, pp. 2999-3010, Nov. 2009.
[70] S. Lee, et al., "A low-energy inductive coupling transceiver with cm-range 50-Mbps data communication in mobile device applications," *IEEE J. Solid-State Cir.*, vol. 45, pp. 2366-2374, Nov. 2010.
[71] A. Chandrakasan, F. Lee, D. Wentzloff, V. Sze, B. Ginsburg, P. Mercier, D. Daly, and R. Blazquez, "Low-power impulse UWB architectures and circuits," *Proc. of the IEEE*, vol. 97, pp. 332-352, Feb. 2009
[72] A. Chandrakasan, N. Verma, and D. Daly, "Ultralow-power electronics for biomedical applications," *Annu. Rev. Biomed. Eng*., vol. 10, pp. 247-274, 2008.
[73] T. Buchegger, G. Oberger, A. Reisenzahn, E. Hochmair, A. Stelzer, and A. Springer, "Ultra-wideband transceivers for cochlear implants," *EURASIP J. Applied Signal Processing*, vol. 18, pp. 3069-3075, 2005.
[74] J. Lin, A. Guy, and C. Johnson, "Power deposition in a spherical model of man exposed to 1-20 MHz electromagnetic fields," IEEE Trans. Microwave Theory Tech., vol. 21, pp. 791-797, Dec. 1973.
[75] M. Catrysse, B. Hermans, and R. Puers, "An inductive power system with integrated bidirectional data-transmission," Sens. Actuators A, vol.115, pp. 221–229, 2004.
[76] G. Bawa and M. Ghovanloo, "Active high power conversion efficiency rectifier with built-in dual-mode back telemetry in standard CMOS technology," *IEEE Trans. Biomed. Circuits Syst.*, vol. 2, no. 3, pp. 184-192, Sept. 2008.
[77] G. M. Clark, *Cochlear Implants: Fundamentals and Applications*. New York: Springer-Verlag, 2003.
[78] K. Chen, Z. Yang, L. Hoang, J. Weiland, M. Humayun, and W. Liu, "An integrated 256-channel epiretinal prosthesis," *IEEE J. Solid-State Circuits*, vol. 45, no. 9, pp. 1946-1956, Sep. 2010.
[79] R. R. Harrison, P. T. Watkins, R. J. Kier, R. O. Lovejoy, D. J. Black, B. Greger, and F. Solzbacher, "A low-power integrated circuit for a wireless 100-electrode neural recording system," *IEEE J. Solid-State Circuits*, vol. 42, no. 1, pp. 123-133, Jan. 2007.
[80] J. Hirai, T. W. Kim, and A. Kawamura, "Study on intelligent battery charging using inductive transmission of power and information," *IEEE Trans. on Power Electronics*, vol. 15, no. 2, pp. 335-345 , Mar. 2000.
[81] S.C.Q. Chen and V. Thomas, "Optimization of inductive RFID technology," *in Proc. IEEE Int. Symp. Electron. Environ.*, pp. 82-87, May 2001.
[82] G. Lazzi, "Thermal effects bioimplants," *IEEE Eng. Med. Biol. Mag.*, vol. 24, pp. 75-81, Sep. 2005.
[83] Federal Communication Commission, Wireless Medical Telemetry [Online]. Available: http://www.wireless.fcc.gov/services/index.htm?job=service_home&id=wireless_medical_telemetr.
[84] W. H. Ko, S. P. Liang, and C. D. F. Fung, "Design of radio-frequency powered coils for implant instruments," *Med. Biol. Eng. Comput.*, vol. 15, pp. 634-640, 1977.

[85] N. N. Donaldson and T. A. Perkins, "Analysis of resonant coupled coils in the design of radio frequency transcutaneous links," *Med. Biol. Eng. Comput.*, vol. 21, no. 5, pp. 612-627, Sep. 1983.
[86] W. J. Heetderks, "RF powering of millimeter and submillimeter-sized neural prosthetic implants," *IEEE Trans. Biomed. Eng.*, vol. 35, no. 5, pp. 323-327, May 1988.
[87] C. M. Zierhofer and E. S. Hochmair, "High-efficiency coupling-in sensitive transcutaneous power and data transmission via an inductive link," *IEEE Trans. Biomed. Eng.*, vol. 37, no. 7, pp. 716-722, July 1990.
[88] C. M. Zierhofer and E. S. Hochmair, "Geometric approach for coupling enhancement of magnetically coupled coils," *IEEE Trans. Biomed. Eng.*, vol. 43, no. 7, pp. 708-714, July 1996.
[89] C. R. Neagu, H. V. Jansen, A. Smith, J. G. E. Gardeniers, and M. C. Elwanspoek, "Characterization of a planar microcoil for implantable microsystems," *Sens. Actuat. A*, vol. 62, pp. 599-611, July 1997.
[90] G. A. Kendir, W. Liu, G. Wang, M. Sivaprakasam, R. Bashirullah, M. S. Humayun, and J. D. Weiland, "An optimal design methodology for inductive power link with class-E amplifier," *IEEE Trans. on Circuits and Systems I*, vol. 52, pp. 857-866, May 2005.
[91] Z. Yang, W. Liu, and E. Basham, "Inductor modeling in wireless links for implantable electronics," *IEEE Trans. on Magnetics*, vol. 43, pp. 3851-3860, Oct. 2007.
[92] A. Kurs, A. Karalis, R. Moffatt, J. D. Joannopoulos, P. Fisher, and M. Soljacic, "Wireless power transfer via strongly coupled magnetic resonances," *Science Express*, vol. 317, pp. 83-86, July 2007.
[93] H. Miranda, V. Gilja, C.A. Chestek, K.V. Shenoy, and T.H. Meng, "HermesD: a high-rate long-range wireless transmission system for simultaneous multichannel neural recording applications," *IEEE Trans. Biomed. Cir. Syst.*, vol. 4, no. 3, pp. 181-191, June 2010.
[94] M. Rizk, C.A. Bossetti, T.A. Jochum, S.H. Callender, M.A.L. Nicolelis, D.A. Turner, and P.D. Wolf, "A fully implantable 96-channel neural data acquisition system," *J. Neural Eng.*, vol. 6, no. 2, art. 026002, Apr. 2009.
[95] D. M. Pozar, *Microwave Engineering*, 2nd ed. New York: Wiley, 1998, ch. 4.
[96] A. Kurs, A. Karalis, R. Moffatt, J. D. Joannopoulos, P. Fisher, and M. Soljacic, "Wireless power transfer via strongly coupled magnetic resonances," *Science Express*, vol. 317, pp. 83-86, July 2007.
[97] R. E. Hamam, A. Karalis, J. D. Joannopoulos, and M. Soljacic, "Efficient weakly-radiative wireless energy transfer: An EIT-like approach," *Annals of Physics*, vol. 324, pp.1783-1795, Aug 2009.
[98] M. K. Kazimierczuk, *RF Power Amplifiers*, NY: Wiley, 2008.
[99] J. Riquelme, F. Segura, and M. Oses, "Simple and efficient inductive telemetry system with data and power transmission," *Microelectronics Journal*, vol. 39, pp. 103-111, Jan. 2008.
[100] C. Wentz, J. Bernstein, P. Monahan, A. Guerra, A. Rodriguez, and E. Boyden, "A wirelessly powered and controlled device for optical neural control of freely-behaving animals," *J. Neural Eng.*, vol. 8, Aug. 2011.
[101] H. Lee and M. Ghovanloo, "An integrated power-efficient active rectifier with offset-controlled high speed comparators for inductively-powered applications," *IEEE Trans. Circuits Syst. I*, vol. 58, no. 8, pp. 1749-1760, Aug. 2011.
[102] R. Xue, K. Cheng, and M. Je, "High-efficiency wireless power transfer for biomedical implants by optimal resonant load transformation," *IEEE Trans. Biomed. Cir. Syst.*, vol. 60, pp. 867-874, Apr. 2013.
[103] M. Zargham and P. Gulak, "Maximum achievable efficiency in near-field coupled power-transfer systems," *IEEE Trans. Biomed. Cir. Syst.*, vol. 6, pp. 228-245, June 2012.
[104] T. Le, J. Han, A. Jouanne, K. Marayam, and T. Fiez, "Piezoelectric micro-power generation interface circuits," *IEEE J. Solid-State Cir.*, vol. 41, no. 6, pp. 1411-1420, Jun. 2006.
[105] A. Rush and P. Troyk, "A power and data link for a wireless-implanted neural recording system," *IEEE Trans. Biomed. Cir. and Sys.*, vol. 59, pp. 3255-3262, Nov. 2012.
[106] U. Jow and M. Ghovanloo, "Optimization of data coils in a multiband wireless link for neuroprosthetic implantable devices," *IEEE Trans. Biomed. Circuits Sys.*, vol. 4, no. 5, pp. 301–310, Oct. 2010.
[107] G. Wang, P. Wang, Y. Tang, and W. Liu, "Analysis of dual band power and data telemetry for biomedical implants," *IEEE Trans. Biomed. Cir. Syst.*, vol. 6, pp. 208-215, June 2012.
[108] G. Simard, M. Sawan, and D. Massicotte, "Novel coils topology intended for biomedical implants with multiple carrier inductive link," *Proc. IEEE Int. Symp. Cir. Syst.*, pp. 537–540, May 2009.

[109] K. Chen, Y. Lo, and W. Liu, "A 37.6mm2 1024-channel high-compliance- voltage SoC for epiretinal prostheses," *Digest of technical papers IEEE Intl. Solid-State Cir. Conf.*, pp. 294-295, Feb. 2013.
[110] E. Greenwald, et al., "A VLSI neural monitoring system with ultra-wideband telemetry for awake behaving subjects," *IEEE Trans. Biomed. Circuits and Systems*, vol. 5, no. 2, pp. 112-119, Apr. 2011.
[111] H. Miranda and T. H. Meng, "A programmable pulse UWB transmitter with 34% energy efficiency for multichannel neuro-recording systems," *in Proc. Custom Integr. Circ. Conf. (CICC'10)*, pp. 1-4, Sept. 2010.
[112] M. S. Chae, et al., "A 128 channel 6 mW wireless neural recording IC with spike feature extraction and UWB transmitter," *IEEE Trans. Neural Syst. Rehab. Eng.*, vol. 17, no. 4, pp. 312-321, Aug. 2009.
[113] A. Hajimiri and T. H. Lee, "A general theory of phase noise in electrical oscillators," *IEEE J. Solid-State Circuits*, vol. 33, no. 2, pp. 179-194, Feb. 1998.
[114] Millard, R.E., and, Shepherd, R.K., "A fully implantable stimulator for use in small laboratory animals," *J. Neuroscience Methods*, vol. 166, pp. 168-177, July 2007.
[115] D. Russell, D. McCormick, A. Taberner, P. Nielsen, P. Hu, D. Budgett, M. Lim, and S. Malpas. "Wireless power delivery system for mouse telemeter," *IEEE Biomed. Circ. Sys. Conf.*, pp. 273–276, Nov. 2009.
[116] P. Cong, N. Chaimanonart, W. Ko, and D. Young, "A wireless and batteryless 130mg 300μW 10b implantable blood-pressure-sensing microsystem for real-time genetically engineered mice monitoring", *Digest of technical papers IEEE Intl. Solid State Cir. Conf.*, pp. 428-429, Feb. 2009.
[117] Kendall Research Systems, [Online] Available: http://www.kendallresearchsys.com/.
[118] M. Kiani, U. Jow, and M. Ghovanloo, "Design and optimization of a 3-coil inductive link for efficient wireless power transmission," *IEEE Trans. Biomed. Cir. Syst.*, vol. 5, pp. 579-591, Dec. 2011.
[119] M. Kiani and M. Ghovanloo, "The circuit theory behind coupled-mode magnetic resonance based power transmission," *IEEE Trans. Cir. Syst I.*, vol. 59, pp. 2065-2074, Sep. 2012.
[120] M. Kiani and M. Ghovanloo, "A figure-of-merit for designing high performance inductive power transmission links," *IEEE Trans. Ind. Elect.*, vol. 60, pp. 5292-5305, Nov. 2013.
[121] M. Kiani and M. Ghovanloo, "An RFID-based closed loop wireless power transmission system for biomedical applications," *IEEE Trans. Cir. Syst. II*, vol. 57, pp. 260-264, Apr. 2010.
[122] M. Kiani and M. Ghovanloo, "A 20 Mbps pulse harmonic modulation transceiver for wideband near-filed data transmission," *IEEE Transaction on Circuits and Systems-II*, 2013.
[123] H. Park, M. Kiani, H. Lee, J. Kim, J. Block, B. Gosselin, and M. Ghovanloo, "A wireless magnetoresistive sensing system for an intraoral tongue-computer interface," *IEEE Transaction on Biomedical Circuits and Systems*, vol. 6, pp. 571-585, Dec. 2012.
[124] M. Kiani and M. Ghovanloo, "An RFID-based closed loop wireless power transmission system for biomedical applications," *IEEE Transaction on Circuits and Systems-II*, vol. 57, no. 4, pp. 260-264, Apr. 2010.
[125] D. Ahn, M. Kiani, and M. Ghovanloo, "Enhanced wireless power transmission using strong paramagnetic response," *IEEE Transaction on Magnetics*, 2013.
[126] M. Kiani and M. Ghovanloo, "A 13.56-Mbps pulse delay modulation based transceiver for simultaneous near-field power and data transmission," Submitted to *IEEE Transaction on Biomedical Circuits and Systems*, 2013.
[127] P. McMenamin, U. Jow, M. Kiani, and M. Ghovanloo, "A smart cage for behavioral experiments on small freely behaving animal subjects," *IEEE Neural Interface Conference*, 2013.
[128] M. Kiani, K. Yong, F. Zhang, K. Oweiss, and M. Ghovanloo, "Evaluation of a closed loop inductive power transmission system on an awake behaving animal subject," *IEEE 33rd Eng. in Med. and Biol. Conf.*, pp. 7658-7661, Sep. 2011.
[129] M. Kiani and M. Ghovanloo, "Pulse delay modulation (PDM) A new wideband data transmission method to implantable medical devices in presence of a power link," *IEEE Biomed. Cir. Syst. Conf.*, 2012.
[130] P. McMenamin, U. Jow, M. Kiani, and M. Ghovanloo, "EnerCage: a novel smart wireless power and tracking system for long-term and large-arena experiments," *IEEE Biomed. Cir. Syst. Conf. (BioCAS)*, 2012.

[131] M. Kiani, and M. Ghovanloo, “A figure-of-merit for design of high performance inductive power transmission links for implantable microelectronic devices,” *IEEE 34th Eng. Med. Biol. Conf. (EMBC)*, pp. 847-850, Sept. 2012.
[132] H. Park, B. Gosselin, M. Kiani, H. Lee, J. Kim, X. Huo, and M. Ghovanloo, "A wireless magnetoresistive sensing system for an intra-oral tongue-computer interface," *IEEE Int. Solid State Cir. Conf. (ISSCC)*, pp. 124-126, Feb. 2012.
[133] U, Jow, M. Kiani, X. Huo, and M. Ghovanloo, “Towards a smart experimental arena for long-term electrophysiology experiments,” *IEEE Biomed. Cir. Syst. Conf. (BioCAS)*, pp. 121-124, 2011.
[134] F. Inanlou, M. Kiani, and M. Ghovanloo, “A novel pulse-based modulation technique for wideband low power communication with neuroprosthetic devices,” *IEEE 32th Eng. Med. Biol. Conf. (EMBC)*, pp. 5326-5329, Sep. 2010.
[135] S. Lee, H. Lee, M. Kiani, U. Jow, and M. Ghovanloo, "An inductively powered scalable 32-ch wireless neural recording system-on-a-chip with power scheduling for neuroscience applications," *IEEE Int. Solid State Cir. Conf. (ISSCC)*, pp. 120-121, Feb. 2010.
[136] M. Kiani, and M. Ghovanloo, “A closed loop wireless power transmission system using a commercial RFID transceiver for biomedical applications,” *IEEE 31st Eng. Med. Biol. Conf. (EMBC)*, pp. 3841-3844, Sep. 2009.
[137] N. Sadiku, *Elements of Electromagnetics*, Orlando, FL: Sounders College Press, 1994.
[138] H. A. A. Wheeler, “Formulas for the skin effect,” *Proc. of the IRE*, vol. 30, issue 9, pp.412-424, Sep. 1942.
[139] W. B. Kuhn and N. M. Ibrahim, “Analysis of current crowding effects in multiturn spiral inductors,” *IEEE Transactions on Microwave Theory and Techniques*, vol. 49, pp. 31-38, Jan. 2001.